



National Library
of Canada

Bibliothèque nationale
du Canada

Canadian Theses Service

Services des thèses canadiennes

Ottawa, Canada
K1A 0N4

CANADIAN THESES

NOTICE

The quality of this microfiche is heavily dependent upon the quality of the original thesis submitted for microfilming. Every effort has been made to ensure the highest quality of reproduction possible.

If pages are missing, contact the university which granted the degree.

Some pages may have indistinct print especially if the original pages were typed with a poor typewriter ribbon or if the university sent us an inferior photocopy.

Previously copyrighted materials (journal articles, published tests, etc.) are not filmed.

Reproduction in full or in part of this film is governed by the Canadian Copyright Act, R.S.C. 1970, c. C-30.

**THIS DISSERTATION
HAS BEEN MICROFILMED
EXACTLY AS RECEIVED**

THÈSES CANADIENNES

AVIS

La qualité de cette microfiche dépend grandement de la qualité de la thèse soumise au microfilmage. Nous avons tout fait pour assurer une qualité supérieure de reproduction.

S'il manque des pages, veuillez communiquer avec l'université qui a conféré le grade.

La qualité d'impression de certaines pages peut laisser à désirer, surtout si les pages originales ont été dactylographiées à l'aide d'un ruban usé ou si l'université nous a fait parvenir une photocopie de qualité inférieure.

Les documents qui font déjà l'objet d'un droit d'auteur (articles de revue, examens publiés, etc.) ne sont pas microfilmés.

La reproduction, même partielle, de ce microfilm est soumise à la Loi canadienne sur le droit d'auteur, SRC 1970, c. C-30.

**LA THÈSE A ÉTÉ
MICROFILMÉE TELLE QUE
NOUS L'AVONS REÇUE**

THE UNIVERSITY OF ALBERTA

FINITE ELEMENT ANALYSIS OF STRAIN SOFTENING MATERIAL

by

DAVE HUNG-KWAN CHAN

A THESIS

SUBMITTED TO THE FACULTY OF GRADUATE STUDIES AND RESEARCH
IN PARTIAL FULFILMENT OF THE REQUIREMENTS FOR THE DEGREE
OF DOCTOR OF PHILOSOPHY

DEPARTMENT OF CIVIL ENGINEERING

EDMONTON, ALBERTA

SPRING 1986

Permission has been granted to the National Library of Canada to microfilm this thesis and to lend or sell copies of the film.

The author (copyright owner) has reserved other publication rights, and neither the thesis nor extensive extracts from it may be printed or otherwise reproduced without his/her written permission.

L'autorisation a été accordée à la Bibliothèque nationale du Canada de microfilmer cette thèse et de prêter ou de vendre des exemplaires du film.

L'auteur (titulaire du droit d'auteur) se réserve les autres droits de publication; ni la thèse ni de longs extraits de celle-ci ne doivent être imprimés ou autrement reproduits sans son autorisation écrite.

ISBN 0-315-30261-5

Professor N. Morgenstern
Dept. of Civil Engineering
University of Alberta
Edmonton, Alberta
T6G 2G7

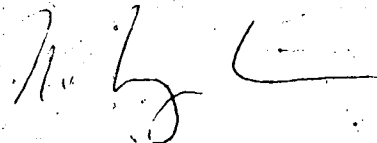
Oct. 10, 1985

To whom it may concern:

This is to authorize Mr. Dave H. Chan to make copies of the figures in the following publications for the purpose of producing his Doctoral thesis at the University of Alberta entitled "Finite Element Analysis of Strain Softening Material":

1. EBA Engineering Consultant Ltd. and Norbert R. Morgenstern Engineering Consultant Ltd. 1979. "Edmonton Convention Center - Geotechnical Evaluation". A report submitted to the City of Edmonton.
2. EBA Engineering Consultant Ltd. and Norbert R. Morgenstern Engineering Consultant Ltd. 1981. "Edmonton Convention Center - Final Construction Inspection Report". A report submitted to the City of Edmonton, Department of Real Estate and Housing.
3. EBA Engineering Consultant Ltd. and Norbert R. Morgenstern Engineering Consultant Ltd. 1984. "Edmonton Convention Center - Geotechnical Instrumentation Report". A report submitted to the City of Edmonton, Department of Real Estate and Housing.

Yours Sincerely,



N.R. Morgenstern

EBA Engineering Consultants Ltd.

1985 10 10



**EARTH-SCIENCES
ENGINEERING**

E. W. Brooker, President
D. W. Hayley, Vice President
L. A. Balanko
C. B. Dawley
C. T. Hwang
A. B. MacDoryld

To whom it may concern:

This is to authorize Mr. Dave H. Chan to make copies of the figures in the following publications for the purpose of producing his Doctoral thesis at the University of Alberta entitled "Finite Element Analysis of Strain Softening Material":

1. EBA Engineering Consultants Ltd. and Norbert R. Morgenstern Engineering Consultant Ltd. 1979. "Edmonton Convention Center - Geotechnical Evaluation". A report submitted to the City of Edmonton.
2. EBA Engineering Consultants Ltd. and Norbert R. Morgenstern Engineering Consultant Ltd. 1981. "Edmonton Convention Center - Final Construction Inspection Report". A report submitted to the City of Edmonton, Department of Real Estate and Housing.
3. EBA Engineering Consultants Ltd. and Norbert R. Morgenstern Engineering Consultant Ltd. 1984. "Edmonton Convention Center - Geotechnical Instrumentation Report". A report submitted to the City of Edmonton, Department of Real Estate and Housing.

Yours Sincerely,

EBA Engineering Consultants Ltd.

L. A. Balanko, P.Eng.
Principal Consultant

/cgb

THE UNIVERSITY OF ALBERTA

RELEASE FORM

NAME OF AUTHOR DAVE HUNG-KWAN CHAN
TITLE OF THESIS FINITE ELEMENT ANALYSIS OF STRAIN
 SOFTENING MATERIAL
DEGREE FOR WHICH THESIS WAS PRESENTED DOCTOR OF PHILOSOPHY
YEAR THIS DEGREE GRANTED SPRING 1986

Permission is hereby granted to THE UNIVERSITY OF ALBERTA LIBRARY to reproduce single copies of this thesis and to lend or sell such copies for private, scholarly or scientific research purposes only.

The author reserves other publication rights, and neither the thesis nor extensive extracts from it may be printed or otherwise reproduced without the author's written permission.

(SIGNED) *Dave Chan*

PERMANENT ADDRESS:

143 Canongate Trail
Scarborough, Ontario
M1V 3G8 Canada

DATED October 15, 1985

THE UNIVERSITY OF ALBERTA
FACULTY OF GRADUATE STUDIES AND RESEARCH

The undersigned certify that they have read, and recommend to the Faculty of Graduate Studies and Research, for acceptance, a thesis entitled FINITE ELEMENT ANALYSIS OF STRAIN SOFTENING MATERIAL submitted by DAVE HUNG-KWAN CHAN in partial fulfilment of the requirements for the degree of DOCTOR OF PHILOSOPHY.

Dr. N.R. Morgenstern

Supervisor

Dr. Z. Eisenstein

Dr. S. Thomson

Dr. T. Hruday

Dr. J.R. Colbourne

Prof. Hon Yim Ko

External Examiner

Date..October.10,..1985.....

To my wife Michele

ABSTRACT

The analysis of progressive failure requires the modelling of a material with strain softening behaviour. The finite element plasticity formulation with various strain softening models is developed to model soil deformation under fully undrained conditions. The first model, which is based on the analytical work by Prevost and Hoeg, is limited to specific stress strain relationships. Therefore, there is a need to develop more general numerical models for analyzing a variety of strain softening materials. The Elastic Brittle Plastic model and the Hyperbolic Strain Softening model are subsequently developed in this research. Numerous simplified and complicated problems have been analyzed to illustrate the effectiveness and applicability of these models. The development of the yielding zone and the propagation of a shear band have been studied in detail in several cases. It is found that in the gradual development of the yielding zone in soil under non-homogeneous deformation, the ultimate collapse load is dependent upon the rate of the post peak softening behaviour of the material. For example, in the study of the bearing capacity of a strip footing on strain softening soil, the maximum footing pressure is not only a function of the peak and the residual strength, but is also highly dependent upon the rate of post peak softening of the soil. Therefore, it is not possible to deduce the material stress strain behaviour based on the response of the system. The

conclusion is extended to the testing of strain softening soil using conventional apparatus in which progressive development of the yielding zone has most likely occurred. The simulation of a plane strain test of a brittle plastic soil reveals a load displacement response of a perfectly plastic soil and the difference between the peak and residual strength is not observed as a result of progressive failure.

The yielding of a strain softening material often leads to the formation of a shear zone and the deformation behaviour of the soil mass is localized in this region. It has been shown that the elasto-plastic finite element formulation presented here satisfies the requirement for shear band bifurcation in capturing localized deformation. A plane strain test has been simulated to illustrate the propagation of the shear band.

Since soil behaviour is dependent on effective stress, there is a need to analyze soil structure using effective stress. A fully undrained or fully drained effective stress finite element formulation has been presented. In this approach, the Skempton pore pressure parameters, A and B , are used in the formulation.

Finally the numerical model is applied in an analysis of the behaviour of the excavation for the Edmonton Convention Center. It is demonstrated that shear band initiation and propagation can be modelled with reasonable accuracy using the numerical models presented. However, it

is also found that the results are sensitive to the in-situ stress field and the material parameters used in the model. Accurate determination of material parameters is essential in predicting the deformation response in soil structure interaction problems.

In the course of the development of the finite element model, difficulties have been encountered concerning solution convergence. Various techniques of stress calculation have been developed to stabilize convergence characteristics of non-linear models especially for strain softening material. Other numerical techniques, such as the extended skyline method, are developed to obtain solutions for non-symmetrical matrices.

ACKNOWLEDGEMENT

The author wishes to express his gratitude to his supervisor Dr. N. R. Morgenstern for his interest and intense enthusiasm in the subject, and his guidance and support for this research. His ideas, time and valuable discussions throughout the course of this research in making it a success are very much appreciated.

Many thanks to Dr. D. W. Murray and Dr. T. M. Hrudehy for their discussions on the numerical aspects of this research. The financial support provided by the Killam Memorial Trust Fund is gratefully acknowledged. Thanks to Dr. S. Thomson for his work on the final review of this thesis. The information made available by EBA Engineering Consultant Ltd. and Norbert R. Morgenstern Consultant Ltd. for the analysis of the Edmonton Convention Center is appreciated. In particular, thanks to Dr. A. Krishnayya of EBA Engineering Consultant Ltd. for the discussion of the analysis of the Edmonton Convention Center. The computer facilities provided by the University of Alberta and also the supercomputer facility provided by the University of Calgary and the Alberta Government in making the numerical work possible are acknowledged. Also thanks to his friends, Mr. T. Casey for the use of his graphic program and his help on the university computer facilities and Mr. Andre Chan for the use of the laboratory test results.

The author also wishes to thank his mother and brother Simon and other members of his family for their

encouragement and support for his study abroad for which he is very much indebted.

Finally the author wish to dedicate this thesis to his beloved wife, Michele, for her great endurance, patience and encouragement throughout his study. Her kindness and positive attitude have provided much hope and help in overcoming many obstacles in the past few years.

Table of Contents

Chapter	Page
1. INTRODUCTION	1
1.1 Problems of Progressive Failure	1
1.2 Purpose of the Research	13
1.3 Notations	15
2. FINITE ELEMENT FORMULATION FOR STRAIN SOFTENING MATERIAL	17
2.1 Theory of Strain Softening Material	17
2.2 Elasto-Plastic Finite Element Formulation	22
2.3 Yield Criteria and Constitutive Matrix	29
2.4 Finite Element Model for Strain Softening Material	33
2.5 Expansion of a Thickwalled Cylinder	38
2.6 Computer Implementation of the Finite Element Method	49
2.6.1 Convergence Scheme and Convergence Criteria	49
2.6.2 Methods of Stress Calculation	53
2.6.3 Computer Program SAFE	58
2.7 Conclusion	58
3. FINITE ELEMENT SIMULATION OF SHEAR BAND DEFORMATION	60
3.1 Theory of Localized Deformation	61
3.2 Eigenvalue Analysis of Elasto-Plastic Finite Element Formulation	65
3.2.1 Physical Meaning of Eigenvalues and Eigenvectors	66
3.2.2 Eigenvalue Analysis of Elasto-Plastic matrix for Elastic Perfectly Plastic Material	68

3.2.3	Eigenvalue Analysis of Elasto-Plastic matrix for Strain Hardening and Softening Material	73
3.3	An Elastic Brittle Plastic Model	76
3.4	Modelling Shear Band Deformation in a Uniaxial Plane Strain Test	79
3.5	The Finite Element Method in Modelling Shear Band	86
3.6	Shear Band Propagation in a Dam Foundation	93
3.7	Conclusion	105
4.	HYPERBOLIC STRAIN SOFTENING MODEL	107
4.1	Introduction	107
4.2	Theory of the Hyperbolic Strain Softening Model	109
4.3	Finite Element Formulation	112
4.4	Determination of the a and b Parameters from Triaxial Test Results	114
4.5	Triaxial Test of a Stiff Brittle Clay	122
4.6	Comparison of Finite Element Results	126
4.7	Bearing Capacity Analysis of Strain Softening Material	127
4.8	Conclusion	138
5.	EFFECTIVE STRESS APPROACH OF UNDRAINED ANALYSIS	139
5.1	Undrained Finite Element Formulation	140
5.1.1	Matrix Solution Scheme	145
5.2	Expansion of a Thickwalled Cylinder	146
5.2.1	Elastic Perfectly Plastic Model	147
5.2.2	Undrained Analysis of Elastic Perfectly Plastic Material	153
5.2.3	Undrained Analysis of Strain Softening Material	160

5.3	Bearing Capacity Analysis	163
5.3.1	Bearing Capacity of $\phi = 0$ Material	172
5.3.2	Bearing Capacity of Frictional Material	176
5.3.3	Effective Stress Undrained Analysis	180
5.3.4	Cost of the Finite Element Analysis	189
5.4	Conclusion	189
6.	EXCAVATION BEHAVIOUR OF EDMONTON CONVENTION CENTRE	191
6.1	Introduction	191
6.2	Geology of the Site	192
6.3	Location of the Edmonton Convention Center	194
6.4	Soil Stratigraphy and Material Properties	196
6.4.1	Soil Stratigraphy	197
6.4.2	Ground Water	202
6.4.3	Material Properties	204
6.4.4	Material Properties of the Shear Zone and Bedrock	204
6.4.5	Excavation for the Convention Center	208
6.4.6	Tangent Piles Wall and Anchor Support	208
6.5	Excavation Performance	211
6.5.1	Slope Indicators	211
6.5.2	Heave Gauges and Settlement Plugs	216
6.6	Linear Elastic Finite Element Analysis	218
6.7	The Effect of k_0 on the Behaviour of the Excavation	225
6.8	The Effect of Elastic Parameters on the Behaviour of the Excavation	234
6.9	Non-Linear Finite Element Analysis	242
6.10	Conclusion	266

7. CONCLUSIONS	268
7.1 Conclusions	268
7.2 Recommendation for Further Research	272
BIBLIOGRAPHY	276
APPENDIX A	282
APPENDIX B	304
APPENDIX C	308
APPENDIX D	314
APPENDIX E	333

List of Tables

Table	Page
2.1 Yield Functions and Gradients	32
3.1 Eigenvalue Analysis of the Elasto-Plastic Constitutive Matrix	71
3.2 Displacements at A with Different Aspect Ratio	92
3.3 Material Parameters used in the Finite Element Analysis	95
4.1 Summary of Soil Parameters of a Stiff Clay	123
6.1. Soil Parameters of the Edmonton Convention Center Site	205
6.2 Anchor Forces Applied in the Finite Element Analysis	226
6.3 Summary of the values of the Elastic Modulus in the Linear Elastic Analyses	235
6.4 Summary of Material Parameters in Non-linear Analysis	250
A.1 Summary of Result of Stress Analysis	298

List of Figures

Figure	Page
1.1 Strain Hardening and Strain Softening Behaviour of Soil	3
1.2 Mobilization of Shear Strength of Slopes for Strain Hardening and Strain Softening Soil	5
2.1 Kinematic and Isotropic Hardening of Plasticity Model	30
2.2 Stress Strain Curve of Strain Softening Model	35
2.3 Expansion of a Long Cylinder	39
2.4 Pressure Displacement Response of Thickwalled Cylinder	42
2.5 Effect of Integration Points on the Response of Thickwalled Cylinder	44
2.6 Hoop Stress Distribution $I(B) = 0.25$	45
2.7 Hoop Stress Distribution $I(B) = 0.50$	46
2.8 Hoop Stress Distribution $I(B) = 0.75$	47
2.9 Unloading Response of Thickwalled Cylinder	48
2.10 Unloading Hoop Stress Distribution	50
3.1 Eigen Mode Shape of Elastic Deformation	69
3.2 Eigenvalues of Strain Softening Material	74
3.3 Stress Strain Relationship of Brittle Plastic Material	77
3.4 Finite Element Idealization of Soil Specimen	80
3.5 Stress Strain Response of Plane Strain Specimen	82
3.6 Yield Zone Development of Plane Strain Specimen	85
3.7 Deformed Shape of Plane Strain Specimen	87

Figure	Page
3.8 Different Stress Conditions to Test Thin Elements	90
3.9 Finite Element Idealization of Dam and Foundation	96
3.10 Mobilization of Shear Strength along the Shear Zone	98
3.11 Displacement Vectors of the Dam and Foundation	100
3.12 Displacement of Dam Foundation	101
3.13 Mobilization of Shear Strains along the Shear Zone	103
3.14 Mobilization of Shear Strength of Brittle Plastic Material	104
4.1 Stress Strain Curve for the Hyperbolic Strain Softening Model	113
4.2 Normalized Plot for the Hyperbolic Strain Softening Model	115
4.3 Stress Strain Relationship for the Hyperbolic Strain Softening Model	119
4.4 Calculation of Strains and Elastic Modulus for Anisotropic Consolidation	121
4.5 Triaxial Test Results of Stiff Clay	124
4.6 Triaxial Test Results of Stiff Clay in Normalized Plot	125
4.7 Simulation of Triaxial Test	128
4.8 Stress Strain Relationship used in Bearing Capacity Analysis	132
4.9 Pressure Displacement Response of Footing	133
4.10 Development of Yield Zone under the Footing	135
5.1 Pressure Displacement Response of the Thickwalled Cylinder	150

Figure	Page
5.2 Hoop Stress Distribution	151
5.3 Pressure Displacement Response of Undrained Analysis	155
5.4 Hoop Stress Distribution	157
5.5 Pore Pressure Distribution	158
5.6 Hoop Stress (Total) Distribution	159
5.7 Hoop Stress Distribution	161
5.8 Pore Pressure Distribution	162
5.9 Pressure Displacement Response of Undrained Analysis	164
5.10 Hoop Stress(Effective) Distribution	165
5.11 Pore Pressure Distribution	166
5.12 Hoop Stress(Total) Distribution	167
5.13 Finite Element Idealization of Soil Foundation	169
5.14 Displacement vs Depth of Foundation	171
5.15 Pressure Displacement Response of Footing	173
5.16 Development of Yield Zone under a Footing	175
5.17 Pressure Displacement Response of Footing	178
5.18 Yield Zone Development of Footing	179
5.19 Center Line Displacement vs Pore Pressure β	182
5.20 Pore Pressure Contour - Linear Elastic Analysis	183
5.21 Center Line Displacement vs Footing Pressure	185
5.22 Yield Zone Development of Undrained Analysis	186

Figure	Page
5.23 Pore Pressure Contours of Plastic Analysis	188
6.1 Geographic Location of the Edmonton Convention Center	193
6.2 Plan View of the Edmonton Convention Center Site - EBA and NRM Consultants Ltd.	195
6.3 Soil Stratigraphy of Section A-A - EBA and NRM Consultants Ltd.	198
6.4 Soil Stratigraphy of Section B-B - EBA and NRM Consultants Ltd.	199
6.5 Soil Stratigraphy of Section C-C - EBA and NRM Consultants Ltd.	200
6.6 Soil Stratigraphy of Section D-D - EBA and NRM Consultants Ltd.	201
6.7 Schematic of Translational Failure - EBA and NRM Consultants Ltd.	203
6.8 Floor Plan of the Excavation of the Edmonton Convention Center - EBA and NRM Consultant Ltd.	209
6.9 Observed Movement of Slope Indicator (SI-804) - EBA and NRM Consultants Ltd.	213
6.10 Slope Indicator (SI-804) Movement vs Volume of Excavation - EBA and NRM Consultants Ltd.	214
6.11 Slope Indicator (SI-802) Movement vs Volume of Excavation - EBA and NRM Consultants Ltd.	215
6.12 Heave of Excavation Floor (HG-4) - EBA and NRM Consultants Ltd.	217
6.13 Finite Element Idealization of the Edmonton Convention Center Site	222
6.14 Material Sequence used in the Finite Element Analysis	223

Figure	Page
6.15 Mobilized Friction along Lower Shear Zone - (Switch-on-Gravity)	229
6.16 Mobilized Friction along Lower Shear Zone - Linear Elastic Analysis	230
6.17 Movement of Soil behind Tangent Pile Wall - Linear Elastic Analysis	232
6.18 Heave of Excavation Floor - Linear Elastic Analysis	233
6.19 Mobilized Friction along Lower Shear Zone - Linear Elastic Analysis	237
6.20 Movement of Soil behind Tangent Pile Wall - Linear Elastic Analysis	238
6.21 Heave of the Excavation Floor - Linear Elastic Analysis	240
6.22 Mobilized Friction along Lower Shear Zone - Non-Linear Analysis	251
6.23 Movement of Soil behind Tangent Pile Wall - Non-Linear Analysis	252
6.24 Heave of Excavation Floor - Non-Linear Analysis	253
6.25 Comparison of Observed and Computed Heave - Final Non-Linear Analysis	259
6.26 Heave of Excavation Floor - Final Non-Linear Analysis	260
6.27 Movement of Soil behind Tangent Pile Wall - Final Non-Linear Analysis	261
6.28 Mobilized Friction along Lower Shear Zone - Final Non-linear Analysis (1)	262
6.29 Mobilized Friction along Lower Shear Zone - Final Non-linear Analysis (2)	263
A.1 Illustration of the Euler Forward Method	288
A.2 Illustration of the Improved Euler Method	291
A.3 Stress Path of Uniaxial Plane Strain Test	295

Figure	Page
A.4 Stress Path of Expansion of Thickwalled Cylinder	296
A.5 Uniaxial Compression of Hyperbolic Elastic Soil	299
A.6 Plane Strain Compression Test of Elastic Perfectly Plastic Material	301
A.7 Stress Path of Plane Strain Test	302
B.1 Solution Procedure of Interval Halving Technique	306
C.1 Stress Calculation Method for Elastic Brittle Plastic Material	312
D.1 Compatibility Relationships of Discontinuity	315
D.2 Body with one Surface of Discontinuity	319
D.3 Body with Two Surfaces of Discontinuity	327
D.4 Different Modes of Shear Band Bifurcation	332
E.1 Reduced Storage Scheme of the Skyline Method	337
E.2 Reduced Storage Scheme of the Extended Skyline Method	339
E.3 Matrix Reduction using Gauss Elimination Method	339
E.4 Listing of Subroutine SOLVER	345

1. INTRODUCTION

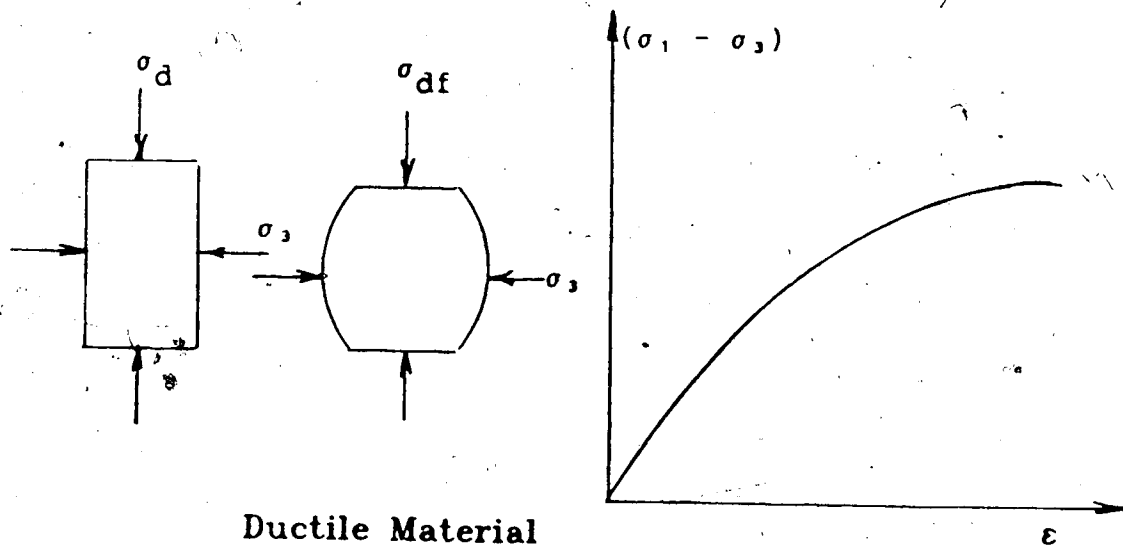
1.1 Problems of Progressive Failure

The analysis of soil structures has traditionally been divided into two main classes of problem. In the first class of problem, the common objective is to determine the pressure or forces applied on the soil mass in order to reach a state of incipient failure. To solve this class of problem, it is sufficient to know the strength of the soil and the stresses inside the soil at the state of failure. The deformation of the soil is not considered and therefore, only the overall equilibrium is satisfied in the analysis. The solution to this class of problem will provide limit loads for the design of soil structures. Examples of this class of problem are the calculation of the bearing capacity of a footing, the factor of safety of a slope and the passive and active pressure on a retaining wall.

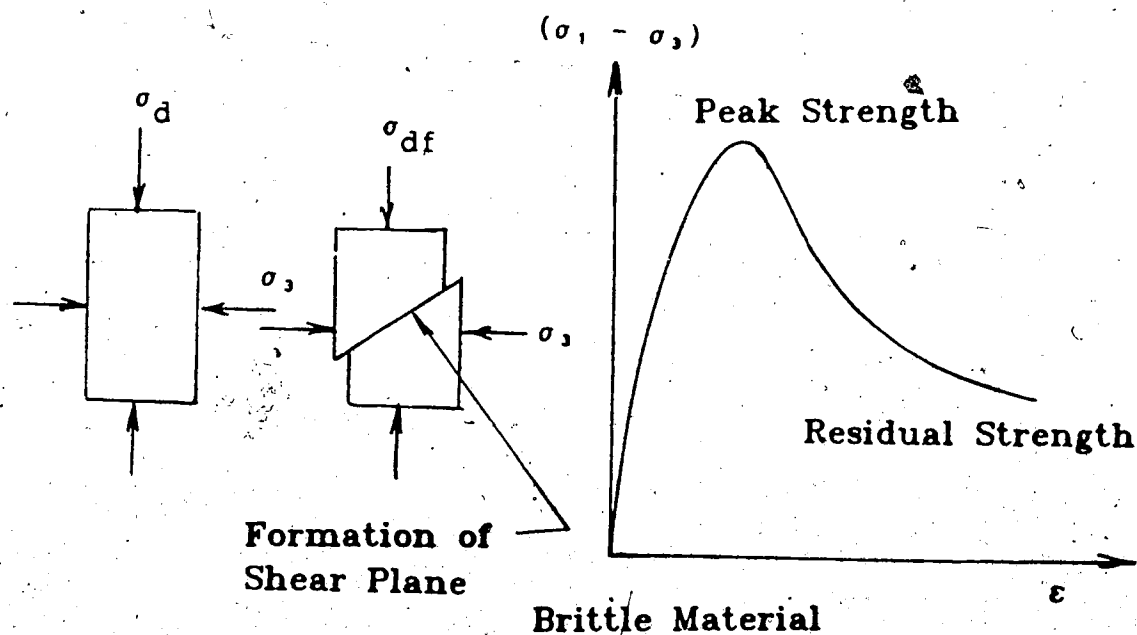
In the second class of problem, the amount of deformation in the soil under some externally applied load is the main concern. Usually the state of stress at every point in the soil mass is below the peak strength of the material and linear elastic material behaviour is often assumed. Therefore, the shear strength properties of the soil are not required in this type of analysis. Examples of this class of problem are the settlement calculation of a shallow footing and building foundation.

These two classes of problems are idealized situations of two extremes where failure either occurs at all points under consideration or does not occur at all. There is, in fact, a third class of problem which may be considered as an intermediate case between the preceding two classes. In this class of problem, some externally applied load causes plastic deformation or failure in only part of the soil mass which may or may not result in the development of a totally collapse mechanism. The assumption of limiting equilibrium is not valid because part of the soil mass is still experiencing stresses below the peak strength of the material. On the other hand, the assumption of linear elastic behaviour cannot be made because of failure in localized regions. Therefore, both the deformation and strength properties of the soil must be considered in this type of analysis.

There are basically two conditions which must be satisfied for progressive failure to occur. The first condition is that the soil must have a stress-strain relationship with a post peak strain softening behaviour. A strain softening material here refers to a decrease in strength after some peak shear strength has been reached. Figure 1.1 illustrates two main types of geotechnical material. The first type is a strain hardening material in which the strength of the material is always increasing as a result of plastic deformation. Examples of this type of material are loose sand and soft clay which do not possess



Behaviour of Soft Clay – Strain Hardening Material



Behaviour of Stiff Clay – Strain Softening Material

Figure 1.1: Strain Hardening and Strain Softening Behaviour of Soil

well defined peak strengths and failure is normally defined by excessive deformation. The mode of failure for this type of material is generally by bulging of the sides of the specimen. The second type of material has a distinct peak in the stress-strain curve and deformation beyond the peak results in a loss of strength and hence the material has been softened by plastic deformation thus traditionally been called a strain softening material. Dense sand and heavily over-consolidated clay are examples of this type and failure normally results in the formation of a localized shear plane. The term strain softening here does not refer to material which loses strength with time. Time, which will be discussed later, is not a necessary factor in progressive failure.

The second condition necessary for progressive failure to occur is that the soil mass must be subjected to non-uniform straining. Non-uniform straining can be caused by material heterogeneity and/or geometry of the soil mass which may result in the development of a localized failure zone and eventually lead to an unstable mechanism. Most slope failures inevitably have some degree of non-uniform straining. These are the two necessary conditions for progressive failure to occur. If the soil has no strain softening behaviour, the mobilized shear strength at failure must be uniform as shown in Figure 1.2. On the other hand, if strain on the failure surface is uniform, then the mobilized strength on the slip surface must be uniform even

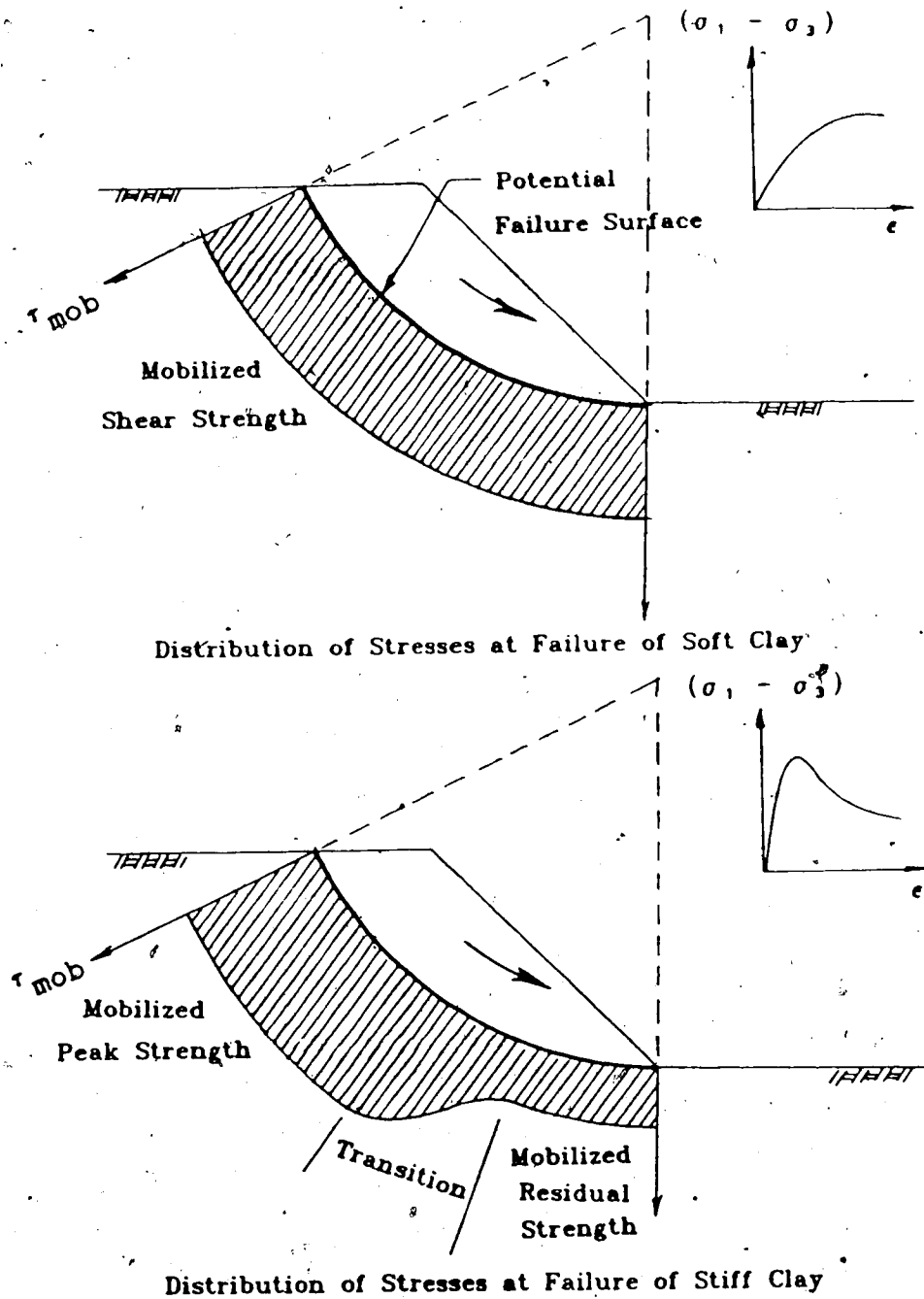


Figure 1.2: Mobilization of Shear Strength of Slopes for Strain Hardening and Strain Softening Soil

if the soil has a strain softening behaviour. Progressive failure will not occur in either case. Under the condition of non-uniform straining of a soil mass with strain softening behaviour, a portion of the failure surface may be subjected to peak strength at the moment of failure while another portion may have already experienced a large strain and the shear strength may have been reduced to residual value. The remaining portion of the failure surface may be in the transition from peak to residual strength as illustrated in Figure 1.2.

There have been several studies on the mechanism and causes of progressive failure. Skempton (1964) in his fourth Rankine lecture discussed the problem of progressive failure. He realized the importance of non-uniform mobilization of shear strength along the slip surface at failure based on the study of many actual landslides. He introduced the residual factor as the proportion of the total slip surface along which strength has fallen to the residual value. However the residual factor neglects the portion of the slip surface where the mobilized shear strength is decreasing from peak to residual strength as shown in Figure 1.2. Nevertheless, the residual factor gives an indication on the type of soil and soil condition where progressive failure is most prominent.

Bjerrum (1967) outlined the basic mechanism of progressive failure in his Terzaghi lecture in which he defines clearly the necessary conditions for progressive

failure. He emphasizes the importance of recoverable strain energy due to unloading of the soil mass and degradation of the diagenetic bonds as the main causes of many slope failures by progressive failure. There is no doubt that the concept of recoverable strain energy and diagenetic bonds are useful in understanding the mechanism of slope failure, but it is not necessary to have either of these to initiate progressive failure. The necessary conditions for progressive failure to occur will be discussed later. In his discussion he also derives the criteria for the propagation of the shear band in a one dimensional model based on the concept of energy balance.

Bishop (1967) recognized the importance of strain softening material in progressive failure and he defined the brittleness index as a measure of the amount of strain softening. The brittleness index, which will be used later, is defined as:

$$\text{Brittleness Index } I_B = \frac{\tau_p - \tau_r}{\tau_p} \times 100\% \quad (1.1)$$

where

τ_p and τ_r are the peak and residual strengths respectively.

It is noted that the degree of brittleness of a soil under fully drained conditions is usually dependent upon the confining stresses. It may therefore be more meaningful to discuss the brittleness of soil in relation to the stress

condition. Bishop (1967) also pointed out that failure of the strain softening material often results in localized deformation. Christian and Whitman (1969) studied a one dimensional progressive failure model for an infinite slope and related the factor of safety to the lateral stress and the amount of strain softening of the material. However, they only considered the equilibrium of the slope and localized straining was neglected.

The advance of modern electronic computer and numerical techniques has greatly enhanced the solution of complicated engineering problems. The invention of the finite element method enables one to depart from the closed form solution of very simple problems to the solution of realistic problems. Lo (1972) applied the finite element method to obtain a solution for progressive failure of slopes. Since it was necessary to have a strain softening material, he adopted a pseudo elastic-plastic approach with a decrease in strength after peak. An interesting hyperbolic elastic model was used to approximate the post peak deformation of strain softening material. Lo also predicted the time to failure by assuming the strength of the soil to decrease with time in a logarithmic manner. Although there is often a time delay in the failure of many slopes due to pore pressure redistribution, local changes in ground water conditions and degradation of bonds may lead to swelling and softening of the material. The time factor is not a necessary condition for progressive failure. It is important to differentiate

between progressive failure and delayed failure. In the latter case, failure occurs some time after the soil mass has reached the configuration just before failure. The reason for the delay can be any one of the causes listed above. Failure may or may not be of the progressive type because the mobilized shear strength can be uniform along the failure surface as in a normally consolidated soil with fairly ductile behaviour. Therefore the time effect may be considered as a change in soil condition or material behaviour which results in a situation in favor of progressive failure. It is observed that the progressive failure of many slopes often involved some time delay.

Lo (1972) also realized that failure in a strain softening material often leads to localized deformation, but he concluded that the effect of the thickness of this localized zone is not an important factor in the overall deformation of the soil mass. The use of elastic model in simulating shear band bifurcation is inappropriate since shear band bifurcation can only occur in unstable material. The aspects of shear band deformation will be discussed in chapter 3. Subsequently, Gates (1972) attempted to obtain the solution of progressive failure using a pseudo elastic finite element approach.

Palmer and Rice (1973) extended the development by Bjerrum (1967) on the criterion for shear band propagation in a one dimensional infinite slope problem. They utilized the concept of J-integral and stress intensity factor from

fracture mechanics to obtain a consistent formulation for shear band propagation. The shear band was treated as a stress and strain discontinuity which has zero thickness. In reality the thickness of the shear band in a soil mass is usually finite although it can be very thin (Morgenstern and Tchalenko 1967).

Burland (1976) obtained a well documented case study of progressive failure. The careful monitoring of the deformation of a clay pit enabled one to observe the propagation of the shear band and the development of localized failure. Simmons (1981) analyzed this case using an elasto-plastic finite element model. Some numerical difficulties had been encountered but it was concluded from the finite element results that only residual strength was mobilized in the field.

Law and Lumb (1978) proposed an interesting approach to analyze progressive failure using the limit equilibrium analysis. However, since only the equilibrium of the slope was considered, the method does not include non-uniform straining. Moreover, a postulated slip surface must be provided prior to the analysis which limits the region for possible stress redistribution during the failure process.

It is clear from the above discussion that progressive failure must involve a strain softening material and the degree of softening is related to the possibility of slope failure by progressive failure. Also there must be non-uniform straining and localized failure. Therefore, the

following conditions must be satisfied for progressive failure to occur (Bjerrum 1967):

1. There must be local differential straining sufficient to strain the soil beyond failure.
2. The soil must exhibit large and rapid decrease in strength after straining beyond the peak strength.
3. The development of a continuous failure surface is possible provided that shear stresses exceed the peak strength of the soil.

Once again the time effect is not considered as a necessary condition for progressive failure. Progressive failure must involve localized straining and often develops into a shear band type of deformation. It has been observed from the failure of heavily over-consolidated clay that a distinct failure plane or shear plane is formed and the deformation of this shear zone subsequently governs the overall behaviour of the soil mass. Although shear band deformation is not a necessary condition in progressive failure, it is definitely an important aspect.

The study of shear bands can be divided basically into two main classes. The first class is that the location and the direction of the propagation of the shear band is predetermined by existing geological conditions such as the case of a one dimensional infinite slope (Palmer and Rice 1976) or a weak layer embedded in more competent strata which is common in Alberta and the rest of Western Canada. Since the location of the shear band is predefined, the

objective is to calculate the extent of the softening zone along the shear band due to some external disturbance. This is a relatively simpler case compared to the case where the location and direction of the shear band are unknown. In the second case, it is necessary to first detect the initiation of localized failure and the formation of the shear band and then search for the direction and extent of shear band propagation. From an analytical point of view, this is a more difficult task.

The analysis of progressive failure is so far limited to simple one dimensional models or pseudo elastic-plastic models. Very often progressive failure may not result in immediate slope instability but the gradual development of a continuous slip surface can cause excessive deformation and eventually leads to slope failure. In this case the deformation history of the soil is of main concern such as the case studied by Burland (1976). In order to model a progressive failure where one is also interested in the amount of deformation of the soil mass, it is necessary to use analytical and numerical models which closely represent the behaviour of soil and include all the necessary conditions for progressive failure. This is basically the aim of this research.

Progressive failure is not only a fascinating subject in soil mechanics but it involves many major slope failures which deserve serious attention. A rational approach to progressive failure is yet to be developed but a consistent

picture in understanding the mechanics and in obtaining solutions to problems seems to be emerging. The development of one dimensional models provides in depth understanding of the mechanism and effect of various factors causing progressive failure. However, simple one dimensional models cannot be used to obtain solutions to real life engineering problems. Numerical methods are definitely one of the most effective ways to obtain solutions for complicated problems. The construction of simple models to understand the basics of progressive failure, the development of numerical models in obtaining solutions to real life problems and the documentation of case histories to verify the theories must be well balanced to obtain technological advances in solving the problem of progressive failure.

1.2 Purpose of the Research

The basic purpose of this research is to develop the analytical capability to analyze strain softening behaviour and progressive failure. The modelling of shear band initiation and propagation in both prescribed and unprescribed manners using the finite element method is also of interest. In addition, the ability of the numerical model to capture localized deformation will be studied.

In order to achieve these goals, the following steps are necessary:

1. Formulate a numerical model which will include strain softening behaviour.

2. Develop a computer program which is capable of analyzing general geotechnical problems.
3. Assess the validity of the numerical models by comparing results with closed form solutions.
4. Apply the method to real case histories in which the model can be evaluated by actual field observations.

Chapter 2 presents a general finite element formulation to analyze strain softening material with a special discussion of one strain softening model for fully undrained analysis. Numerical examples are given. The modelling of shear band initiation and propagation using the finite element method will be given in Chapter 3. A second strain softening model will be introduced in this Chapter and the theory of shear band formation and some numerical aspects will be also be discussed. Another strain softening model is introduced in Chapter 4 with a higher degree of sophistication than the previous two models. A strip footing will be analyzed to study the effect of the rate of post peak softening on the development of the yield zones and the limit loads. Chapter 5 introduces a finite element formulation for effective stress analysis in which pore pressure can be calculated given the soil properties in terms of effective stresses. This enables one to depart from the total stress analysis which is often assumed in analyzing undrained deformation of soil. Since soil behaviour depends on effective stresses and not total stresses, it is therefore more appropriate to use the soil

parameters in terms of effective stresses in the analysis. Only the fully drained condition and fully undrained condition will be considered here and no pore pressure diffusion or consolidation will be studied. It is hoped that this will initiate some interest in using effective stresses in the analysis of soil structures and serve as a starting point for further study in progressive failure using effective stresses. The development of the numerical model and computer program is then applied to a real engineering problem. In Chapter 6, the behaviour of an excavation during the construction of the Edmonton Convention Center will be studied and compared with the results obtained by the finite element analysis. Conclusions and recommendations for further research are given in Chapter 7.

1.3 Notations

Both matrix and tensor notations will be used throughout the text and the appendices of this thesis. It is convenient to use matrix notation in the finite element formulation, however tensor notation sometimes provide more compact and concise expressions. In matrix notation, the following conventions are adopted:

1. $[]$ denotes a matrix, not necessarily square.
2. $[]^T$ denotes the transpose of a matrix.
3. $\{ . \}$ denotes a vector with elements placed vertically.
4. $\langle \rangle$ denotes the transpose of a vector, i.e., $\langle \rangle^T = \{ \}$.

Matrices and vectors placed side by side represent matrix

multiplication. In tensor notation, the usual summation convention over repeated indices is assumed unless otherwise stated. In most cases the three dimensional Euclidean space is used and the indices are summed from 1 to 3. Also a comma in the subscripts represents differentiation with respect to the spatial coordinates and a dot represents differentiation with respect to time. However, since the formulation is independent of time, the differentiation is taken with respect to strains or external loads or simply represents incremental quantities. Additional subscripts and superscripts will be explained in due course.

2. FINITE ELEMENT FORMULATION FOR STRAIN SOFTENING MATERIAL

The discussion in Chapter 1 concludes that a finite element formulation with strain softening is a necessary ingredient in obtaining a solution to progressive failure problems. In this chapter a finite element formulation for strain hardening and softening material is presented. The formulation is based on the theory of plasticity and therefore the basic assumption of the theory of plasticity will be applied. It is not possible to review the theory of plasticity but excellent books on this subject are available (Hill 1953). However, a brief discussion of the theory of plasticity pertinent to strain softening materials will be given. A strain softening model for fully undrained analysis using total stress formulation will be discussed and results from the finite element analysis will be compared to the analytical solution.

2.1 Theory of Strain Softening Material

Many attempts have been made to analyze the strain softening behaviour of soil using the finite element method. The methods of analysis can be divided basically into two main types. The first type assumes that the material behaves elastically up to a peak value and remains elastic after peak with a decrease in elastic modulus or with a negative elastic modulus followed by a reduction in strength. The

post peak softening part is often modelled using a positive elastic modulus with the application of an unbalanced forces to bring the stress state to the post peak strength value. Several authors (Hoeg 1972, Lo 1973) have used this pseudo elastic approach to obtain solutions for bearing capacity problems and progressive failure of slopes. As is pointed out by Hoeg (1972) the pseudo elastic approach does not differentiate between elastic deformation and plastic deformation, and leads to an incorrect prediction of volume change. For example if the material is assumed to be under fully undrained conditions, which can be simulated by using a Poisson's ratio close to 0.5, the decrease in elastic modulus in post peak deformation results in an equal amount of reduction in both the shear modulus and bulk modulus which leads to a decrease in volume when the material is supposed to be incompressible. The pseudo elastic approach may be useful in obtaining limit loads for certain problems, however it does not provide a consistent formulation in accounting for the plastic deformation of the material after yielding.

A second approach is based on the theory of plasticity where the material is commonly assumed to behave elastically up to a peak strength and deform plastically thereafter. Zienkiewicz (1972) and others (Pietruszczak 1981, Terzi 1982) have used this approach to obtain solutions to several engineering problems. The theory of plasticity differentiates between elastic and plastic strain and thus

allows the modelling of complicated stress paths which involve loading and unloading situations. This approach will be used in this research. The material model which will be discussed here will have a strain hardening behaviour prior to the peak strength and a gradual reduction of strength after peak.

The basic problem associated with the analysis of strain softening material is the inherent unstable nature of the material. Drucker (1956) discussed the criteria for stable material where he considered stability as stability in the large and stability in the small. Stability in the large is defined as:

$$(\sigma_{ij} - \sigma_{ij}^p) d\epsilon_{ij}^p > 0 ; \quad (2.1)$$

and stability in the small is defined as:

$$d\sigma_{ij} d\epsilon_{ij}^p > 0 , \quad (2.2)$$

where

σ_{ij} is the current state of stress;

σ_{ij}^p is the stress state on the yield surface,

and $d\epsilon_{ij}^p$ is the increment of plastic strain tensor.

If a material satisfies both inequalities (2.1) and (2.2), then it can be shown that the solution for a well posed boundary value problem exists and that the solution is unique (Drucker 1956). Within the context of the theory of

plasticity, inequality (2.1) requires that the yield surface must be convex with respect to the origin and inequality (2.2) requires that the material must have a strain hardening behaviour. It has been shown (Bland 1957) that for stable materials as defined by Drucker, the plastic potential must be identical to the yield function which is sometimes referred to as the normality principle. Although there are many materials which satisfy both inequalities (2.1) and (2.2), there are many which may violate either one or both conditions. The material model that is of interest in this research may not violate inequality (2.1) but certainly will violate inequality (2.2).

From a physical point of view, there are materials in nature which violate Drucker's postulate but they exist in stable conditions in their natural environment. An example is a slope made of sensitive clay. Strictly speaking, Drucker's postulate is too restrictive. Consider for example the deformation of a body of strain softening soil, if the existing loading on the soil can do sufficient work for further plastic deformation and against some increment of load, then no laws of thermo-dynamics will be violated. Drucker's postulate seems to be overconstraining the possible constitutive relationship of a material and they are in fact sufficient but not necessary conditions to ensure existence and uniqueness of solutions.

Prevost and Hoeg (1975) studied the problem of strain softening material and they have shown that material

violating inequality (2.2) can have a unique solution. A mass of soil with a strain softening behaviour can be stable under certain stress conditions. The deformation of this mass of soil is always stable if the displacements on the surface are prescribed or controlled as opposed to when constant surface tractions are applied. Experience in testing strain softening materials indicates that a stress controlled test cannot be used to obtain the post-peak stress strain behaviour of an over-consolidated clay because the decrease in strength with constant externally applied load leads to a completely collapse mechanism. Therefore such cases will not have a stable solution. A strain controlled test must be used and solutions to this problem do exist regardless of whether the material itself is stable or not. Therefore, unique and stable solution can be obtained for a material which may not satisfy Drucker's postulate.

Concerning the uniqueness problem in the theory of plasticity, sometimes there can be no unique solution if there are corners on the plastic potential when the stress state is at a corner. For example, the Tresca and Mohr-Coulomb yield criteria which have been used extensively in metal and soils have corners. Corners in yield surfaces and plastic potentials are really mathematical artifacts but provide leeway in obtaining solutions for some problems without violating some basic principles. At the corner of a yield surface or plastic potential, the plastic strain

increment is undefined and gives the analyst some freedom to select from the possible solutions for the problem the one which best agrees with experimental observations (Christoffersen and Hutchinson 1979). The study of these aspects in plasticity is profound and is beyond the scope of this research. For a yield function with corners, it is assumed that the plastic strain increment is the average of the plastic strain increment from either side of a corner.

2.2 Elasto-Plastic Finite Element Formulation

The following finite element formulation assumes small strains and small deformations and no distinction is made between the deformed state and the undeformed state. Cauchy stress and engineering strain are used as basic quantities of measurement. Also the time effect is neglected and the differential quantities of stress and strain refer to the differentiation with respect to changes in externally applied loads.

The incremental finite element equilibrium equation based on virtual displacement is given by (Bathe 1982):

$$\int_{V} [B]^T \{\Delta\sigma\} dv = \{\Delta R\}, \quad (2.3a)$$

where

$[B]^T$ = strain displacement matrix;

$\{\Delta\sigma\}$ = increment of total stress vector;

$= \langle \Delta\sigma_{xx}, \Delta\sigma_{yy}, \Delta\sigma_{xy}, \Delta\sigma_{zz}, \Delta\sigma_{yz}, \Delta\sigma_{xz} \rangle^T$;

$\{\Delta R\}$ = increment of external applied load;

v = entire volume of the body.

The incremental load vector $\{\Delta R\}$ includes the load due to the body force and surface traction.

The load vector $\{\Delta R\}$ is given by:

$$\{\Delta R\} = \int_V [N]^T \{\gamma\} dv + \int_{S_i} [N]^T [N] \{P\} ds \quad (2.3b)$$

where

$[N]$ = interpolation function matrix;

$\{\gamma\}$ = body force vector;

$\{P\}$ = nodal surface traction vector;

S_i = surface subjected to external traction.

The standard technique for modifying the stiffness matrix and load vector is used to incorporate any prescribed displacements which can be found in most finite element texts (Zienkiewicz 1977, Bathe, 1982). Equation (2.3) can be rewritten as:

$$\sum_{e=1}^n \int_V [B]^e \{\Delta \sigma\}^e dv = \{\Delta R\} \quad (2.4)$$

where

the superscript e denotes elemental quantities and n is the total number of elements.

The summations are performed to ensure nodal equilibrium and compatibility. Introducing the incremental constitutive relationship [C] of the material:

$$\{\Delta\sigma\} = [C]\{\Delta\epsilon\} , \quad (2.5)$$

and the strain displacement relationship [B] using an isoparametric finite element formulation:

$$\{\Delta\epsilon\} = [B]\{\Delta\delta\} , \quad (2.6)$$

one arrives at the following matrix equation:

$$[K]\{\Delta\delta\} = \{\Delta R\} , \quad (2.7a)$$

where

$$[K] = \int_V [B]^T [C] [B] dv ; \quad (2.7b)$$

$\langle \Delta\delta \rangle$ = increments of displacement.

To obtain an expression for the elasto-plastic constitutive matrix [C], the following assumptions are made:

1. The total strain increment is the sum of the elastic strain increment and plastic strain increment. That is:

$$\{d\epsilon\} = \{d\epsilon^E\} + \{d\epsilon^P\} ; \quad (2.8)$$

2. The change in stresses is due to change in elastic strains only:

$$\{d\sigma\} = [C^E] \{d\epsilon^E\}; \quad (2.9)$$

where

$[C^E]$ is the elastic constitutive matrix.

3. There exists a yield function in which:

$$F(\sigma_{ij}^P, \epsilon_{ij}^P) < 0, \quad F(\sigma_{ij}^P + \Delta\sigma_{ij}^P, \epsilon_{ij}^P + \Delta\epsilon_{ij}^P) < 0$$

for elastic deformation; (2.10a)

$$F(\sigma_{ij}^P, \epsilon_{ij}^P) = 0, \quad F(\sigma_{ij}^P + \Delta\sigma_{ij}^P, \epsilon_{ij}^P + \Delta\epsilon_{ij}^P) < 0$$

$$\text{and} \quad \left\langle \frac{\partial F}{\partial \sigma_{ij}} \right\rangle \{d\sigma_{ij}\} < 0$$

for elastic unloading; (2.10b)

$$F(\sigma_{ij}^P, \epsilon_{ij}^P) = 0, \quad F(\sigma_{ij}^P + \Delta\sigma_{ij}^P, \epsilon_{ij}^P + \Delta\epsilon_{ij}^P) = 0$$

$$\text{and} \quad \left\langle \frac{\partial F}{\partial \sigma_{ij}} \right\rangle \{d\sigma_{ij}\} > 0$$

for plastic deformation and strain hardening; (2.10c)

$$F(\sigma_{ij}^P, \epsilon_{ij}^P) = 0, \quad F(\sigma_{ij}^P + \Delta\sigma_{ij}^P, \epsilon_{ij}^P + \Delta\epsilon_{ij}^P) = 0$$

$$\text{and } \left\langle \frac{\partial F}{\partial \sigma_{ij}} \right\rangle \{d\sigma_{ij}\} < 0$$

for plastic deformation and strain softening. (2.10d)

4. There exists a plastic potential such that:

$$\{d\epsilon^P\} = \lambda \left\{ \frac{\partial Q}{\partial \sigma} \right\}; \quad (2.11)$$

5. The consistency condition in which:

$$F(\sigma_{ij}, \epsilon_{ij}^P) > 0 \text{ is not permissible;}$$

$$F(\sigma_{ij}, \epsilon_{ij}^P) = 0 \text{ for plastic deformation.} \quad (2.12)$$

The above 5 assumptions are commonly made in plasticity analyses. The only difference here is assumption (3) for strain softening materials in which a portion of the body or the entire body is actually undergoing unloading but the stress state remains on the yield surface. This is different from elastic unloading which is also possible for strain softening when the final state of stress lies within the yield surface.

Substituting Equations (2.8) and (2.11) into (2.9), one obtains:

$$\{d\sigma\} = [C]^E \{d\epsilon\} - \lambda \left\{ \frac{\partial Q}{\partial \sigma} \right\} \quad (2.13)$$

From Equation (2.12),

$$dF = \left\langle \frac{\partial F}{\partial \sigma} \right\rangle \{d\sigma\} + \left\langle \frac{\partial F}{\partial \epsilon} \right\rangle^P \{d\epsilon\} = 0 \quad (2.14)$$

Substituting Equations (2.11) and (2.13) into (2.14),

$$\left\langle \frac{\partial F}{\partial \sigma} \right\rangle [C]^E \{d\epsilon\} - \lambda \left\langle \frac{\partial F}{\partial \sigma} \right\rangle [C]^E \left\{ \frac{\partial Q}{\partial \sigma} \right\} + \lambda \left\langle \frac{\partial F}{\partial \epsilon} \right\rangle^P \left\{ \frac{\partial Q}{\partial \sigma} \right\} = 0,$$

therefore,

$$\lambda = \frac{\left\langle \frac{\partial F}{\partial \sigma} \right\rangle [C]^E}{\left\langle \frac{\partial F}{\partial \sigma} \right\rangle [C]^E \left\{ \frac{\partial Q}{\partial \sigma} \right\} - \left\langle \frac{\partial F}{\partial \epsilon} \right\rangle^P \left\{ \frac{\partial Q}{\partial \sigma} \right\}} \{d\epsilon\} \quad (2.15)$$

Finally substituting Equation (2.15) into (2.13), one derives the following elasto-plastic matrix:

$$\{d\sigma\} = [C] \{d\epsilon\}, \quad (2.16a)$$

where

$$[C] = [C]^E - \frac{[C]^E \left\{ \frac{\partial Q}{\partial \sigma} \right\} \left\langle \frac{\partial F}{\partial \sigma} \right\rangle [C]^E}{\left\langle \frac{\partial F}{\partial \sigma} \right\rangle [C]^E \left\{ \frac{\partial Q}{\partial \sigma} \right\} - \left\langle \frac{\partial F}{\partial \epsilon} \right\rangle^P \left\{ \frac{\partial Q}{\partial \sigma} \right\}} \quad (2.16b)$$

Note that the first term in the denominator represents

perfectly plastic deformation and the second term represents strain hardening and softening deformation. The following three conditions may occur:

1. $\left\langle \frac{\partial F}{\partial \epsilon} P \right\rangle \left\{ \frac{\partial Q}{\partial \sigma} \right\} < 0$ for strain softening deformation;
2. $\left\langle \frac{\partial F}{\partial \epsilon} P \right\rangle \left\{ \frac{\partial Q}{\partial \sigma} \right\} = 0$ for perfectly plastic deformation;
3. $\left\langle \frac{\partial F}{\partial \epsilon} P \right\rangle \left\{ \frac{\partial Q}{\partial \sigma} \right\} > 0$ for strain hardening deformation.

Due to strain softening deformation, the elasto-plastic matrix may not be positive definite. An eigenvalue analysis of the elasto-plastic matrix given in Chapter 3 will reveal this fact. Also if the non-associated flow rule is used the [C] matrix may not, in general, be symmetric.

Traditionally, the hardening behaviour of a material is divided into kinematic hardening and isotropic hardening. That is:

$$F = F(\sigma_{ij}, \epsilon_{ij}^P, \kappa), \quad (2.17)$$

where

$$\epsilon_{ij}^P = \int d\epsilon_{ij}^P, \text{ the cumulative plastic strain;}$$

and κ is a hardening parameter which can be dependent upon ϵ_{ij}^P .

The term $\left\langle \frac{\partial F}{\partial \epsilon} P \right\rangle \left\{ \frac{\partial Q}{\partial \sigma} \right\}$ can be written as:

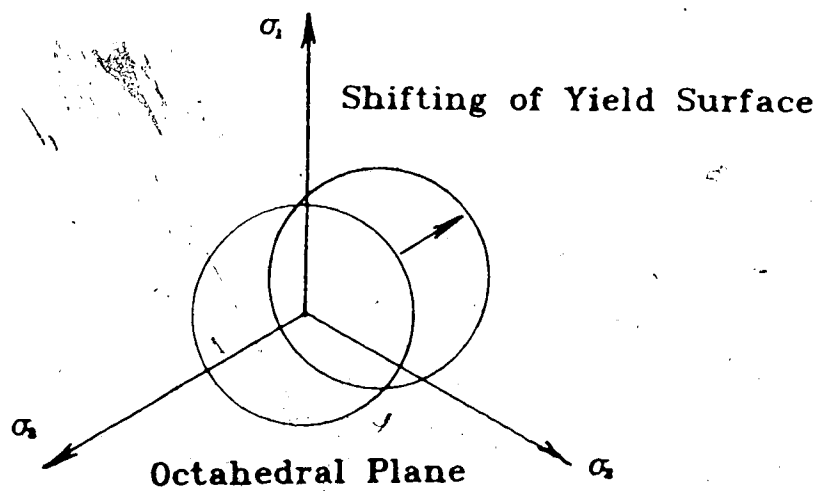
$$\left\langle \frac{\partial F}{\partial \epsilon} P \right\rangle \left\{ \frac{\partial Q}{\partial \sigma} \right\} = \left\langle \frac{\partial F}{\partial \epsilon} P \right\rangle \left\{ \frac{\partial Q}{\partial \sigma} \right\} + \frac{\partial F}{\partial \kappa} \frac{\partial \kappa}{\partial \epsilon} \left\langle P \right\rangle \left\{ \frac{\partial Q}{\partial \sigma} \right\}, \quad (2.18)$$

where the first term represent kinematic hardening and the second term represent isotropic hardening.

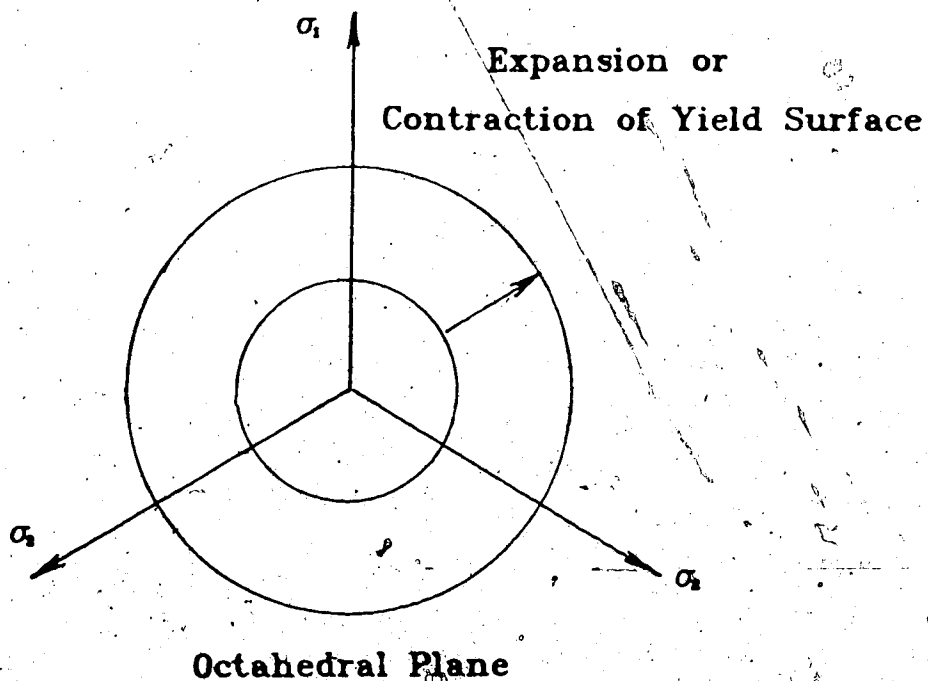
Although the first term in the right side of Equation (2.18) has the same form as the left side, they actually have different meanings. The differentiation of the yield function with respect to the plastic strain on the right side is performed by keeping the hardening coefficient κ constant. Graphically, this is equivalent to keeping the size of the yield surface constant while moving the yield surface in the stress space as shown in Figure 2.1, which is kinematic hardening. The second term on the right side of Equation (2.18) represents equal expansion of the yield surface in all directions and the rate of expansion is dependent upon the amount of plastic straining, which is isotropic hardening. Therefore, the term on the left side is the combined effect of the kinematic hardening and isotropic hardening.

2.3 Yield Criteria and Constitutive Matrix

Various material models and yield criteria will be used in this thesis. Expressions for the the von Mises, Tresca, Drucker and Prager, and Mohr Coulomb yield criterion and



Kinematic Hardening



Isotropic Hardening

Figure 2.1: Kinematic and Isotropic Hardening of Plasticity Model

their gradients are summarized in Table 2.1. The von Mises yield criterion can be considered as a special case of the Drucker-Prager yield criterion with a zero friction angle. Similarly, the Tresca criteria can be considered as a special case of the Mohr Coulomb criteria. Note that the Tresca and Mohr Coulomb criteria have corners in the yield surface and their gradients are undefined at these points. The corners are smoothed in this study by fitting a von Mises criterion on the Tresca criterion and the Drucker and Prager criterion on the Mohr Coulomb criterion when the stress state approaches the corner of the yield surface.

With the yield functions and their gradients given in Table 2.1, the elasto-plastic constitutive matrix of Equation (2.16) can be partially determined. To specify a material model completely, it is necessary to know the stress strain relationship of the material. Elastic deformation is assumed here to be linear elastic although a non-linear elastic model such as the hyperbolic model can be used. Unloading and reloading moduli are considered to be the same. The elastic constitutive relationship from Hooke's law is given by:

$$C_{ijklmn} = \frac{E\nu}{(1+\nu)(1-2\nu)}\delta_{ij}\delta_{mn} + \frac{E}{(1+\nu)}\delta_{mi}\delta_{jn}, \quad (2.19)$$

where

E and ν are the elastic modulus and Poisson's ratio respectively,

Table 2.1 Yield Functions and Gradients

	F	$\partial F / \partial \sigma_{ij}$
von Mises	$\sqrt{3}\bar{\sigma} - Y$	$\frac{\sqrt{3}\sigma_{ij}^d}{\sqrt{2}\bar{\sigma}}$
Tresca	$2\bar{\sigma}\cos\theta_0 - Y$	$\sigma_{ij}^d \cos\theta_0 / \bar{\sigma} - \bar{\sigma} \Lambda_{ij} \sin\theta_0$
Drucker Prager	$3\alpha\sigma_m + \bar{\sigma} - \kappa$	$\alpha\delta_{ij} + \sigma_{ij}^d / (\sqrt{2}\bar{\sigma})$
Mohr Coulomb	$\sigma_m \sin\phi + \bar{\sigma} \cos\theta_0$ $- \bar{\sigma} \sin\phi \sin\theta_0 / \sqrt{3}$ $- C \cos\phi$	$\sin\phi \delta_{ij} / 3 +$ $\sigma_{ij}^d (\cos\theta_0 - \sin\theta_0 \sin\phi / \sqrt{3}) / (\sqrt{2}\bar{\sigma})$ $- \bar{\sigma} (\sin\theta_0 + \cos\theta_0 \sin\phi / \sqrt{3}) \Lambda_{ij}$

$$\sigma_m = \sigma_{kk}/3; \quad \sigma_{ij}^d = \sigma_{ij} - \delta_{ij}\sigma_{kk}/3; \quad \delta_{ij} = \text{kronecker delta};$$

$$J_2 = \sigma_{ij}^d \sigma_{ij}^d / 2; \quad \bar{\sigma} = \sqrt{J_2}; \quad J_3 = \sigma_{ij}^d \sigma_{jk}^d \sigma_{ki}^d / 3;$$

$$\theta_0 = 1/3 \sin^{-1} [(-3\sqrt{3}J_3)/(2J_2^{3/2})], \quad -\pi/6 < \theta_0 < \pi/6;$$

$$\Lambda_{ij} = \frac{3}{\sqrt{4J_2^3 - 27J_3^2}} (\sigma_{ik}^d \sigma_{kj}^d - 2\delta_{ij} J_2 / 3 - 3J_3 J_2^{-1} \sigma_{ij}^d / 2);$$

Y - Uniaxial yield strength;

α, κ - Drucker and Prager's cohesion & frictional parameters;

C, ϕ - Mohr Coulomb cohesion and frictional parameters.

and δ_{ij} is the Kronecker delta.

For an elastic perfectly plastic material model, the hardening term in the denominator of Equation (2.16) is zero and therefore the yield function given in Table 2.1 together with Equation (2.19) are sufficient to define the model by assuming an associated flow rule. The elastic deformation is isotropic but some degree of anisotropy is introduced through plastic deformation which will be seen later in the discussion of eigenvalues given in Chapter 3.

2.4 Finite Element Model for Strain Softening Material

An elasto-plastic strain softening model has been introduced by Prevost and Hoeg (1975) to simulate deformation under undrained conditions. The stress strain relationship, or more precisely, the loading function (i.e. yield function) for this model is given by:

$$F = q - \kappa = 0 \quad (2.20)$$

where

$$q = \sqrt{3J_2} ;$$

$$\kappa = A \left[\frac{B(\bar{\epsilon}^P)^2 + \bar{\epsilon}^P}{1 + (\bar{\epsilon}^P)^2} \right] ;$$

A and B are material parameters;

$\bar{\epsilon}^P = \int d\bar{\epsilon}^P = \text{equivalent plastic strain ;}$

$$d\bar{\epsilon}^P = \left(\frac{2}{3} d\epsilon_{ij}^P d\epsilon_{ij}^P \right)^{1/2} ;$$

$$d\epsilon_{ij}^P = d\epsilon_{ij}^F - d\epsilon_{kk}^P \delta_{ij}/3 ;$$

$d\epsilon_{ij}^P = \text{increment of plastic strain.}$

A plot of this loading function versus the equivalent plastic strain (stress strain relationship) is shown in Figure 2.2. It is noted that there are at least 3 essential parameters in describing a strain softening model. They are the peak strength $\kappa(\text{peak})$, residual strength $\kappa(\text{res})$, and the equivalent plastic strain at peak strength $\bar{\epsilon}^P(\text{peak})$.

However, there are only 2 parameters, A and B, in this model, therefore these 3 quantities are inter-related.

The parameter B is dependent only upon the amount of post peak softening. Using the brittleness index introduced by Bishop (1967) which can be expressed as:

$$I_B = 1 - \kappa(\text{res})/\kappa(\text{peak}) , \quad (2.21)$$

then the parameter B is given by:

$$B = \frac{1 - I_B}{2\sqrt{I_B}} . \quad (2.22)$$

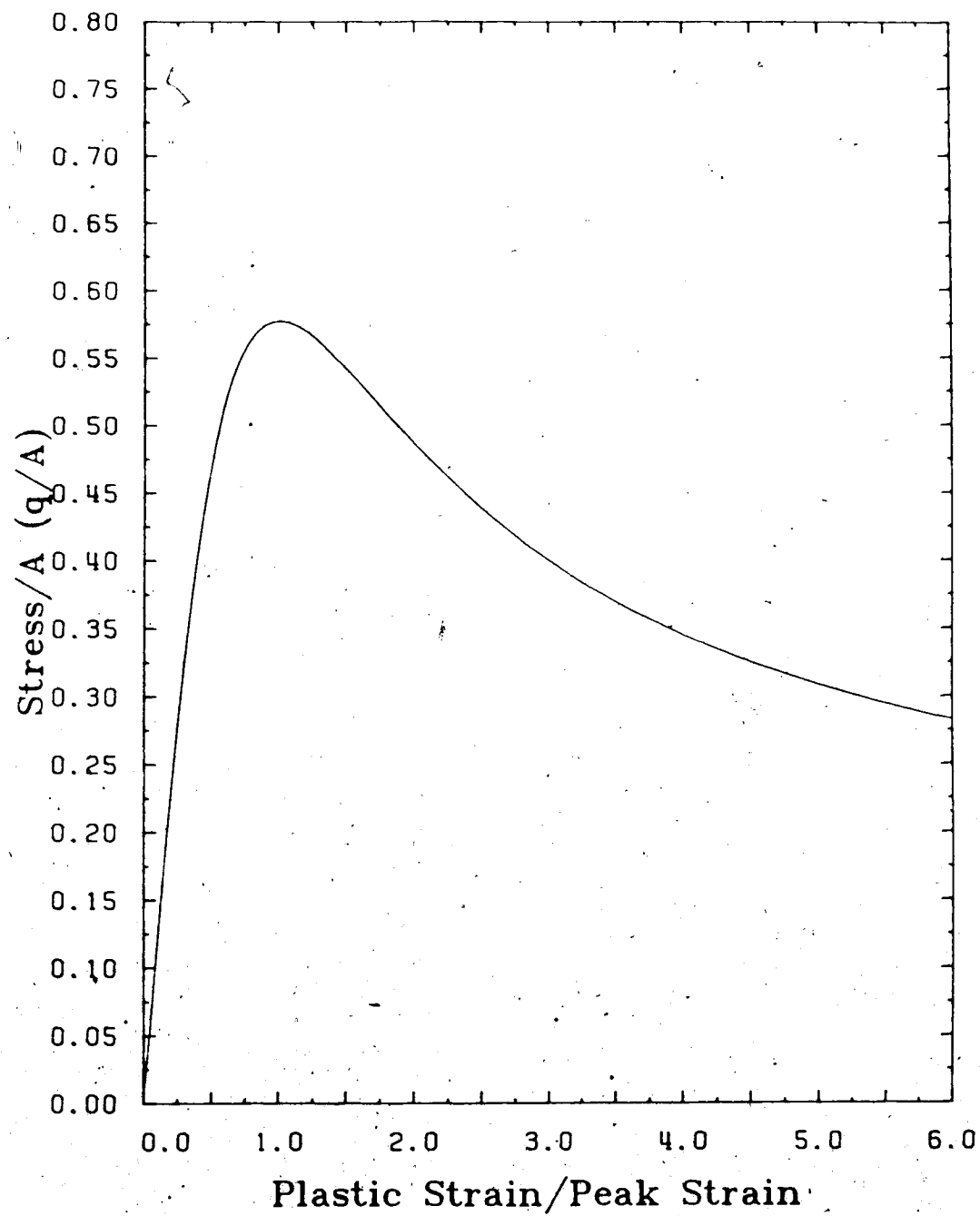


Figure 2.2: Stress Strain Curve of Strain Softening Model

The peak plastic strain $\bar{\epsilon}^P$ (peak) is a function of B only which can be calculated from:

$$\bar{\epsilon}^P \text{ (peak)} = B + \sqrt{1 + B^2} . \quad (2.23)$$

The parameter A can be determined by letting $\bar{\epsilon}^P = \infty$ in Equation (2.20) and $\kappa = \kappa(\text{res})$, then:

$$A = \kappa(\text{res})/B . \quad (2.24)$$

The parameter B has no units and the parameter A will have the same stress units as $\kappa(\text{res})$. The plastic strain $\bar{\epsilon}^P$ must be expressed in percentage in the above equations.

The finite element formulation for this model requires the evaluation of the hardening terms in the elasto-plastic matrix which will not be zero as in the case of elastic perfectly plastic material. That is:

$$\frac{\partial F}{\partial \epsilon} \langle \frac{\partial Q}{\partial \sigma} \rangle + \frac{\partial F}{\partial \kappa} \langle \frac{\partial Q}{\partial \epsilon} \rangle \neq 0 . \quad (2.25)$$

It is assumed that the material is strain hardened and softened isotropically, therefore the first term in Equation (2.25) is zero. Since the hardening parameter κ of the yield function is in terms of the equivalent plastic strain $\bar{\epsilon}^P$, it is more convenient to express the second term in Equation (2.25) in terms of $\bar{\epsilon}^P$. Rewriting the consistency condition of Equation (2.14) as:

$$dF = \left\langle \frac{\partial F}{\partial \sigma} \right\rangle \{d\sigma\} + \frac{\partial F}{\partial \kappa} \frac{\partial \kappa}{\partial \bar{\epsilon}} P d\bar{\epsilon} = 0 \quad (2.26)$$

where

$$d\bar{\epsilon}^P = \lambda \bar{Q};$$

$$\bar{Q} = \frac{1}{\sqrt{3}} \left(\frac{\partial Q}{\partial \sigma_{11}} \frac{\partial Q}{\partial \sigma_{11}} + \frac{1}{3} \frac{\partial Q}{\partial \sigma_{mm}} \frac{\partial Q}{\partial \sigma_{nn}} \right)^{1/2}$$

Q = plastic potential

= F for associated flow rule.

From Equation (2.26), it can be easily shown that the hardening term in the elasto-plastic matrix can be replaced by:

$$\left\langle \frac{\partial F}{\partial \bar{\epsilon}} P \right\rangle \left\{ \frac{\partial Q}{\partial \sigma} \right\} = \frac{\partial F}{\partial \kappa} \frac{\partial \kappa}{\partial \bar{\epsilon}} P \bar{Q} \quad (2.27)$$

From Equation (2.20):

$$\frac{\partial F}{\partial \kappa} = -1 \quad (2.28a)$$

$$\text{and } \frac{\partial \kappa}{\partial \bar{\epsilon}} P = A \left[\frac{1 + 2B\bar{\epsilon}^P - (\bar{\epsilon}^P)^2}{(1 + (\bar{\epsilon}^P)^2)^2} \right] \quad (2.28b)$$

Equations (2.28) and (2.27) are substituted into Equation (2.26) to evaluate the elasto-plastic constitutive matrix given by Equation (2.16). The current yield stress κ can be found from Equation (2.20).

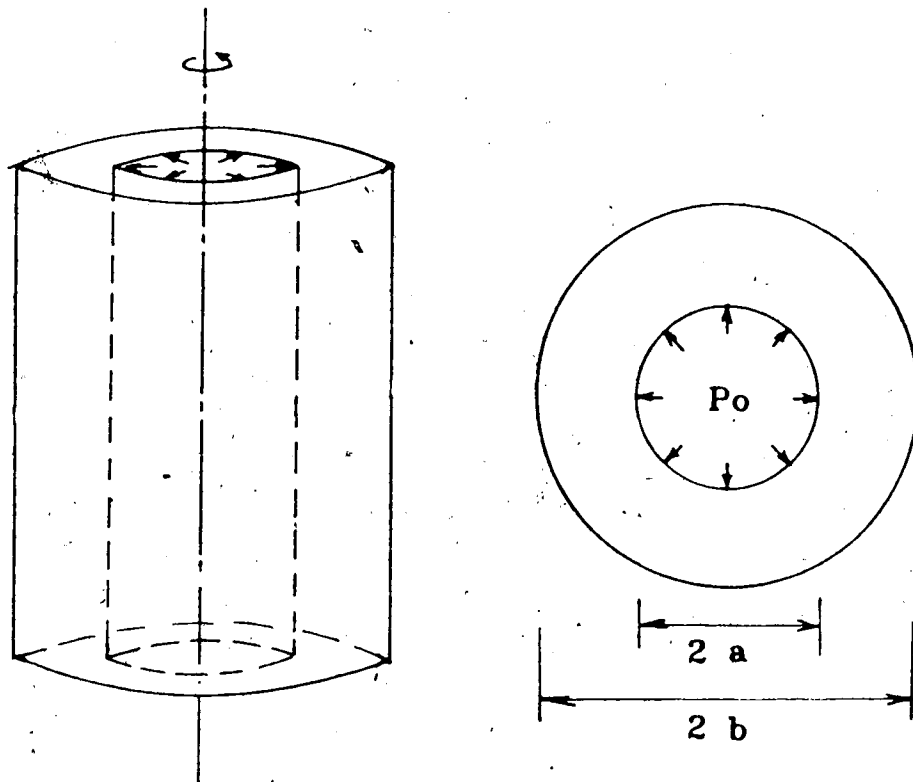
It is noted that this model neglects elastic deformation and the material will yield immediately under infinitesimal shear stresses. However in the finite element formulation the elastic deformation cannot be neglected and a finite initial yield strength is required because the gradient of the loading function is undefined when the yield stress is zero. Therefore, to simulate the rigid plastic deformation using the finite element method, a small initial yield stress and a high elastic modulus with Poisson's ratio close to 0.50 are used. In other words, the stress strain law of Equation (2.20) should be rewritten as:

$$F = q - (\kappa + \kappa_0) = 0 \quad (2.29)$$

where κ_0 is an initial yield strength which can be very small.

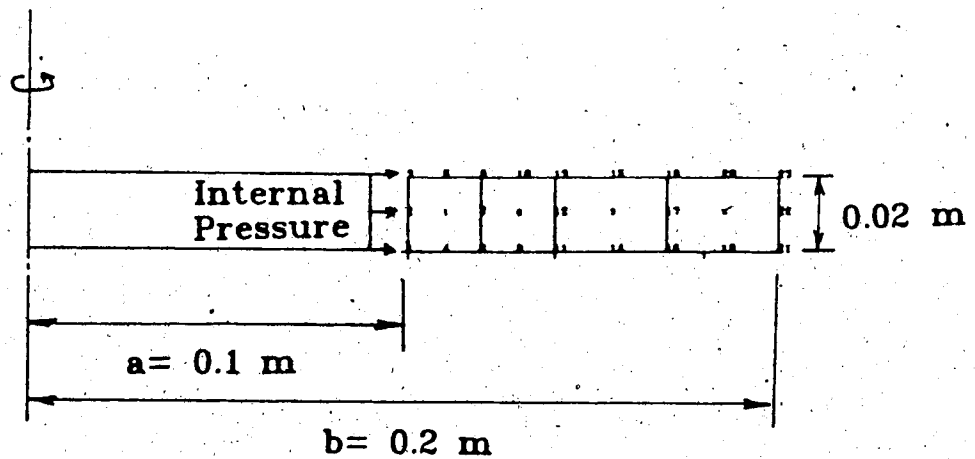
2.5 Expansion of a Thickwalled Cylinder

In this section a thickwalled cylinder subjected to internal pressure will be analyzed as shown in Figure 2.3. The external pressure of the cylinder is assumed to be zero for all cases being considered. The problem can be reduced to a one dimensional problem by considering a plane strain condition along the axis and axisymmetric conditions about the axis of the cylinder. The finite element idealization of the cylinder is also shown in Figure 2.3. The material of the cylinder is assumed to have a stress strain relationship



Infinitely Long Cylinder

Plan View



Finite Element Mesh

Figure 2.3: Expansion of a Long Cylinder

according to Equation (2.29). The closed form solution for the thickwalled cylinder problem using the stress strain relationship given by Equation (2.20) has been obtained by Prevost and Hoeg (1975) where the internal pressure and inner wall displacement relationship is given by:

$$\frac{P}{A} = \frac{1}{\sqrt{3}} \left[\frac{B}{2} \ln \left(\frac{1 + \bar{\epsilon}_0^2}{1 + \bar{\epsilon}_1^2} \right) + \tan^{-1} \left(\frac{\bar{\epsilon}_0 - \bar{\epsilon}_1}{1 + \bar{\epsilon}_0 \bar{\epsilon}_1} \right) \right] \quad (2.30)$$

where

$$\bar{\epsilon}_0 = \frac{2}{\sqrt{3}} \frac{u_0}{b};$$

$$\bar{\epsilon}_1 = \frac{2}{\sqrt{3}} \frac{a}{b^2} u_0;$$

u_0 - inner wall displacement;

P - internal pressure.

The hoop stress inside the cylinder is given by:

$$\frac{\sigma_r}{A} = \frac{1}{\sqrt{3}} \left[\frac{B}{2} \ln \left(\frac{1 + \bar{\epsilon}^2}{1 + \bar{\epsilon}_1^2} \right) + \tan^{-1} \left(\frac{\bar{\epsilon} - \bar{\epsilon}_1}{1 + \bar{\epsilon} \bar{\epsilon}_1} \right) \right] \quad (2.30a)$$

$$\frac{\sigma_\theta}{A} = \frac{\sigma_r}{A} - \frac{4}{\sqrt{3}} \left(\frac{B\bar{\epsilon}/2 + 1/2}{1 + \bar{\epsilon}^2} \right) \bar{\epsilon} \quad (2.30b)$$

where

σ_r - major principal stress;

σ_θ - hoop stress;

$\bar{\epsilon}$

$$\bar{\epsilon} = \frac{2}{\sqrt{3}} \frac{a}{r^2} u_0 .$$

The following values for the material parameters are used in the analysis:

$$E = 10000. \text{ kPa}$$

$$\nu = 0.49$$

$$A = 40/3 \text{ kPa}$$

$$I^* = 0.25, 0.50, 0.75$$

$$\kappa_0 = 0.01 \text{ for the finite element solution.}$$

The result of the finite element analysis using the finite element formulation presented in this chapter is shown in Figure 2.4. It is seen in Figure 2.4 that excellent agreement between the analytical and the finite element solution is obtained especially in the region of post peak deformation. In all cases being considered the displacement at the inner wall of the cylinder is prescribed and the internal pressure is back calculated. It is not possible to obtain the post peak behaviour of the cylinder if the internal pressure is prescribed. Since elastic deformation, although very small, is included in the finite element model, this results in larger displacements than that obtained from the analytical solution for any given internal pressure. The portion of the elastic strain becomes smaller in comparison to the plastic strain with an increased amount

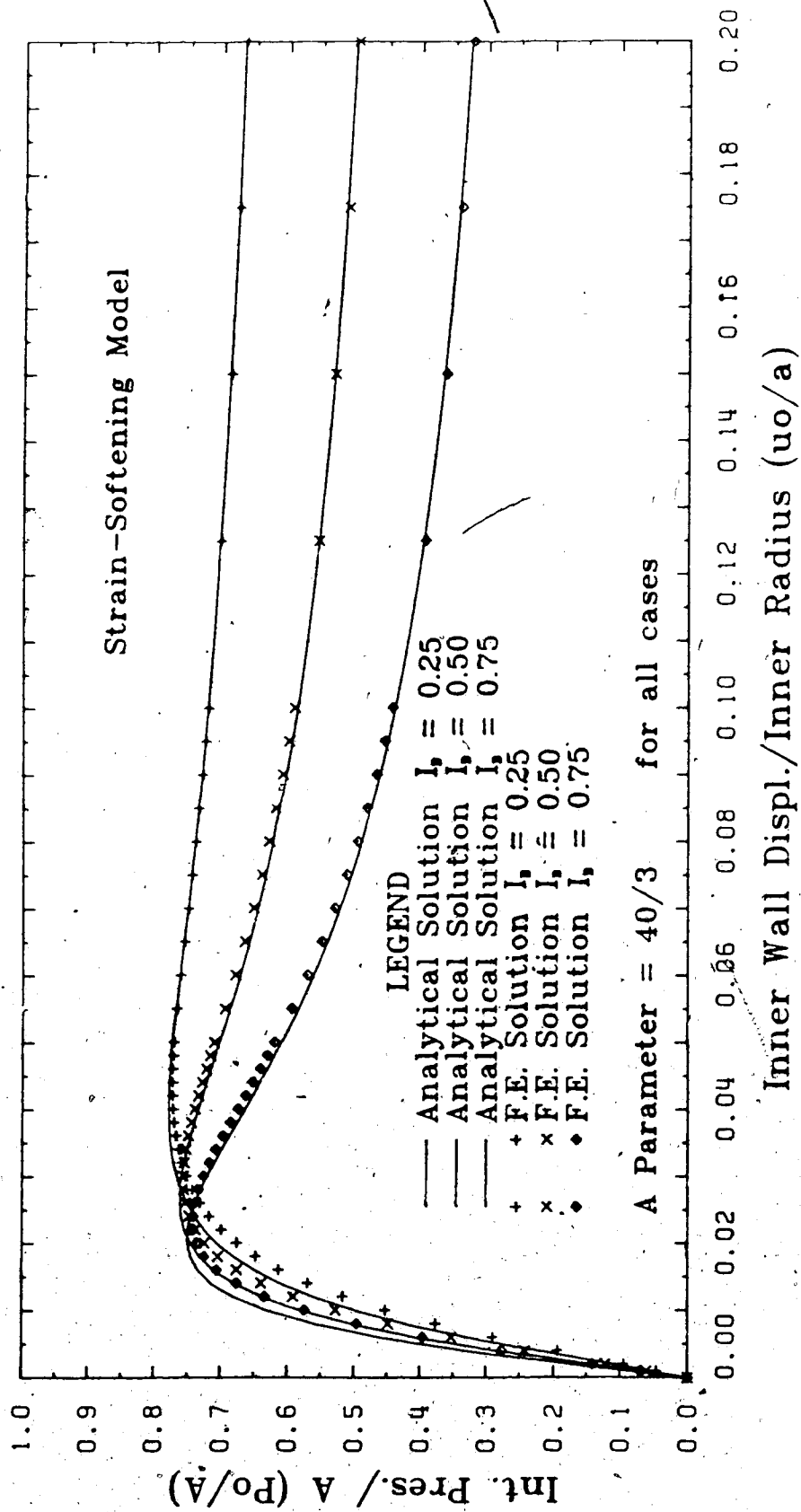


Figure 2.4: Pressure Displacement Response of Thickwalled Cylinder

of deformation, this results in a better agreement between the analytical and finite element solutions. Also there is a finite initial yield strength of 0.01 kPa being used in the finite element model which may account for some of the discrepancy.

The effect of the number of integration points is shown in Figure 2.5. It is noted that the use of the 3x3 integration scheme results in a stiffer element in the post peak region because of the additional constraints imposed by this integration scheme over the 2x2 integration scheme. Since the problem itself is highly constrained due to plane strain and axisymmetrical conditions combined with the incompressible behaviour of the material, the use of the 2x2 integration scheme will introduce a spurious zero energy mode and will help in reducing the element locking behaviour. Therefore, a higher order integration scheme does not always lead to better results.

The hoop stress distribution at various internal pressures are shown in Figure 2.6 to 2.8. It is seen that the discrepancy in stresses between the analytical and finite element solutions becomes smaller for higher internal pressures. Again, this is due to the presence of elastic deformation in the finite element model.

The unloading and reloading behaviour of the cylinder is shown in Figure 2.9. The cylinder is loaded close to peak strength and then elastic unloading and reloading occurred. In order to detect elastic unloading in the finite element

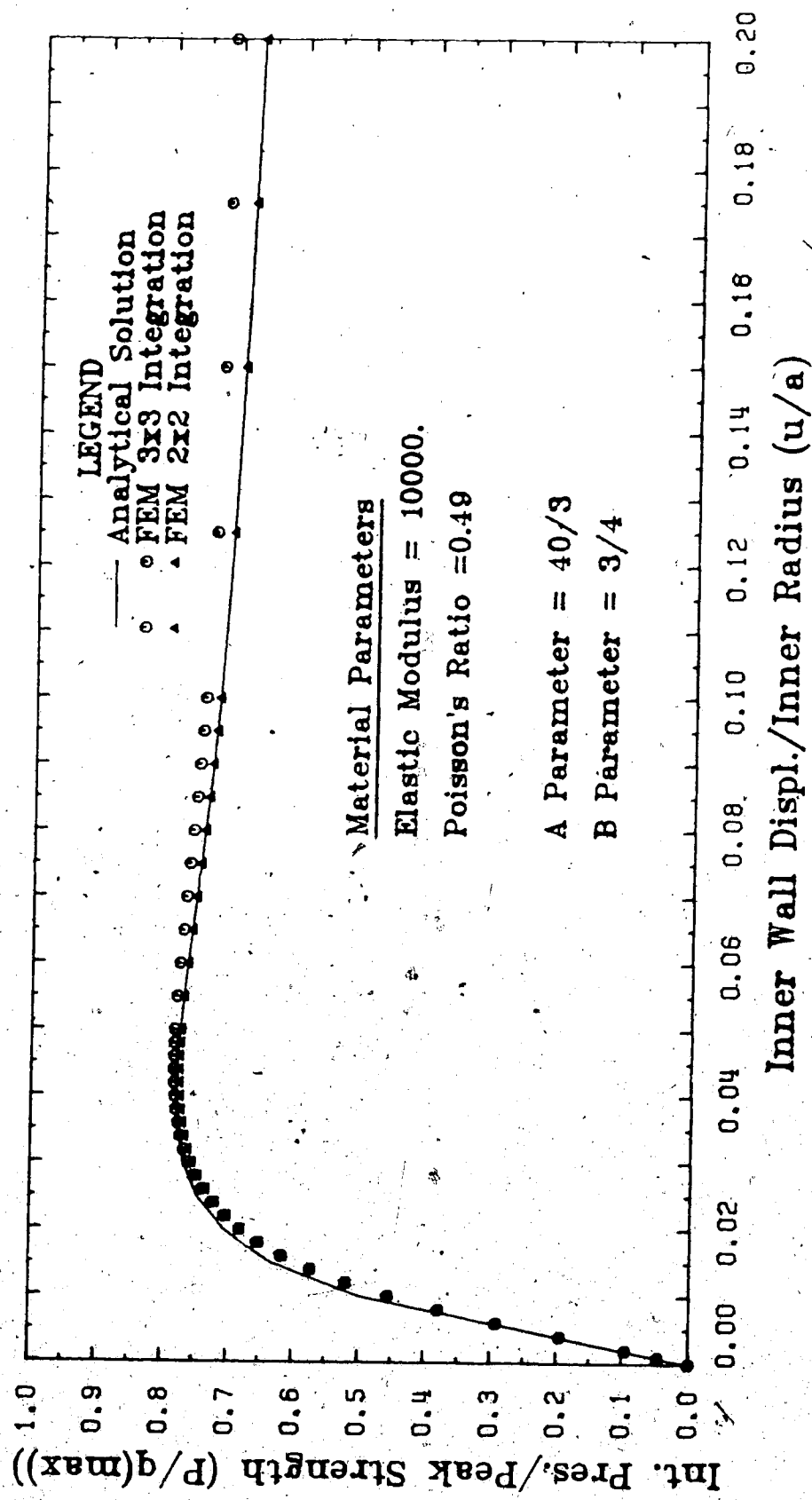


Figure 2.5: Effect of Intergration Points on the Response of Thickwalled Cylinder

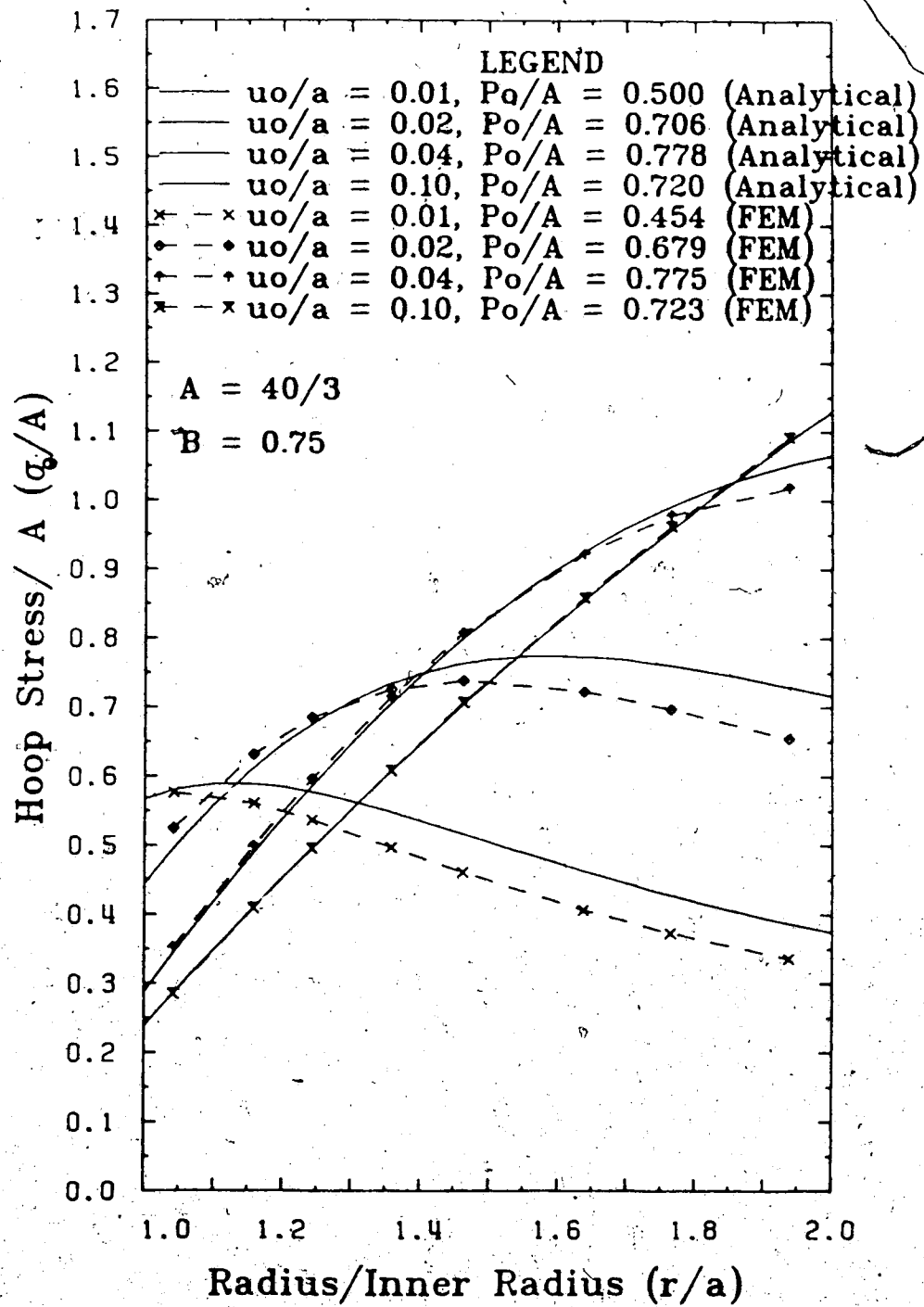


Figure 2.6: Hoop Stress Distribution $I(B) = 0.25$

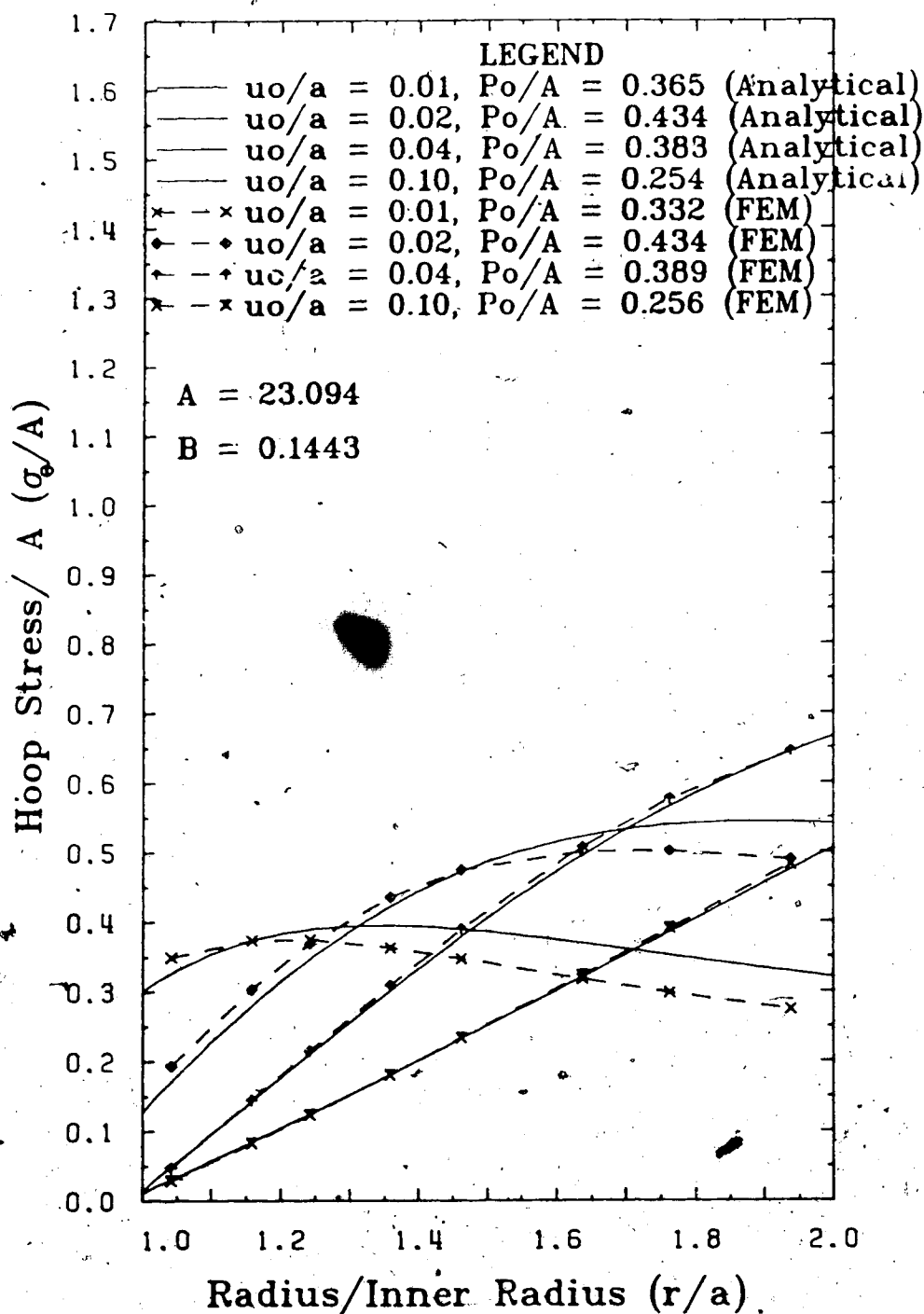


Figure 2.7: Hoop Stress Distribution $I(B) = 0.50$

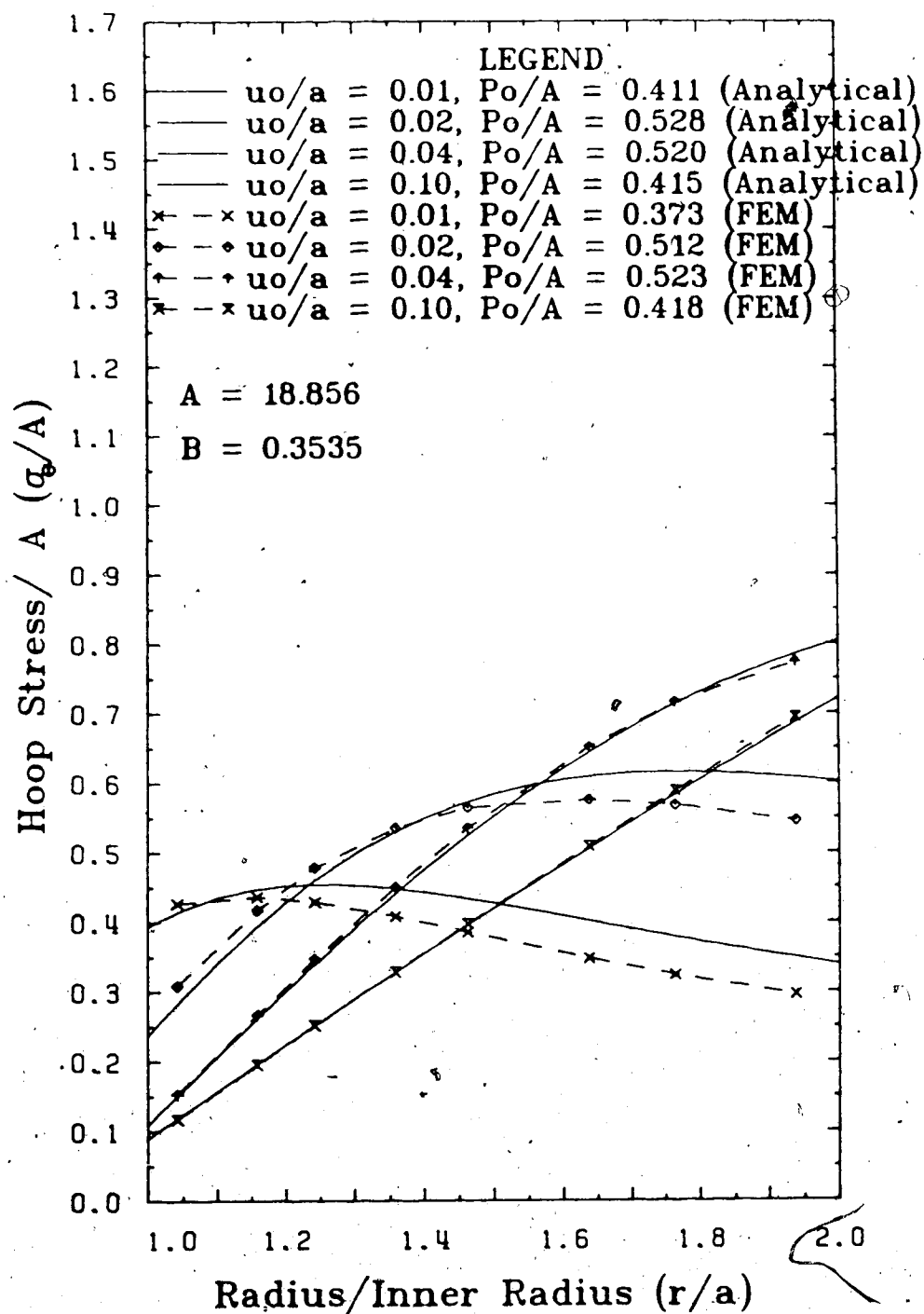


Figure 2.8: Hoop Stress Distribution $I(B) = 0.75$

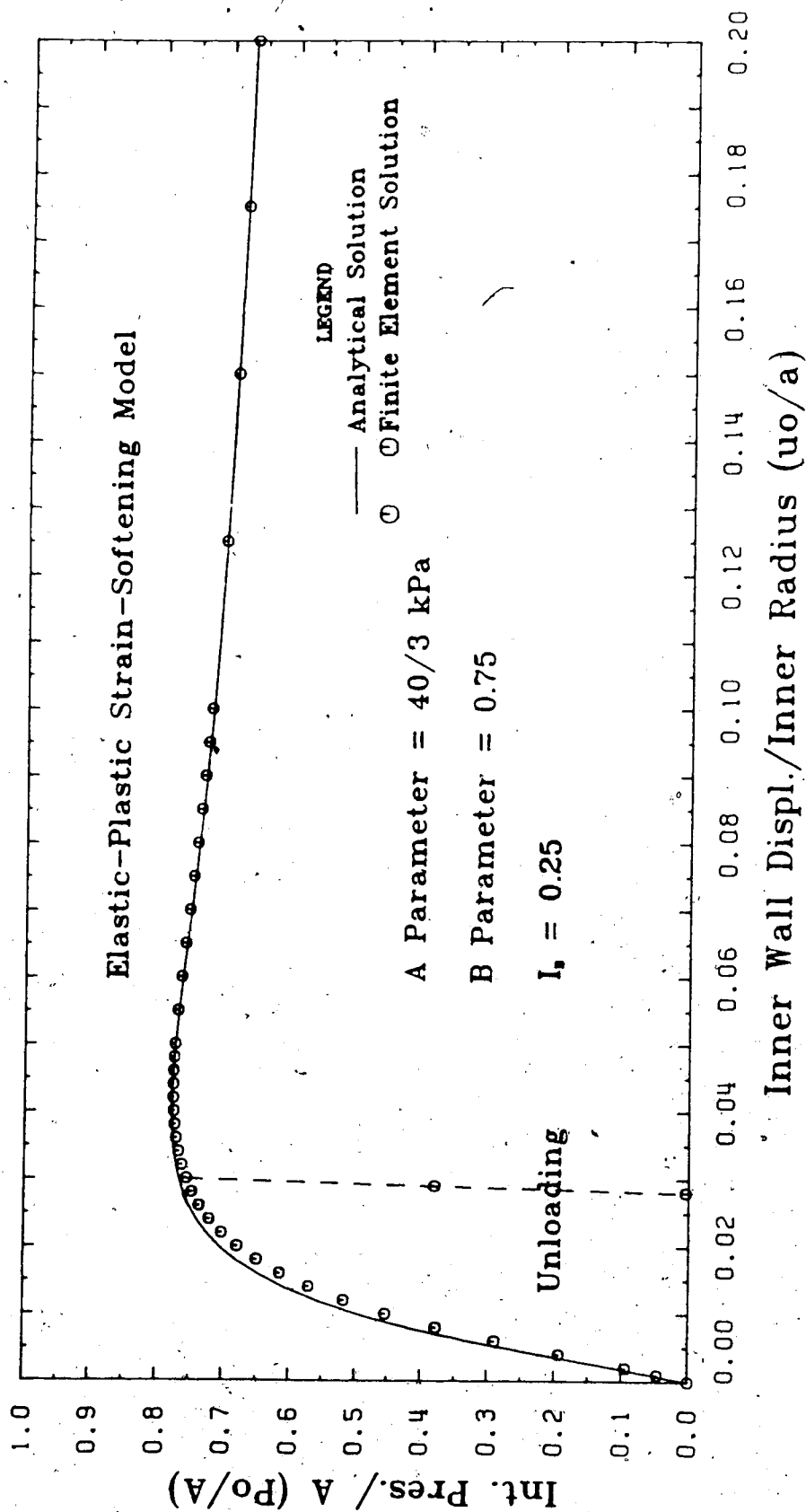


Figure 2.9: Unloading Response of Thickwalled Cylinder

analysis in general, and be able not to differentiate between this and the reduction of load due to strain softening deformation, an elastic analysis is first performed. A determination of which of the conditions in Equations (2.10) is being satisfied must be made in order to decide whether the material is undergoing plastic or elastic deformation. Further discussion of the numerical aspect of the analysis will be given later. The hoop stress for the unloading and reloading cases are shown in Figure 2.10. Complete unloading to almost zero internal pressure after some plastic deformation results in non-zero stresses inside the cylinder ($P/A = 0.0043$ in Figure 2.10). This is expected of a plastically deformed material.

2.6 Computer Implementation of the Finite Element Method

The implementation of the finite element method requires the development of a computer program. A program called SAFE (Soil Analysis by Finite Element) has been developed for this research. The program is intended for use in other applications in solving geotechnical problems. Special techniques employed in the program, such as convergency scheme, matrix solution technique and stress calculation procedure, will be discussed briefly below.

2.6.1 Convergence Scheme and Convergence Criteria

The matrix finite element equation given by Equation (2.7) is a set of non-linear algebraic equations because the

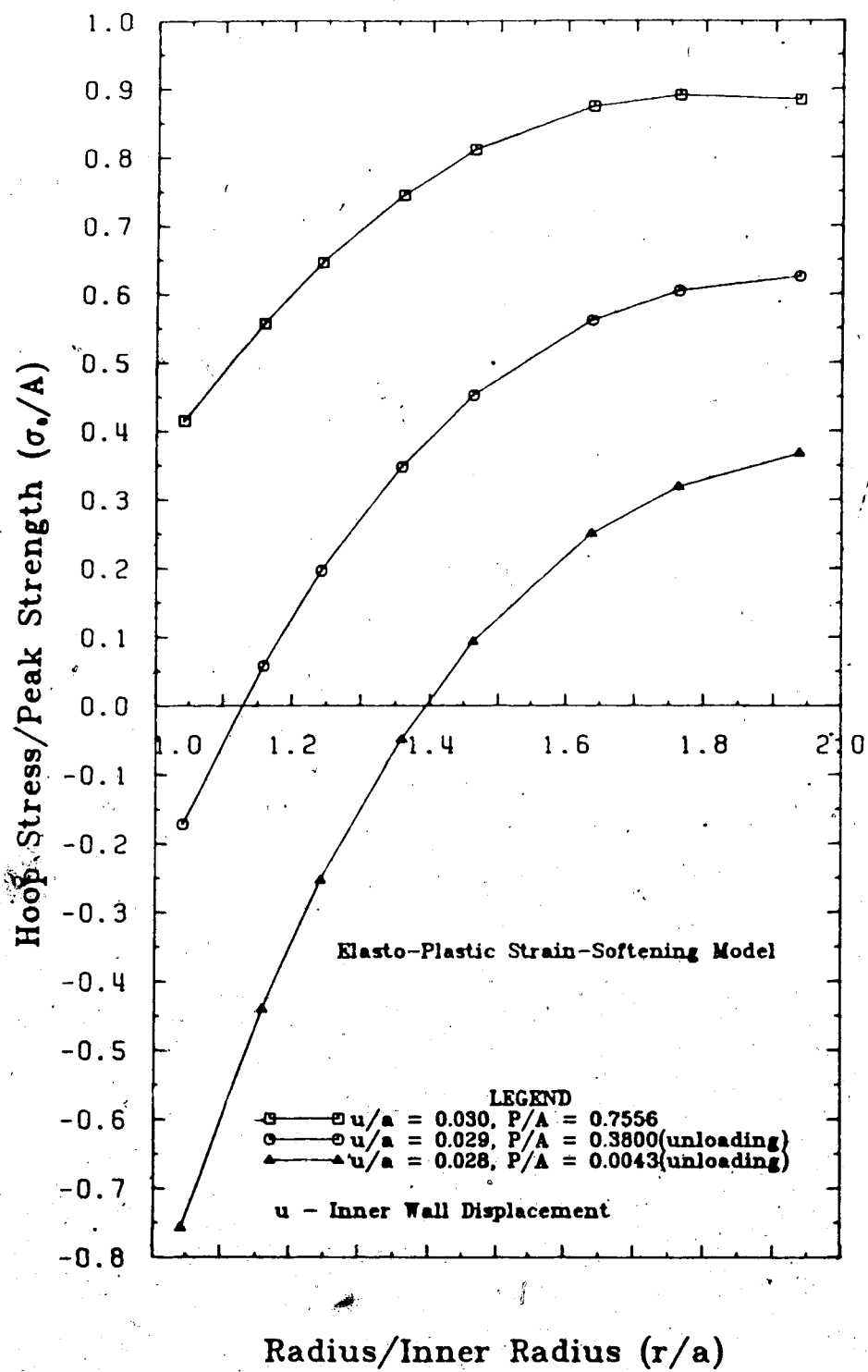


Figure 2.10: Unloading Hoop Stress Distribution

stiffness matrix $[K]$ is dependent upon on the current state of stress. Therefore an iterative procedure is required to obtain a solution. The Newton-Raphson method is used to obtain an approximate solution to this equation. However, to update the stiffness matrix at every iteration for the full Newton-Raphson method can sometimes be very expensive. Combining the Newton-Raphson and the modified Newton-Raphson to update the stiffness at selected intervals can give a more effective solution scheme. The frequency of updating the stiffness matrix can be changed easily by the analyst in the SAFE program to suit the convergence characteristics of individual problems. Experience in this research indicates that updating the stiffness at every 3 to 5 iterations for strain hardening materials provides a good rate of convergence. Usually updating the stiffness matrix at every iteration is necessary for strain softening materials to obtain stable convergence.

In elasto-plastic and non-linear elastic analysis, unloading can occur in part of the structure during the analysis. Using the loading modulus for unloading can lead to sudden divergence. Therefore, it is important to detect unloading and use the appropriate modulus in the analysis. In this program, elastic loading or unloading is assumed in the first iteration of every load increment, and if the assumption is incorrect, the stiffness matrix will be updated in the second iteration. Since the elastic loading modulus is usually higher than the elasto-plastic modulus

for most materials, this approach will result in a more stable solution scheme than that using the elasto-plastic modulus in the first iteration. Moreover, experience has indicated that updating the stiffness matrix in the second iteration results in a faster convergence rate due to better stress approximation in formulating the stiffness matrix. Furthermore the cost of the elastic analysis in the first iteration is relatively low.

Since the equations of equilibrium will not be satisfied exactly in numerical analyses, it is important to ensure the error is small and will not be accumulated in subsequent steps of the analysis. The error in convergence in this program is defined as:

$$\text{error} = \frac{|\Delta\delta^i|}{|\delta^i|} \leq \text{tol} , \quad (2.31)$$

where

$|\Delta\delta^i|$ is the Euclidean norm of the change in incremental nodal displacements of the whole structure at iteration i ;

and $|\delta^i|$ is the Euclidean norm of the total nodal displacements of the whole structure at iteration i .

The tolerance in Equation (2.31) is usually set to be less than 0.01%. It is important to ensure the error is small in order to obtain stable convergence although this accuracy in

displacements and stresses may not be required in the final result.

Ensuring that the error in displacements is less than the tolerance for each load increment is not quite sufficient since this error can accumulate in subsequent steps and eventually lead to numerical instability. One way to minimize the accumulation of error is to ensure that the total equilibrium equation is satisfied at each step and not the incremental equilibrium equation. That is:

$$\int_V [B]^T \{\sigma\} dv = \{R\} \quad (2.32)$$

is being satisfied and not:

$$\int_V [B]^T \{\Delta\sigma\} dv = \{\Delta R\} \quad (2.33)$$

is being satisfied.

This approach will transfer the error of each loading step to the next load increment so that the accumulation of error can be minimized. The result is a more stable and accurate solution scheme.

2.6.2 Methods of Stress Calculation

The method of stress calculation for non-linear and elasto-plastic problems is much more involved than for elastic problems. Basically, the increment of strain is

first calculated from the increment nodal displacement given by:

$$\{\Delta \epsilon\} = [B]\{\Delta \delta\} , \quad (2.34)$$

and the stresses are calculated from:

$$\{\Delta \sigma\} = \int_{\Delta \epsilon} [C]\{d\epsilon\} . \quad (2.35)$$

However, the constitutive matrix $[C]$ is stress dependent. Therefore the integral must be evaluated by some numerical techniques. In this program, the Euler Forward Integration Method, Improved Euler Method and the Runge Kutta method are used to evaluate this integral. In the Euler forward integration method, the $[C]$ matrix is updated using the current stress state. That is:

$$\{\Delta \sigma^i\} = \frac{1}{n} [C^{i-1}]\{\Delta \epsilon\} , \quad (2.36)$$

and

$$\{\Delta \sigma\} = \sum_{i=1}^n \{\Delta \sigma^i\} = \sum_{i=1}^n \frac{1}{n} [C^{i-1}]\{\Delta \epsilon\} , \quad (2.37)$$

where

n is the number of sub-increments;

$\{\Delta \sigma^i\}$ is the change in stresses of sub-increment i ;

$[C^{i-1}]$ is the constitutive matrix based on the stress state of the previous sub-increment $i-1$.

This approach will result in the constitutive matrix being

one sub-increment behind the stress increment. The Euler Forward Method is also called the first order method because only the first order terms in the Taylor series expansion of Equation (2.35) are used in the integration scheme where higher order terms are neglected. A detailed discussion of these three methods and the errors involved are given in Appendix A.

It is important to notice that the integration limits in Equation (2.35) are over the changes in strains due to the entire load increment and summing the results of all iterations in that load increment, and not simply over the changes in strains within each iteration. In other words the stresses are always calculated from those based on the previous loading step to which the solution has converged. This approach will minimize the error in stresses due to the iterative procedure. It must be emphasized that accurate stress calculation is vital in obtaining stable convergence characteristics because the entire elasto-plastic non-linear finite element formulation presented here is based on the current state of stresses. Therefore, effort spent in stress calculation is rewarded by more rapid and stable convergence which is particularly important in analyzing strain softening material.

The stress calculation for plastically deformed material is a little more complicated than non-linear elastic material such as the hyperbolic model (Duncan and Cheung 1969). If the material is elastic, or under elastic

unloading or loading, the elastic constitutive matrix should be used which is given by Equation (2.35). If the material is fully plastic, then the elasto-plastic matrix should be used. However, if the material changes from an elastic state to a plastic state in one load increment, then part of the deformation will be elastic and part will be plastic. Therefore, it is necessary to distinguish the portion of elastic deformation from plastic deformation.

The algorithm for elasto-plastic stress calculation used here follows the approach discussed by Bathe(1982). In this method it is first assumed that the stress changes are all elastic and then the final stresses are substituted into the yield function. If the function is less than zero, then the assumption of elastic deformation is correct. If the yield function is greater than zero and the previous stress state was plastic, then it is simply a case of continuous loading in the plastic region. If the yield function is greater than zero and the previous stress state is elastic, then yielding occurs within this loading step. Let R be the proportion of the elastic deformation defined as:

$$F(\sigma_{ij} + R\Delta\sigma_{ij}) = 0, \quad (2.38)$$

where F is the yield function.

The value of R can be determined using the 'Interval Halving technique'. Since R has a lower limit of zero and upper

limit of one, this technique will always guarantee convergence as long as F is continuous in R and no other restriction on the form of F is required. A description of the 'Interval Halving Technique' is given in Appendix B.

During the stress calculation procedure, the yield criteria may not be satisfied exactly. It is important to satisfy the yield criteria within allowable tolerance at all stages in the analysis even at the expense of violating the flow rule locally (Zienkiewicz 1972). If the state of stress is outside the yield surface, then an iterative procedure is used to bring the stress state back to the yield surface. Details of this procedure is given in Appendix C.

At this stage, one can see the complication involved in obtaining a solution using non-linear elasto-plastic analysis. First of all, the sequence of loading is divided into several steps and possibly each loading step is subdivided into several load increments. Then an iterative procedure is used to obtain convergence of each load increment. Within each iteration, the stresses are calculated in subintervals and within each subinterval, the yield criterion is to be satisfied by using an iterative procedure. Therefore the cost of obtaining a non-linear solution is at least an order of magnitude higher than that of the linear solution.

2.6.3 Computer Program SAFE

The computer program SAFE is capable of performing plane stress, plane strain, axisymmetric and three dimensional analyses with special features for many geotechnical applications. Such features include the incorporation of in-situ stress fields with different K_0 conditions, modelling excavation and embankment construction or merely a change of the material properties of the elements during the analysis. No tension analysis, hyperbolic elastic and various frictional and non-frictional plastic models with associated and non-associated flow rule to perform fully drained and fully undrained analysis (Chapter 5) are also available. Material models with non-associated flow rule or undrained effective stress analysis will result in non-symmetric stiffness matrices. The program SAFE is also capable of solving non-symmetric matrices.

2.7 Conclusion

A general elasto-plastic finite element formulation is presented in this chapter. The formulation is kept as general as possible such that it can be applied to a variety of different material models as long as they are within the context of the theory of plasticity. A strain softening model for frictionless material is presented and the finite element solution is compared with the analytical result with considerable success for the simple problem of the expansion

of a thickwalled cylinder under internal pressure. The finite element procedure is found to be quite efficient in modelling strain softening materials. The strain softening model presented here requires only two material parameters to define the material which cannot allow independent variation of peak strength, residual strength, peak strain and post peak softening behaviour. Two more strain softening models will be presented in subsequent chapters with a higher degree of flexibility.

3. FINITE ELEMENT SIMULATION OF SHEAR BAND DEFORMATION

In Chapter 2 the finite element formulation for a strain softening material was presented. In principle with this strain softening model, the basic ingredients in analyzing progressive failure as outlined in chapter 1 are now available. However, the deformation of a strain softening material such as stiff heavily overconsolidated clay often results in the formation of a localized shear zone (sometimes also referred as a shear band), and the overall behaviour of the soil mass is thus governed by the deformation of this localized shear zone. Therefore it is essential to understand the mechanism of shear zone deformation and to capture this behaviour, if possible, using the finite element model. One of the aims of this chapter is to study the mechanism of localized deformation and to evaluate the finite element formulation presented in Chapter 2 in capturing shear band deformation.

As mentioned briefly in Chapter 1, shear band deformation can be broadly classified into two main types. The first type refers to the situation where the location of the shear band is predetermined by local geology due to the depositional and geological history of the area which result in inherent zones of weaknesses. The second type deals with a more or less homogeneous material and shear band initiation and propagation are unknown prior to the analysis. The theory for this latter case will be discussed

first.

3.1 Theory of Localized Deformation

One of the theories of shear band deformation is focussed on the idea that localization may be considered as an instability in the constitutive description of homogeneous deformation. The material instability here constitutes a necessary but not sufficient condition for shear band bifurcation. For example, a specimen of unstable material (the definition of unstable material will be discussed later) tested in an uniaxial testing machine which is capable of producing a perfectly uniform stress throughout a perfectly homogeneous specimen free of defects will not undergo localized deformation because of symmetry, isotropy and homogeneity. This ideal case can only occur in mathematical and numerical models since in reality slight imperfections in material and/or loading conditions will destroy the conditions of symmetry and homogeneity. Therefore, in numerical modelling it is important to ensure that these basic conditions for localization (which are discussed in Appendix D) are incorporated into the model when simulating shear band bifurcation.

The study of bifurcation and discontinuity relations in solid mechanics was pioneered by Hill (1961) and later extended (Hill 1962) to study the propagation of wave fronts in solids. Leuder bands are one kind of localized deformation being studied extensively by metallurgists. The

slip line field is a mathematical model that approximates idealized metal deformation in the form of distinct shear planes in obtaining limit loads for classical plasticity problems. The propagation of a wave front results in a discontinuity of stresses and strains across the front and static equilibrium is not satisfied due to the inertia effect of the wave. However, a stationary wave degenerates to a discontinuity in which only some components of the stresses and strains are discontinuous across the discontinuity. The governing equations for a stationary wave is the same as that for a discontinuity (Hill 1962). Houlsby and Wroth (1980) have classified kinematic discontinuities into five different categories depending on the continuity of velocities and velocity gradients (see Appendix D). In the present study it is assumed that there is no separation along the discontinuity which can lead to fracture and disintegration of the body.

The solution to most continuum problems must satisfy two basic conditions. These are the conditions of equilibrium and of compatibility. The equilibrium equation for a discontinuity is given by:

$$\Delta \sigma_{ij} \nu_j = 0, \quad (3.1)$$

where

$\dot{\sigma}_{ij}$ are the components of the material time derivative of the Cauchy stress tensor;

ν_j are the components of the unit normal of the

discontinuity;

and Δ denotes the difference in stress field inside and outside of the discontinuity.

Equation (3.1) expresses that the traction on one side of the discontinuity must be equal to that on the other side of the discontinuity. If Equation (3.1) is not satisfied, then the discontinuity will not be stationary and the problem becomes the propagation of a wave front. The condition of compatibility at the discontinuity can be expressed as:

$$\Delta u_{i,j} = \lambda_i \nu_j, \quad (3.2)$$

where

$\Delta u_{i,j}$ are the components of the velocity gradient tensor;

ν_j are the components of the unit normal of the discontinuity;

λ_i are proportionality constants;

and Δ denotes the difference in velocity gradient field inside and outside of the discontinuity.

Equation (3.2) is to ensure that there is no separation or slip of the body at the discontinuity but allows some components of the velocity gradient to be discontinuous. By combining Equations (3.1) and (3.2) with a constitutive relationship of the material of the following form:

$$\overset{\nabla}{\Delta}\sigma_{ij} = C_{ijmn} D_{mn} , \quad (3.3)$$

where

$\overset{\nabla}{\Delta}\sigma_{ij}$ is the Jaumann stress rate tensor;

D_{mn} is the symmetric part of the velocity gradient tensor;

and C_{ijmn} is the incremental constitutive tensor.

one can derive the following relationship for infinitesimal deformation and uniform stress field within the discontinuity (see Appendix D):

$$\det[\nu_i C_{ijmn} \nu_n] = 0 . \quad (3.4)$$

It is noted that Equation (3.4) is a necessary, but not sufficient condition, for bifurcation to occur as discussed earlier. This condition indicates that for bifurcation to occur the matrix $[\nu_i C_{ijmn} \nu_n]$ must be singular. This implies the loss of ellipticity of the velocity equations of equilibrium in the form:

$$(C_{ijmn} \Delta u_{m,n})_{,i} = 0 . \quad (3.5)$$

An equivalent statement of Equation (3.4) is that the constitutive relationship tensor C_{ijmn} is not positive definite in which non-positive definiteness is defined as:

$$C_{ijkl} \epsilon_{ij} \epsilon_{kl} \leq 0 \quad (3.6)$$

for at least one arbitrary tensor ϵ_{ij} and not all components of ϵ_{ij} are zero.

One should realize that of all the incremental constitutive tensors which satisfy Equations (3.3) and (3.5), the one which satisfies Equation (3.4) will also satisfy Equation (3.6). This restricts the possible choices of material models if localization is to be captured in numerical analysis.

3.2 Eigenvalue Analysis of Elasto-Plastic Finite Element Formulation

The above discussion reveals that the incremental constitutive matrix of the elasto-plastic finite element formulation must satisfy Equation (3.6) in modelling localized deformation. In other words, some of the eigenvalues of the incremental constitutive matrix must be less than or equal to zero.

The eigenvalues of finite elements have been studied for a linear elastic material (Bathe and Wilson 1976). However, the non-linear constitutive matrix, especially using the elasto-plastic formulation, has not been studied in detail yet. Since the constitutive matrix depends on the stress state in the body, the eigenvalues are not characteristic of the particular formulation. Therefore only

special cases will be considered below.

3.2.1 Physical Meaning of Eigenvalues and Eigenvectors

To understand the importance of eigenvalue analysis, let us first consider the following quantity termed the perturbation energy. The perturbation energy of an element dv is defined as:

$$dw = \Delta\sigma_{ij} \Delta\epsilon_{ij} dv, \quad (3.7)$$

where

$\Delta\sigma_{ij}$, $\Delta\epsilon_{ij}$ are the incremental stress tensor and incremental strain tensor associated with $\Delta\sigma_{ij}$ respectively.

The perturbation energy is a measure of the stability of the structure subjected to a slight external disturbance. For elastic and strain hardening material, the perturbation energy is always positive. For perfectly plastic material, it is zero and for strain softening material it is negative. Therefore, a zero or negative perturbation energy indicates unstable behaviour. The perturbation energy is different from plastic work since work is still required to deform a perfectly plastic or strain-softening material, and plastic work is always positive.

Expressing the incremental stress strain relationship of the material as:

$$\Delta \sigma_{ij} = C_{ijkl} \Delta \epsilon_{kl}$$

$$\text{then } dw = \sigma_{ij} \Delta \epsilon_{ij} dv \quad (3.8a)$$

$$\text{or } \frac{dw}{dv} = \Delta \epsilon_{ij} C_{ijkl} \Delta \epsilon_{kl} \quad (3.8b)$$

Therefore, it is clear that the eigenvalues of the incremental constitutive matrix are related to the perturbation energy per unit volume. Moreover the incremental strains are given by the eigenvectors in which the perturbation energy is given by the corresponding eigenvalues if the eigenvectors are normalized. By comparing Equations (3.8b) and (3.6) it is seen that a non-positive definite constitutive tensor which satisfies Equation (3.6) will result in a zero or negative eigenvalue. This type of material is termed an unstable material. From Equations (3.4), (3.6) and (3.8) it is also suggested that shear band bifurcation should occur either at or close to the peak strength of the material or in the post peak range.

Eigenvalue analysis can be considered as a change of base from Euclidean space to eigenspace. The eigenvectors are the base vectors of the eigenspace in terms of the Euclidean space. Since the eigenvectors here are the strain increments, therefore they represent different modes of deformation and the associated energy required per unit volume is given by the corresponding eigenvalues. All possible modes of deformation are included in the

transformed eigenspace thus the eigenvalue analysis basically provides an insight to the problem from a different point of view.

3.2.2 Eigenvalue Analysis of Elasto-Plastic matrix for Elastic Perfectly Plastic Material

The eigenvalue of the constitutive matrix for a linear elastic material will first be considered here to give a basis of comparison with the plastic case. For a linear elastic material under plane strain condition, the largest eigenvalue and the corresponding eigenvector represents the hydrostatic compression (or hydrostatic extension) mode of deformation, see Figure 3.1. The remaining two eigenmodes are simple shear modes. These two modes are basically the same mode as shown in the strain circle in Figure 3.1. For example, if the strain state of mode 2 is represented by a state of pure shear, point 3, instead of the extension mode, then $\Delta\epsilon_{xx} = \Delta\epsilon_{yy} = 0$ and $\Delta\epsilon_{xy} = 1/\sqrt{2}$. Note that $\Delta\gamma_{xy} = 2\Delta\epsilon_{xy} = \sqrt{2}$ therefore the perturbation energy is given by:

$$\text{Perturbation energy} = \langle 0, 0, \sqrt{2} \rangle [C] \begin{Bmatrix} 0 \\ 0 \\ \sqrt{2} \end{Bmatrix}$$

$$= \langle 0, 0, \sqrt{2} \rangle \lambda_2 \begin{Bmatrix} 0 \\ 0 \\ \sqrt{2} \end{Bmatrix}$$

where

λ_2 is the eigenvalue of mode 2 represented by point 3 in the strain circle.

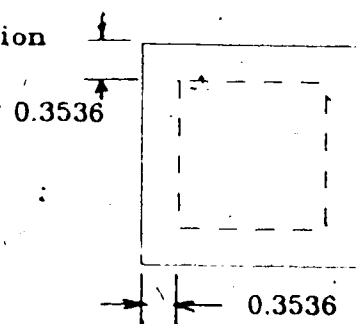
Mode 1 - Hydrostatic Compression

$$\lambda/E = 19.23, \nu = 0.3$$

$$\epsilon_x = 0.7071$$

$$\epsilon_y = 0.7071$$

$$\gamma_{xy} = 0.0$$



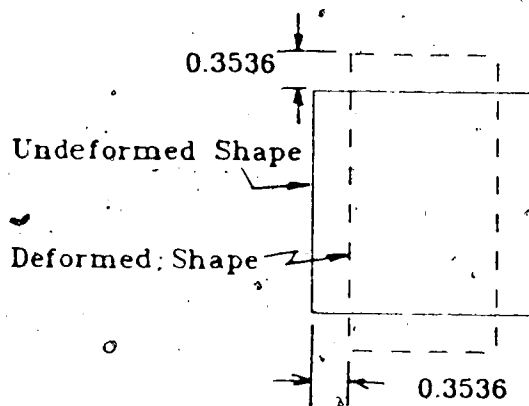
Mode 2 - Extension

$$\lambda/E = 76.69$$

$$\epsilon_x = -0.7071$$

$$\epsilon_y = 0.7071$$

$$\gamma_{xy} = 0.0$$



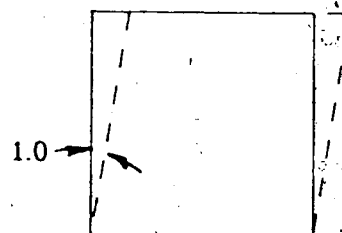
Mode 3 - Simple Shear

$$\lambda/E = 38.46$$

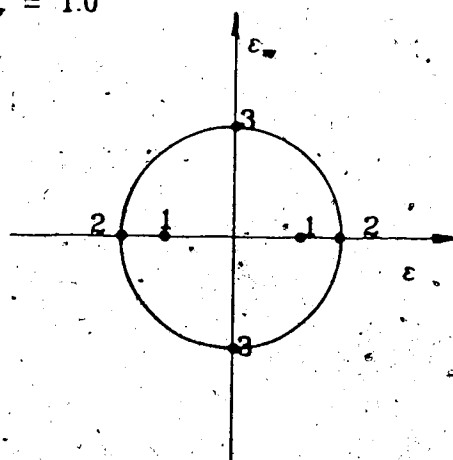
$$\epsilon_x = 0.0$$

$$\epsilon_y = 0.0$$

$$\gamma_{xy} = 1.0$$



(Plane Strain)



Mohr Strain Circle

Figure 3.1: Eigen Mode Shape of Elastic Deformation

Since both points 2 and 3 represent the same strain state, the perturbation energy must be the same. Therefore:

$$\text{Perturbation Energy} = \lambda_2 = 7.692 = \langle 0, 0, \sqrt{2} \rangle \lambda_2^{(1)}$$

$$\begin{Bmatrix} 0 \\ 0 \\ \sqrt{2} \end{Bmatrix}$$

$$\text{or } \lambda_2^{(1)} = 7.692/2 = 3.846,$$

which is the eigenvalue of mode 3.

The eigenvalue of mode 2 can be derived from mode 3 in a similar manner. This indicates that there are only 2 basic modes of deformation in an elastic isotropic material and therefore only two parameters are required to define a linear elastic material. This result is not surprising since shearing in different directions of an elastic isotropic material must require the same amount of energy. The same conclusion cannot be made for a plastically deformed material.

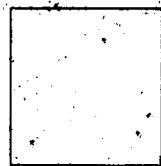
The result of the eigenvalue analysis for the elastic perfectly plastic material is shown in Table 3.1. Since the constitutive matrix is stress dependent, two special cases will be considered. The first case is a simple uniaxial compression mode of deformation. In this case the vertical stress is increased until yielding occurs. The second case is a simple shear mode of deformation. Both the von-Mises and Tresca yield criteria are considered.

Table 3.1 Eigenvalue Analysis of the Elasto-Plastic Constitutive Matrix

		Eigenvalue λ	Eigenvector (Normalized)		
			ϵ_{xx}	ϵ_{yy}	γ_{xy}
Linear elastic		1.9231×10^4	0.7071	0.7071	0.0
		0.7692×10^4	-0.7071	0.7071	0.0
		0.3846×10^4	0.0	0.0	1.0
Elastic	unia.	1.9156×10^4	0.7419	0.6705	0.0
	comp.	0.3846×10^4	0.0	0.0	1.0
		0.0321×10^4	0.6705	-0.7419	0.0
Plastic	unia.	1.9231×10^4	0.7071	0.7071	0.0
	shear	0.7692×10^4	-0.7071	0.7071	0.0
		0.0	0.0	0.0	1.0
Plastic	unia.	1.9231×10^4	-0.7071	-0.7071	0.0
	comp.	0.3846×10^4	0.0	0.0	-1.0
		0.0	-0.7071	0.7071	0.0
Plastic	unia.	1.9231×10^4	0.7071	0.7071	0.0
	shear	0.7692×10^4	-0.7071	0.7071	0.0
		0.0	0.0	0.0	-1.0

$$E = 1000.0 \text{ kPa} \quad \nu = 0.30 \quad \sigma_y = 10.0 \text{ kPa}$$

+++++ $\sigma = 1.0 \text{ kPa}$



+++++

uniaxial compression

+++++ $\tau = 1.0 \text{ kPa}$



+++++

uniform shear

(plane strain condition)

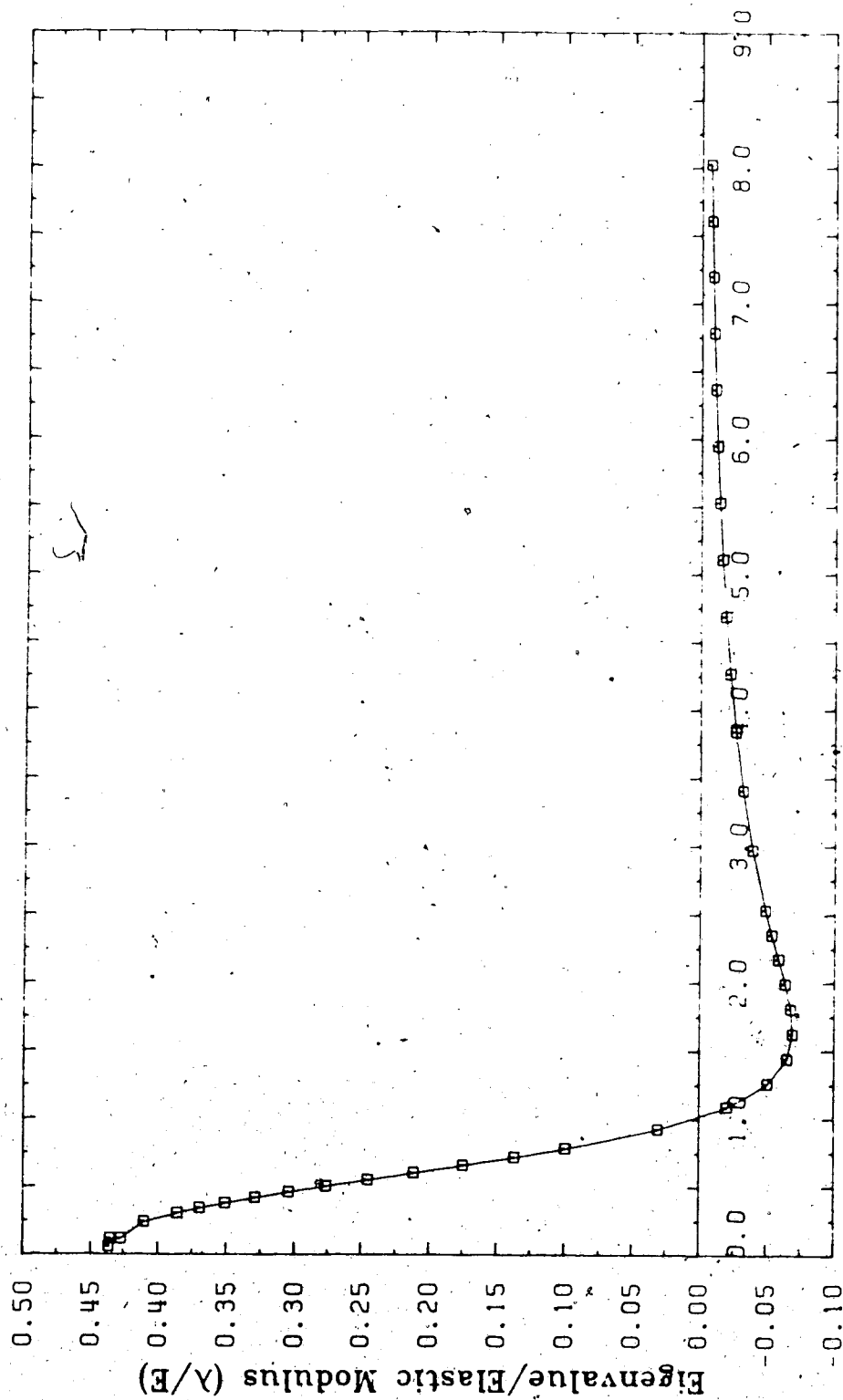
For the perfectly plastic case, there is at least one zero eigenvalue except in the case of uniaxial compression of von-Mises material as shown in Table 3.1. The two basic modes of deformation, hydrostatic compression and simple shear, are present in all cases. The eigenvalues for these two modes are the same as for the elastic case. Note that there is a zero energy mode for the case of uniaxial compression for Tresca material at 45 degrees with respect to horizontal. However the zero energy mode for the case of uniform shear for both material are in the horizontal directions. This indicates that the material has a "weak direction" which is dependent upon the state of stress. The perturbation energy in this direction is zero. This is in agreement with the understanding of non-frictional material which fails at 45 degrees in a uniaxial compression test.

For the case of uniaxial compression of von-Mises material, there is no zero energy mode. The eigenvalue for simple shear is identical to the other cases while the eigenvalue for the hydrostatic compression mode is slightly lower. It is not clear why the von-Mises material does not have a zero energy mode for this case. However, it is clear that the formulation does have a zero energy mode as shown in the simple shear case. The above analysis demonstrates clearly that the elasto-plastic formulation does satisfy Equation (3.6).

3.2.3 Eigenvalue Analysis of Elasto-Plastic matrix for Strain Hardening and Softening Material

It is seen from above that the perturbation energy for a perfectly plastic material must be greater than or equal to zero. Negative perturbation energy can only be obtained from a strain softening material with a gradual post peak softening behaviour. The strain softening model discussed in Chapter 2 will be analyzed here to remind the reader that this model has a strain hardening behaviour prior to peak strength and a strain softening behaviour after peak. Therefore it is expected that all of the eigenvalues will be positive in the pre-peak range and some eigenvalues will be negative in the post peak range. Also since the stiffness of the material decreases with strain except in the post peak region, it is also expected that the eigenvalues, or at least some eigenvalues, will decrease prior to peak strength.

The eigenvalues are obtained by simulating an uniaxial compression test as shown in Table 3.1. The results of the analysis are given in Figure 3.2. The eigenvalues for isotropic compression and horizontal shear remain basically constant during plastic deformation both in the pre-peak and post-peak range. The eigenvalues for simple shear mode at 45° decreases with plastic strain as shown in Figure 3.2. The plastic strain in this figure is normalized with respect to the peak plastic strain and one can see that the eigenvalues become negative in the post peak range.



Plastic Strain/Peak Strain ($\epsilon'/\epsilon'_{max}$)

Figure 3.2: Eigenvalues of Strain Softening Material

Therefore, shearing along this plane actually resulted in a release in energy due to strain softening behaviour but the isotropic compression and shearing mode at different directions require positive perturbation energy. This again creates a 'weak' direction in which the material is more easily sheared. In other words 'anisotropy' has been induced by plastic deformation which is one of the main differences between the elastic and plastic formulations.

The orientations of the 'weak direction' varies slightly during plastic deformation but remains very close to 45° . The variation ranges from 44.4° to 45° (or 45.6° to 45°) and eventually approaches 45° at large plastic strain. This is different from the result obtained from the perfectly plastic case where the 'weak direction' is always at 45° . The eigenvalue for the isotropic compression mode also varies slightly and the strains $\Delta\epsilon_{xx}$, $\Delta\epsilon_{yy}$ are not the same during plastic deformation. At large strain these two strains become closer to each other. The eigenvalue for the simple shear mode remains constant throughout the analysis.

The above analysis demonstrates two important aspects of the plasticity formulation. First the perturbation energy decreases with plastic strain and becomes negative in the post peak range of deformation for a strain softening material. In the pre-peak range the perturbation energy is always positive. Therefore shear band bifurcation is expected to occur at or close to peak strength. The second point is that during plastic deformation, the material has a

weak direction in which less energy is required to shear. This weak direction occurs at 45° with respect to the principal stresses for a frictionless material. The material thus locally becomes anisotropic. For strain softening material, the orientation of the 'weak direction' is not exactly 45° as would be expected for a non-frictional material. This departure from 45° is probably too small to be of practical concern but theoretically, the propagation of the shear band may locally depart from the 45° direction depending on the amount of plastic straining which usually varies along the shear band.

3.3 An Elastic Brittle Plastic Model

In this section a different strain softening model is introduced to model shear band deformation. The strain softening model discussed in Chapter 2 has a gradual reduction of shear strength after peak. For a very sensitive material the post peak deformation can be abrupt. An approximation to the abrupt softening behaviour can be made by an elastic brittle plastic material. The stress strain relationship for this material is shown in Figure 3.3. In this model the material is assumed to behave linear elastically up to the peak strength followed by a sudden decrease in strength from peak to residual. The material is assumed to deform in a perfectly plastic manner after peak. It has been shown previously that the elastic perfectly plastic material can be used in modelling a shear band

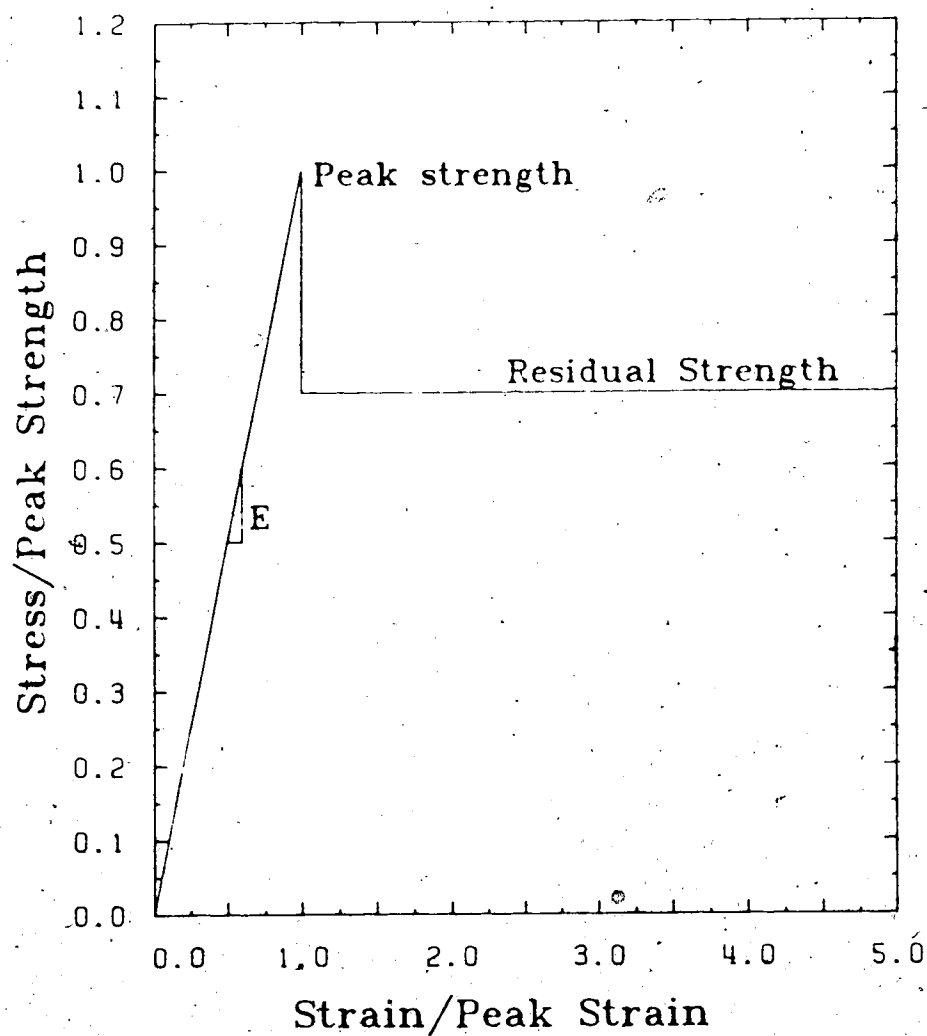


Figure 3.3: Stress Strain Relationship of Brittle Plastic Material

therefore it is expected that this model can also be used to model shear band deformation. The advantage of this model is that the peak strength, residual strength and peak strain can be specified independently. Therefore at least three parameters are required to define the model.

In this model the transition from peak to residual strength is abrupt. Therefore the method of stress calculation discussed in Appendix A cannot be used during the transition from peak strength to residual strength because the constitutive relationship of the material at the transition is undefined. There are several methods available to determine the stresses for this material and the method used in this research is discussed in Appendix D.

Several yield criteria can be used in this model. The Tresca, von-Mises, Mohr-Coulomb and Drucker-Prager yield criteria are available for this model in the computer program SA 3. Frictional materials with brittle plastic behaviour can be modelled by using the Mohr-Coulomb yield criterion. However it is known that the degree of brittleness varies with the hydrostatic stresses for many materials. This aspect has not been studied here and is not implemented in this model.

Since this is a plastic model, unloading after peak strength will lead to plastic deformation. Reloading in this model will cause yielding to occur at residual strength and therefore peak strength will only be reached once.

3.4 Modelling Shear Band Deformation in a Uniaxial Plane

Strain Test

In this section, a plane strain uniaxial test is simulated numerically using the finite element method with the elasto-plastic formulation presented. The material is assumed to behave in an elastic brittle plastic manner as shown in Figure 3.3 with an abrupt decrease in yield strength after peak.

The finite element idealization of the specimen is shown in Figure 3.4. The specimen is 10 cm high and 5 cm wide and is subjected to plane strain conditions with zero confining pressure on the sides. The top and bottom platens are assumed to be perfectly smooth and rigid. Eight node isoparametric elements were used with 661 nodes and 200 elements. To introduce non-homogeneous deformation or imperfections into the specimen, a weak element is placed on the edge of the specimen at a height of 6 cm as shown in Figure 3.4. Yielding is expected to be initiated at this location.

The following material parameters are used in the analysis:

$$E = 10,000. \text{ kPa};$$

$$\nu = 0.30;$$

$$S_p = 200 \text{ kPa};$$

p

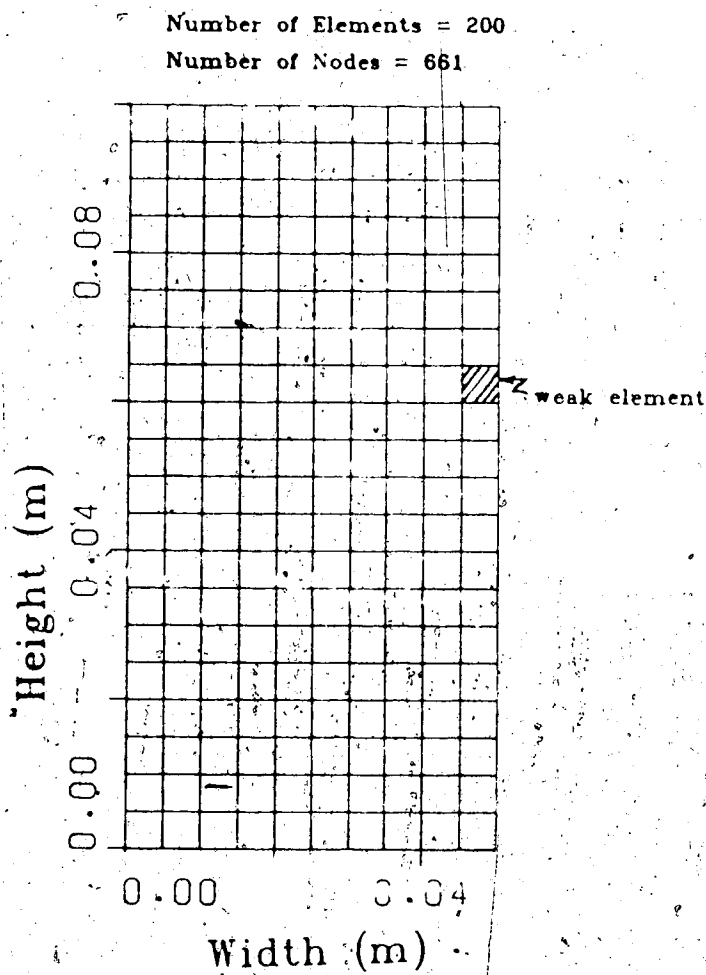


Figure 3.4: Finite Element Idealization of Soil Specimen

$$S_r = 190 \text{ kPa};$$

$$S_p = 150 \text{ kPa for weak element};$$

$$S_r = 140 \text{ kPa for weak element};$$

where

S_p , S_r are the peak and residual uniaxial compressive strength respectively.

The Tresca yield condition is used to model frictionless material. In order to capture the propagation of the shear band inside the specimen, a high residual strength is used. Low residual strength will result in large amount of energy release after peak which may lead to abrupt failure and the process of shear band propagation cannot be observed. Moreover, a strain controlled test is simulated in order to obtain the post peak behaviour of the material.

The results of the analysis are shown in Figure 3.5. It is seen in this figure, that the applied stress does not reach the peak strength of the material due to the presence of the weak element. There is also only a slight decrease in the applied stress after peak and the stress at residual is approximately $0.94 S_p$. It is interesting to note that there is no appreciable increase in strength after peak, and it is difficult to distinguish between the peak and residual strength. The test reveals that the material is behaving

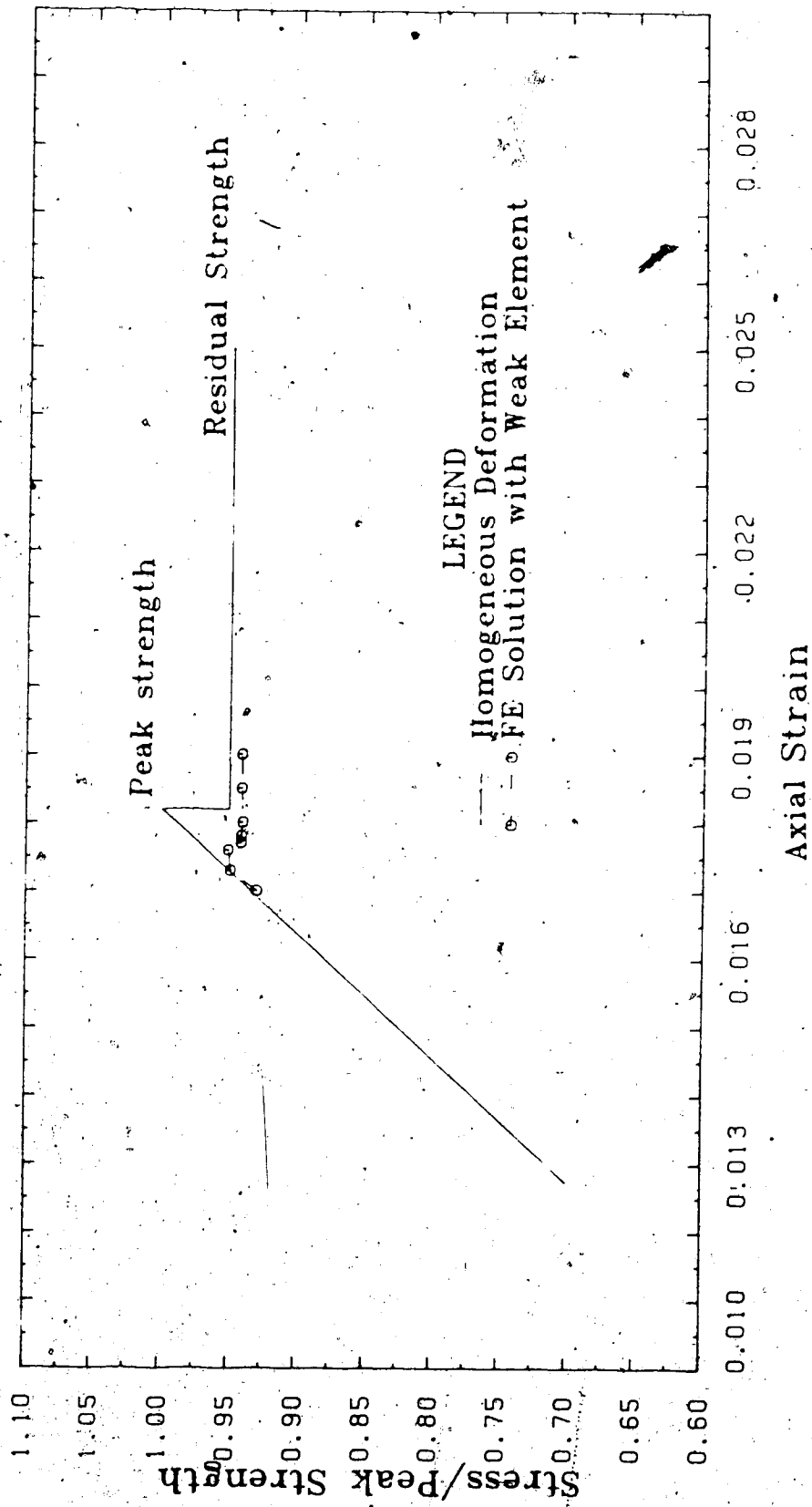
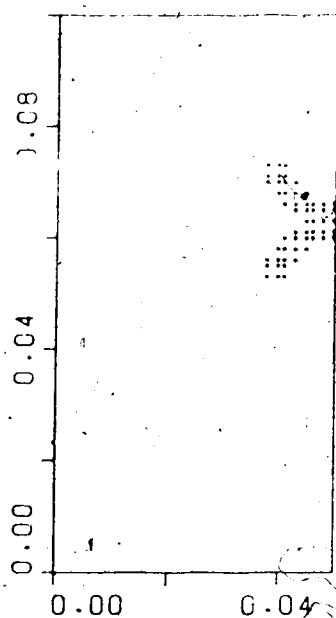


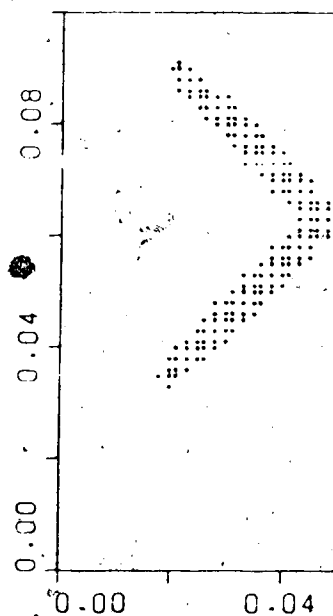
Figure 3.5: Stress Strain Response of Plane Strain Specimen

like an elastic perfectly plastic material but in fact the material is a brittle plastic material with distinct peak and residual strength. Failure to reach the peak strength is due to the gradual development of the shear zone and progressive failure of the specimen. If the strain within the specimen is uniform, that is without the weak element, the mobilization of the shear strength at all points within the specimen will occur at the same time. Therefore peak strength will be reached and the observer is able to measure the peak strength. Further deformation beyond peak will be followed by an abrupt decrease in strength, and the observer will also be able to measure the residual strength. However, since yielding initiates at one location in the specimen, due to the brittle behaviour of the material the shear strength at this location is quickly reduced to the residual value. The excess load or energy is redistributed to the surrounding material. Since the reduction in strength is relatively small, the amount of energy released is small enough to be absorbed by the rest of the material. However, part of the shear zone now is subjected to residual strength, and therefore when the entire shear zone is formed, the shear stress that can be sustained by the specimen is that of the residual value. Therefore the observer will not be able to measure the real peak strength of the material. This important aspect of progressive failure will further be illustrated in the next chapter.

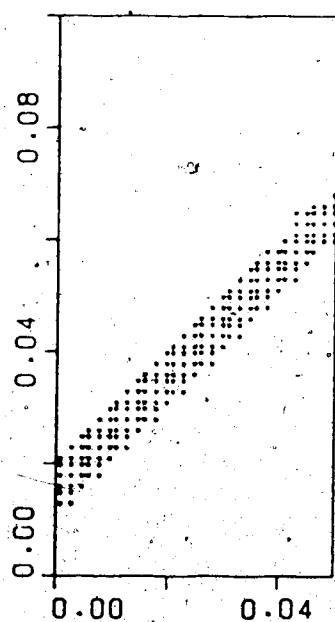
The development of the yielding zone at various stages of the test is shown in Figure 3.6. The yielding zone initially propagates at 45° in two directions, above and below the weak element, in the form of a band around the weak element. A very slight increase in displacement triggers further propagation of the band in both directions. The weak element is deliberately placed above the mid height of the specimen to eliminate symmetry. Two shear bands are initially developed because of the preferred shearing directions in two orthogonal planes. The top shear band eventually intercepts the top platform therefore any further propagation in this direction is prohibited. The lower shear band extends through the specimen and results in a continuous band across the specimen. It is noted that once the lower band has developed across the specimen, the recoverable energy stored in the upper half of the specimen is released and absorbed by the lower band. Very little movement is required to trigger this reaction and the upper band eventually 'disappeared' in this unloading process. This is why very high residual strength is used in this example in order to study the propagation of the shear band inside the specimen. Low residual strength may result in abrupt failure and possible numerical instability. Once the lower band is fully extended across the specimen, a collapse mechanism is formed and any further deformation will be localized in this region. Subsequent deformation leads to widening of the shear band although there is a tendency to



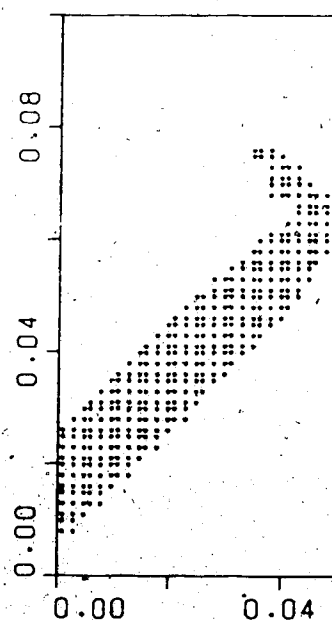
DISPL. = 0.00173 m



DISPL. = 0.00176 m



DISPL. = 0.00177 m



DISPL. = 0.00190 m

Figure 3.6: Yield Zone Development of Plane Strain Specimen

reform the upper shear band around the weak element due to some stress concentration effect. The deformed shape of the element at an axial strain of 1.9% is shown in Figure 3.7. It is seen that a "kink" is formed on both sides of the specimen. Incidentally, the angle of the shear band is at 45° with respect to the major principal plane which is expected from the discussion earlier.

This example demonstrates that shear band bifurcation can be modelled effectively using the elasto-plastic formulation. In this case, the location and direction of the shear band were not predefined prior to the analysis but were captured successfully in the numerical model.

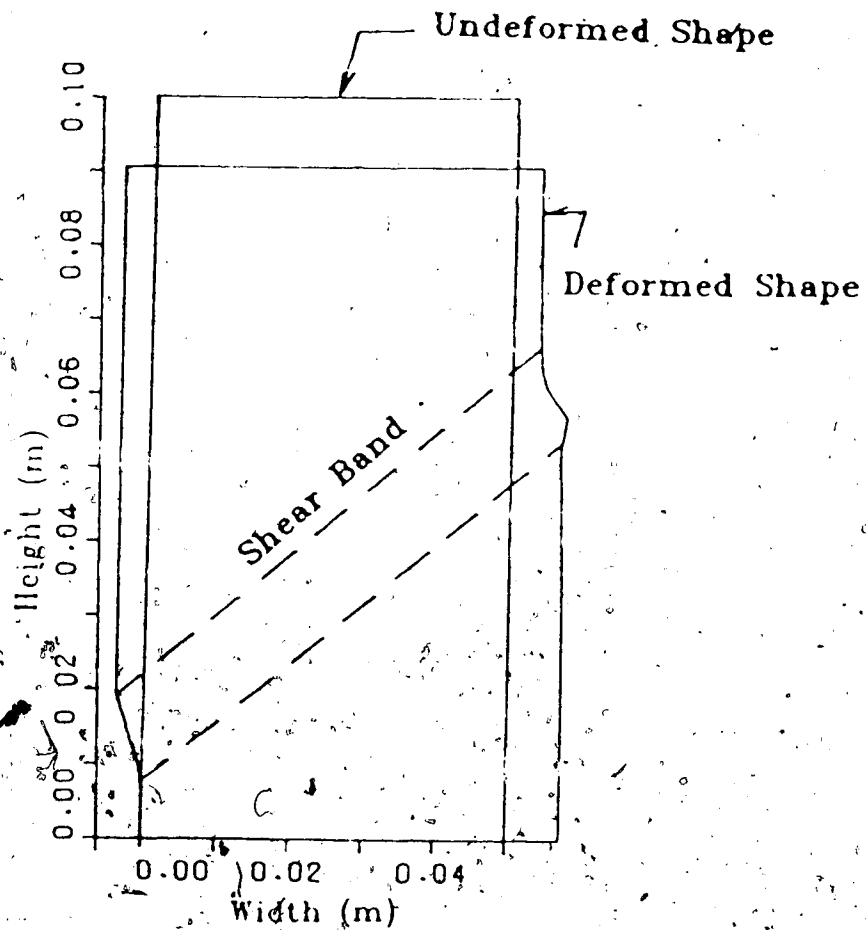
3.5 The Finite Element Method in Modelling Shear Band

The previous section dealt with the modelling of the shear band in which the direction and location of the shear band are not prescribed. In certain circumstances the presence of a weak layer between more competent strata result in local weaknesses and deformation is most likely to be concentrated in this region. In this case it is not necessary to satisfy the criteria discussed in Section 2.2 for the initiation of shear band deformation. However there are numerical difficulties associated with this class of problem.

To model a shear band using the finite element method, it is sometimes necessary to have an element which can provide rapid stress variation along the element as well as

Horizontal Displacement Scale 1:20

Vertical Displacement Scale 1:5



DISPL = 0.001900 m

Figure 3.7: Deformed Shape of Plane Strain Specimen

across the element. Since convergence of the displacement finite element formulation can be obtained by reducing the size of the element, any complicated variation in stresses and strains can in principle be modelled by this technique. However, any practical finite element analysis will have a limited number of elements, and the element is finite in size and is usually dictated by the computer resources available to the analyst. The thickness of the shear zone in certain geological settings can be very thin (from several mm to several cm thick). This will require the use of very thin elements. Goodman's joint element is a type of element with zero thickness which is used to model rock joints and interfaces (Goodman 1970). However, the type of shear zone that is of interest here will always have finite thickness and therefore a solid element will be more appropriate.

Ghaboussi and Wilson (1973) proposed a relative displacement finite element formulation in which relative displacements among the nodes are taken as the prime variable rather than the absolute displacements of the individual nodes as the prime variables. Pande (1979) conducted a study comparing the relative displacement element with the conventional isoparametric element and concluded that there is no significant difference in results between these two types of elements as far as numerical ill-conditioning is concerned. The aspect ratio of the element in his study was as high as one to one million. However there was no indication on the limit of aspect ratio

that could be used with respect to the precision of calculations without introducing significant round off errors.

A numerical experiment is conducted here to determine the limits of aspect ratio for 8-node isoparametric elements before numerical ill-conditioning of the stiffness matrix occurs. Three cases are considered to test the element under different stress conditions:

1. An uniform uniaxial tensile test with thin elements being placed parallel and perpendicular to the direction of the applied stress.
2. An uniform shear stress with thin elements being placed in the horizontal and vertical directions.
3. A cantilever with uniformly distributed load with thin elements at the neutral axis.

These three cases are shown in Figure 3.8. For the second case of uniform shear, the result for the thin element being placed horizontally should in principle be identical to that placed vertically. However, due to the slight differences in boundary conditions, they are not identical problems in numerical analysis.

The first and second cases are used to test the elements under uniform stress conditions while the third case is for a more complicated stress condition. The thin elements in all cases are within an element assembly. The tests were conducted using the Amdahl 470v computer with

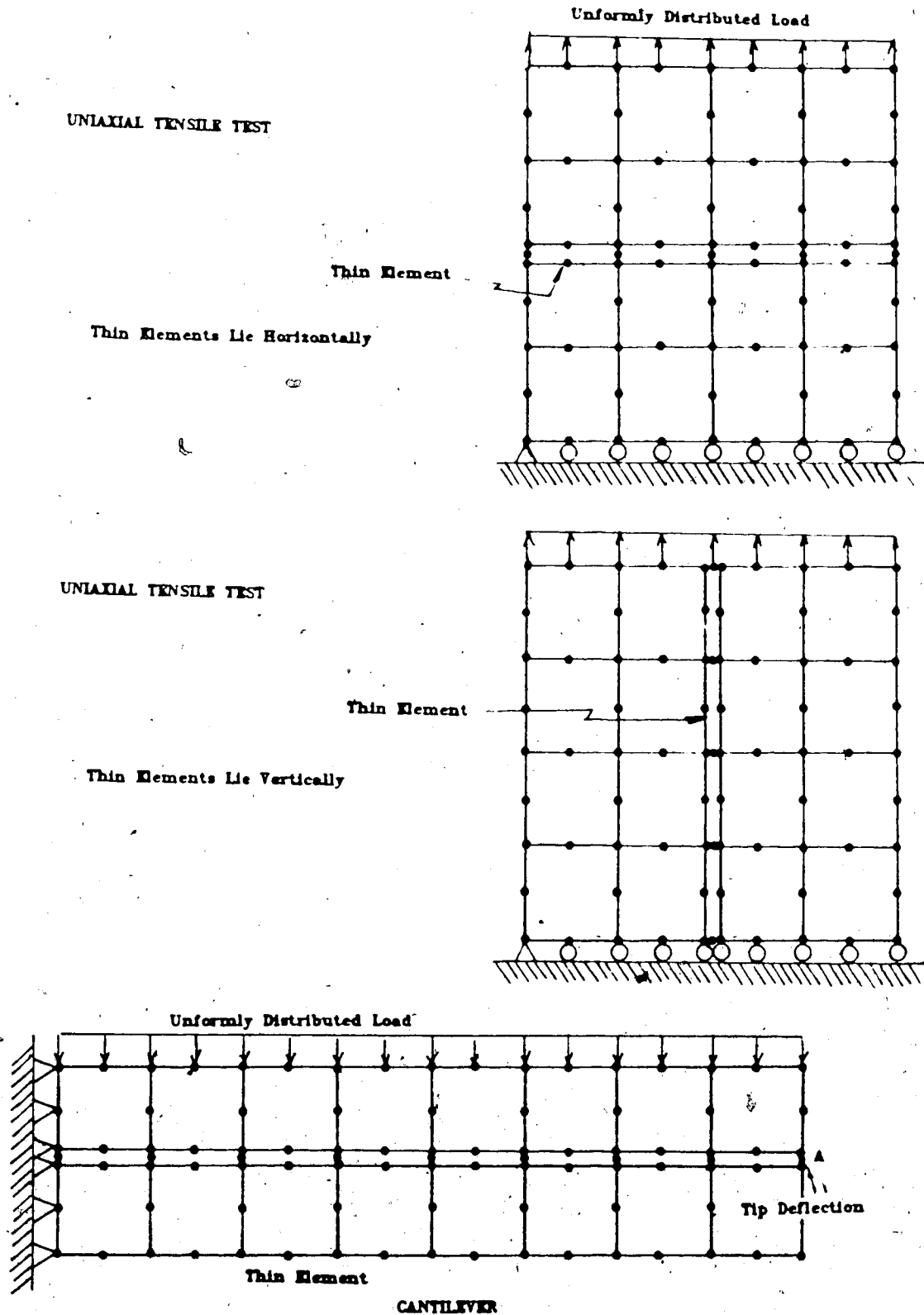


Figure 3.8: Different Stress Conditions to Test Thin Elements.

single and double precision arithmetics. Single precision here means 4 bytes per word with 24 bits mantissa, 7 bits exponent and 1 bit for sign which is equivalent to about 7 to 8 significant digits. Double precision here means 8 bytes per word with 56 bits mantissa, 7 bits exponent and 1 bit for sign which is equivalent to about 16 significant digits. The result of the analyses are summarized in Table 3.2

For the first 2 cases, only single precision calculations were used. Practically no ill-conditioning effect was observed up to an aspect ratio of 10,000 with errors in displacements of less than 2 percent. For the cantilever problem, both single and double precision arithmetic was used. It is seen that when using single precision arithmetic, the errors in tip displacement are quite large even for relatively low aspect ratios. The tip displacement calculated from the beam theory does not give the exact solution for this problem because the plane strain condition is assumed in the finite element analysis and also no shearing effect is included in the beam theory. The tip displacement for the same cantilever is determined without thin elements in the neutral axis for the purpose of comparison. When double precision arithmetic is used, the error in tip displacement compared to that without the thin elements does not exceed 0.5 % for an aspect ratio as high as 10,000. In general, increasing the aspect ratio results in smaller displacement due to the stiffening of the element. The stiffening effect is caused by the reduction in

Table 3.2 Displacements at A with Different Aspect Ratio

Aspect Ratio			10	100	1,000	10,000
R e c t .	t e n s i	hor.	0.363927	0.364041	0.362078	0.357488
		vert.	0.363928	0.363970	0.362740	0.358075
B l o c k	s h e a r	hor.	1.03920	1.03946	1.03202	0.997851
		vert.	1.03893	1.04053	0.986730	0.855857
canti- lever		single precis.	70.0377	55.6878	17.7827	17.7434
		Double precis.	73.7762	73.7304	73.7273	73.7230

All values are in centimeters.

Exact Solutions

Rectangular Block.

Tension - upward displacement at A = 0.364000 cm.

shear - horizontal displacement at A = 1.04000 cm.

Cantilever

Beam Theory - downward displacement at
A = 76.800 cm.

Finite element solution without thin elements -
downward displacement at A = 73.3907 cm.

area as the aspect ratio is increased.

It is seen that ill-conditioning effects can be reduced by using more precision in performing the calculation. Double precision arithmetic seems to give very good results with adequate accuracy and therefore will be used for the rest of the analyses. In these cases it is seen that 8-node isoparametric elements can be used to model a shear band for an aspect ratio not exceeding 10,000 when double precision arithmetic is used.

3.6 Shear Band Propagation in a Dam Foundation

The final exercise in this chapter deals with the development of a shear band in a more realistic situation. A dam 15 m high is to be constructed on a shale bedrock foundation with a bentonite seam 5 m below the ground surface. It is assumed that the bentonite seam is practically horizontal and 5 cm in thickness. The construction of the dam will likely impose severe straining on the bentonite seam. Since the bentonite possesses strain softening behaviour, the amount of strain softening in the bentonite seam is useful in performing a stability analysis. In other words, it is required to know the extent of the bentonite seam which is at residual strength so that appropriate strength parameters can be used in the stability analysis. Moreover the deformation behaviour of the dam and the underlying foundation are also of great interest. To accomplish this will require a finite element analysis with

a strain softening material model to simulate the bentonite seam.

In order to simulate the construction of the dam in a realistic manner using the finite element method, a step-wise approach is used. The dam is to be constructed in six layers and in-situ stresses for the foundation are imposed using the switch-on-gravity technique. A high Poisson's ratio of 0.499 is used to obtain the in-situ stresses which will give the value of k_0 of approximately 1.0. It is also assumed that the construction of the dam is relatively fast so that a total stress, fully undrained analysis is valid. Poisson's ratio of 0.49 is used in the bentonite seam throughout the analysis. The finite element idealization of the dam and foundation is shown in Figure 3.9.

A strain softening material model is used to simulate the behaviour of the material of the dam, the shale bedrock and the bentonite seam. The stress-strain relationship of the material model is given by Equation (2.20). The model is a strain hardening and softening material discussed in the previous chapter. The material parameters used in the analysis are given in Table (3.3). The residual strength for the bentonite seam is quite high in compared to the peak strength to reduce the number of iterations required for convergence. Even for this high residual strength, the computer time required to obtain a solution is quite long as will be discussed later.

Table 3.3 Material Parameters used in the Finite Element Analysis

Material Parameters	Dam	Shale Bedrock		Bentonite Seam
		Below Shear Zone	Above Shear Zone	
E' (kPa)	150000.0	150000.0	150000.0
v'	0.499	0.499	0.499
E (kPa)	20000.0	100000.0	20000.0	10000.0
V	0.40	0.35	0.40	0.49
G (kN/m ²)	19.0	22.0	22.0	20.0
Cu (peak)	200.5	Linear	200.5	15.5
Cu (resid)	150.5	Elastic	150.5	13.0

E' - Elastic Modulus used in Switch-on-gravity analysis.

v' - Poisson's ratio used in Switch-on-gravity analysis.

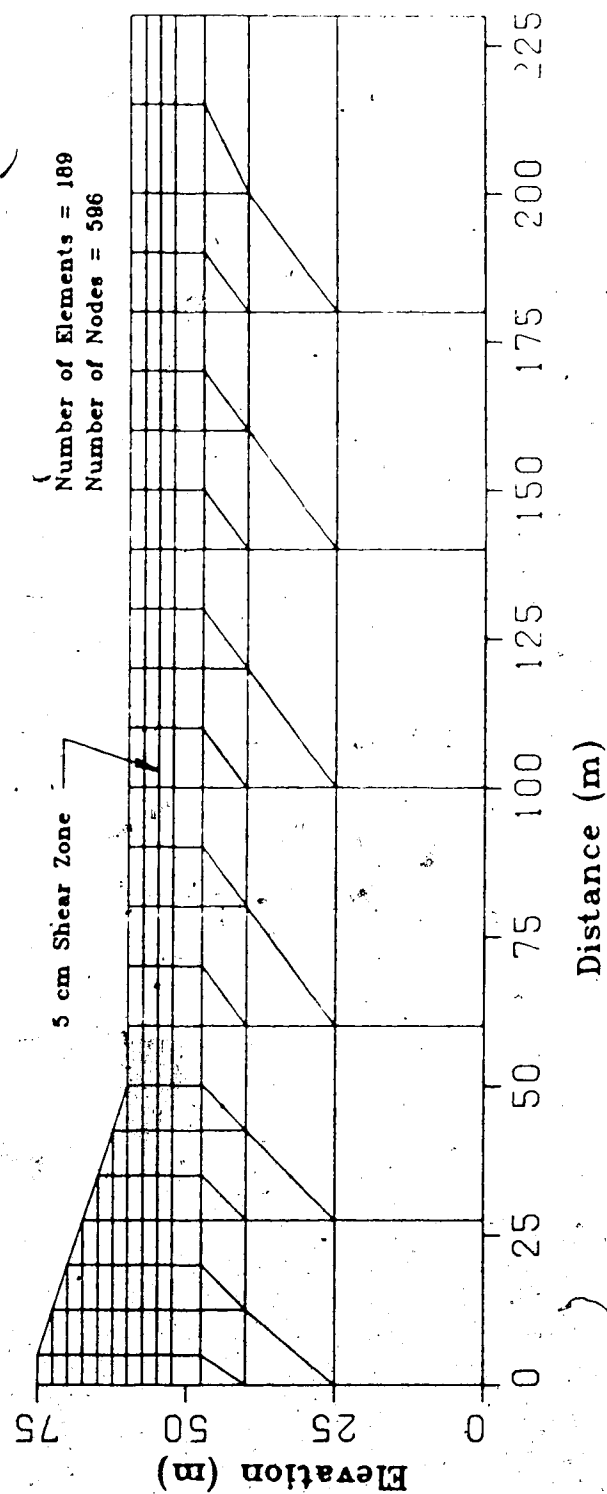


Figure 3.9: Finite Element Idealization of Dam and Foundation

The finite element model consists of a total of 189 eight nodes and six nodes isoparametric elements with 596 nodes. Only half of the dam is analyzed by taking into account the symmetry of the problem. The dam is 180 meters wide and the depth of the foundation is taken to be 60 m with a fully fixed boundary at the bottom of the foundation. Since the extent of the shear zone is not known, the width of the foundation is taken to be 230 m wide so that the boundary condition on the side will not affect the propagation of the shear zone. The aspect ratio of the element at the shear zone does not exceed 400 and is even smaller at locations near the dam. This aspect ratio is found to be quite satisfactory using the 8-node elements with double precision calculation.

Figure 3.10 shows the mobilization of the shear strength along the shear zone at various stages. Peak strength is mobilized at portions of the shear zone during the second stage of dam construction when some softening behaviour is observed. The length of the softening zone was about 5 m and is located near the toe of the dam. The residual strength of the seam has not yet been reached at this stage. The construction of an additional lift of 2.5 m triggers a rapid propagation of the shear zone. The softening zone has been extended from 5 m to 35 m. The propagation is mainly in the upstream direction with only 10 m extension beyond the toe of the dam. The fourth lift further extends the shear zone from 35 m to 55 m with

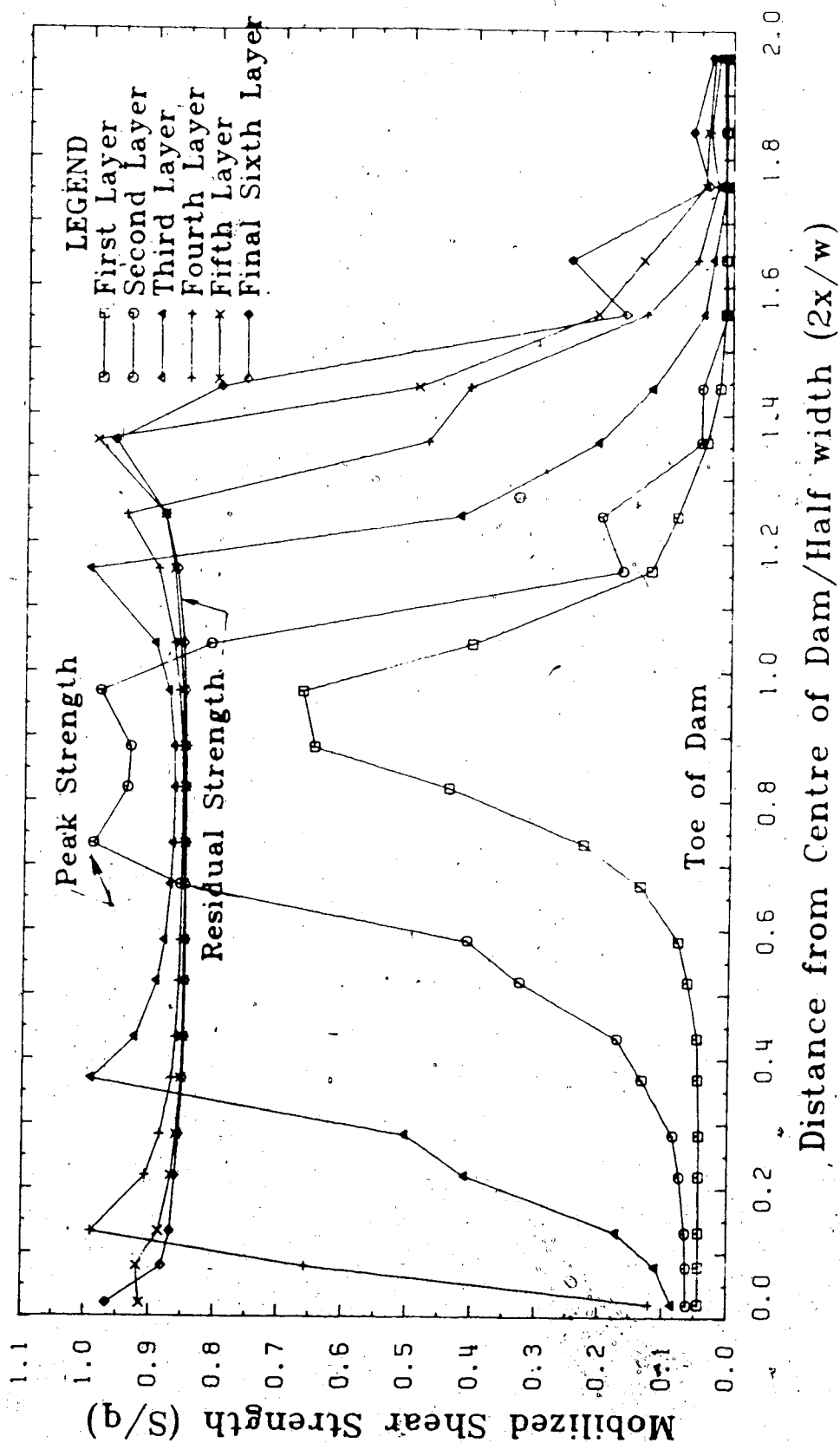


Figure 3.10: Mobilization of Shear Strength along the Shear Zone

propagation almost equal in both the upstream and downstream directions. The stresses to calculate the degree of mobilization of shear strength are evaluated at the lower Gaussian points of the elements at the shear zone. As discussed in Chapter 2 the peak strength may or may not coincide with the Gaussian points of the element. Therefore, it is possible that the peak strength shown may not be equal to the peak strength of the shear zone. This simply means that the location of the peak strength in this particular instance does not coincide with the Gaussian point. The construction of the fifth lift has extended the shear zone to its maximum length of 70 m. The addition of the sixth lift results in further shearing at the shear zone especially towards center of the dam. It is noted that in all of these steps the stresses are decreasing very rapidly beyond the toe of the dam. The mobilized strength at about 15 m from the location of the peak strength has been reduced to only 5 percent of the peak strength. The entire section of the shear zone underneath the dam in this case has been reduced to the residual strength value when construction has been completed.

Figure 3.11 shows the displacement vectors indicating the flow of material of the dam and the foundation. Some heaving occurs at the toe of the dam and relatively large displacements are observed at the shear zone. Figure 3.12 shows the horizontal displacements at various locations at different stages of construction of the dam. The foundation

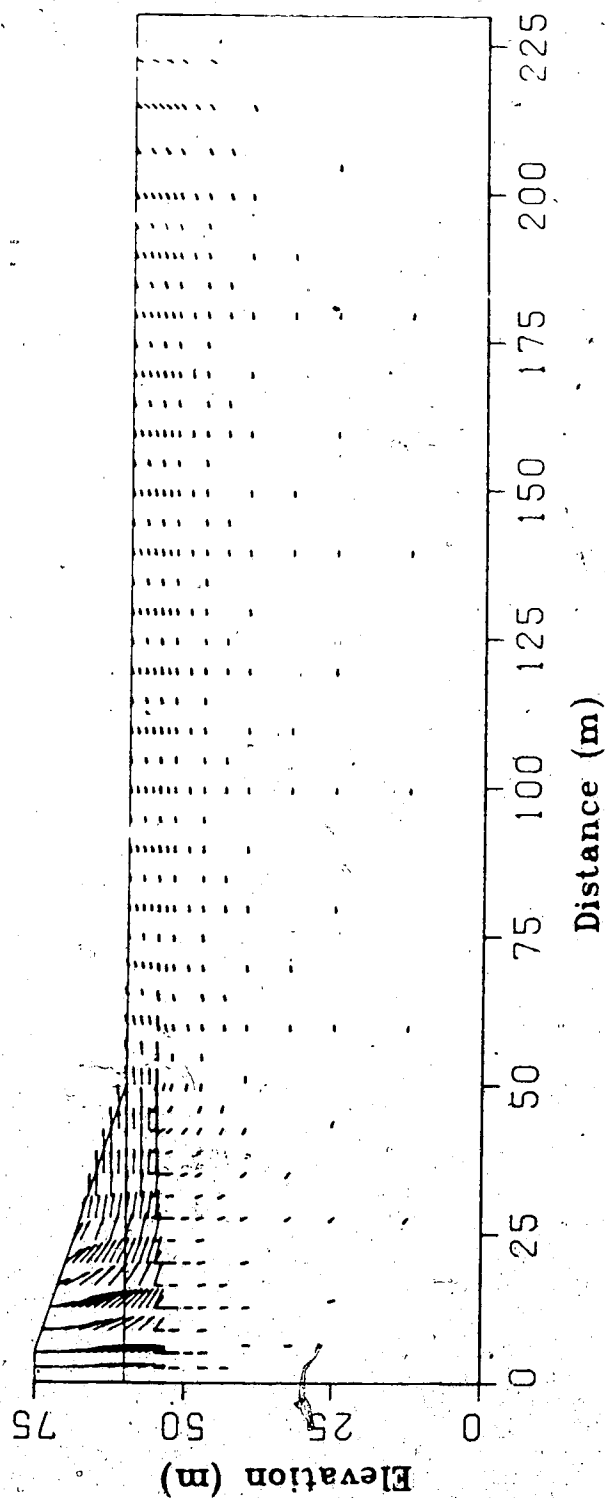


Figure 3.11: Displacement Vectors of the Dam and Foundation

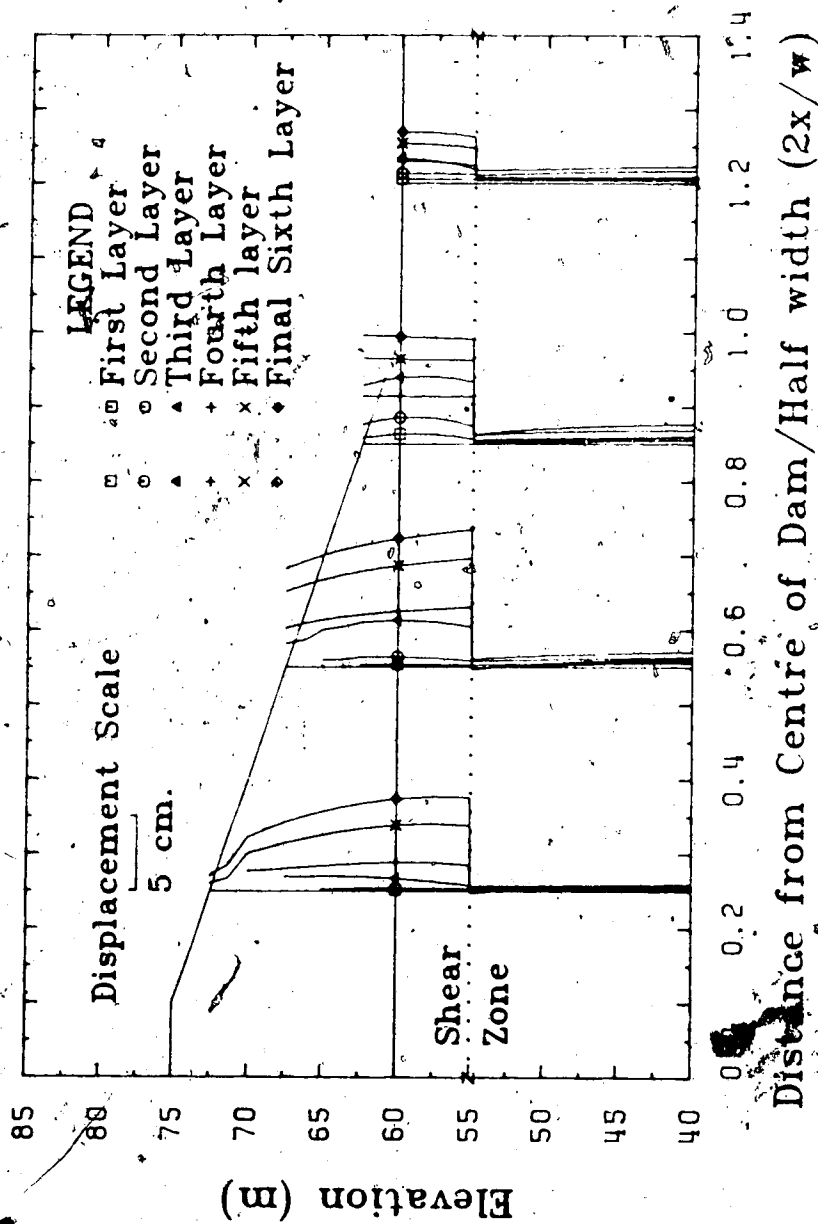


Figure 3.12: Displacement of Dam Foundation

movement is mainly localized at the shear zone with the maximum displacement of about 8 cm. The amount of movement generally increases with increasing height of the dam except at locations near the toe of the dam where more movement is detected at the third lift of the dam than at the fourth lift. However, horizontal displacements increase after the fourth lift. The strains at the shear zone are shown in Figure 3.13. Severe straining occurs at the shear zone due to the weaker material and strain softening behaviour at the shear zone.

To compare the difference in behaviour of the elasto-plastic strain softening model and the elastic brittle plastic model, this analysis is repeated using identical parameters with the exception that the softening model is replaced by the brittle plastic model. Von-Mises yield criterion is used in the brittle plastic model with uniaxial yield strength of 31 kPa and residual strength of 26 kPa as in the softening model. Figure 3.14 shows the result of the brittle plastic model. The transition zone from the peak strength to residual strength along the shear band disappears because of the brittle behaviour of the material. The extent of the softening zone is very similar to the strain softening model. Even the initiation of yielding occurs at the same step. As before, the mobilized strength decreases very rapidly beyond the toe of the dam.

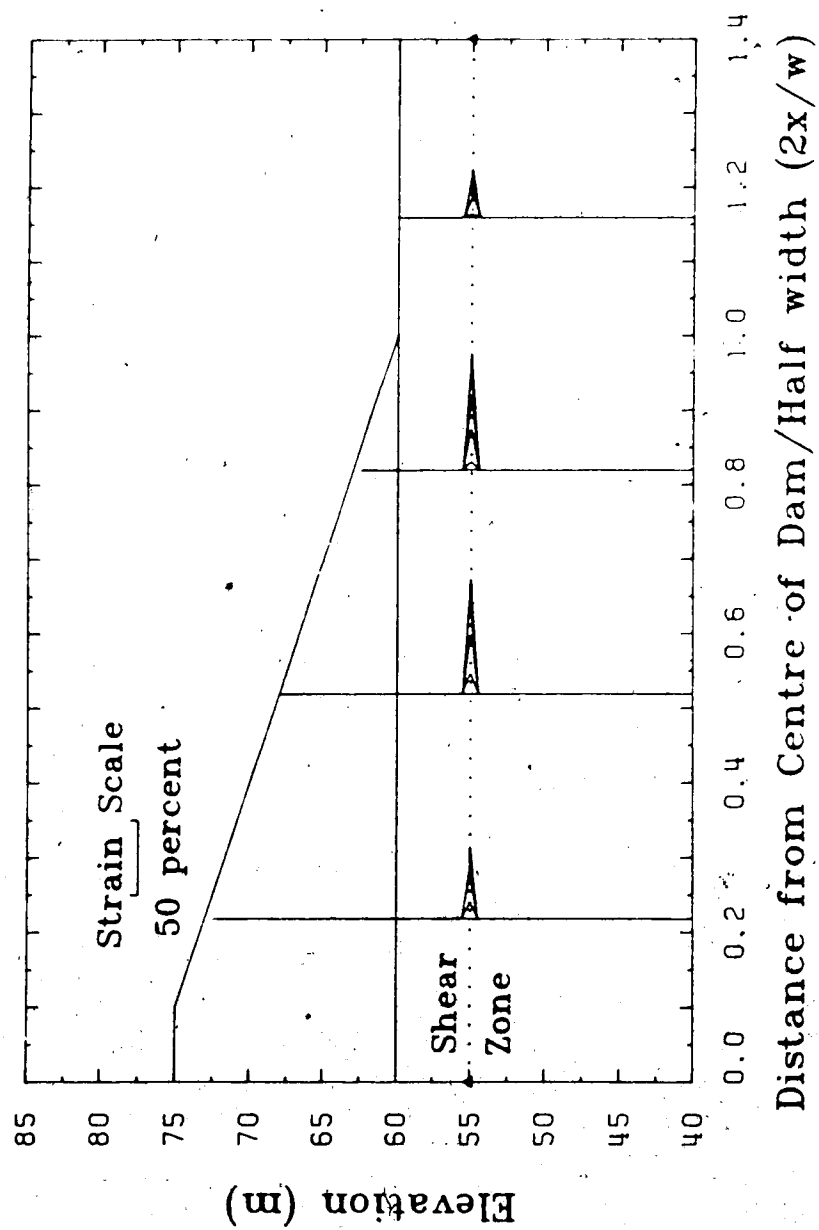


Figure 3.13: Mobilization of Shear Strains along the Shear Zone

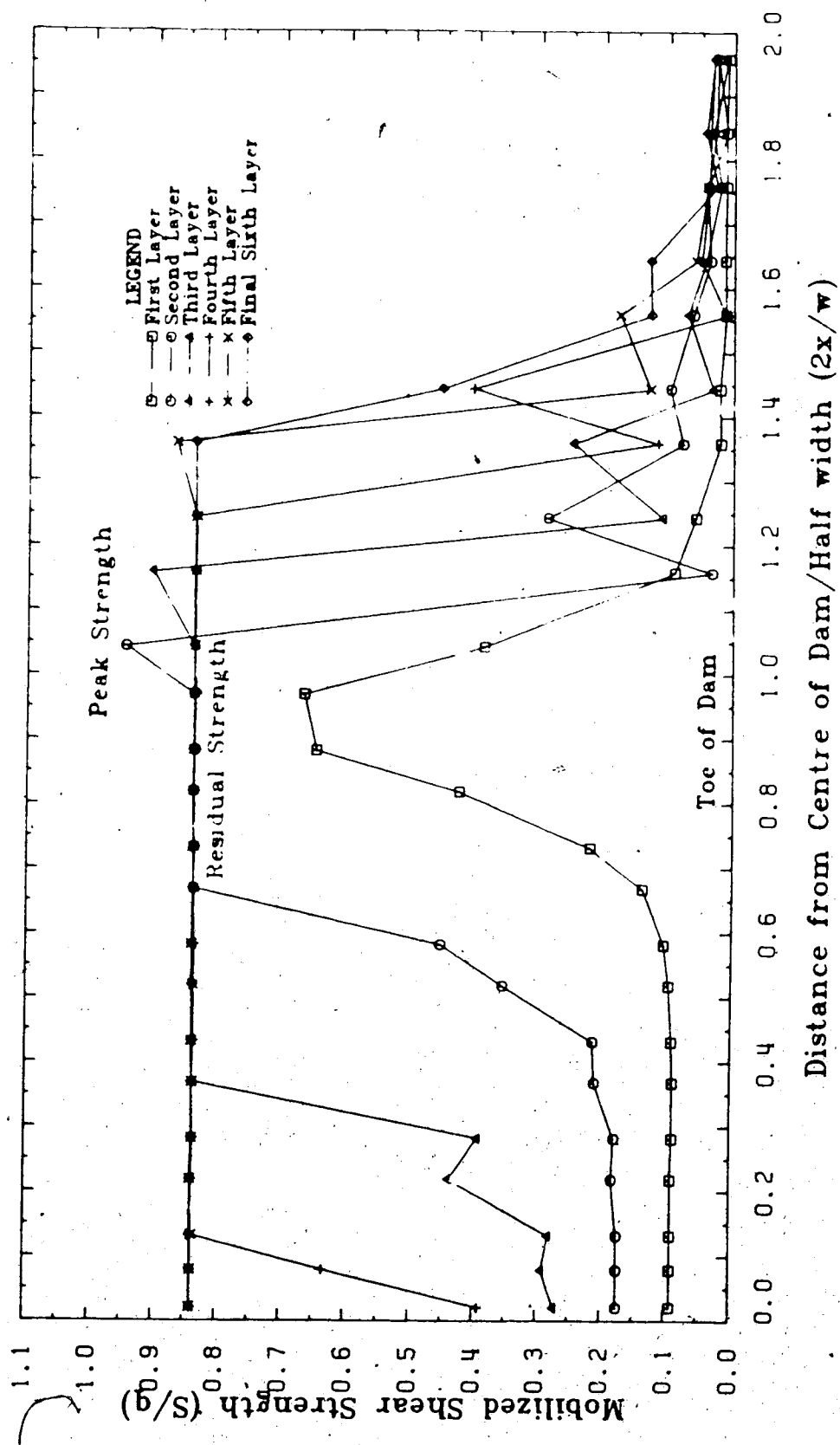


Figure 3.14: Mobilization of Shear Strength of Brittle Plastic Material

3.7 Conclusion

The preceeding two examples have demonstrated that shear band deformation and propagation can be captured using the elasto-plastic finite element formulation for situations where either the location of the shear band is prescribed or is not prescribed. To obtain the solution of an analysis with strain softening material behaviour requires considerable patience and computer resources. The material itself is inherently unstable and therefore requires a large number of iterations for the numerical solution to converge. Before introducing the stress calculation methods discussed in Appendix A, the solution process often oscillates and sometimes diverges because of the error introduced during the iteration procedure. Using the new methods of stress calculation, the convergence rate is often very fast but sometimes when the increment of load introduces extensive yielding and large propagation of the shear band, the convergence rate can be quite slow. Physically this represents the release of a large amount of energy and energy redistribution, which must be absorbed by the adjacent media in order to maintain overall stability. This absorption process can be very slow if it in turn triggers further release of energy. In numerical models, such processes require considerable redistribution of unbalanced energy and hence requires much computational effort. However, due to the rapid rate of advancement of modern computer technology, these obstacles will gradually be

minimized. The formulation and solution procedure nevertheless provides a viable method for modelling the unstable behaviour of the strain softening material and shear band deformation.

4. HYPERBOLIC STRAIN SOFTENING MODEL

4.1 Introduction

The strain softening model introduced in Chapter 2 can be used to simulate material with gradual post peak strain softening behaviour. However, this model has only two material parameters (A and B) to describe the stress strain relationship of the material. These two parameters are often related to the peak and residual strength of the material. Once the peak and residual strengths are specified, the peak strain and post-peak softening behaviour for the material are determined and cannot be varied independently. This model is therefore restricted to only one stress strain relationship for one value of peak strength and residual strength. Ideally it is desirable to specify the peak strength, residual strength, peak strain and post peak softening behaviour independently, in order to model a variety of stress strain relationships. The brittle plastic model discussed in Chapter 3 has relieved one restriction from the Prevost strain softening model. Peak strength, residual strength and peak strain can be specified independently in the brittle plastic model. This model can also be used to model frictional material with residual cohesion and friction angles different from the peak values. The abrupt decrease in strength after peak is an approximation to the extremely brittle behaviour of some sensitive soils. However, not all soil is so sensitive and

this model lacks the ability of prescribing the post peak softening behaviour of the material. In this chapter another strain softening model will be introduced which will allow a more precise description of the stress strain relationship of the material.

The new model basically assumes that the material behaves elastically up to a peak value and then the shear strength decreases gradually after peak. This model will require four parameters to describe the material, namely, the peak strength, the residual strength, the peak strain (strain at peak strength) and the rate of post peak softening. Unlike other strain softening models introduced by some authors who often assume pseudo elastic behaviour after peak or constant rate of softening after peak in plasticity models (Hoeg and Whitman 1968), this model is based on the plasticity formulation discussed earlier with a variable rate of post peak softening. The post peak behaviour is approximated by an inverted hyperbola asymptotic to the residual strength value. Lo (1972) has used the hyperbolic relationship to model the post peak softening behaviour of soil under limit equilibrium conditions. The strain measure used in his analysis was taken to be the total strain less the peak strain. The model which will be presented in this chapter adopts the plastic strain to be the strain measure in the formulation of the finite element model. Before discussing the applicability of the model in describing the post peak behaviour of a real

soil, the theory of the model and relevant finite element formulation will be presented. Results from laboratory tests will be used to demonstrate the validity of the model and methods of obtaining parameters for this model from conventional triaxial tests will be discussed. Since this model uses a hyperbola to approximate the post peak softening behaviour of the soil, it will be termed the 'Hyperbolic Strain Softening Model'. Although the present model is restricted to frictionless material, extension of the theory to frictional soil should not be difficult.

4.2 Theory of the Hyperbolic Strain Softening Model

The hyperbolic strain softening model assumes linear elastic behaviour for deformation prior to peak strength. Generalized Hooke's Laws will be used for elastic deformation. At peak strength, yielding is defined as:

$$F = q - \kappa = 0 \quad (4.1)$$

where

$$q = \sqrt{3J_2} ;$$

$$\text{and } \kappa = \kappa_p$$

= uniaxial compressive peak strength.

The strength of the material decreases gradually after peak and the yield function in the post peak region is defined

as:

$$F = q - \kappa = 0 \quad (4.2a)$$

where

$$\kappa = \kappa_p \left(1 - \frac{\bar{\epsilon}^p}{a + b\bar{\epsilon}^p} \right) \quad (4.2b)$$


and

$$\bar{\epsilon}^p = \int d\bar{\epsilon}^p = \text{equivalent plastic strain}; \quad (4.2c)$$

$$d\bar{\epsilon}^p = \left(\frac{2}{3} d\epsilon_{ij}^p d\epsilon_{ij}^p \right)^{1/2};$$

$$d\epsilon_{ij}^p = d\epsilon_{ij} - d\epsilon_{kk} \delta_{ij} / 3;$$

$$d\epsilon_{ij}^p = \text{increment of plastic strain tensors};$$

and a and b are material parameters.

At peak strength, $\bar{\epsilon}^p = 0$, Equation (4.2) reduces to Equation (4.1). At very large strain, $\bar{\epsilon}^p = \infty$, the shear strength should approximate the residual strength of the material. Substitute $\bar{\epsilon}^p = \infty$ into Equation (4.2), the yield function becomes:

$$F = q - \kappa_r = 0 \quad (4.3)$$

where

$$\kappa_r = \kappa_p (1 - 1/b).$$

Therefore,

$$b = 1 / (1 - \kappa_r / \kappa_p) \quad (4.4)$$

Recall that the brittleness index I_B is defined as:

$$I_B = (\kappa_p - \kappa_r) / \kappa_p = 1 - \kappa_r / \kappa_p, \quad (4.5)$$

thus the b parameter is simply the reciprocal of the brittleness index:

$$b = 1 / I_B. \quad (4.6)$$

The b parameter depends only on the amount of softening of the material. The significance of the a parameter can be found by differentiating κ with respect to ϵ^p in Equation (4.2). One obtains:

$$\frac{\partial \kappa}{\partial \epsilon^p} = -a \kappa_p / (a + b \epsilon^p)^2. \quad (4.7)$$

Let $\epsilon^p = 0$;

$$\frac{\partial \kappa}{\partial \epsilon^p} = - \left(\frac{\kappa_p}{a} \right) \quad (4.8)$$

In other words κ_p / a is the tangent of the initial slope of the post peak stress strain relationship of the material. A

typical stress strain relationship of this model and the meaning of the a and b parameters are illustrated in Figures 4.1 and 4.3.

4.3 Finite Element Formulation

The finite element formulation is similar to the Prevost softening model discussed in Chapter 2. First the consistency condition is expressed in terms of the equivalent plastic strain as:

$$dF = \left\langle \frac{\partial F}{\partial \sigma} \right\rangle \{d\sigma\} + \frac{\partial F}{\partial \kappa} \frac{\partial \kappa}{\partial \bar{\epsilon}}^P d\bar{\epsilon}^P = 0 \quad (4.9)$$

where

$$d\bar{\epsilon}^P = \lambda \bar{Q};$$

$$\bar{Q} = \sqrt{\frac{2}{3} \left(\frac{\partial Q}{\partial \sigma_{11}} \frac{\partial Q}{\partial \sigma_{11}} + \frac{1}{3} \frac{\partial Q}{\partial \sigma_{mm}} \frac{\partial Q}{\partial \sigma_{mm}} \right)}$$

Q = plastic potential

= F for associated flow rule.

From Equation (4.9), the hardening term in the elasto-plastic matrix can be replaced by:

$$\left\langle \frac{\partial F}{\partial \bar{\epsilon}} \right\rangle \left\{ \frac{\partial Q}{\partial \sigma} \right\} = \frac{\partial F}{\partial \kappa} \frac{\partial \kappa}{\partial \bar{\epsilon}}^P \bar{Q} \quad (4.10)$$

From Equation (4.2):

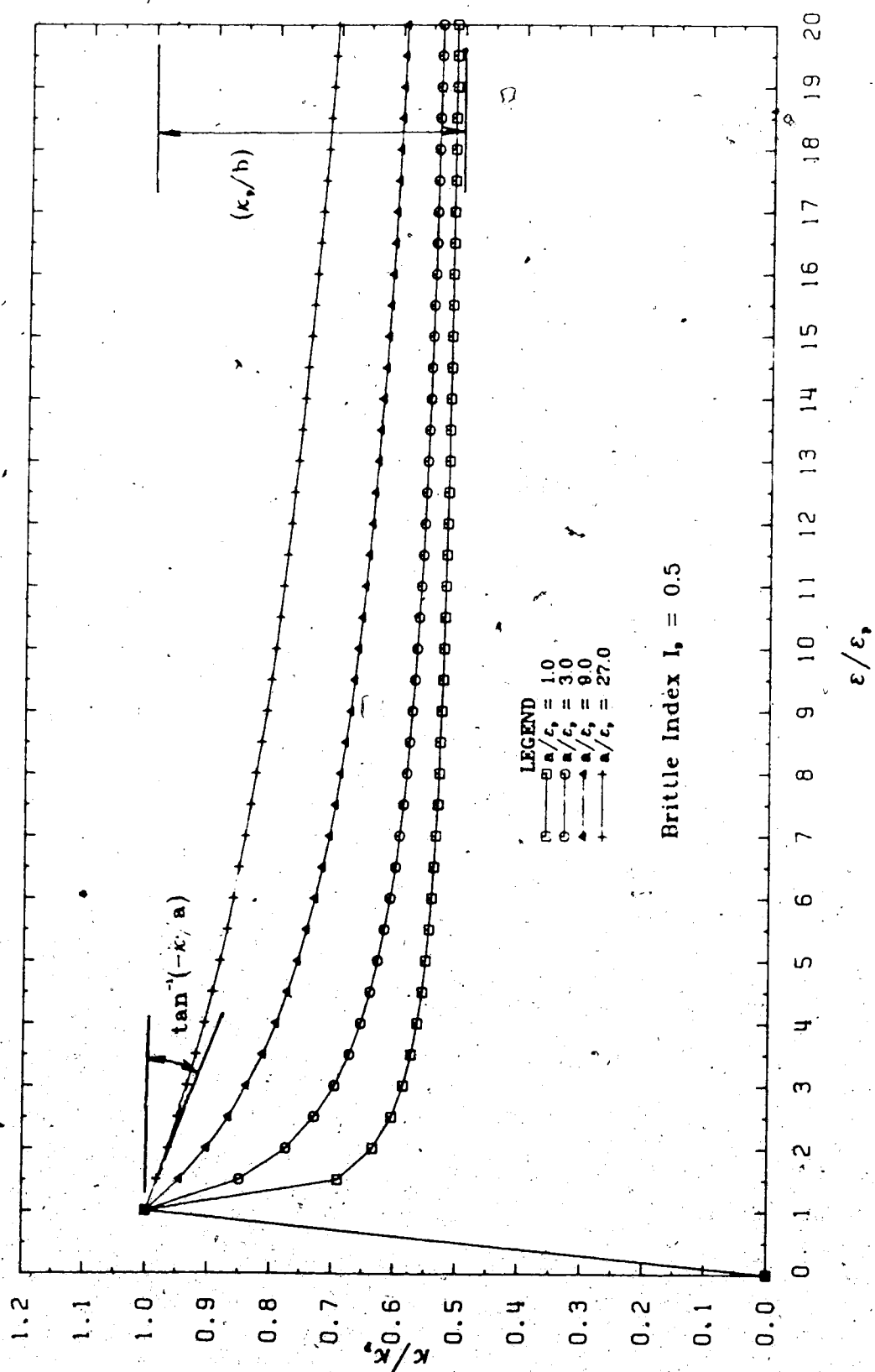


Figure 4.1: Stress Strain Curve for the Hyperbolic Strain Softening Model

$$\frac{\partial F}{\partial \kappa} = -1 \quad (4.11)$$

$$\text{and } \frac{\partial \kappa}{\partial \bar{\epsilon}} = - \frac{a \kappa}{\kappa_p} / (a + b \bar{\epsilon}^p) \quad (4.12)$$

Equations (4.10) to (4.12) can then be substituted into the elasto-plastic matrix in stiffness formulation and stress calculations as discussed earlier.

4.4 Determination of the a and b Parameters from Triaxial Test Results

To determine the a and b parameters from triaxial test results, Equation (4.2b) should be rewritten in a linear form as:

$$\left(\frac{\bar{\epsilon}^p}{1 - \kappa/\kappa_p} \right) = a + b \bar{\epsilon}^p \quad (4.13)$$

By plotting $(\bar{\epsilon}^p / 1 - \kappa/\kappa_p)$ as the ordinates and $\bar{\epsilon}^p$ as the abscissae, the y intercept will yield the a parameter and the slope of the straight line will be equal to the b parameter, as illustrated in Figure 4.2. It can be shown by assuming a triaxial stress condition that the value of κ and κ_p in Equation (4.10) are the current deviator stress after peak and the deviator stress at peak strength respectively.

That is :

$$\kappa_p = (\sigma_1 - \sigma_3)_f = \sigma_{df} \text{ at peak strength} \quad (4.14)$$

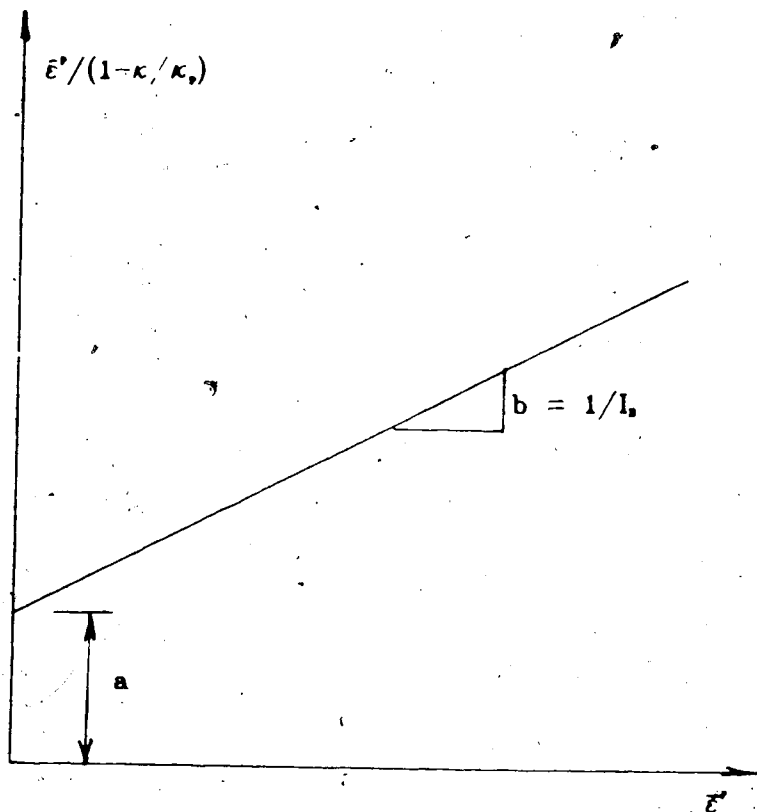


Figure 4.2: Normalized Plot for the Hyperbolic Strain Softening Model

$$\kappa = (\sigma_1 - \sigma_3) = \sigma_d \text{ for post peak deformation} \quad (4.15)$$

To determine the equivalent plastic strain, it is necessary to determine the total and the elastic strains. The plastic strain is given by:

$$\epsilon_{ij}^p = \epsilon_{ij} - \epsilon_{ij}^E \quad (4.16)$$

where

ϵ_{ij}^E are the total and elastic strain tensors respectively.

Defining:

$$\bar{\epsilon} = \int d\bar{\epsilon}_{ij} \quad (4.17)$$

where

$$d\bar{\epsilon}_{ij} = (2/3 d\epsilon_{ij}d\epsilon_{ij})^{1/2},$$

$$\text{and } d\epsilon_{ij} = d\epsilon_{ij} - d\epsilon_{kk}\delta_{ij}/3,$$

it can be shown that by assuming fully undrained triaxial stress condition and $d\epsilon_{22} = d\epsilon_{33}$:

$$d\epsilon_{kk} = 0, \quad (4.18a)$$

$$\text{and } d\epsilon_{22} = d\epsilon_{33} = -1/2 d\epsilon_{11}, \quad (4.18b)$$

the equivalent strain $\bar{\epsilon}$ can be expressed by the uniaxial strain as:

$$\bar{\epsilon} = \epsilon_{11} = \epsilon_1 \quad (4.19)$$

The elastic strain can be calculated using Hooke's Law as:

$$\epsilon_1 = (\sigma_1 - \nu(\sigma_2 + \sigma_3))/E \quad (4.20)$$

and assuming that $\sigma_2 = \sigma_3$ and $\nu = 0.5$ for undrained analysis, then:

$$\epsilon_1 = \frac{\sigma_1 - \sigma_3}{E} \quad (4.21)$$

At peak strength $(\sigma_1 - \sigma_3) = (\sigma_1 - \sigma_3)_f$ and $\epsilon_1 = \epsilon_1^E$ and $\epsilon_1^p = 0$ prior to peak strength, therefore the elastic modulus can be determined from equation (4.21) as:

$$E = \frac{(\sigma_1 - \sigma_3)_f}{\epsilon_1^E} \quad (4.22)$$

To determine the plastic strain for Equation (4.13), it can be shown by assuming $d\epsilon_{kk}^p = 0$ for frictionless material and $d\epsilon_{23}^p = -d\epsilon_{11}^p/2$, under triaxial stress state that the equivalent plastic strain is given by:

$$\epsilon^p = \epsilon_{11}^p = \epsilon_1^p = \epsilon_1 - \epsilon_1^e$$

$$= \epsilon_1 - (\sigma_1 - \sigma_3)/E \quad (4.23)$$

where

$(\sigma_1 - \sigma_3)$ is the current deviator stress after peak as illustrated in Figure 4.3.

When $(\sigma_1 - \sigma_3) = (\sigma_1 - \sigma_3)^p$, the total strain is equal to the elastic strain and $\epsilon^p = 0$. The peak elastic strain is always greater than the elastic strain after peak for strain softening material. By using Equation (4.22) to find the elastic modulus and Equation (4.23) to find the plastic strain, a normalized relationship can be plotted using Equation (4.13).

If anisotropic consolidation is used in the triaxial test, the method of calculation of the elastic modulus will be slightly different. To calculate the elastic modulus, one must choose the datum for the strain to be the state of isotropic stress condition. However, very often the strains are measured from the end of the consolidation process, therefore it is necessary to calculate the initial strain which was caused by the application of the deviator stress during the consolidation process. Let k_0 be the ratio of σ_1/σ_3 , where the superscript $_0$ denotes the quantity at the end of the consolidation process. Therefore the initial strain can be calculated from:

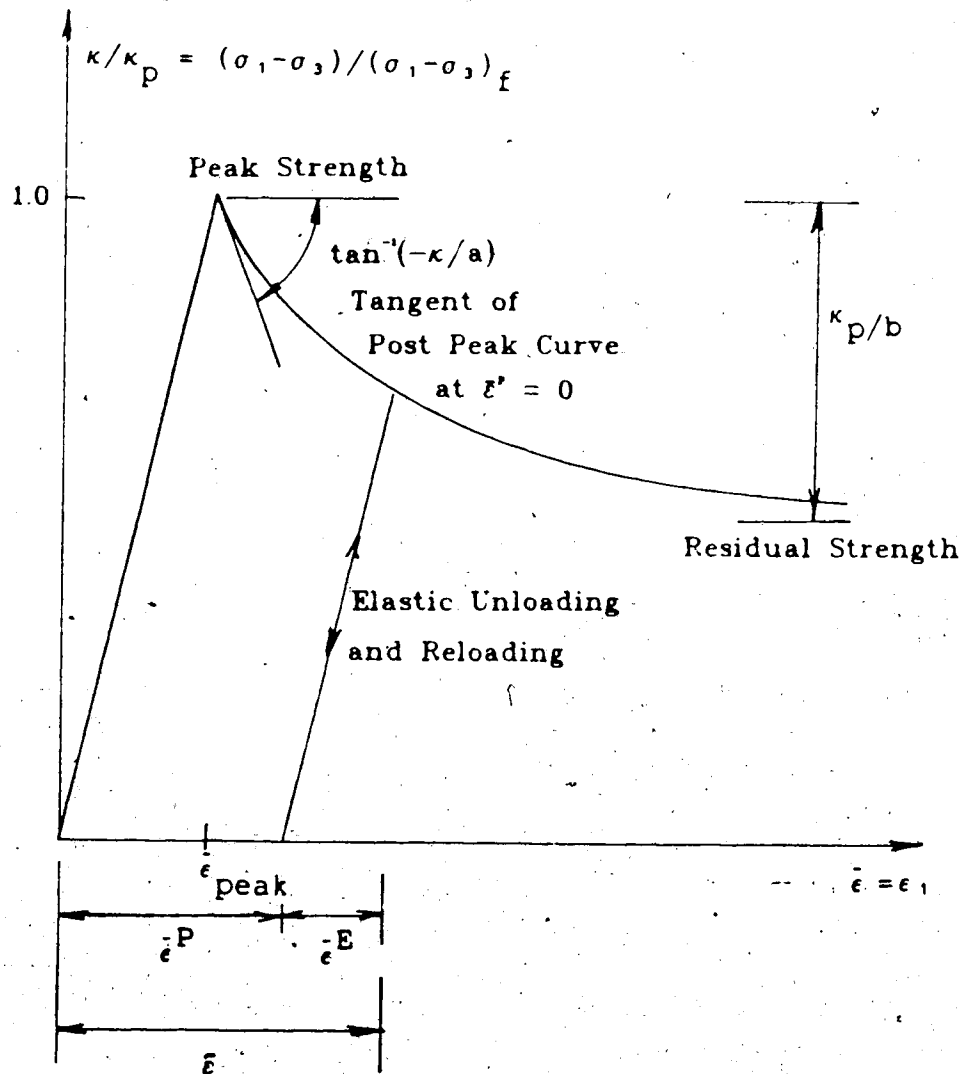


Figure 4.3: Stress Strain Relationship for the Hyperbolic Strain Softening Model

$$\epsilon_i^e = (\sigma_i^e - \sigma^*)/E = \sigma_i^e(1 - k_0)/E \quad (4.24)$$

and the total strain becomes:

$$\epsilon_1^T = \epsilon_i^e + \epsilon_1 \quad (4.25)$$

where

ϵ_1 is the strain measured from the end of the consolidation process as illustrated in Figure 4.4.

The elastic modulus is then calculated from:

$$E = \frac{(\sigma_1 - \sigma_3) - (\sigma_i^e - \sigma_3^e)}{\epsilon_1} \quad (4.26)$$

and the initial strain is given by:

$$\epsilon_0 = \frac{\sigma_i^e - \sigma_3^e}{E} \quad (4.27)$$

After determining ϵ_0 , the total strain should be referenced to the zero strain state corresponding to the isotropic stress state. Therefore the total strain calculated by Equation (4.25) should be used in calculating the plastic strain in Equation (4.23).

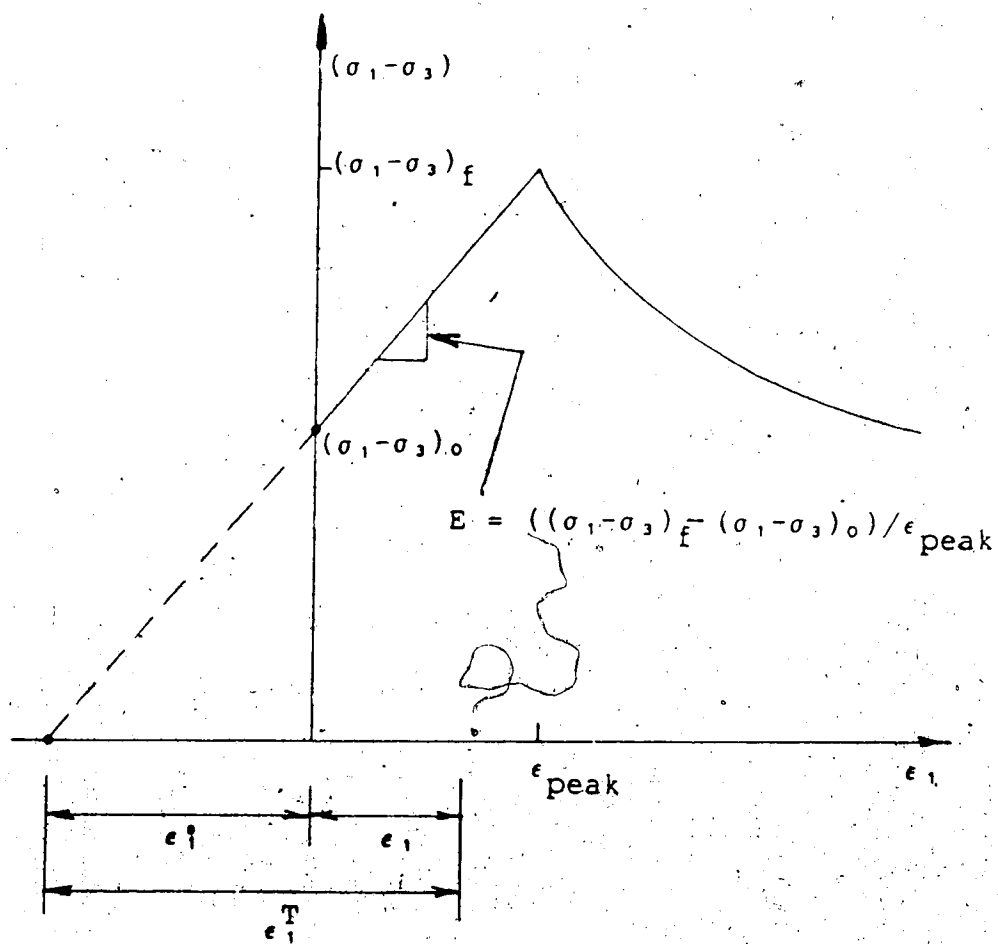


Figure 4.4: Calculation of Strains and Elastic Modulus for Anisotropic Consolidation

4.5 Triaxial Test of a Stiff Brittle Clay

A series of triaxial tests were performed by Mr. Andre Chan (a Ph.D. student at the University of Alberta) on a stiff clay obtained from a site located about 65 km west of Edmonton. Conventional consolidated undrained tests were performed with stress strain relationships shown in Figure 4.5. The water contents and Atterberg limits of these samples are given in Table 4.1. The test results are also plotted on the normalized plot using Equation (4.13) as shown in Figure 4.6. It is noted from Figure 4.6 that the post peak deformation closely follows a straight line on the normalized plot which indicates that the assumption of a hyperbola in the post peak region is valid for this soil. There are some points close to peak strength which do not follow the straight line because there is a change of curvature of the stress strain curve immediately after peak strength which cannot be approximated by a hyperbola. However, the majority of the post peak deformation closely follows the hyperbolic relationship. The a and b parameters for all four samples are given in Table (4.1). It is found that the brittleness indices determined from the peak strength and residual strength are usually slightly lower than those calculated from the b parameter. This is because the residual strength calculated from the hyperbolic strain softening model assumes that residual strength is reached when the plastic strain is infinite. Since the residual strength in actual stress strain relationships is obtained

Table 4.1: Summary of Soil Parameters of a Stiff Clay

	Atterberg Limits			Elastic Parameters				Strength Parameters			Other Parameters			
	w(n) %	LL %	PL %	Unit Wt. %	Elast. Modul. kN/m ³	Poisson Ratio	Peak strain %	Peak Streng. kPa	Resid. Streng. kPa	Confin Press kPa	ko	a	b	I(B)
Sample 1 (T3-8)	38	27	72	19.0	4194.5	0.499	3.29	138.0	80.0	110.0	1.0	5.4	1.62	0.414
Sample 2 (T3-9)	52	30	76	19.0	3852.2	0.499	3.45	132.9	75.9	125.0	1.0	4.5	1.69	0.429
Sample 3 (T4-9)	32	33	64	19.0	3756.1	0.499	3.28	123.2	65.0	140.0	1.0	3.0	1.69	0.472
Sample 4 (T2-8)	39	23	57	19.0	6032.8	0.499	3.05	184.0	120	123.0	0.6	2.25	2.64	0.348

* - I(B) Brittleness Index is calculated based on the peak and residual strength.

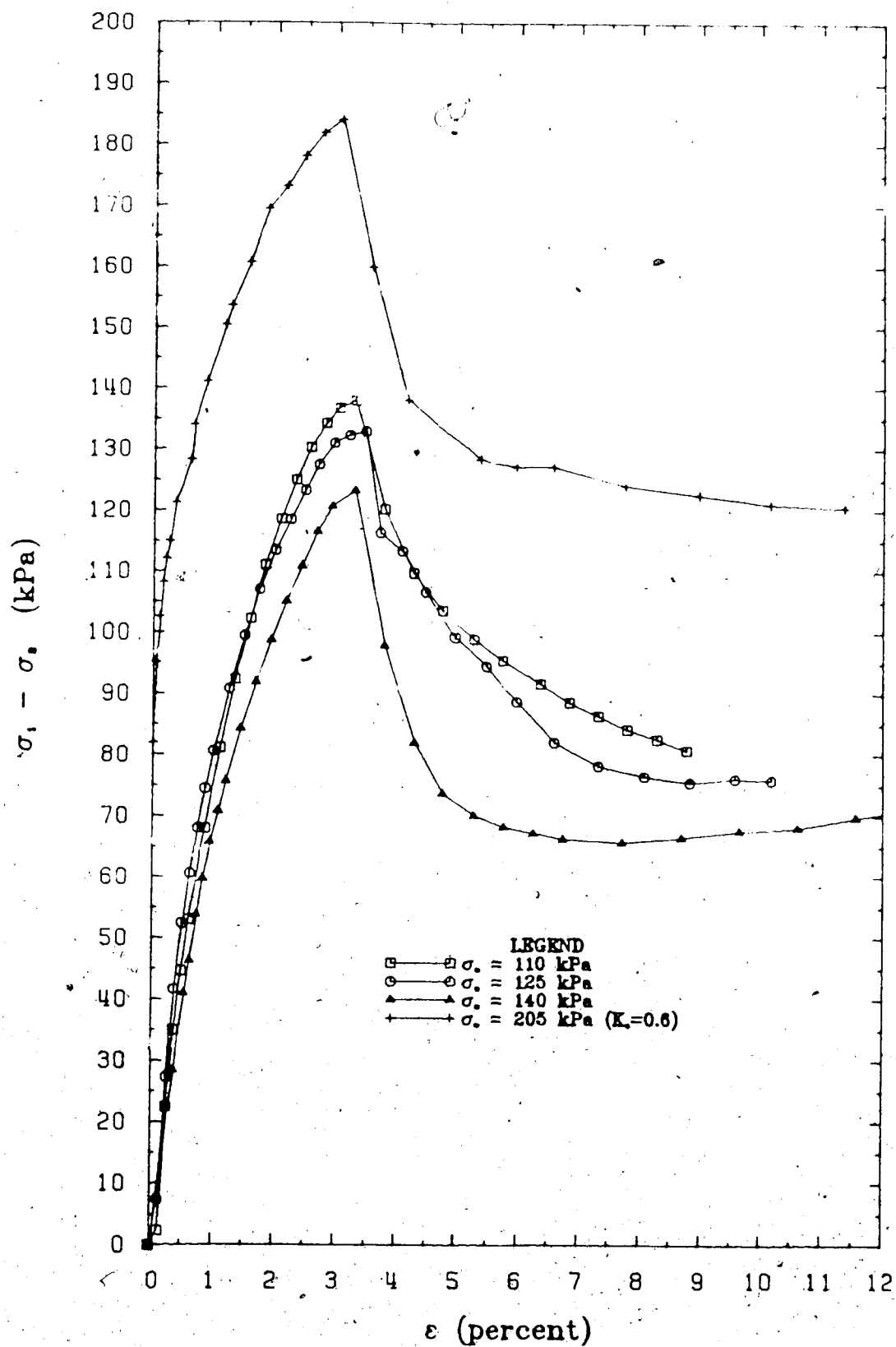


Figure 4.5: Triaxial Test Results of Stiff Clay

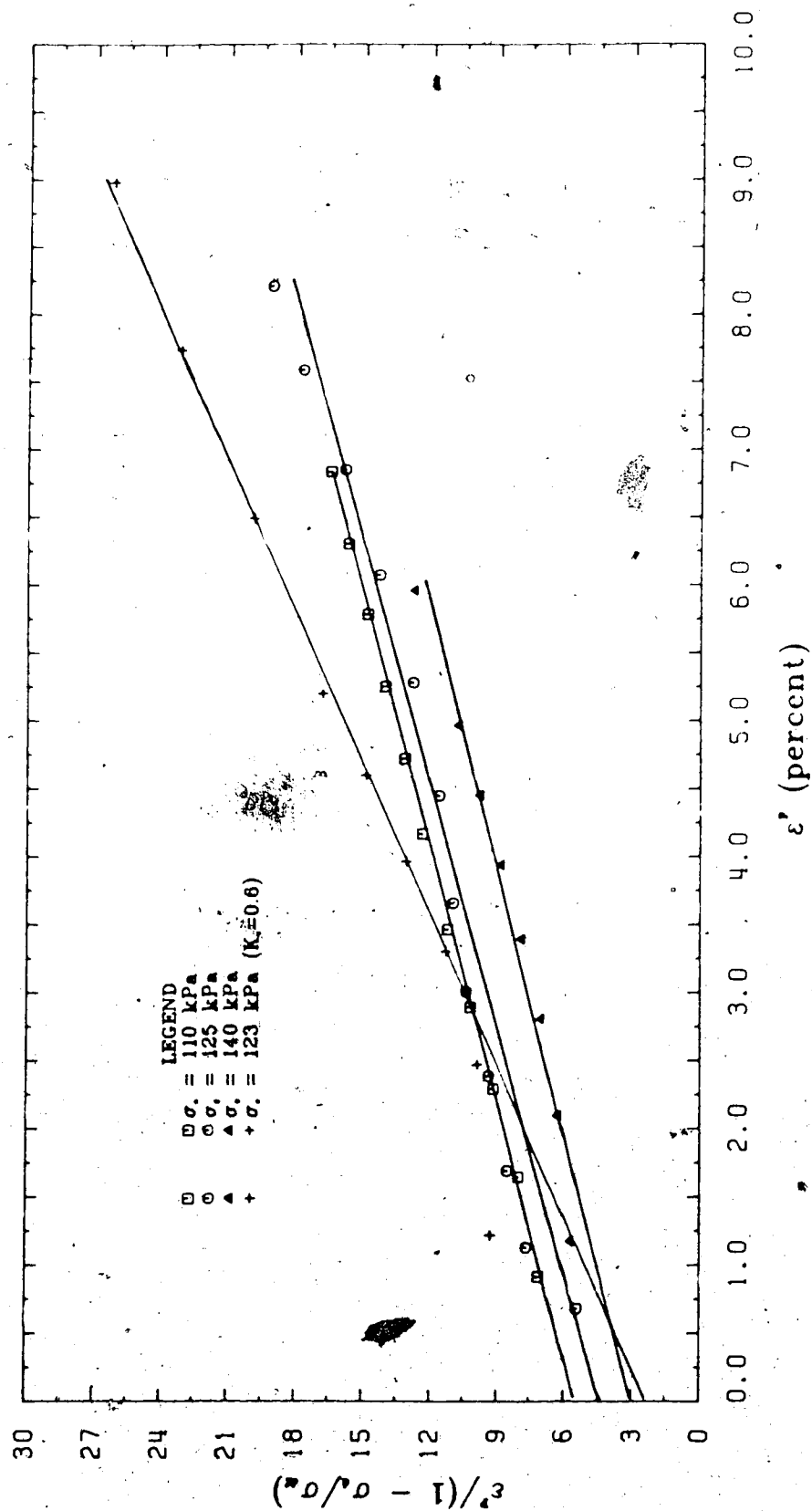


Figure 4.6: Triaxial Test Results of Stiff Clay in Normalized Plot

from a strain less than infinity, therefore in general the value of I_B calculated from the b parameter is larger than the value from κ_r and κ_p . There are, however, occasional exceptions as shown in Table 4.1. The I_B value calculated from the b parameter should be used in the analysis.

4.6 Comparison of Finite Element Results

To investigate the assumption of the hyperbolic model and also to verify the finite element formulation, the triaxial test is simulated using the finite element model. The test was conducted using a specimen of 76 mm high and 38 mm diameter. By considering the symmetry of the specimen, only one quarter of the specimen need be analyzed. One 8-node isoparametric rectangular element is used to model the specimen.

The analysis consists of applying an initial all around pressure to simulate the consolidation part of the experiment. Since the yield criterion is independent of the hydrostatic component of the stress tensor, the application of the confining pressure will have no effect on the yielding of the material. An exception occurs when the specimen is undergoing anisotropic consolidation such as specimen number 4 which is subjected to a k_0 value of 0.6 during consolidation. After the application of the confining pressure, the axial strain is increased beyond failure and into the post peak softening range. The parameters used in the analyses are given in Table 4.1. The results of the

analyses are shown in Figure 4.7. It is seen from Figure 4.7 that the post peak softening region of the stress strain curve follows a hyperbola curve with reasonable accuracy especially for $\sigma = 110$ kPa and 123 kPa. For $\sigma = 140$ kPa the shear strength of the clay increases after reaching a minimum value of about 65 kPa. This type of behaviour cannot be modelled by the hyperbolic strain softening relationship. However the increase in strength is usually not very large and can be neglected for all practical purposes. The pre-peak deformation for the real soil behaves in a non-linear manner while the model assumes linear elastic behaviour. This introduces some error in pre-peak deformation. However, the prediction of yielding or peak strength is not affected by the linear elastic assumption because the peak strength and the corresponding strain are independent quantities in the model. The analysis here indicates that this model yields promising results for modelling the post peak deformation of an actual strain softening soil.

4.7 Bearing Capacity Analysis of Strain Softening Material

To illustrate the effect of progressive failure in a more realistic engineering problem using the hyperbolic strain softening model, a strip footing will be analyzed. Bearing capacity of a footing is an interesting and challenging problem in plasticity and soil mechanics because the failure of a footing involves plastic flow around the

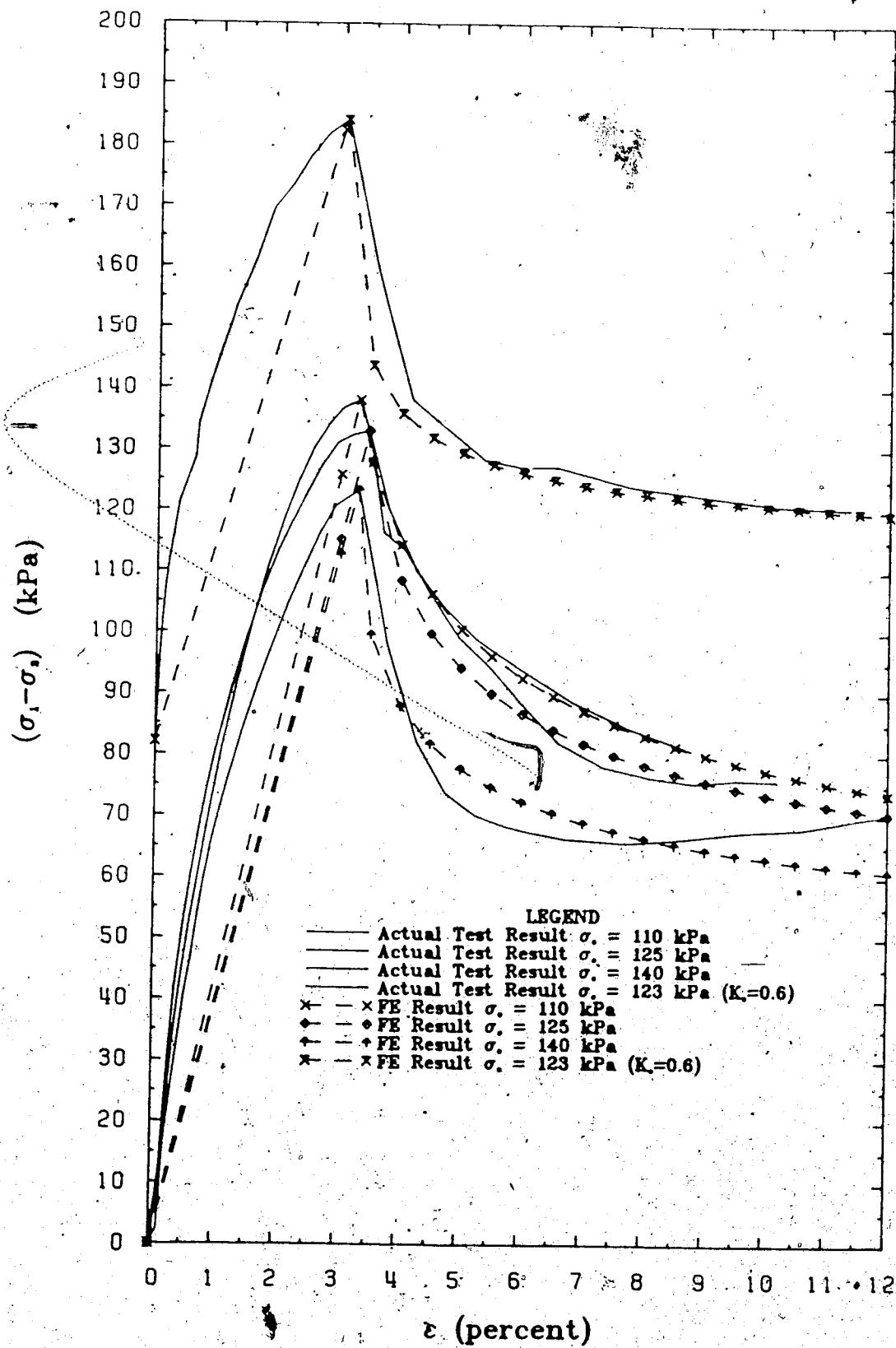


Figure 4.7: Simulation of Triaxial Test

footing, stress concentration at the edge of the footing and a hydrostatic compression zone underneath the footing. The limit load for a perfectly flexible footing on frictionless material can be determined from a slip line field and since the upper and lower bounds of the footing pressure coincide, this implies that the bound solution gives the exact collapse load for a rigid plastic material.

The footing being analyzed in this chapter is a perfectly smooth, rigid, strip footing. In many bearing capacity analyses ~~the~~ footing is often assumed to be perfectly flexible. This results in a uniform pressure underneath the footing. By assuming the footing to be rigid, the pressure distribution will not be uniform and one may expect stress concentration at the edge of the footing. The reason for analyzing a rigid footing rather than a flexible footing is because the displacement of the footing can be specified in the analysis instead of prescribing a uniform pressure in the case of a flexible footing. Prescribing the displacement not only results in a more stable numerical solution in most cases but, more importantly, it enables one to determine the post peak response of the system. If pressure is prescribed, the footing will collapse when the limit load is reached and it is not possible to obtain a numerical solution or any solution after peak. However if displacements are prescribed, the pressure distribution underneath the footing varies in such a way as to maintain equilibrium of the system after the collapse load is

reached. This point has been discussed in some detail in Chapter 2 of this thesis.

The width of the strip footing that will be analyzed here is 10 feet and the depth of the soil underneath the footing is taken to be 150 feet. A no slip boundary condition is assumed at depth 150 feet. More elaborate analyses of the bearing capacity problem of the strip footing will be given in Chapter 5 in studying the effect of the propagation of the plastic zone and the pore pressure effect. Therefore details of the finite element mesh and the rationale for determining the size of the foundation soil are given in the next chapter. As illustrated in Figure 5.14, 229 8-node isoparametric elements with 736 nodes with a 2×2 integration scheme are used in the analysis. Very small elements are used near the footing to model accurately, the rapid variation of stresses in this region.

The soil underneath the footing is assumed to have a peak cohesion of 1440 psf and residual cohesion of 720 psf which gives a brittleness index of 0.5. The material is assumed to be frictionless with a Poisson's ratio of 0.499 to model the fully undrained condition.

Five separate cases will be considered. The first case assumes that the material behaves in an elastic perfectly plastic manner with a cohesion equal to 1440 psf. This will give the upper limit of the bearing capacity of the footing. The second, third and fourth cases assume strain softening behaviour after a peak cohesion of 1440 psf is reached with

the residual cohesion of 720 psf with different rates of post peak softening. The second case has the highest rate of softening with the a parameter equal to 9 and the third and fourth cases have a more gradual rate of softening with a values of 27 and 81 respectively. The final case assumes the material behaves in an elastic plastic perfectly manner with peak cohesion of 720 psf. This will give the lower limit of the bearing capacity of the footing. The strain to peak strength for all five cases is equal to 3%. The stress strain relationships for all five cases are shown on Figure 4.8.

The pressure displacement responses of the footing for all five cases are shown in Figure 4.9. The limit load for cases 1 and 5 are approximately equal to 8875 psf and 4272 psf at about 6 ft settlement respectively. The limit loads are still increasing at a very slow rate as shown in Figure 4.9. This limit load is slightly higher than that calculated using $(\pi+2)C_u$ for a perfectly flexible footing due to the constraints imposed by the rigidity of the footing. The maximum pressure for cases 2, 3 and 4 are considerably lower than case 1 but higher than case 5. Case 4 shows higher footing pressure than case 3 which in turn is higher than case 2. Since all 3 cases have the same peak and residual strengths, the only difference among these cases is the rate of softening after peak. A higher rate of softening results in a lower maximum footing pressure due to the development of the plastic zone and partial failure underneath the

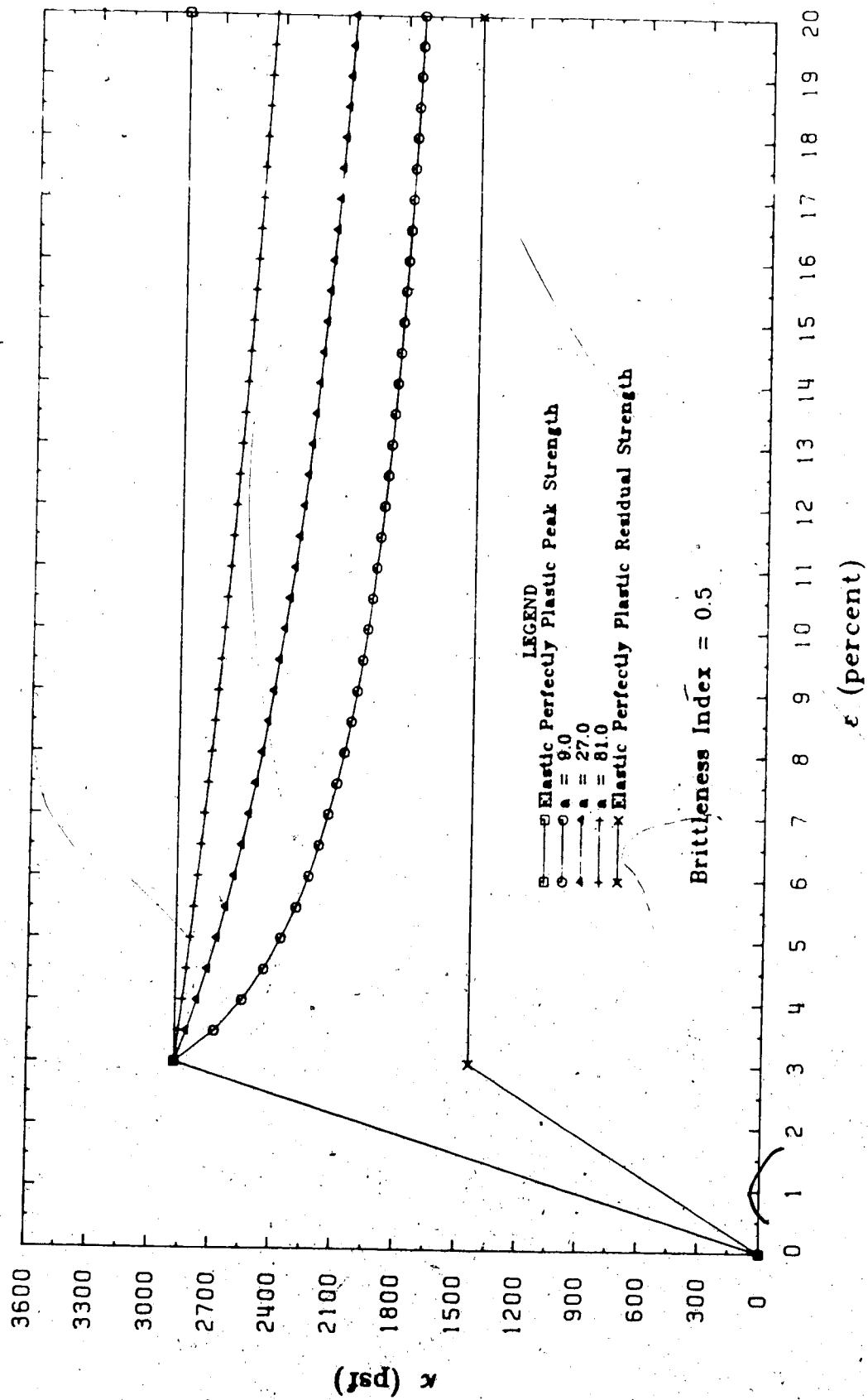


Figure 4.8: Stress Strain Relationship used in Bearing Capacity Analysis

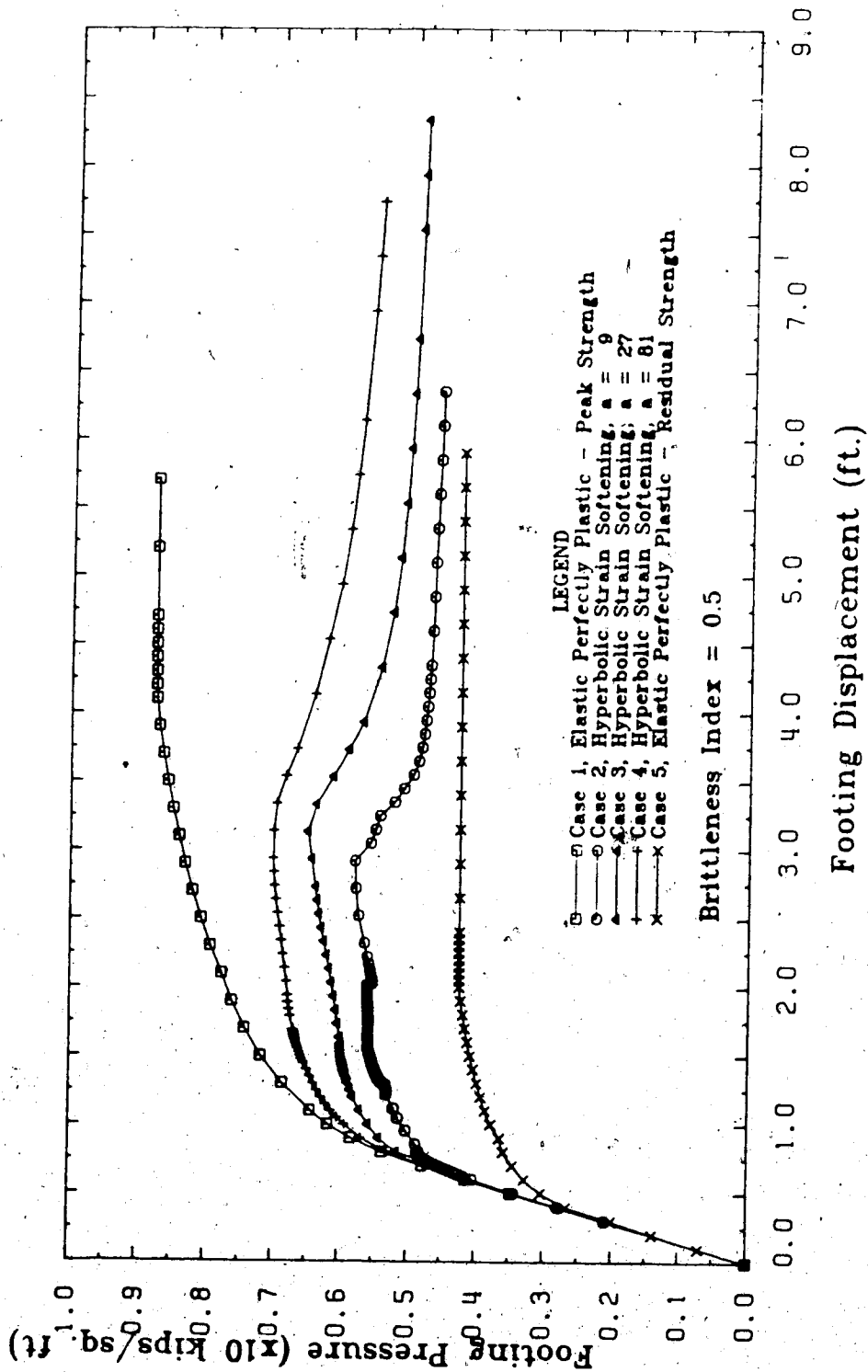


Figure 4.9: Pressure Displacement Response of Footing

footing. For a more brittle material, in the sense that it reaches the residual strength faster, the localized yielding results in a larger release of recoverable energy and thus leads to an earlier collapse mechanism as well as a lower maximum pressure. The effect of progressive failure is clearly illustrated in Figure 4.9.

Figure 4.10 shows the development of the plastic zone underneath the footing at different stages of the analysis. The footing displacements are selected at 1.5 ft, 2.5 ft, 3.5 ft and 4.5 ft or as close to these values as possible to give an idea of the yield zone at pre-peak, near peak and post peak deformation. The dots shown in Figure 4.10 represent yielding having occurred at these particular locations. These locations are selected at the Gaussian point of the elements. Therefore, the spacing of the dots is dependent upon the size of the element. It is seen that for the elastic perfectly plastic cases, cases 1 and 5, the yield zone is in the shape of a bulb that extends to approximately $3 \times B$ before reaching the maximum footing pressure, where B is the width of the footing. At the ultimate load, a triangular wedge is formed close to the ground surface and the shape and sizes of the yield zone for cases 1 and 5 are very similar although the shear strengths for these two materials are different. For the strain softening cases, the extent of the yield zones are considerably smaller than the perfectly plastic cases. The yield zone initially extends downward and then spreads

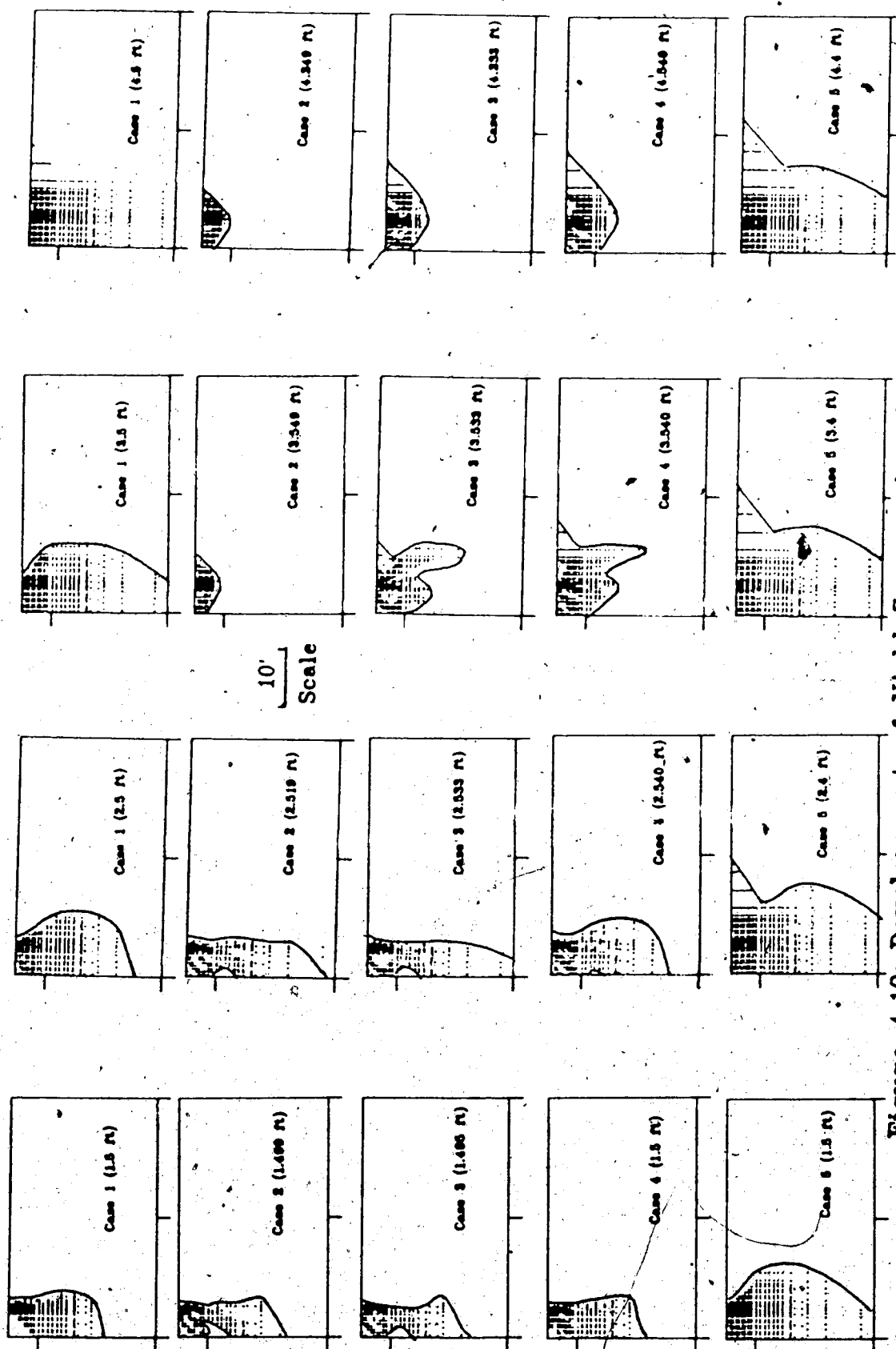


Figure 4.10: Development of Yield Zone under the Footing

laterally. However, the lateral extension is followed by unloading of the plastic zone underneath the footing.

Eventually only a small plastic zone remains at the surface during post peak deformation. It seems that the more brittle is the material, the smaller is the post peak plastic zone. More discussion of the development of the plastic zone under a footing will be given in next chapter.

The results in Figure 4.9 have another important implication. Since the peak strength of the material for cases 1 to 4 are all the same and the residual strength for cases 2 to 5 are all the same, the difference in limit load for cases 2 to 4 is mainly due to the different rate of post peak softening of the material. Therefore, the determination of the maximum pressure of the footing is not possible simply based on the peak and residual strength alone without knowing the post peak strain softening characteristics of the material. Another point is that by observing the limit load of the footing, the calculation of the peak strength of the material is impossible without a knowledge of the post peak softening behaviour. This is because the progressive development of the yielding zone is dependent upon the rate of post peak softening.

One may extend the above argument to the testing of stiff clay using triaxial and shear box apparatus. Since in triaxial or shear box testing, one is observing the response of a system, which is composed of a collection of soil particles, from which the stress strain relationship of the

material at a point are deduced. The results here show such a deduction for a strain softening material is impossible whenever progressive failure occurs in the sample. Thus the stress strain relationship obtained from the laboratory testing of a strain softening material do not give the true response of the material at a point, it is simply the response of the sample and, strictly speaking, cannot be generalized to other situations. Fortunately, the observed peak strength from the test is always lower than the actual peak strength of the material and one is on the safe side as far as design is concerned. This point can be further clarified using the uniaxial compression test example in Chapter 3. The material in this example is assumed to be elastic brittle plastic with the residual strength being lower than the peak strength. However, in simulating the uniaxial test the observed load displacement response resembles that of a perfectly plastic material with no decrease in strength after peak. The maximum mobilized strength is actually at residual. The reason is due to the abrupt decrease in strength after peak of the actual material and the effect of progressive failure occurring in the sample which gives a lower system response. By using the result from this test in deducing the strength of this material, the observer will conclude that the material has no softening behaviour and report a lower shear strength than the actual peak strength of the material.

4.8 Conclusion

The hyperbolic strain softening model presented in this chapter enables one to analyze progressive failure of soil structures with realistic stress strain relationships. The formulation of this model is relatively simple and the material parameters can be determined quite readily from triaxial tests. Much has been learned from the exercise of the bearing capacity problem and it has been demonstrated clearly that the effect of progressive failure can change the bearing capacity of the footing drastically. The amount and rate of post peak softening are equally important to the behaviour of the soil structure.

5. EFFECTIVE STRESS APPROACH OF UNDRAINED ANALYSIS

The effective stress principle is one of the greatest discoveries in soil mechanics. Since it is known that soil behaviour is dependent upon effective stresses and not total stresses, there is a need in numerical modelling to analyze soil deformation in terms of effective stresses. It is often assumed in the analysis that soil is either under fully drained or fully undrained conditions. Sometimes when neither assumption can be made, the effect of pore pressure diffusion must be considered. Under ~~fully~~ drained conditions, the pore pressure remains constant and any change in total stress must be accompanied by an equal change in effective stress. However under fully undrained condition the pore pressure is not constant and the change in pore pressure is a result of soil deformation. The deformation of the soil is, in turn, dependent upon the pore pressure. It is often assumed in the total stress analysis that the undrained parameters determined from laboratory tests can be used in the field. This implies that the pore pressure generated in the laboratory experiment will be the same as that of the soil at the site. However, since the generation of pore pressure is dependent upon the deformation of the soil and stress history, this assumption cannot be true throughout the soil mass. It is the purpose in this chapter to introduce a finite element formulation for ~~fully~~ undrained analyses in terms of effective stresses.

For the case where there is significant pore pressure diffusion and the fully undrained assumption cannot be made, the solution to this problem has been studied (Hwang 1971) and will not be considered here.

Many finite element formulations for undrained analysis have been proposed (Hwang 1971, Desai C.S., 1977). Most of these analyses relate the change in pore pressure to the change in volumetric strain under fully saturated conditions. In conventional geotechnical analysis the change in pore pressure is normally related to the change in total stress using the Skempton A and B pore pressure parameters. These parameters can be measured in the laboratory and the range of values of these parameters reflects different soil conditions which are familiar to geotechnical engineers. The following formulation utilizes these parameters although they are, in fact Henkel's parameters which can be easily related to the Skempton parameters (Henkel, 1960). This formulation can be used in fully drained and fully undrained analysis.

5.1 Undrained Finite Element Formulation

The elasto-plastic formulation discussed in Chapter 2 will be used here. Therefore the material model can be any one of the models discussed in this thesis. In fact, there is very little restriction on the constitutive relationship of the material, but obviously the assumptions made in the plasticity formulation in Chapter 2 will also be applied

here. To formulate the problem in terms of effective stress, the change in total stress must now be separated into the change in effective stress and in pore pressure. These are given by:

$$\Delta\sigma'_{ij} = \Delta\sigma_{ij} - \delta_{ij}\Delta u \quad (5.1)$$

or in matrix notations:

$$\{\Delta\sigma'\} = \{\Delta\sigma\} - \{m\}\Delta u \quad (5.2)$$

where

$\{\Delta\sigma'\}$ is the increment of effective stress;

i.e. $\{\Delta\sigma\} = \langle \Delta\sigma'_{xx}, \Delta\sigma'_{yy}, \Delta\sigma'_{xy}, \Delta\sigma'_{zz}, \Delta\sigma'_{yz}, \Delta\sigma'_{xz} \rangle^T$;

Δu is the increment of pore pressure;

$\langle m \rangle$ is a vector defined as

$$\langle m \rangle = \langle 1, 1, 0, 1, 0, 0 \rangle.$$

The pore pressure generated due to the changes in total stresses can be calculated by (Henkel 1960):

$$\Delta u = \frac{\beta}{3}(\Delta\sigma_1 + \Delta\sigma_2 + \Delta\sigma_3) - \frac{\alpha\sqrt{(\Delta\sigma_1 - \Delta\sigma_2)^2 + (\Delta\sigma_2 - \Delta\sigma_3)^2 + (\Delta\sigma_3 - \Delta\sigma_1)^2}}{3} \quad (5.3)$$

where

$\Delta\sigma_1, \Delta\sigma_2, \Delta\sigma_3$ are the changes in total principal stresses;

and α, β are pore pressure parameters.

It is assumed that the changes in pore pressure are due to the following two effects:

1. Δu_a is the change in pore pressure due to changes in the second stress invariant of the stress tensor.
2. Δu_β is the change in pore pressure due to changes in mean hydrostatic stress.

The total change in pore pressure will be given by the sum of Δu_a and Δu_β , that is:

$$\Delta u = \Delta u_a + \Delta u_\beta \quad (5.4)$$

In matrix notation:

$$\Delta u_a = -\alpha \sqrt{\langle \Delta \sigma^d \rangle} \{ \Delta \sigma^d \} \quad (5.5a)$$

$$\Delta u_\beta = \beta \langle m \rangle \{ \Delta \sigma \} \quad (5.5b)$$

where

$$\langle \Delta \sigma^d \rangle = \langle \Delta \sigma \rangle - \frac{1}{3} \langle m \rangle \langle m \rangle \{ \Delta \sigma \}$$

The negative sign in Equation (5.5a) is due to compressive stresses which are being considered as negative quantities.

It can easily be shown that:

$$\langle \Delta \sigma'^d \rangle = \langle \Delta \sigma^d \rangle \quad (5.6)$$

Using Equations (5.2), (5.3), (5.4), (5.5a), (5.5b), and (5.6), one can show that:

$$\Delta u = \frac{\beta}{3(1-\beta)} \langle m \rangle \{ \Delta \sigma' \} - \alpha \sqrt{\langle \Delta \sigma'^d \rangle \{ \Delta \sigma'^d \}} \quad (5.7)$$

Multiplying and dividing the second term by $\langle \Delta \sigma' \rangle \{ \Delta \sigma' \}$ results in:

$$\Delta u = \langle P \rangle \{ \Delta \sigma' \} ; \quad (5.8)$$

where

$$\langle P \rangle = \left(\frac{\beta}{3(1-\beta)} \langle m \rangle - \frac{\alpha \sqrt{\langle \Delta \sigma'^d \rangle \{ \Delta \sigma'^d \}} \langle \Delta \sigma' \rangle}{\langle \Delta \sigma' \rangle \{ \Delta \sigma' \}} \right)$$

Note that for $\beta=1.0$, which implies incompressibility, the change in pore pressure is theoretically indeterminate. It is because for an incompressible material, any arbitrary increment of hydrostatic stress which is in equilibrium can be superimposed on the existing stress state without causing additional deformation. Substituting (5.8) into (5.2) and (2.3), the equilibrium equation becomes:

$$\int_V [B]^T [D] \{ \Delta \sigma' \} dv = \{ \Delta R \} , \quad (5.9a)$$

where

$$[D] = [I] + \{ m \} \langle P \rangle . \quad (5.9b)$$

Expressing the incremental constitutive relationship of the material in terms of effective stresses:

$$\{ \Delta \sigma' \} = [C'] \{ \Delta \epsilon \} , \quad (5.10)$$

and the strain displacement relationship using isoparametric

formulation:

$$\{\Delta \epsilon\} = [\beta] \{\Delta \delta\} , \quad (5.11)$$

one arrives at the following matrix equation:

$$[K] \{\Delta \delta\} = \{\Delta R\} , \quad (5.12a)$$

where

$$[K] = \int_V [\beta]^T [D] [C'] [\beta] dv ; \quad (5.12b)$$

$\langle \Delta \delta \rangle$ = increments of displacement.

Note that the matrix $[D]$ can be symmetric or unsymmetric. $[D]$ is symmetric if only the Δu effect is being considered, otherwise, $[D]$ is unsymmetric. If $[D]$ is unsymmetric, then $[K]$ is unsymmetric. However, from Equation (5.12b), even if $[D]$ is symmetric, $[K]$ can be symmetric or unsymmetric. It is found that for linear elastic material and non-frictional plastic material with the associated flow rule neglecting the Δu effect, the matrix $[K]$ is always symmetric. For frictional plastic material with an associated or non-associated flow rule, $[K]$ is unsymmetric.

The symmetric property of $[K]$ has some interesting implications. If $[K]$ is not symmetric, not only will it require a non-symmetric equation solver to obtain a solution, but it will also violate Maxwell's reciprocal relationship of stiffness coefficients. The principle of superposition is no longer valid even for linear elastic

material if the shearing effect of the pore pressure is to be considered. Due to the path dependent nature of elasto-plastic material, the principle of superposition cannot be applied in any event. However it is assumed that in an incremental analysis, the material is piecewise linear. The results here emphasize that the correct loading sequence is very important in an effective stress analysis using this formulation. It is noted that the unsymmetric property of the stiffness matrix is due to the generation of pore pressure due to the shearing component of the stress tensor because the pore pressure acts in reducing only the normal stresses and not shear stresses. Also an iterative procedure is required if the Δu effect is included since $\langle P \rangle$ becomes stress dependent.

The formulation of the incremental constitutive matrix $[C']$ follows the same procedure as in Chapter 2 but all stress quantities must now be expressed in terms of effective stresses. It is noted that the formulation is valid for elastic, elasto-plastic strain hardening and softening materials. Therefore all of the soil models discussed earlier can be applied in this formulation.

5.1.1 Matrix Solution Scheme

Since the undrained formulation results in a non-symmetrical stiffness matrix, it is necessary to have an equation solver for non-symmetric matrices. The plasticity formulation presented in Chapter 2 may also result in a

non-symmetrical stiffness matrix if the non-associated flow rule is used. In the finite element program SAFE, a compact storage scheme called the 'Skyline Method' is used to store the global stiffness matrix. The Gauss elimination procedure is used to obtain a solution with this method which was initially proposed by Bathe and Wilson (1976). To obtain a solution of non-symmetrical matrices, it is desirable to have a non-symmetric matrix solution solver which uses the compacted storage scheme and is able to solve non-positive definite matrices. For non-symmetrical matrices a new 'Extended Skyline method' has been developed. For strain softening material, the stiffness matrix is non-positive definite and can be solved using the 'Extended Skyline method'. Details of this method is given in Appendix E.

5.2 Expansion of a Thickwalled Cylinder

The thickwalled cylinder analyzed in Chapter 2 will be reconsidered here. First, the solutions using the total stresses are obtained. This will serve as a basis of comparison for the effective stress analysis. Both the elastic perfectly plastic and strain softening cases will be considered. For the elastic perfectly plastic material the Tresca and von Mises yield criterion will be used. For the strain softening material, the model discussed in Chapter 2 will be used.

5.2.1 Elastic Perfectly Plastic Model

The analytical solution for this problem with Tresca and von Mises yield criteria have been discussed by Hill (1953) and Hodge and White (1950). A closed form solution using the Tresca criterion is available. The pressure displacement relationships are given by (Hill, 1953):

$$\frac{P}{Y} = \ln\left(\frac{c}{a}\right) + \frac{1}{2}\left(1 - \frac{c^2}{b^2}\right), \quad (5.13a)$$

$$\frac{u}{a} = \frac{Y(1+\nu)c^2}{2Eb^2} \left[\left(1 - 2\nu\right) + \frac{b^2}{a^2} \right], \quad (5.13b)$$

where

a - inner radius of the cylinder;

b - outer radius of the cylinder;

Y - uniaxial yield strength;

P - internal pressure (external pressure is assumed to be zero);

u_a - inner wall displacement;

c - radius to the elastic-plastic boundary.

The stresses in the elastic region is given by:

$$\frac{\sigma_r}{Y} = -\frac{c^2 b^2}{2b^2 r^2} \left(\frac{c^2}{b^2} - 1 \right), \quad (5.14a)$$

for $c \leq r \leq b$

$$\frac{\sigma_\theta}{Y} = \frac{c^2 b^2}{2b^2 r^2} \left(\frac{c^2}{b^2} + 1 \right), \quad (5.14b)$$

where

σ_r - radial stress

and σ_θ - circumferential (hoop) stress.

The stresses in the plastic region are given by:

$$\frac{\sigma_r}{Y} = -1/2 - \ln\left(\frac{c}{r}\right) + \frac{c^2}{2b^2}, \quad (5.15a)$$

for $a \leq r \leq c$

$$\frac{\sigma_\theta}{Y} = 1/2 - \ln\left(\frac{c}{r}\right) + \frac{c^2}{2b^2}. \quad (5.15b)$$

The radius to the elastic-plastic boundary c can be taken as the independent variable in these equations and the displacements and stresses for different internal pressures can be determined. The initial yielding occurs at the inner radius at an internal pressure of:

$$\frac{P_0}{Y} = 1/2 \left(1 - \frac{a^2}{b^2}\right). \quad (5.16)$$

When the Tresca yield criterion is used, the radial stress σ_r and the hoop stress σ_θ are always the minor and major principal stresses respectively, which simplifies the algebra in obtaining the closed form solution. No closed form solution has been obtained when the von Mises yield criterion is used and numerical procedures are required in solving the governing differential equations. However, the initial yielding pressure using the von Mises criterion can

be calculated from:

$$\frac{P}{Y} = \frac{1}{\sqrt{3}} \left(1 - \frac{a^2}{b^2} \right) / \sqrt{1 + (1 - 2\nu^2) \frac{a^4}{b^4}} \quad (5.17)$$

Finite element solutions have been obtained using both the Tresca and von Mises criteria for the mesh shown in Figure 2.3. Figure 5.1 shows the relationship between the internal pressure versus the outer wall displacement. The material parameters used in the analysis are also shown in Figure 5.1. The outer wall displacement has been normalized with respect to the shear modulus G , yield stress Y and the radius of the inner wall a . Excellent agreement between the analytical and finite element solution is obtained. Elastic unloading and reloading behaviour of the cylinder are also shown. It is noted that the yielding pressure for reloading after plastic deformation is higher than that for the initial loading even though the material behaves in a perfectly plastic manner. The apparent increase in yielding pressure is not due to the strain hardening effect but due to the build up of residual stresses and spreading of the plastic zone during plastic deformation. Thus complete unloading after plastic deformation will not bring about a return to the initial stress free state.

Figure 5.2 shows the hoop stress distribution throughout the cylinder at various internal pressures using the Tresca criterion. A 3x3 Gaussian integration scheme is used in the finite element solution and the location of the

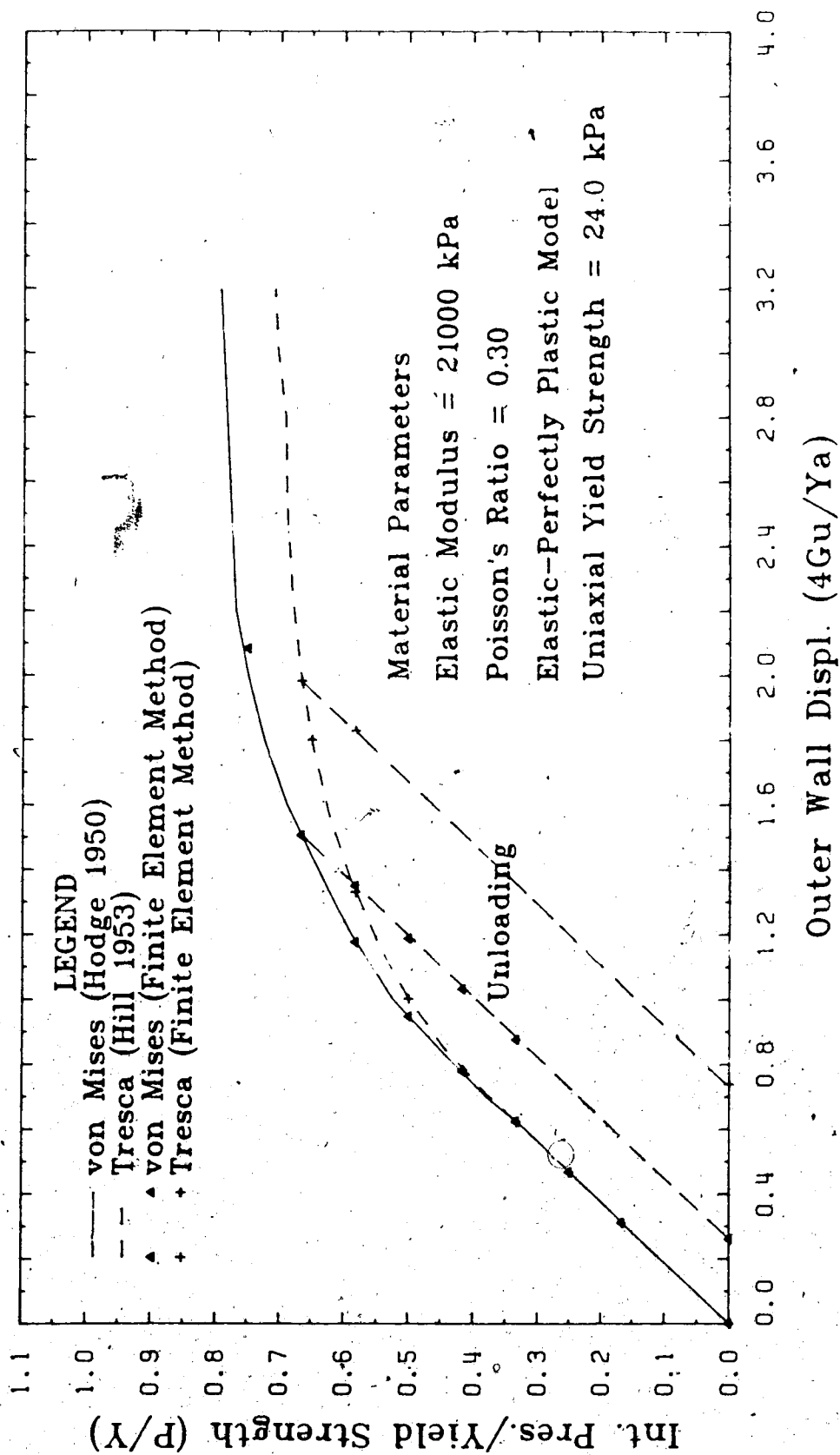


Figure 5.1: Pressure Displacement Response of the Thickwalled Cylinder

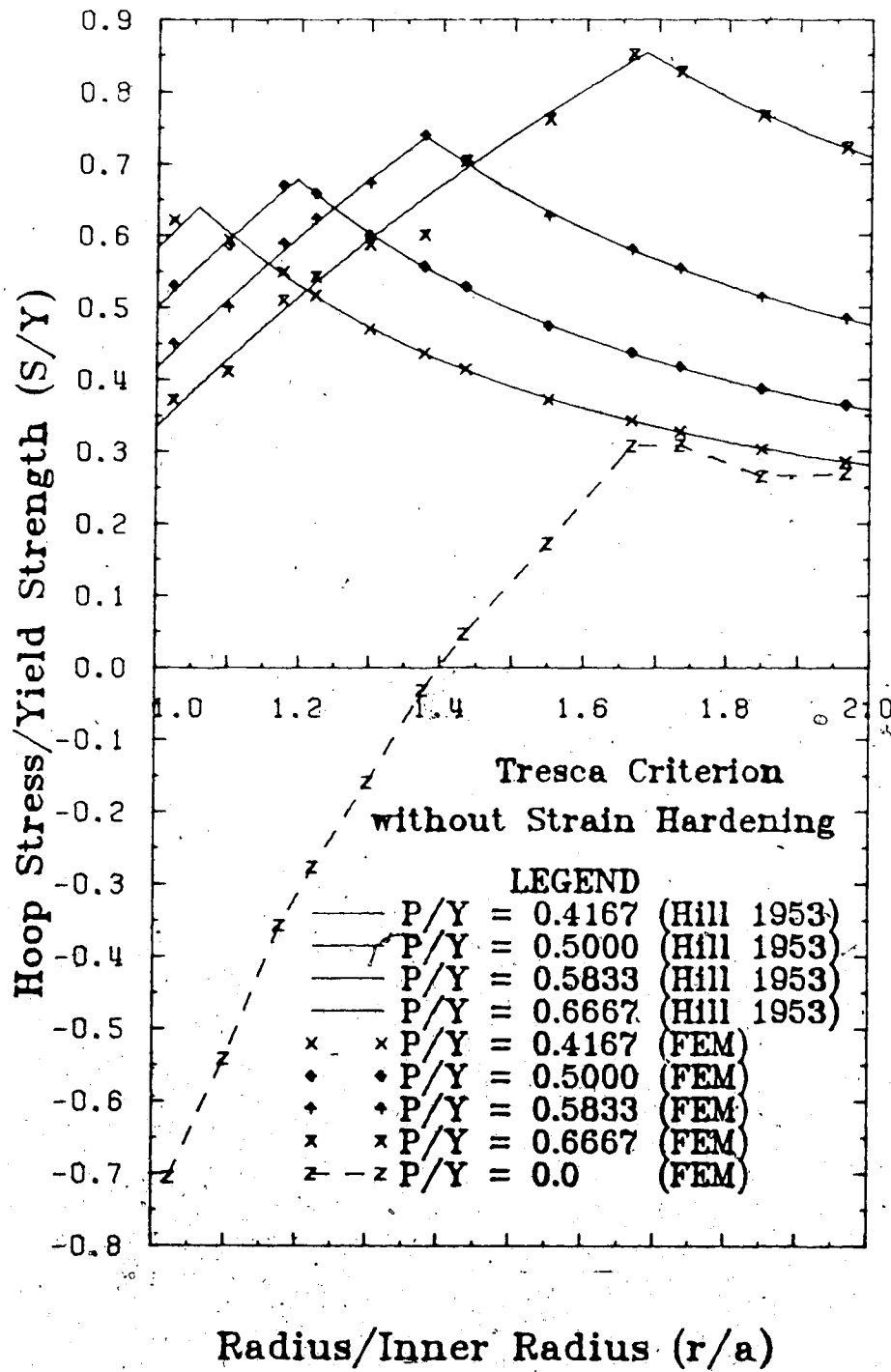


Figure 5.2: Hoop Stress Distribution

integration point may not coincide with the elastic plastic boundary. It happens that for $P/Y = 0.5833$ the elastic plastic boundary coincides with the third integration point of the second element but this is not true for other cases. The propagation of the plastic zone and the elastic plastic boundary are clearly shown in Figure 5.2. In the finite element analysis, the elastic plastic boundaries in many cases are inside the element thus making part of the element elastic and part plastic. Therefore, in the element stiffness formulation, the element will be treated as both elastic and plastic depending on the location of the integration points. Such is the case for $P/Y = 0.4167$ as shown in Figure 5.2 where the first integration point (actually the first three integration points to be precise) are in the plastic region and the remaining integration points are in the elastic region. If the elastic plastic boundary falls between the integration points and the element boundary, then the presence of the boundary within the element will not be detected by the integration scheme. An example of this situation is the case for $P/Y = 0.6667$ in Figure 5.2. Since the integration points are close to the element boundary, no significant error will result if the elements are small.

Complete unloading is simulated in the finite element analysis after the internal pressure has reached a value of $P/Y = 0.6667$. The residual stress due to plastic deformation is shown in Figure 5.2 and part of the cylinder is under

tension during unloading. Compression yielding can occur if the cylinder is sufficiently thick and the pressure is high enough to cause a large plastic zone prior to unloading. Reloading is performed in which the stress state before unloading is restored.

The convergence rate of the finite element analysis is monotonic and quite rapid. With a displacement tolerance of 0.001 (see Equation (2.31)), only 3 to 4 iterations are required to reach convergence. Boundary pressure at the inner wall of the cylinder was prescribed rather than specifying the inner wall displacement as the other alternative which would result in an even more stable and rapid convergence rate.

5.2.2 Undrained Analysis of Elastic Perfectly Plastic

Material

In the following section the result of the undrained finite element analysis of the same cylinder is presented. The effective stress parameters used in the undrained analysis are the same as the parameters used previously and the material is assumed to be fully saturated. Earlier discussions in this chapter indicate that the pore pressure under undrained conditions can be separated into that due to the hydrostatic stresses and that due to the deviatoric stresses. For a fully saturated material, the pore pressure parameter β will be equal to unity. Since unity represents incompressibility which results in the pore pressure being

undetermined, a β value of 0.99 is used in these examples. Two cases are considered. In the first case it is assumed that no pore pressure is generated due to the deviatoric stress component, therefore $\alpha = 0.0$. In the second case an α value of 0.5 is used to study the effect of shearing on the generation of pore pressure.

The results of the undrained analysis using Tresca yield criterion with an elastic perfectly plastic model are shown in Figures (5.3) to (5.9). Figure 5.3 shows the pressure displacement response of the thickwalled cylinder as compared to the fully drained case. The result here shows that the cylinder is considerably stiffer due to the nearly incompressible behaviour of the material. Very little difference in the result is observed between the case of $\alpha = 0.5$ and $\alpha = 0.0$. However, it is noted that the unloading and reloading path for the case of $\alpha = 0.0$ are the same but there are noticeable but small differences in the unloading and reloading behaviour for the case of $\alpha \neq 0$. Although the material is linearly elastic during unloading and reloading, the path dependent deformation is due to the fact that the constitutive relationship is dependent upon the stress increment and becomes non-symmetric when the dilatancy effect is taken into account for $\alpha \neq 0$ as discussed earlier. Therefore, unloading and reloading are performed in several load increments for $\alpha \neq 0$ but only one increment is required for the case of $\alpha = 0$.

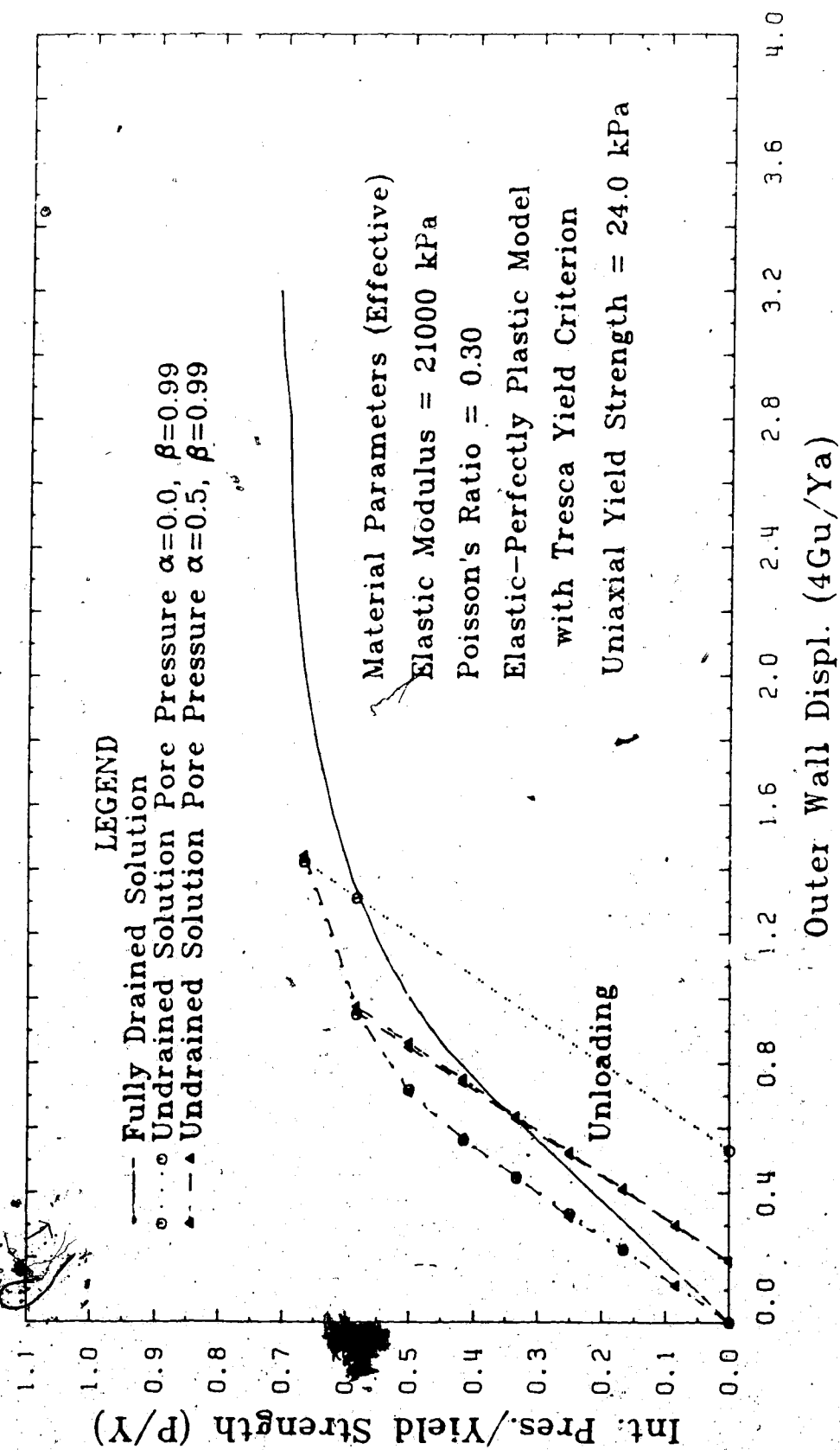


Figure 5.3: Pressure Displacement Response of Undrained Analysis

The effective hoop stresses inside the cylinder at various internal pressures are shown in Figure 5.4. As expected the effective stress is reduced due to the generation of pore pressure. However, it is interesting to see that the effective stress remains constant within the plastic zone while in the drained case it shows an increase in stresses from the inner wall within the plastic zone. To maintain equilibrium, while keeping the effective hoop stress constant, one would expect an increase or decrease in pore pressure within the plastic zone. Figure 5.5 shows the pore pressure distribution inside the cylinder. The positive pore pressure in Figure 5.5 actually means negative pore pressure (or dilation) in the conventional geotechnical sense. Since compression is taken as negative in this thesis, the pore pressure due to compressive stresses is also considered as a negative quantity. The pore pressure is constant in the elastic region throughout the analysis. Since the pore pressure depends on the hydrostatic stresses only for $\alpha = 0.0$, constant pore pressure implies constant hydrostatic stresses within the elastic zone. Examination of the hydrostatic stresses for the drained case indicates that they are indeed constant in the elastic region. Further discussion on the stress path of this problem is given in Appendix A. A total stress plot obtained by combining Figures 5.4 and 5.5 is shown in Figure 5.6. The total stress agrees extremely well with the results from the drained analysis. Although the total stresses are the same for the

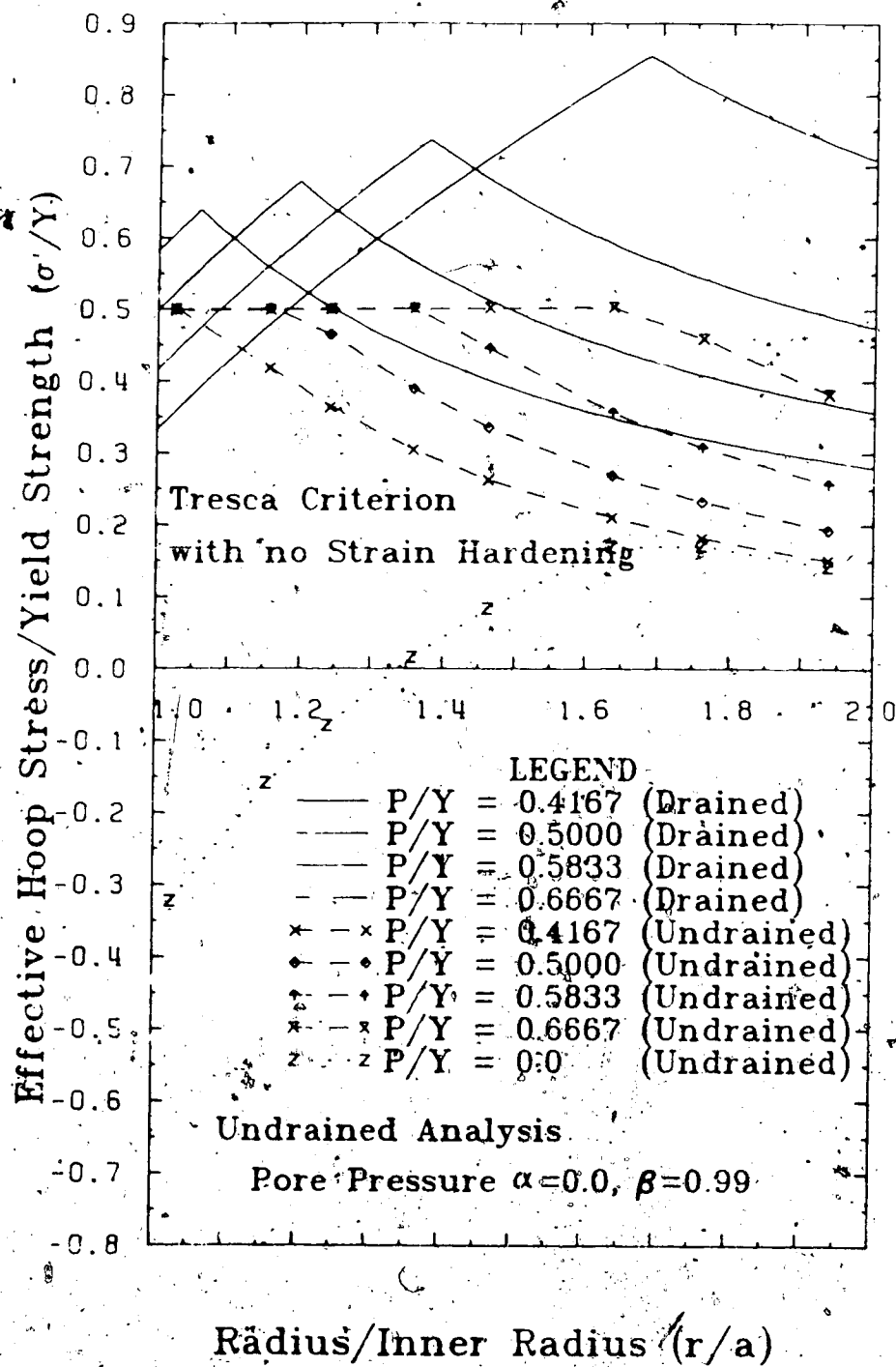


Figure 5.4: Hoop Stress Distribution

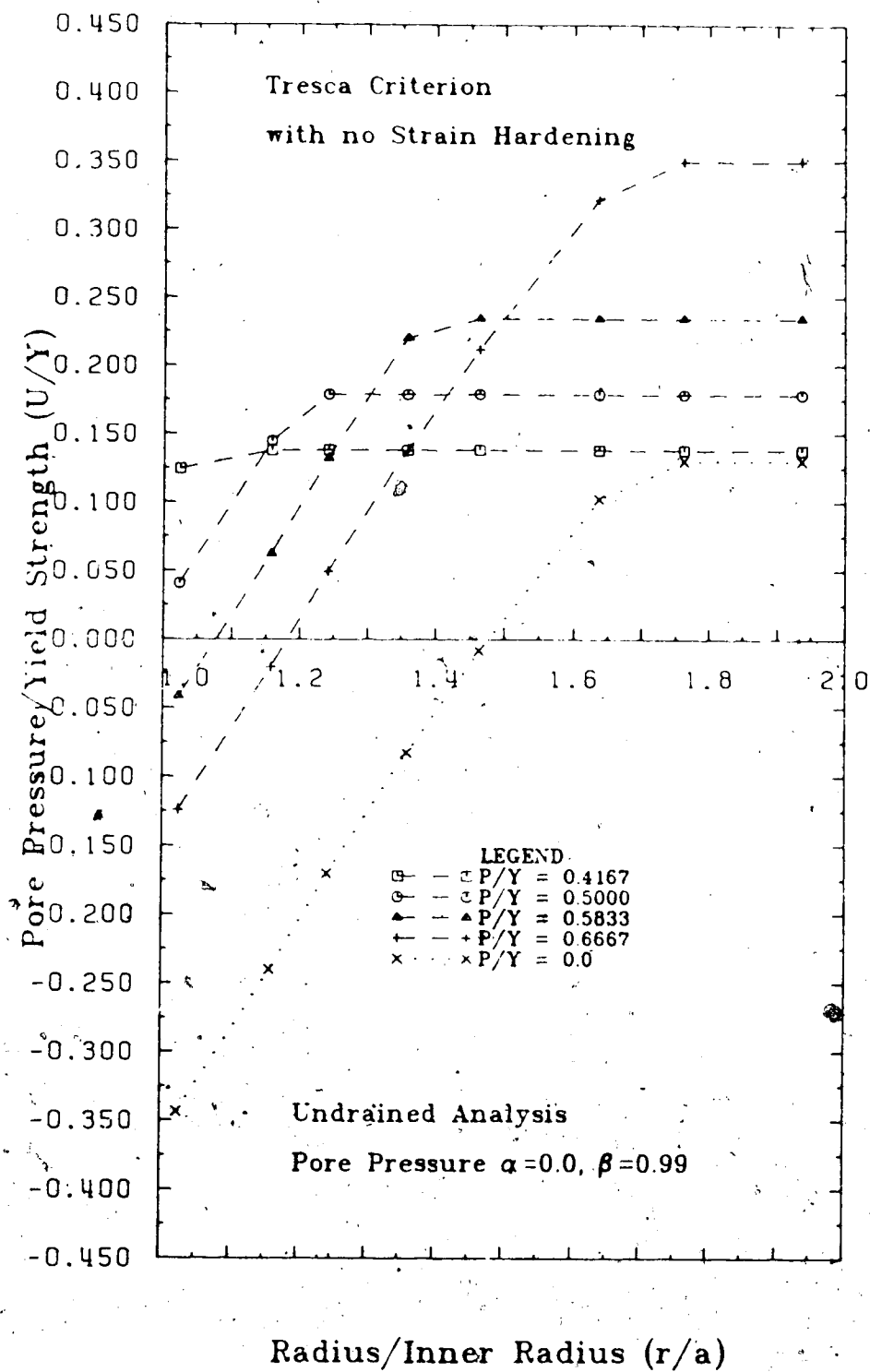


Figure 5.5: Pore Pressure Distribution

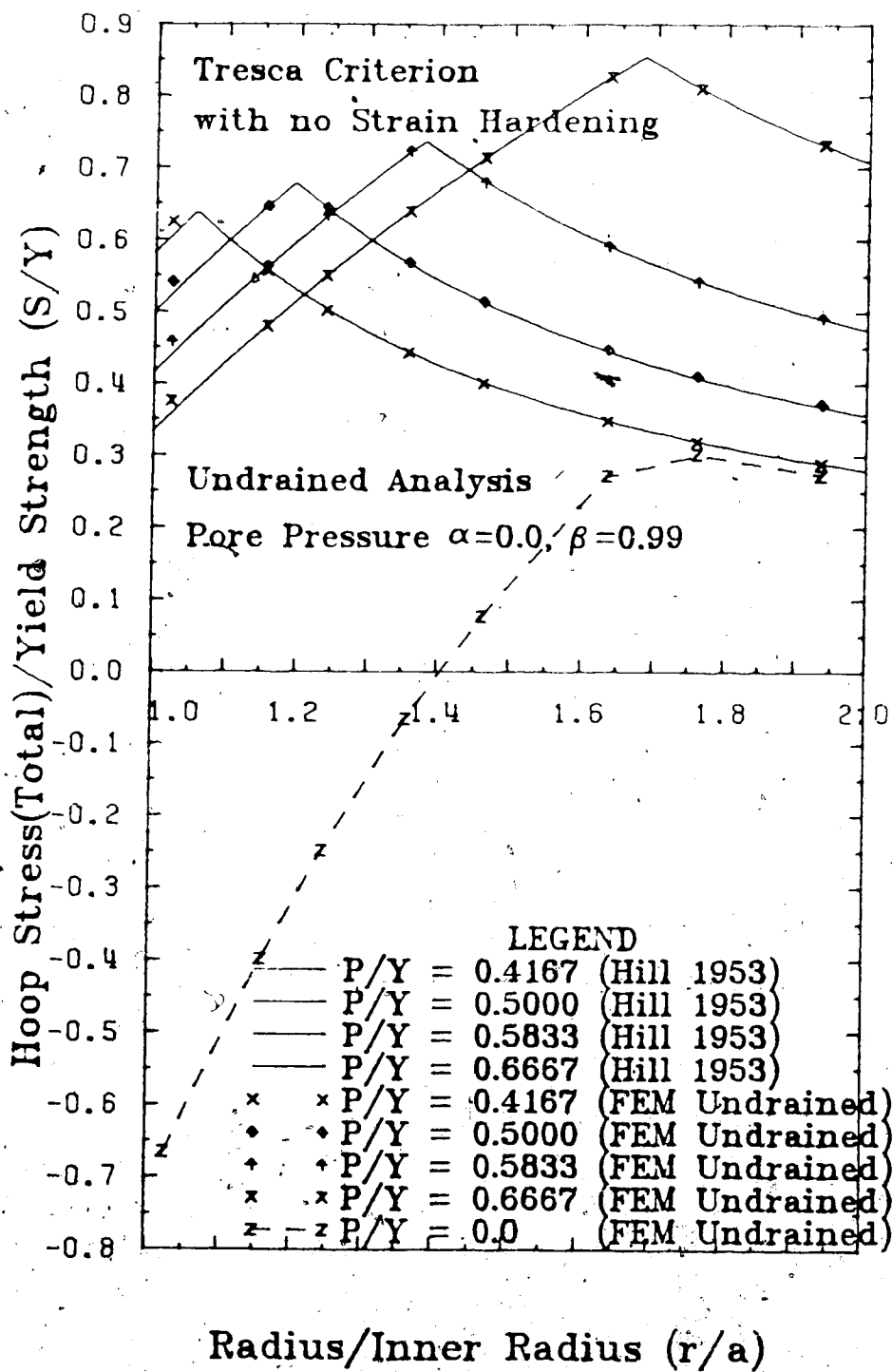


Figure 5.6: Hoop Stress (Total) Distribution.

drained and undrained analysis, the strains are different as would be expected from Figure 5.3

The pore pressure generated due to shearing is modelled using a non zero α value of 0.5. The results of the analysis are shown in Figure 5.7 and 5.8. It is seen in Figure 5.7 that the pore pressure is not very different from that for $\alpha = 0.0$. Since a positive α value is used, negative pore pressure (compression is negative) is generated due to shearing. This reduces the pore pressure inside the cylinder thus resulting in an increase in effective stress as shown in Figure 5.8. In reality the α parameter may be positive or negative and its values normally vary during the deformation of the soil. Therefore, the total pore pressure can be higher or lower than that due to hydrostatic pressure depending on the value of α . Varying the α value can be modelled by specifying the dependence of α as a function of strain using an algebraic expression or a piece-wise linear approach.

5.2.3 Undrained Analysis of Strain Softening Material

The strain softening model discussed in Chapter 2 is used here to study the effect of softening on the generation of pore pressure. The material parameters are the same as in Chapter 2 except that the material is under fully undrained conditions with $\alpha = 0.0$ and 0.5 and $\beta = 0.99$. The brittleness index in this case is equal to 0.25. A similar set of results using the strain softening model is shown in

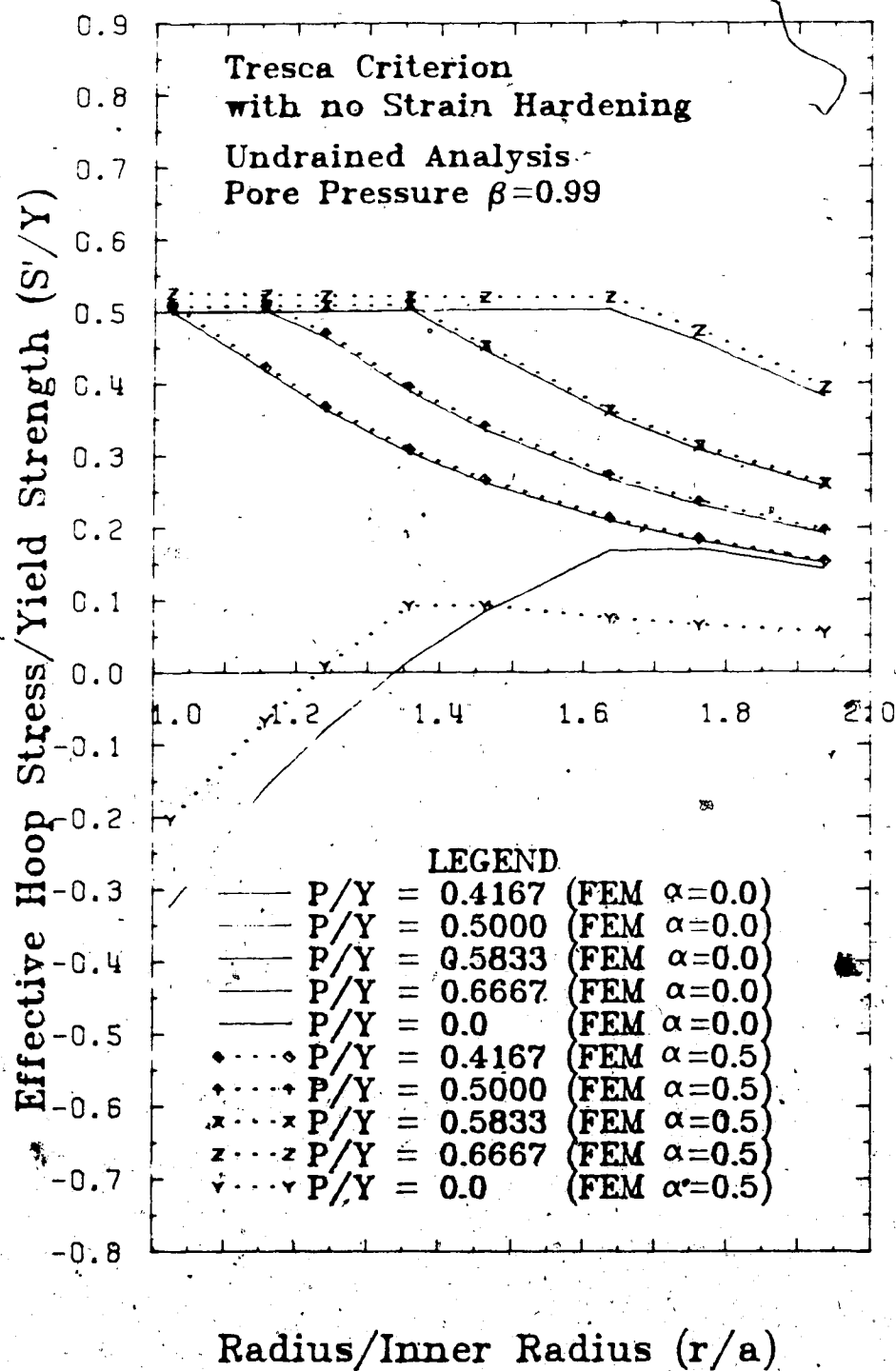


Figure 5.7: Hoop Stress Distribution

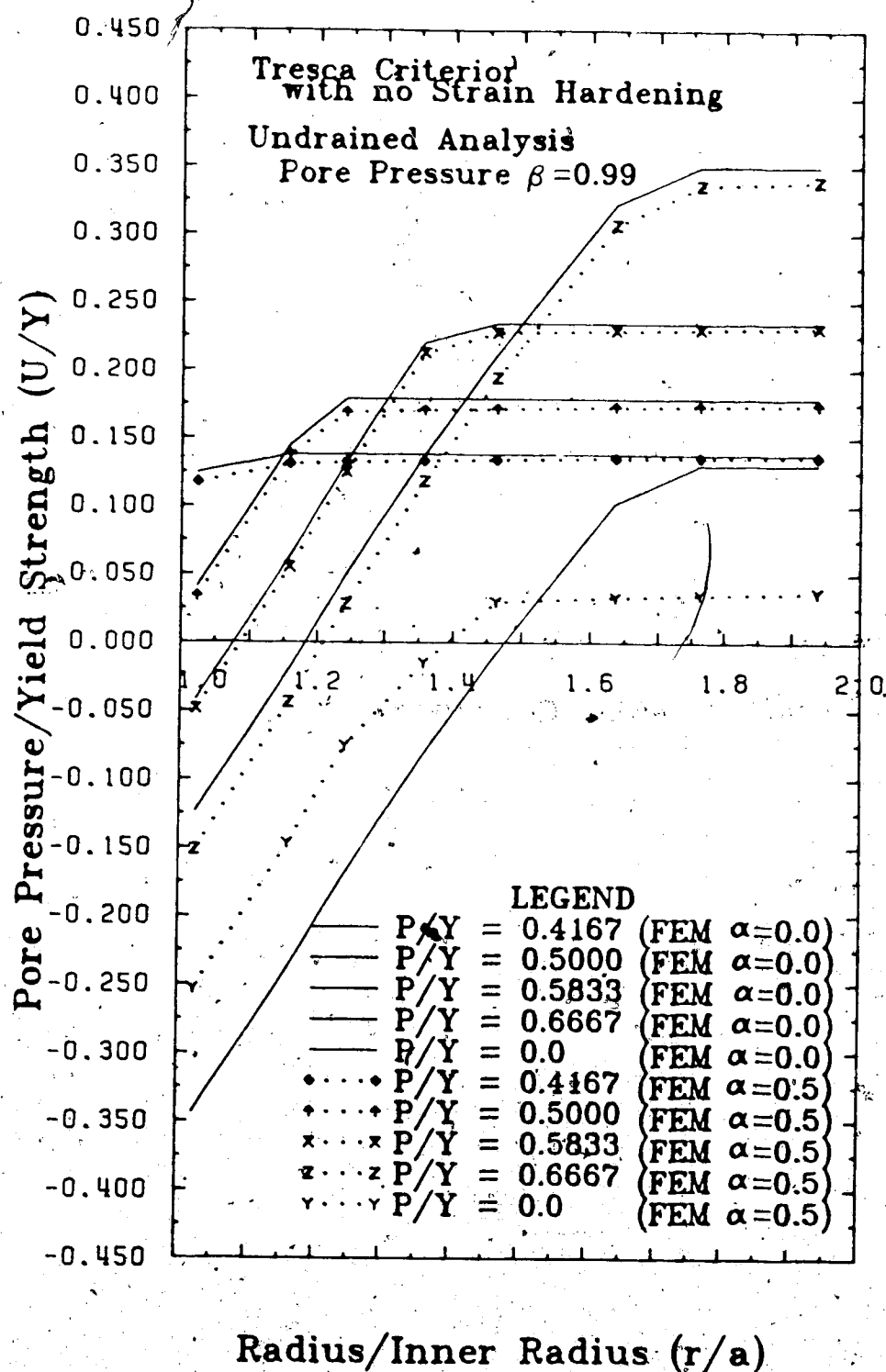


Figure 5.8: Pore Pressure Distribution

Figures 5.9 to 5.12. There is very little difference in response between the drained cases and undrained case because the material is almost incompressible ($\nu \approx 0.5$) non-frictional, non-dilating material. However, considerable pore pressure is generated and the effective stress is much lower than the total stresses as shown in Figure 5.10 to 5.12. Again there are noticeable but small differences in stresses and pore pressures for $\alpha = 0.0$ and $\alpha = 0.5$.

5.3 Bearing Capacity Analysis

In this section the bearing capacity and the load deformation response of a strip footing in a semi-infinite half space will be studied. Both the drained and undrained analysis in terms of total and effective stresses for frictional and frictionless material will be considered. The footing is assumed to be perfectly flexible and smooth so that the applied pressure is uniformly distributed over the entire area of the footing. The soil is assumed to be weightless and to behave in an elastic-perfectly plastic manner. Both the Tresca ($\phi=0$) and Mohr-Coulomb ($\phi \neq 0$) criteria will be used with associated flow rule. The objective here is to determine the ultimate load of the footing and to compare it with existing solutions and to study the propagation of the yield zone and deformation response during the loading history of the footing. The pore pressure during plastic deformation is also of interest.

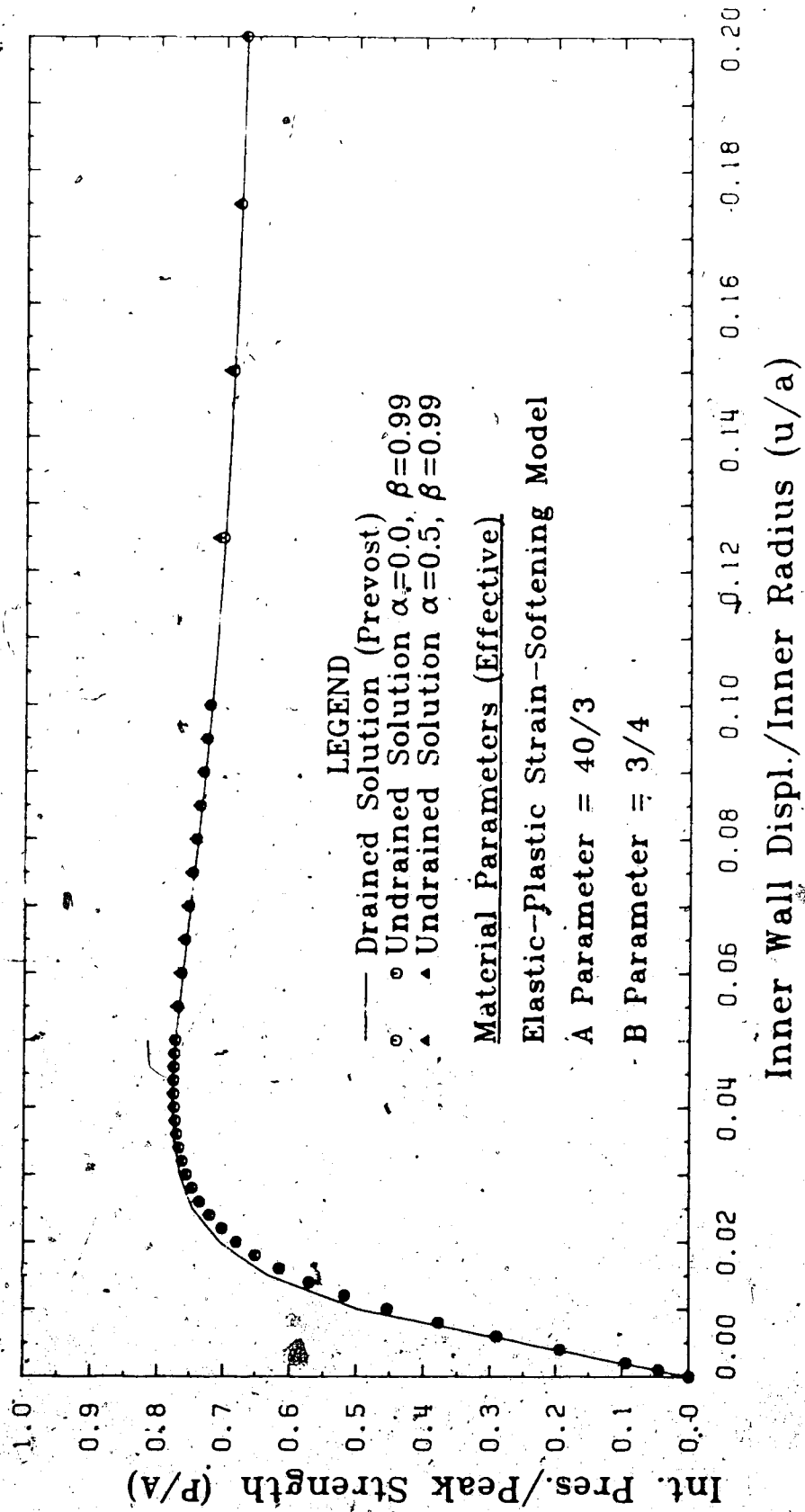


Figure 5.9: Pressure Displacement Response of Undrained Analysis

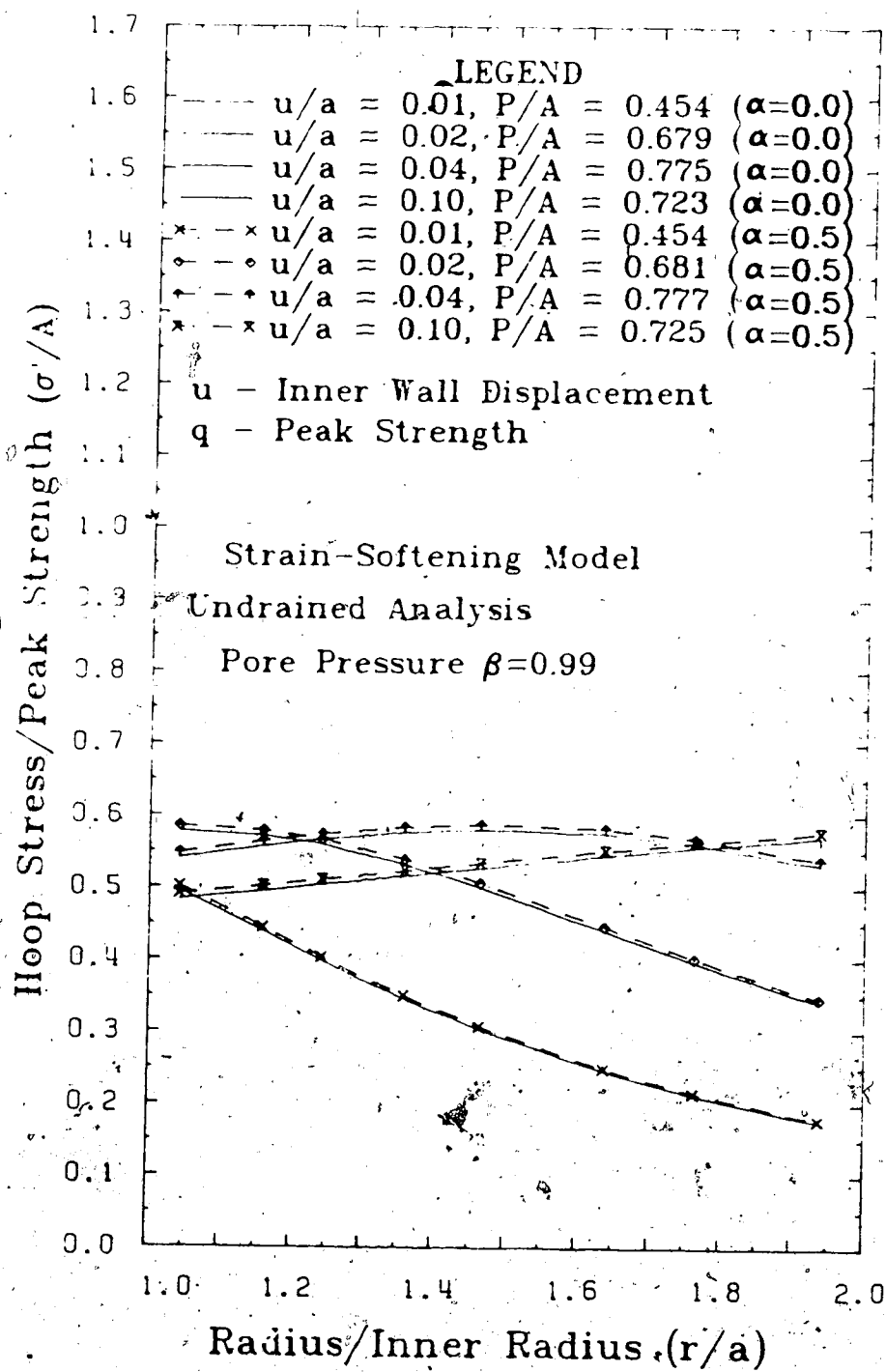


Figure 5.10: Hoop Stress(Effective) Distribution

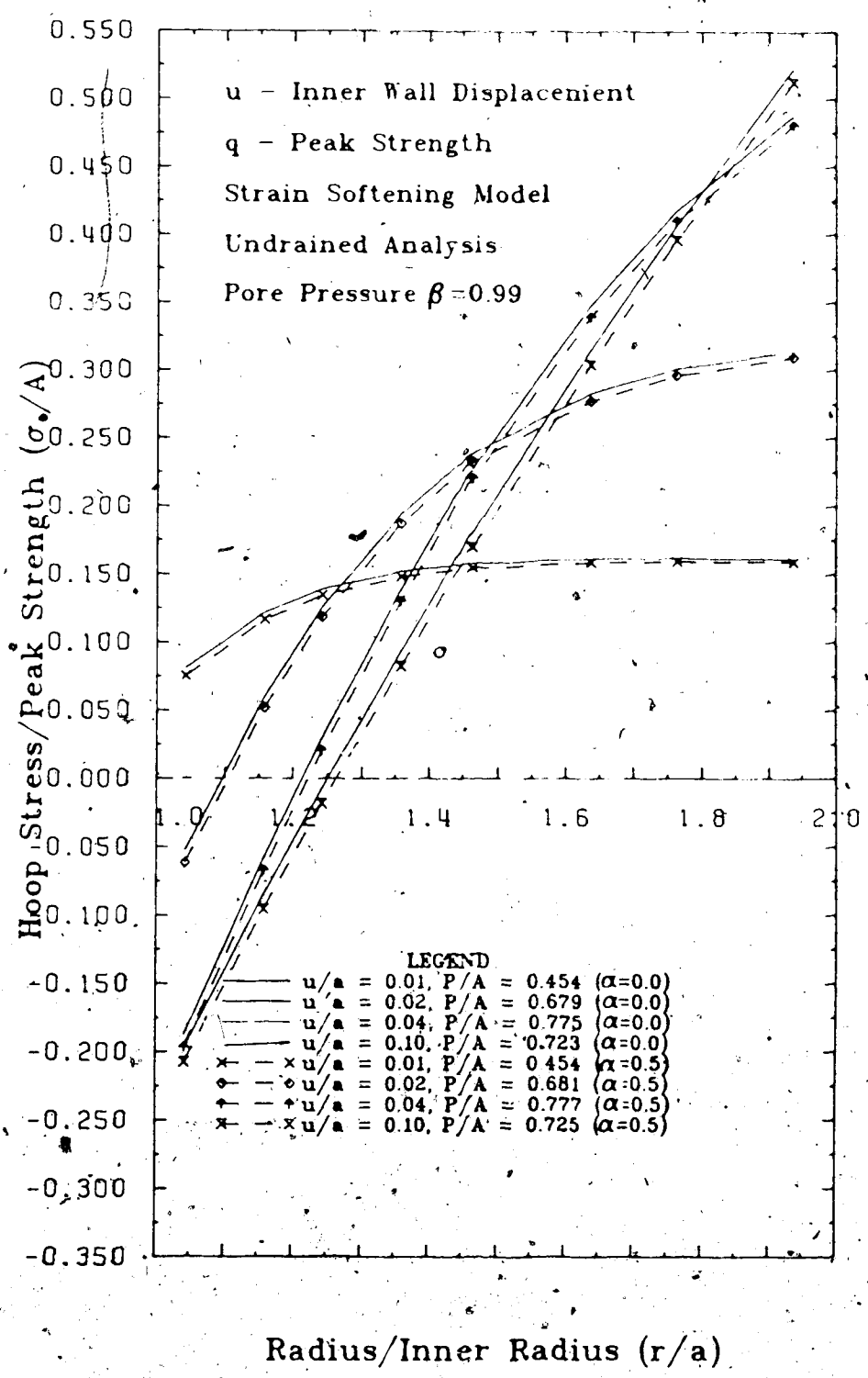


Figure 5.11: Pore Pressure Distribution

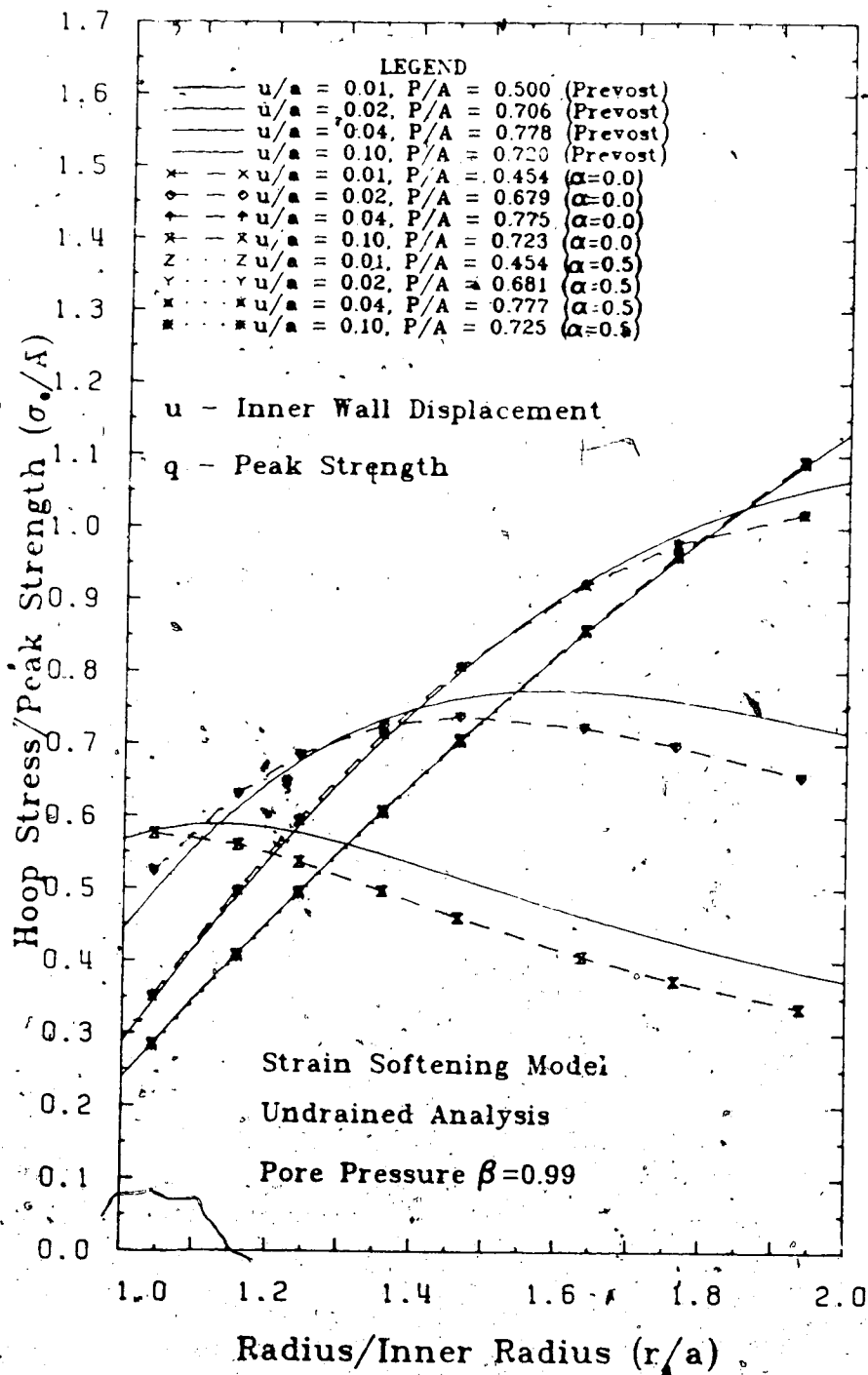
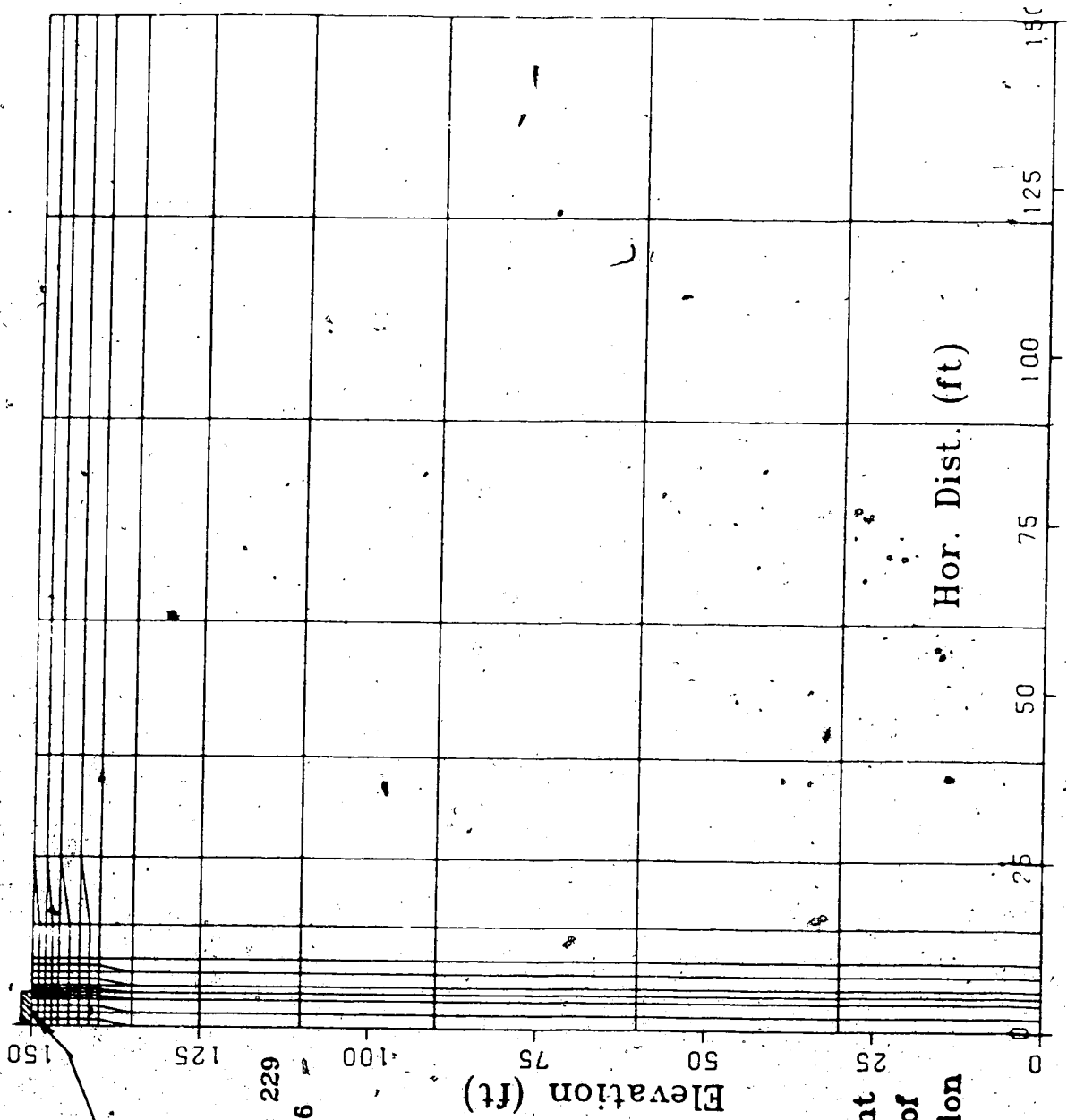


Figure 5.12: Hoop Stress(Total) Distribution

The elastic solution for a strip footing in a semi-infinite medium is given by Poulos and Davis (1974). It is known that the surface displacement under a strip footing in a semi-infinite elastic medium is infinite. Therefore, only relative displacement is meaningful in this case. In the case of a finite element model, since it is not possible to model a semi-infinite medium with the conventional isoparametric finite element formulation, the surface displacement will thus depend on the size of the foundation being considered. The stresses under the footing are finite for the case of a semi-infinite half space and in fact the maximum shear stress for the elastic case occurs on a circular arc with radius $B/2$ below the footing where B is the width of the footing (Poulos and Davis, 1974). Since it is not possible to have a semi-infinite foundation in the finite element model, it is important to ensure that the size of the foundation is large enough so that the results are not affected by the finite element boundaries.

One method of studying the boundary effect is to change the boundary conditions at the bottom of the finite element mesh and to observe any changes in response near the surface. If there is little change in response near the surface, then the effect of the boundary is not significant and the size of the foundation is considered to be acceptable.

The finite element mesh for this study is shown in Figure 5.13. Only half of the problem is analyzed due to



Total Number of Elements = 229
 Total Number of Nodes = 736

Figure 5.13: Finite Element
 Idealization of
 Soil Foundation

symmetry about the center line of footing. A plane strain condition is assumed. The width of the footing is assumed to be 10 feet and the depth and width of the foundation is taken to be 150 feet or 15B. The total number of elements and nodes in this mesh are 229 and 736 respectively. Eight node isoparametric rectangular and 6 node triangular elements with a 2x2 integration scheme were used.

The size of the foundation in this study is considerably larger than normally recommended by other researchers to minimize the boundary effect on the results near the surface. To ensure the boundaries are far enough away, a parametric study was conducted by varying the boundary condition at the bottom of the finite element mesh. By varying the depth of the foundation and changing the bottom boundary from a fixed boundary (no slip boundary) to a frictionless boundary, the change in displacement at the surface can be observed. If the bottom boundary is indeed far enough away, then a change from fixed to free boundary will not affect the surface displacement at any considerable extent. The results of the analyses are shown in Figure 5.14. It is seen that there is practically no change in center line displacement at a depth/footing width ratio 15. Therefore, the depth of the foundation is taken to be 150 feet.

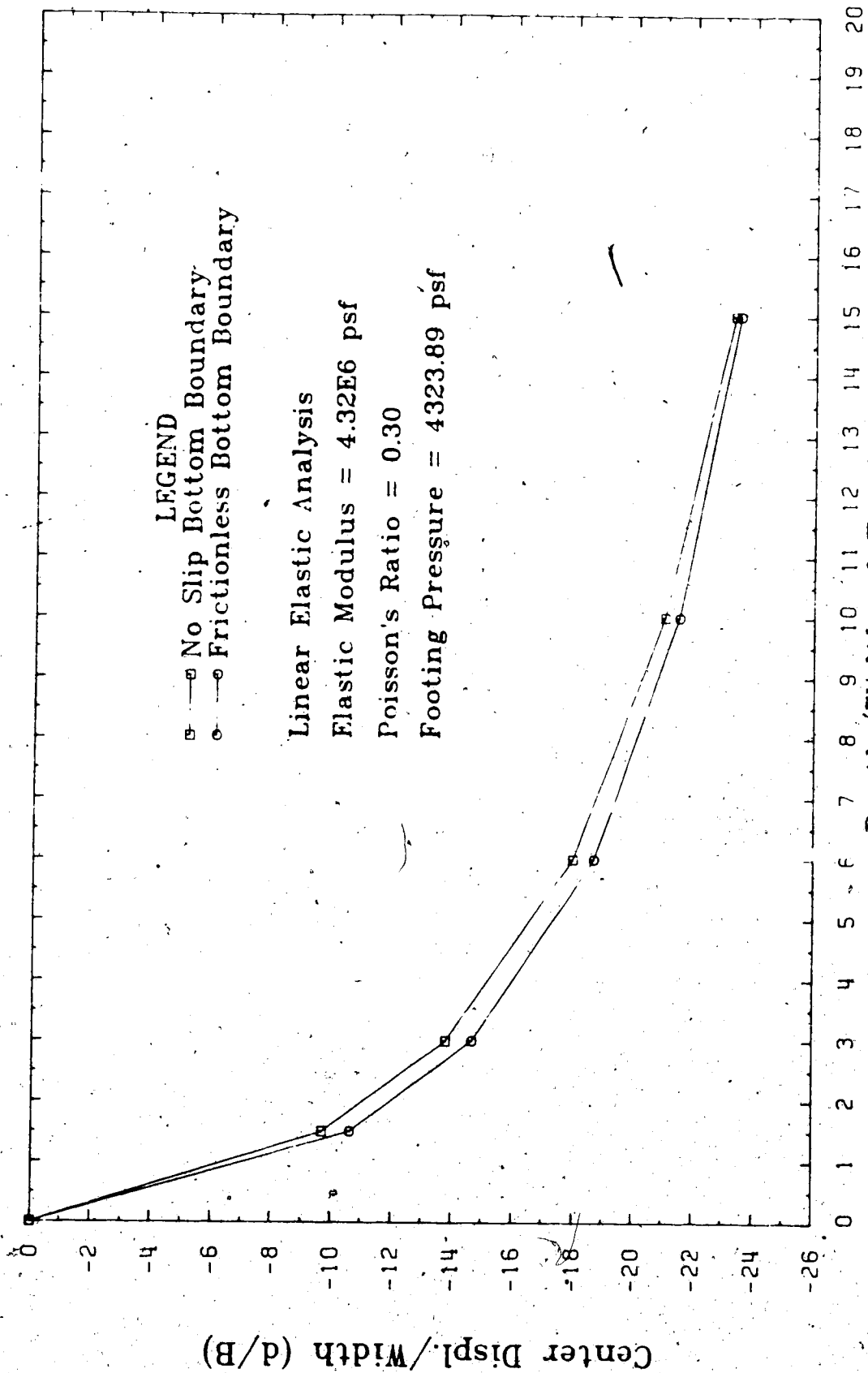


Figure 5.14: Displacement vs Depth of Foundation

5.3.1 Bearing Capacity of $\phi = 0$ Material

The ultimate load of a flexible footing in a rigid plastic half space is given by:

$$\text{First yield: } q = \pi C_u, \quad (5.19a)$$

$$\text{Ultimate load: } q = (\pi+2)C_u. \quad (5.19b)$$

where q is the applied footing pressure
and C_u is the undrained shear strength.

The result of the finite element analysis is shown in Figure 5.15. The predicted ultimate load lies between $5.14C_u$ and $5.18C_u$ compared with the exact solution of $(\pi+2)C_u$ (or $5.1416C_u$). Convergence rate of the solution process is quite rapid as indicated in Figure 5.15 except when the applied pressure is close to the ultimate pressure. A smaller load increment was used to obtain more stable convergence when approaching the limit load. The stiffness matrix of the elements were updated at every iteration except for the case of a footing pressure of $3.8C_u$. It is found that not only is the convergence rate slower if the matrix is not updated at every iteration, but also that the convergence characteristic is less stable especially near the limit load. A very high elastic modulus and Poisson's ratio are used to minimize the elastic deformation in simulating the rigid plastic behaviour of the material. The amount of displacement at the surface is dependent upon the size of

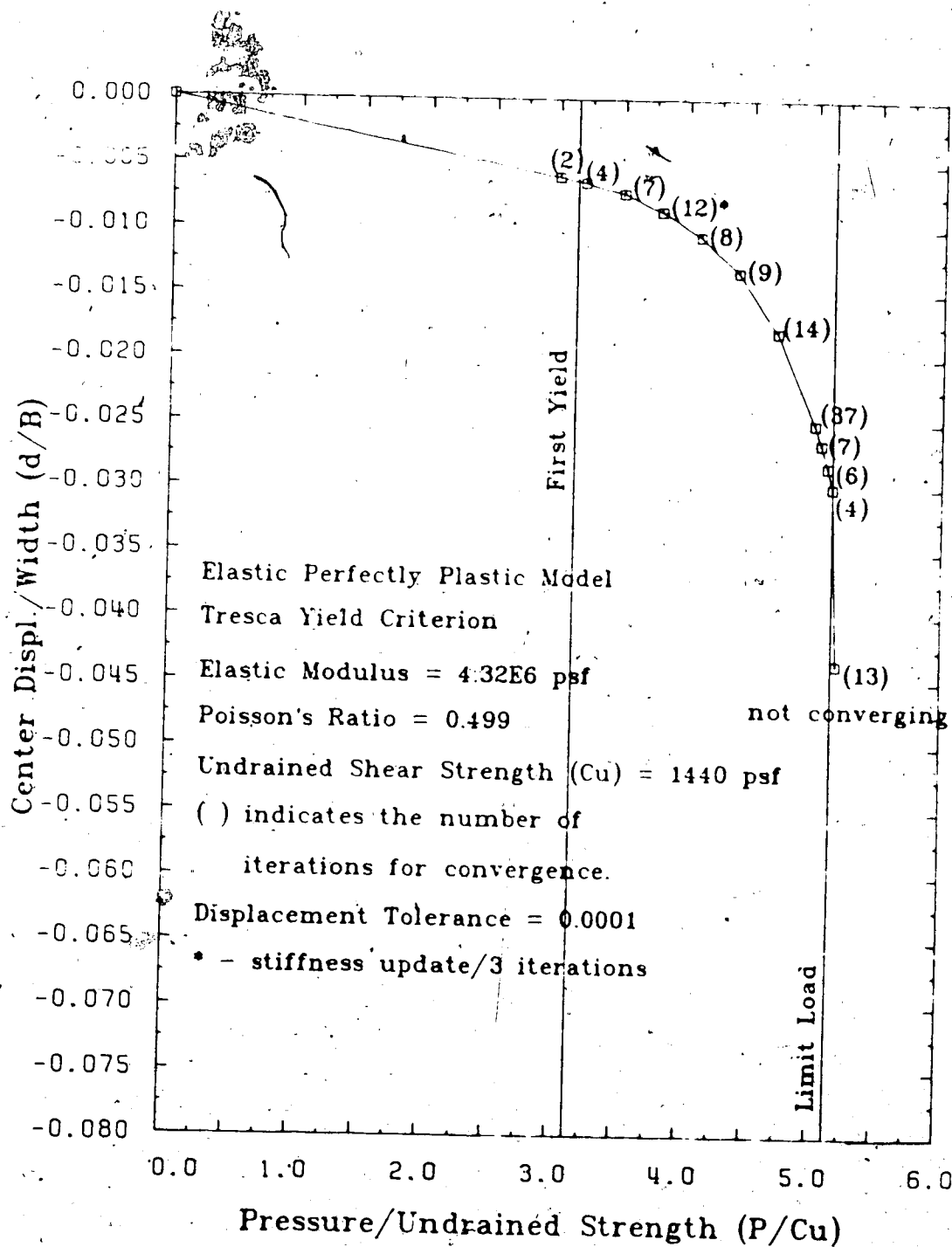


Figure 5.15: Pressure Displacement Response of Footing

the foundation as discussed earlier and no comparison of results is made here.

Figure 5.16 shows the development of the yield zone throughout the loading history of the footing. The yielding zone is initiated at the edge of the footing at about $3C_u$. The dots in Figure 5.16 indicate yielding has occurred at that particular integration point of the element. The exact pressure for initial yielding to occur is πC_u or $3.1416C_u$. The finite element result has slightly underpredicted this value. The initiation of the yielding zone occurs at the edge of the footing due to the high stress concentration at this location. At a footing pressure of $3.2C_u$, a semi-circular yield zone is developed which corresponds to the location of maximum shear stress from the elastic solution. The yielding zone starts propagating downward to a depth of $2B$ and expands laterally between depths of $0.5B$ and $1.5B$. The increase in spacing among the dots with depth in Figure 5.16 is due to the increase in the size of the elements. Therefore the region between the dots has also yielded. A very large yielding zone of depth $2B$ and width $3B$ has developed when the applied pressure is close to the ultimate pressure. However, the yielding zone for a footing pressure of $5.14C_u$ is contained by the surrounding soil which is still elastic. Therefore, the footing will not fail unless a collapse mechanism is formed. At an applied pressure of $5.18C_u$, the soil adjacent to the footing has yielded and the yielding zone becomes unconfined. This

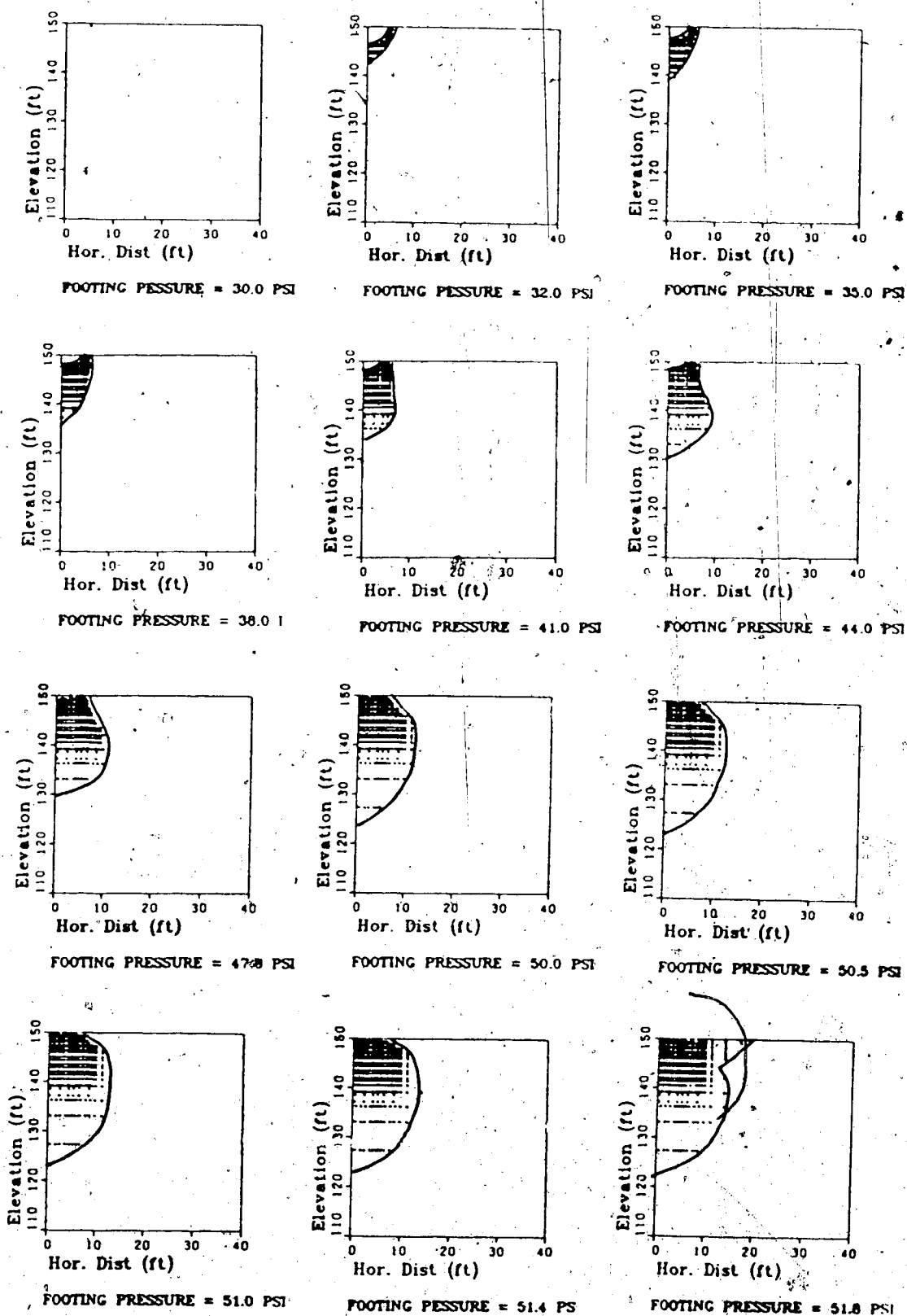


Figure 5.16: Development of Yield Zone under a Footing

results in a collapse mechanism. Note that the adjacent soil formed a triangular yield zone and shear at an angle of approximately 45° with respect to the horizontal. This is similar to the failure mechanism postulated by Terzaghi and other authors in determining the limit load for a footing.

5.3.2 Bearing Capacity of Frictional Material

Zienkiewicz (1975) published results of an analysis of a footing for cohesive frictional material using an elasto-plastic finite element formulation. Simmons (1981) also conducted similar studies and obtained very similar results for the limit load of the footing. However, there is a considerable difference in the development of the yield zone under the footing in these two cases. In both cases, the yield zones extended to the bottom boundary of the foundation, therefore, the yield zone may be affected by the boundary conditions being imposed. The bearing capacity problem is re-analyzed here with a much larger mesh to study the development of the yielding zone.

The elastic perfectly plastic model is used in this analysis with Mohr-Coulomb yield criterion. An associated flow rule is used with friction angle of $\phi = 20^\circ$. An elastic modulus of 300,000 psi and a Poisson's ratio of 0.30 are assumed. The finite element mesh used in the previous example is used here.

The collapse loads for this problem have been given by Prandtl and Terzaghi as 143 and 175 psi respectively. Cox

(1973) also calculated the collapse load to be 151 psi. The result of the finite element analysis is shown in Figure (5.17). It is noted that failure is more abrupt than the case of frictionless material. Similar behaviour is also obtained by Zienkiewicz (1975) which is in good agreement with the present analysis. The magnitude of displacement cannot be compared due to the difference in the size of the finite element mesh.

The development of the yield zone in the soil is shown in Figure 5.18. The yield zone is considerably deeper and more extensive than the case of the frictionless material. The yield zone is in the shape of a bulb and collapse occurs when yielding has extended to the ground surface with the development of a triangular yielding zone adjacent to the footing. The angle of the failure planes in the triangular region should be equal to $45 - \phi/2$ from slip line field solution which is equal to 35° for $\phi = 20^\circ$. It is seen that the angle of the triangular yield zone is smaller in this case than in the previous case but it is difficult to conclude that this angle is indeed 35° . Also the shape of the yielding zone is different from the result published by Zienkiewicz and Simmons. 0

The above analysis employed a 3×3 integration scheme rather than 2×2 integration scheme which was used in the previous example. A 2×2 integration scheme was used initially but the convergence characteristic was very unstable. The unstable behaviour may be due to the presence

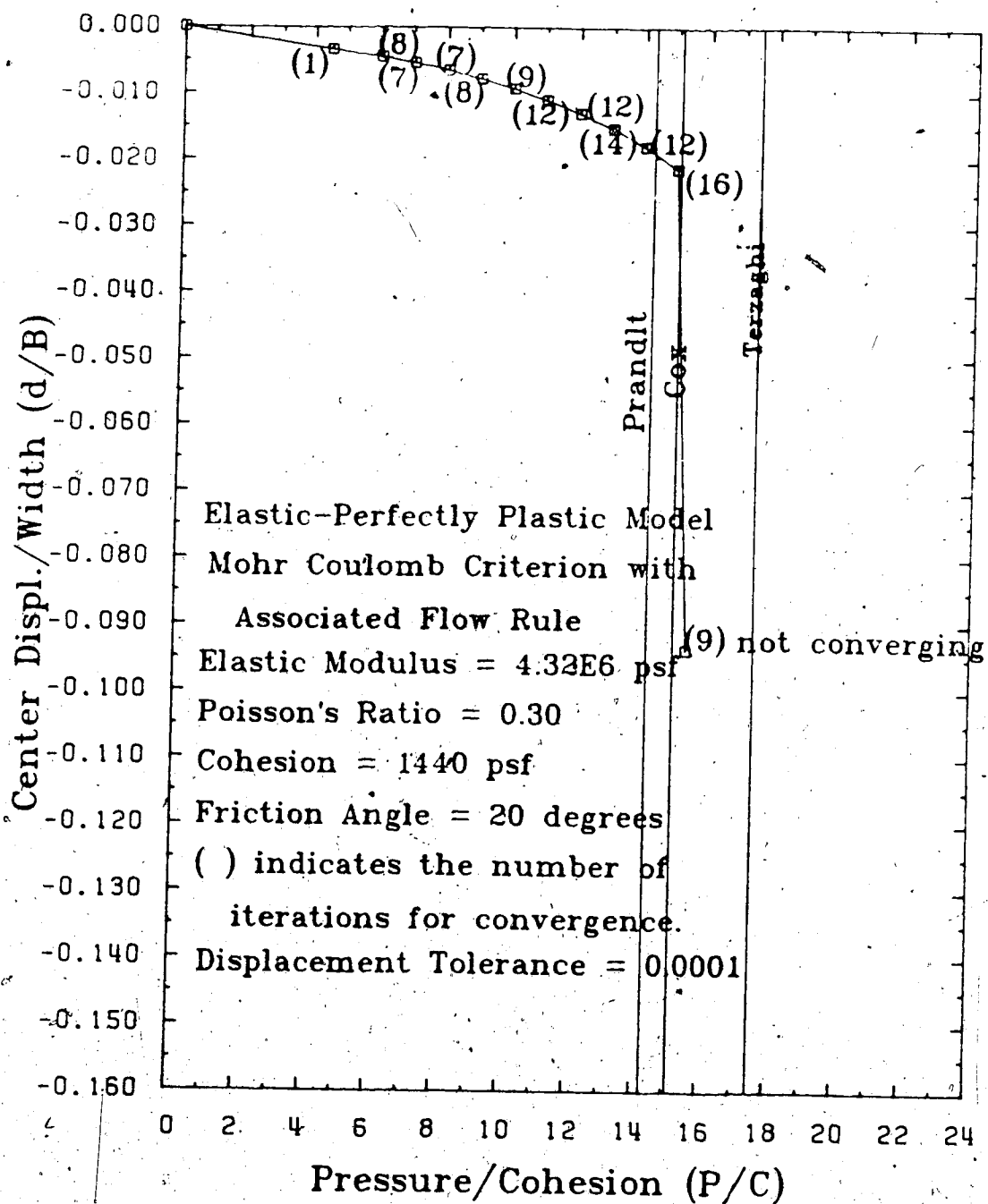


Figure 5.17: Pressure Displacement Response of Footing

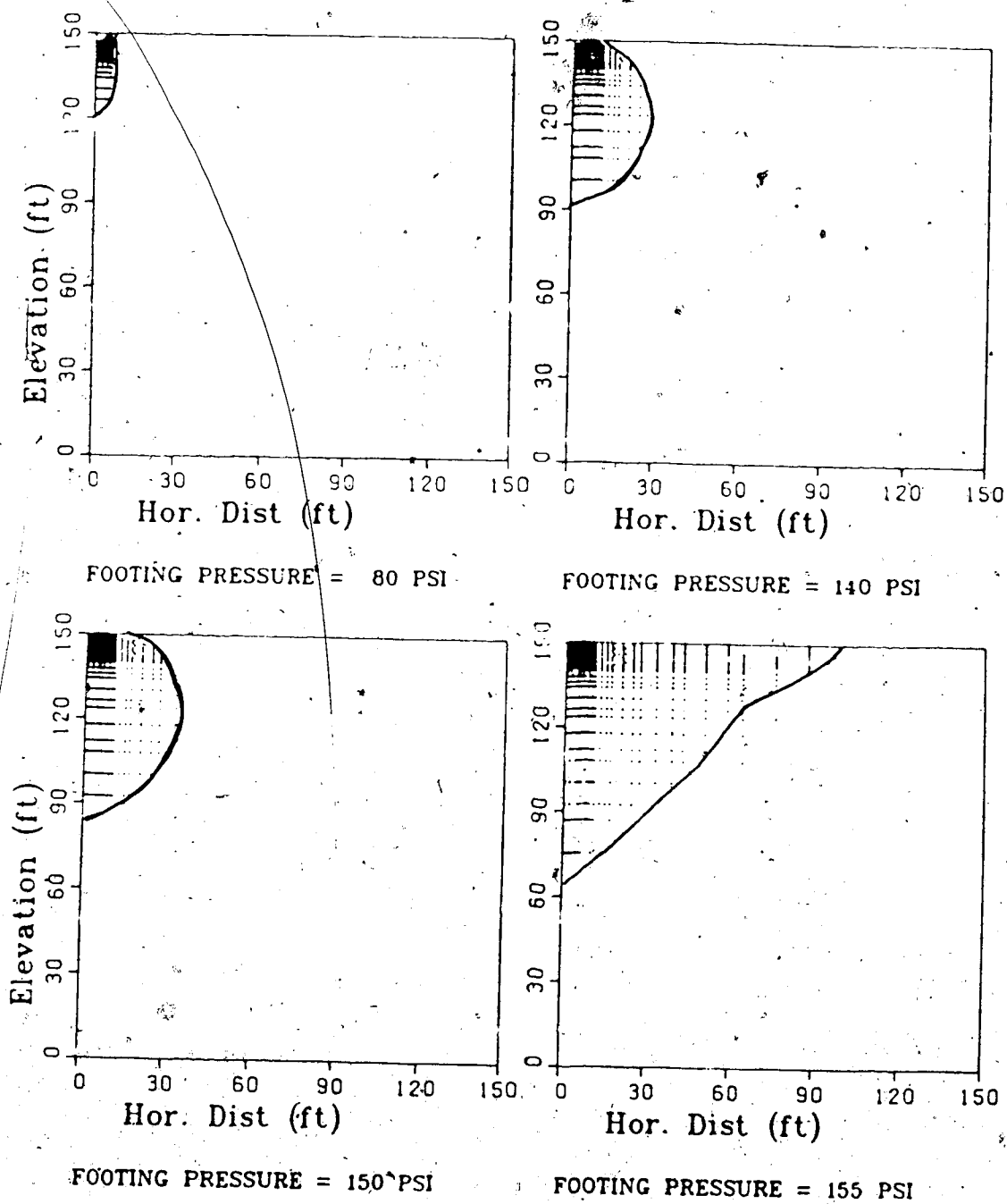


Figure 5.18: Yield Zone Development of Footing

of spurious energy modes in this case since the material is compressible both elastically and plastically. A very stable and rapid convergence rate is obtained when the 3x3 integration scheme is used as illustrated in Figure 5.17.

5.3.3 Effective Stress Undrained Analysis

An undrained analysis is performed to study the effect of pore pressure on the footing pressure and the propagation of the yield zone. The Mohr Coulomb yield criterion is used and the effective stress parameters are the same as in the previous case. The soil is assumed to be fully saturated with $\beta = 0.99$ and $\alpha = 0.0$.

In the undrained analysis, the stiffness matrix of the element is unsymmetric and the global stiffness matrix for this problem requires 389,056 storage locations and with double precision arithmetic, the in-core storage exceeds 1.5 megabytes. This amount of storage exceeds the maximum amount available on the Amdahl computer at the University of Alberta and therefore the analysis is performed using the super computer, Cyber 205, recently installed at the University of Calgary.

Before performing non-linear elasto-plastic analysis, a linear elastic analysis was first carried out to study the generation of pore pressure under the footing due to different values of the pore pressure β parameter. The pore pressure parameter β was varied from 0.99 to 0.0 to study the effect on footing settlement. The pore pressure

parameter α was assigned to be zero. The strip footing is assumed to be perfectly flexible as in the previous analysis and the applied footing pressure was kept constant at 45 psi. The result of the analysis is shown in Figure 5.19. The footing displacement increases with decreasing value of β since the material becomes more compressible as β decreases. The difference in displacement for a fully saturated soil with $\beta = 1$ and a perfectly dry soil with $\beta = 0$ is as much as 70 %. The pore pressure contours at different β values are shown in Figure 5.20. Very high pore pressure is developed just underneath the footing. The stress condition in this region is basically isotropic and the pore pressure being developed is close to the footing pressure. Therefore one would expect the effective stress to be very low. The variation of pore pressure is very rapid near the edge of the footing and a pressure bulb is developed similar to the stress contour underneath the footing discussed earlier. The pore pressure decreases to about 15% of the footing pressure (about 1000 psf) at a depth of about twice the width of the footing. As the value of β decreases to 0.5, the pore pressure generated is considerably less. The 15% contour extends to a depth of 80% of the width of the footing. At a β value of 0.2 the 15% contour only extends to a depth of 10% of the width. Very small pore pressure is developed in this case.

The result for this analysis was performed using a 2x2 integration scheme. Initially a 3x3 integration scheme was

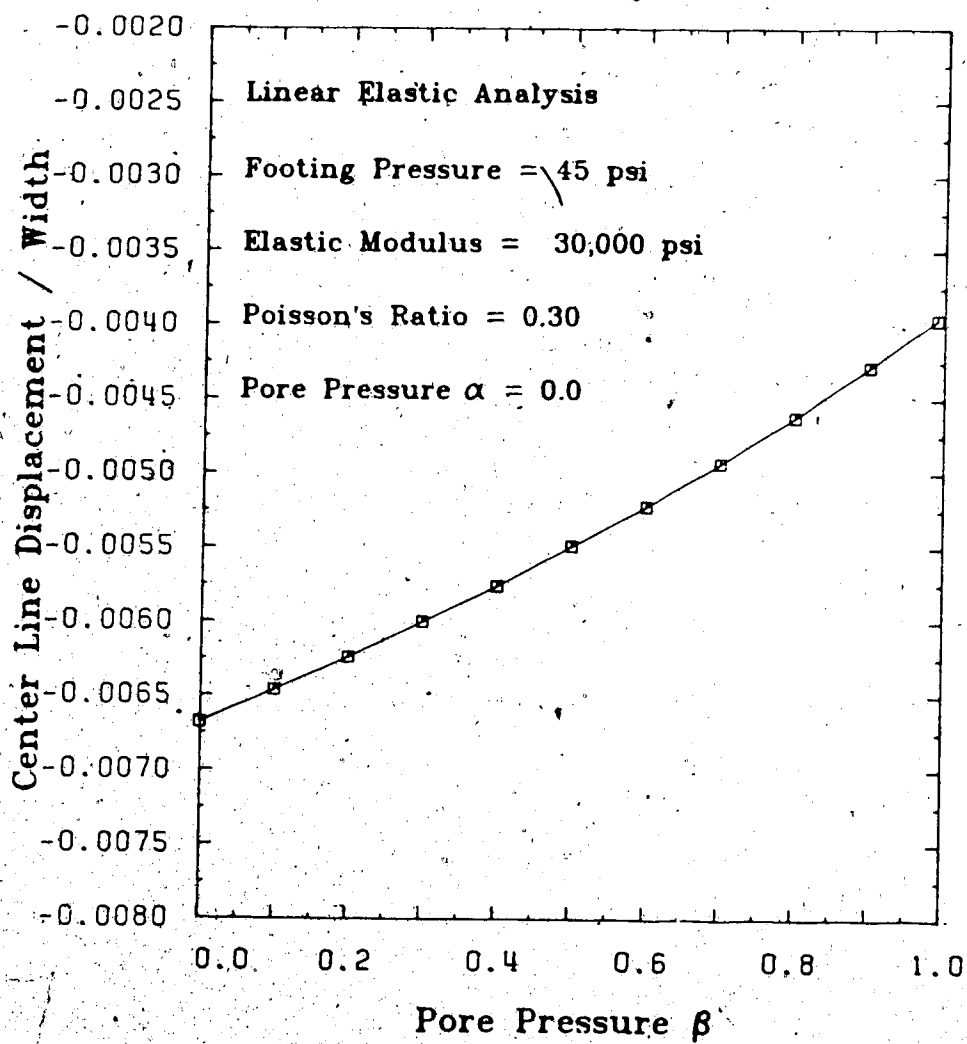
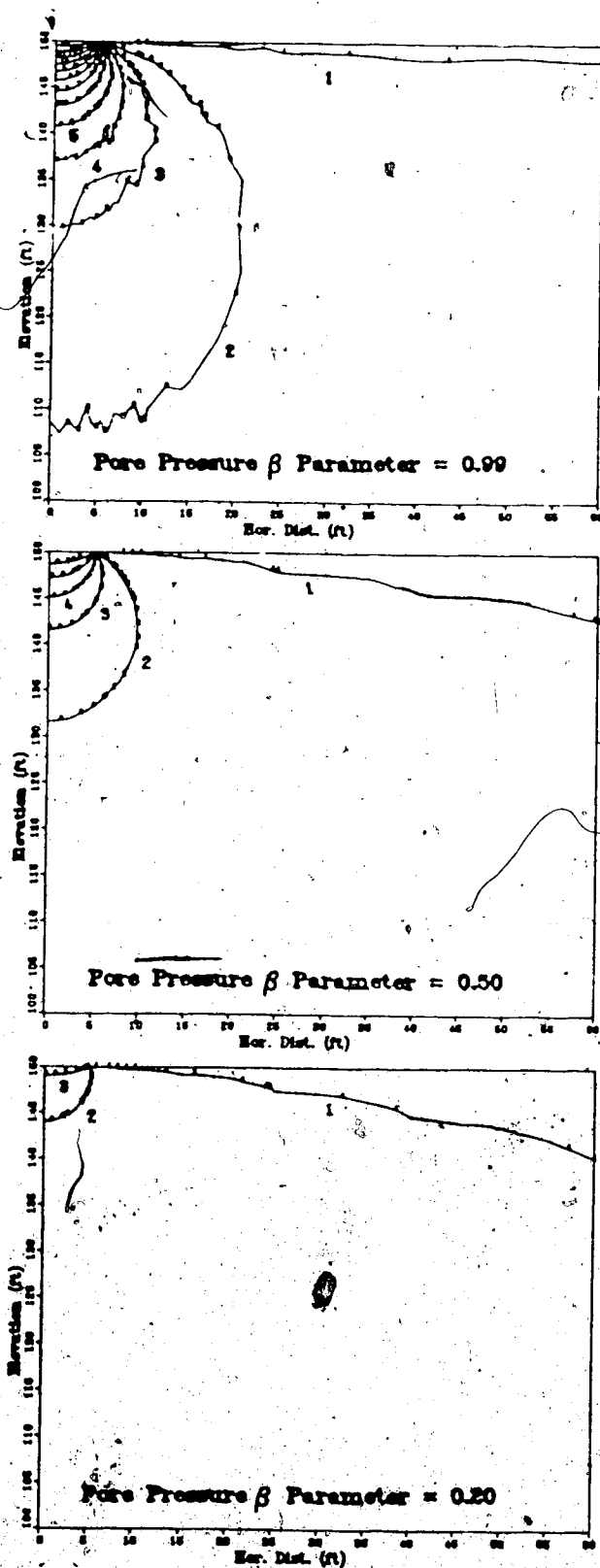


Figure 5.19: Center Line Displacement vs Pore Pressure β



LEGEND

- 1 - 0.000
- 2 - -500.000
- 3 - -1000.000
- 4 - -1500.000
- 5 - -2000.000
- 6 - -2500.000
- 7 - -3000.000
- 8 - -3500.000
- 9 - -4000.000
- 10 - -4500.000
- 11 - -5000.000
- 12 - -5500.000
- 13 - -6000.000

Figure 5.20: Pore Pressure Contour - Linear Elastic Analysis

used but the variation of pore pressure is very erratic for $\beta = 0.99$. This is due to the fact that the element is almost incompressible and therefore the 3x3 integration scheme will result in element locking. This effect was discussed earlier for material with Poisson's ratio close to 0.5.

The result of the non-linear elasto plastic analysis is shown in Figure 5.21. Initial yielding occurs at a footing pressure around 30 psi which is much less than the yielding pressure in the fully drained case of over 45 psi. The initial yielding pressure is close to that for the frictionless material of 31.14 psi. The center line displacement under the footing varies nonlinearly with the increment of footing pressure and the convergence of the problem becomes very sensitive to the size of the increment of the footing pressure. Figure 5.21 shows that a very small load step was used to obtain stable convergence. Although it seems that a larger load step was applied towards the limit load of 5 C, the load increment at this stage was divided into many sub-increments in order to obtain a solution. A total of 71 load increments was applied with an average of 5 iterations per load increment in order to obtain stable convergence characteristics. The number of iterations increases drastically towards the limit load. The extent of the yielding zone under the footing is shown in Figure 5.22. An initial semi-circular yielding zone is formed similar to the case of frictionless material. The yield zone subsequently extends to a depth of about 2.5 B before

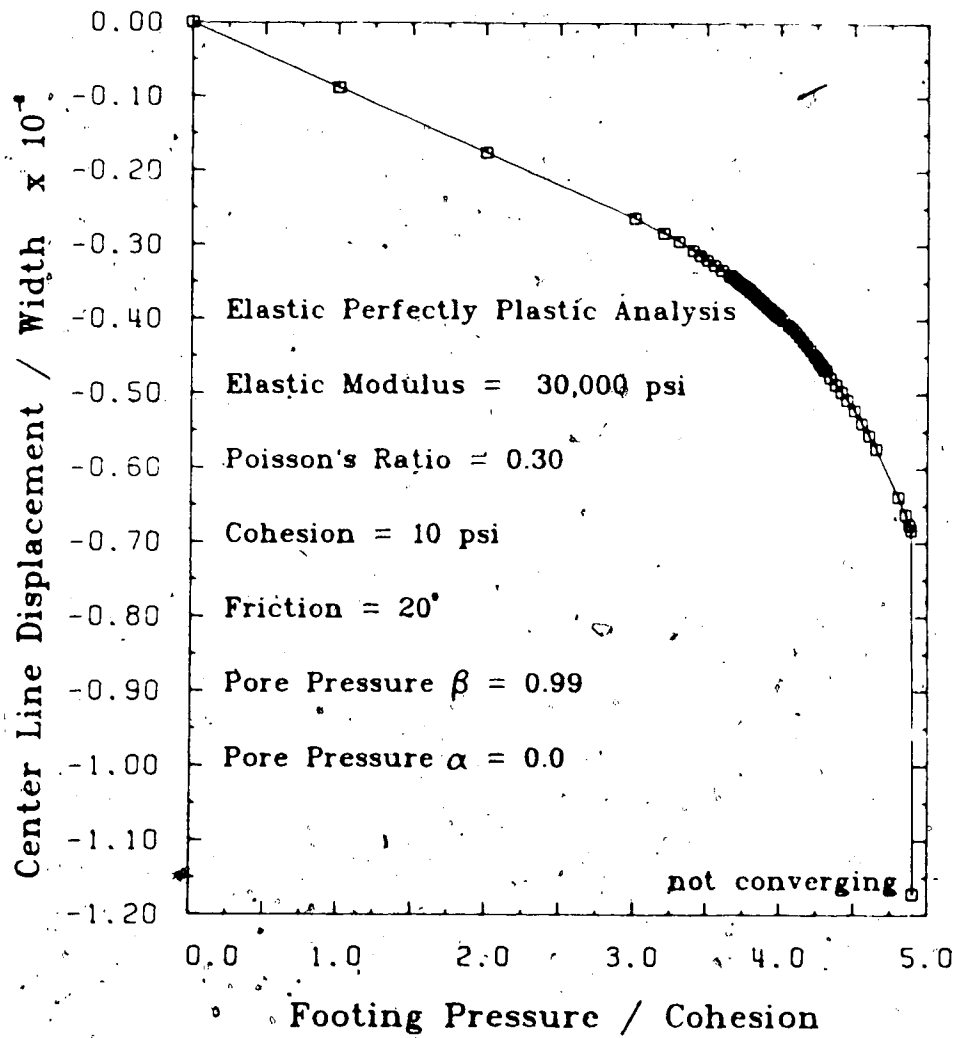
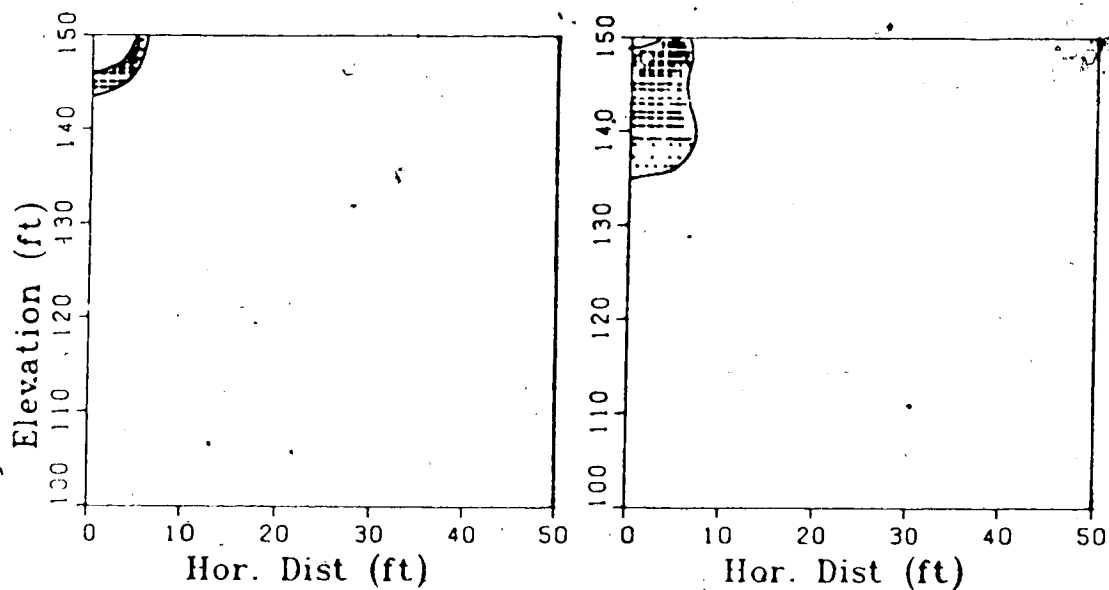
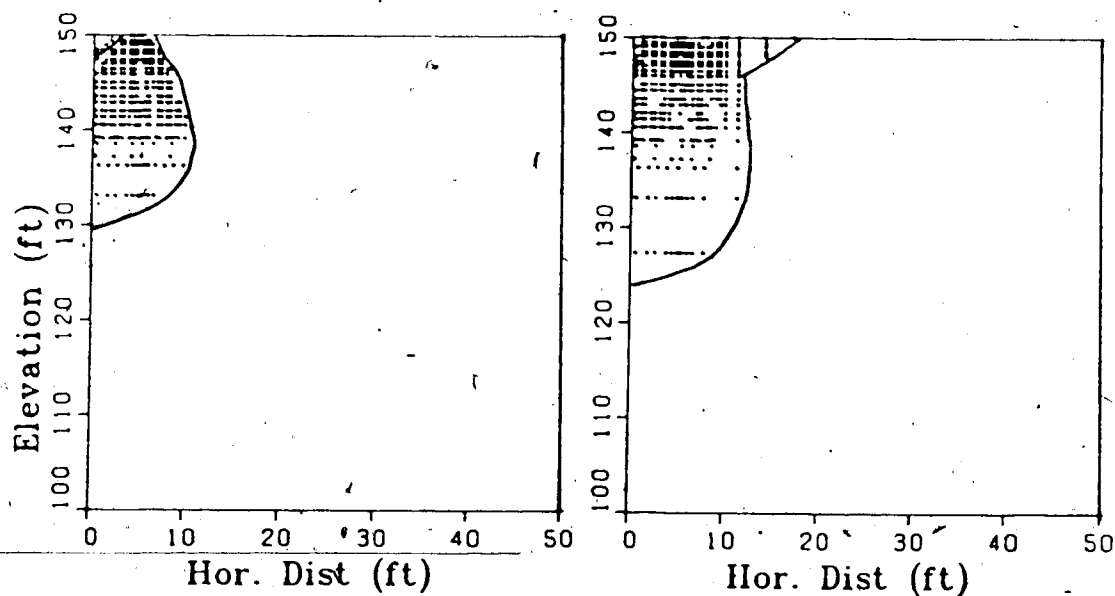


Figure 5.21: Center Line Displacement vs Footing Pressure



Footing Pressure = 30 psi Footing Pressure = 39.5 psi



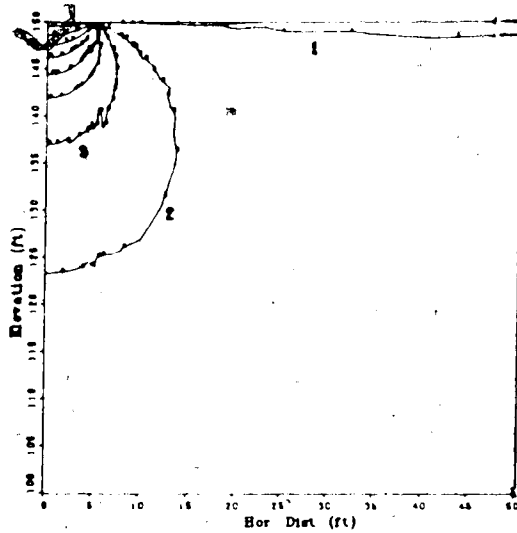
Footing Pressure = 45 psi Footing Pressure = 48.875 psi

Figure 5.22: Yield Zone Development of Undrained Analysis

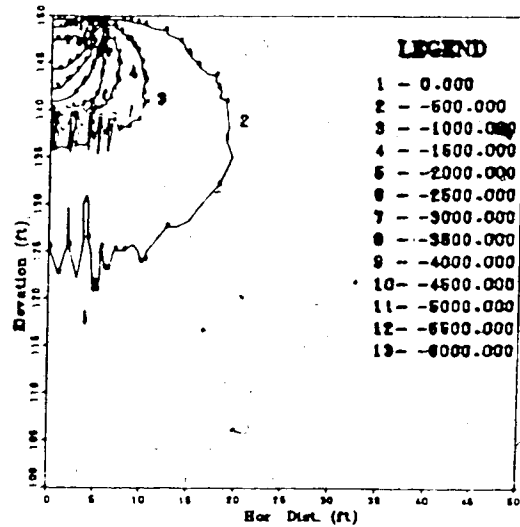
collapse finally occurred. The extent of the yield zone is much less than that of the fully drained case for the frictional material and very similar to that of the frictionless material. At the collapse load, a yielding zone of the shape of a triangular wedge is formed adjacent to the footing but it is difficult to conclude that the failure plane of this triangular zone is at 45° .

The pore pressure distribution under the footing is shown in Figure 5.23. Initially a semi circular pore pressure contour is formed with decreasing values away from the footing similar to the elastic case. When yielding has propagated to about $1 \frac{1}{2}$ times the width of the footing, the shape of the contours is affected by the extent of the yielding zone and the shape and size of the elements being used in that region. Triangular elements and larger rectangular elements are used in this region which may explain the rapid variation of the contours in this region.

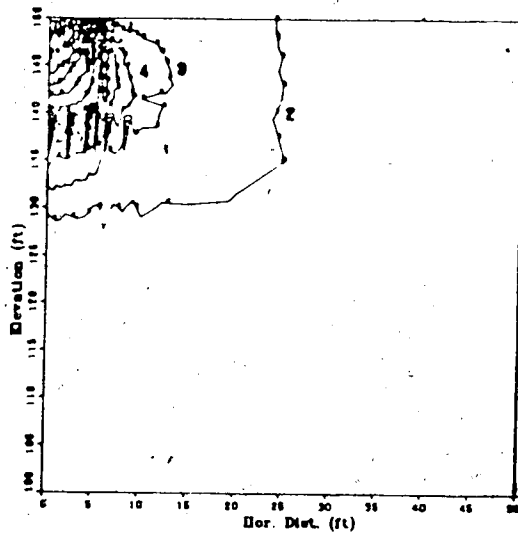
The above analysis shows that a very high pore pressure is developed under a footing for a fully saturated soil. Also the limit load of the footing is much less than that in the fully drained case. In fact the limit load is very close to that of the frictionless material of $5.14 C$. Since the frictional component of the shear strength is not mobilized due to the generation of the pore pressure, the material actually behaves as a purely cohesive material with cohesion C' . Therefore the limit load should be equal to $(\pi + 2) C'$.



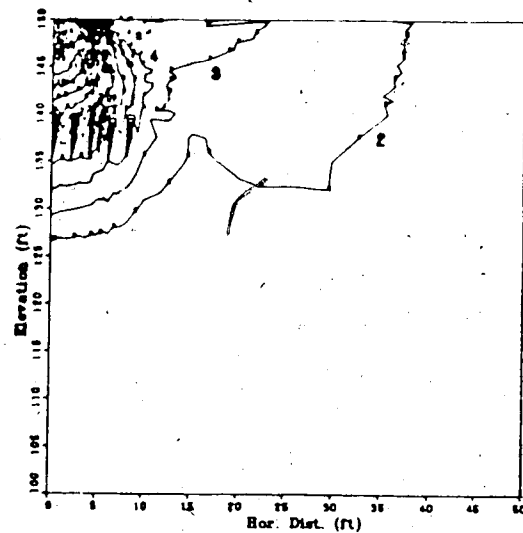
Footing Pressure = 30 psi



Footing Pressure = 39.5 psi



Footing Pressure = 45 psi



Footing Pressure = 48.875 psi

Figure 5.23: Pore Pressure Contours of Plastic Analysis

5.3.4 Cost of the Finite Element Analysis

Due to the large number of nodes and elements being used in this analysis, considerable computer resources were used to obtain one set of results. The CPU time required to obtain a set of results with 10-12 steps was longer than an hour on the Amdahl 470 computer. Double precision arithmetic was used in all of these analyses because single precision arithmetic does not give sufficient accuracy for non-linear problems. By using the skyline technique, the amount of storage space for the global stiffness has been reduced from 204,900 to 97,947 storage locations when compared with the conventional half bandwidth method. Although considerable saving in memory is obtained in using the skyline method, the present memory capacity of the Amdahl is not enough for an undrained analysis which requires a memory space of 194,528 storage locations (about 1.5 megabytes) using the extended skyline method. This exceeds the maximum core memory of 1 megabytes available in the computer.

Fortunately, the use of the super-computer made these analyses possible.

5.4 Conclusion

The undrained analyses presented in this chapter enable engineers to analyze soil deformation under fully undrained or fully drained situations using effective stress parameters. This formulation is unique in the sense that total stress pore pressure parameters α and β are used which

can be measured quite readily in the laboratory. Moreover the pore pressure parameter β can be less than one to model unsaturated soil. Although there is no analytical solution to compare with the finite element solution for the problems presented, the results of the finite element solutions reveal no contradiction based on the present understanding of soil mechanics. In situations in which fully drained or fully undrained assumptions cannot be made, this approach can be used to provide initial stress conditions for pore pressure diffusion problems.

6. EXCAVATION BEHAVIOUR OF EDMONTON CONVENTION CENTRE

6.1 Introduction

In previous chapters, two finite element formulations and several strain softening models have been presented. Numerous simple and complicated problems have been studied to compare the finite element results with analytical solutions whenever possible. In this chapter, the strain softening model and the finite element formulation are applied to a real life engineering problem to evaluate the effectiveness of the present approach. The study will involve a back analysis of a well documented case history on the behaviour of an excavation during the construction of the Edmonton Convention Center.

The Edmonton Convention Center is located on the north bank of the North Saskatchewan River which flows through the center of the city of Edmonton. The construction of the convention center required an excavation 20 m deep on the river valley wall. Tangent piles walls were used to support the excavation with 6 levels of pre-stressed anchors embedded into the underlying soil and bedrock. The performance of the excavation was carefully monitored to minimize the risk of damaging nearby structures due to excessive deformation of the surrounding soil. Site investigation had indicated the presence of three major zones of bentonite lying practically horizontal and having a relatively low shear strength. A finite element model was

used to simulate the excavation process and it was concluded that the stability and performance of the structure were predominantly governed by the behaviour of these bentonite layers. Observations from the slope indicator measurements during the excavation process indicated that there had been substantial movement in excess of the values predicted by the finite element analysis at the lowest of the three bentonite layers. It is the objective here to re-evaluate the finite element model and study the causes of such discrepancies.

6.2 Geology of the Site

The city of Edmonton is situated within the Eastern Alberta Plains in central Alberta. The North Saskatchewan River, which flows from the Rocky Mountains to Hudson's Bay, divides the city basically into north and south regions as shown in Figure 6.1. Extensive urban development occurs on both sides of the river and slope instabilities are fairly common on the river valley walls. The general geology of the city and its vicinity has been reported by Rathol and McPherson (1975) and others (May and Thomson, 1978). The dominant surficial features in this area are glacial landforms such as ground moraines, till ridges and a glacio-lacustrine plain.

The glacio-lacustrine sediments near the ground surface are interbedded clay, silt and sand with some gravel and occasionally pockets of diamicton. The underlying till

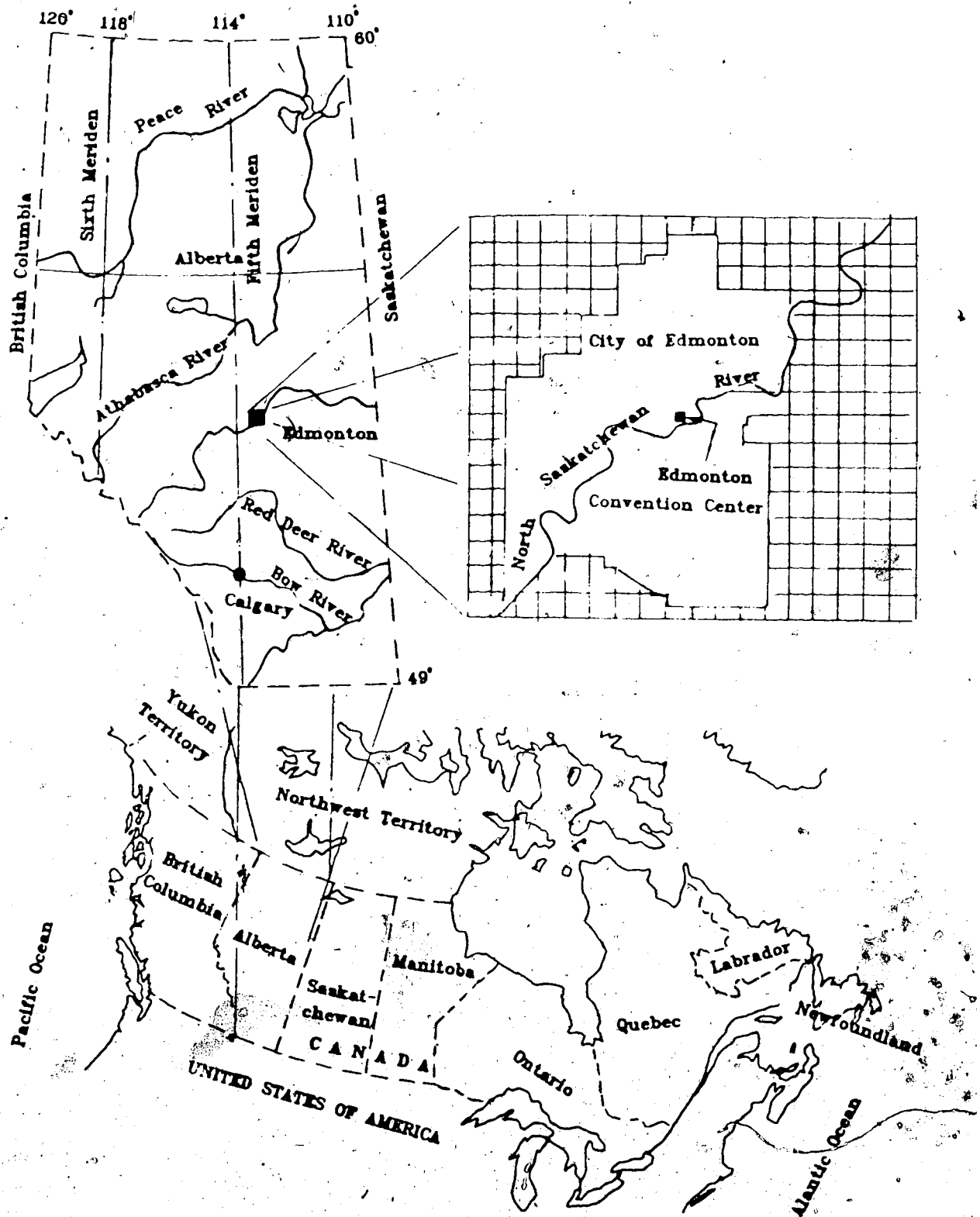


Figure 8.1: Geographic Location of the Edmonton Convention Center

deposits are heterogeneous and consists of 40 to 45% sand, 25 to 35% silt and 20 to 30% clay sizes that contain a high proportion of montmorillonite. The liquid limit for the till ranges from 20% to 40% and plastic limit from 10 to 20% (May and Thomson, 1978). Water bearing sand lenses are commonly found in the till. The Saskatchewan sands and gravels are dominantly composed of quartzite rock fragments with small amounts of chert, petrified wood, coal and clay ironstone. The bedrock is basically bentonitic shale, siltstone, coal seams and bentonite beds of the upper Cretaceous period. The bedrock is commonly referred as the Horseshoe Canyon Formation. At greater depths the Paleozoic strata are mainly composed of limestones, dolomites and evaporites. The bedding in general dips south-westward at a slope of about three to five meters per kilometer.

6.3 Location of the Edmonton Convention Center

The Edmonton Convention Center is located on Grierson Hill on the North Saskatchewan River as shown in Figure 6.1 and 6.2. The Convention Center is situated in an area of active slope instability. There have been at least two major slope failures at the east and west end of the Grierson Hill area and the first slide is within the site. The time at which the first slide occurred is not known but is believed to be many centuries ago. The second slide which occurred about 1905 extends from the east boundary of the site to approximately the eastern extremity of the Grierson Hill

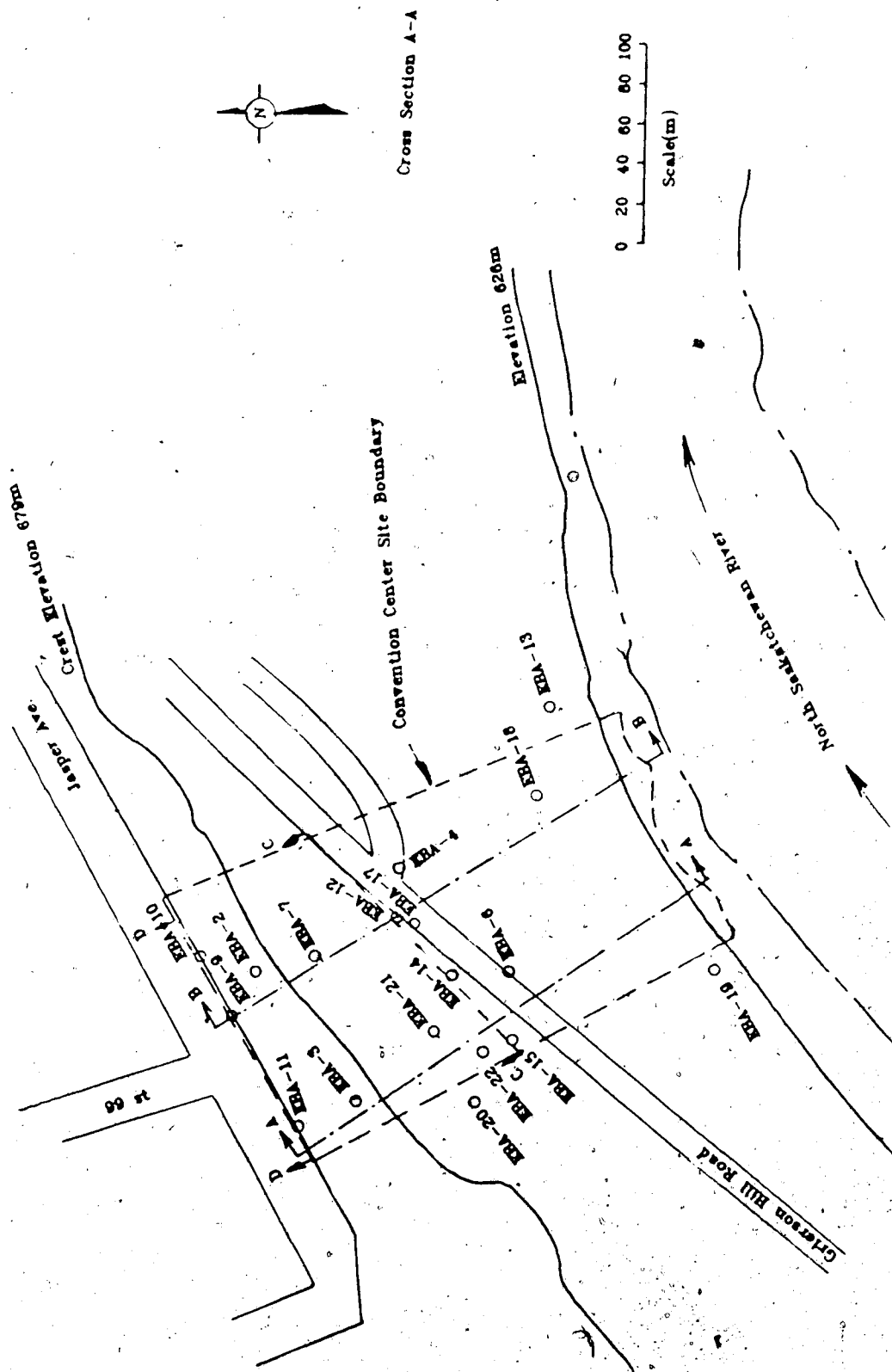


Figure 6.2: Plan View of the Edmonton Convention Center Site -
EBA and NRM Consultants Ltd.

area. The mode of failure was a translational motion along a horizontal plane and subsidence at the crest of the slide was about 1 to 2 meters. Coal mining activities took place at the end of the nineteenth century but were terminated shortly after the second slide.

Concerns for the stability of Grierson Hill have resulted in extensive studies of this area. It was concluded that pore pressure, in addition to the river erosion along the river bank, were the major causes of slope instability. A 1.5 meter diameter drainage gallery was installed in 1960 which extended into about the mid-point of the present convention center site. It has considerably reduced the sliding activity in this area. More detailed discussions of the stability of Grierson Hill can be found from other publications (EBA 1981).

6.4 Soil Stratigraphy and Material Properties

Since the Convention Center site is an area of landslide instability, a careful and comprehensive site investigation is crucial to the safety of the structure during the construction period and its long term performance. Information is available for this area from previous studies of landslide activity and also from the record of construction of nearby structures. However, a microscopic study of the material behaviour is necessary and identification of zones of weaknesses is critical to the design of the excavation. High quality samples using triple

tube core barrel samplers were obtained by EBA Engineering Consultant Company and a comprehensive report on the geotechnical properties of the site is available (EBA 1978).

6.4.1 Soil Stratigraphy

A layout of the borehole locations of the site is shown in Figure 6.2. Several soil profiles have been produced from the borehole information and they are given in Figures (6.3) to (6.6). The surface stratigraphic sequence of the upper portion of the site is fairly typical of the area. It consists of approximately 3.1 m of undifferentiated sand-silt-clay fill with organic inclusions underlain by 1.7 meters of lacustrine clayey-silt with low to medium plasticity. Beneath the silt is a highly plastic, stiff to very stiff clay to a depth of 8.8 meters. Sandy clay (till) of low to medium plasticity is found beneath the lacustrine clay to a depth of 15.2 meters which often contains water bearing sand lenses. Saskatchewan sands and gravels are found beneath the till and above the clay shale bedrock.

The bedrock is interbedded shale and sandstone starting at an average depth of 18.3 meters. Coal seams and bentonite layers are found throughout the bedrock to a depth of over 60 meters. The extent of the bentonite layers are not known, but there are three bentonite layers at depths of about 20 meters, 30 meters and 45 meters which, from local experience, are believed to be continuous. The properties and continuity of these bentonite layers are crucial to the

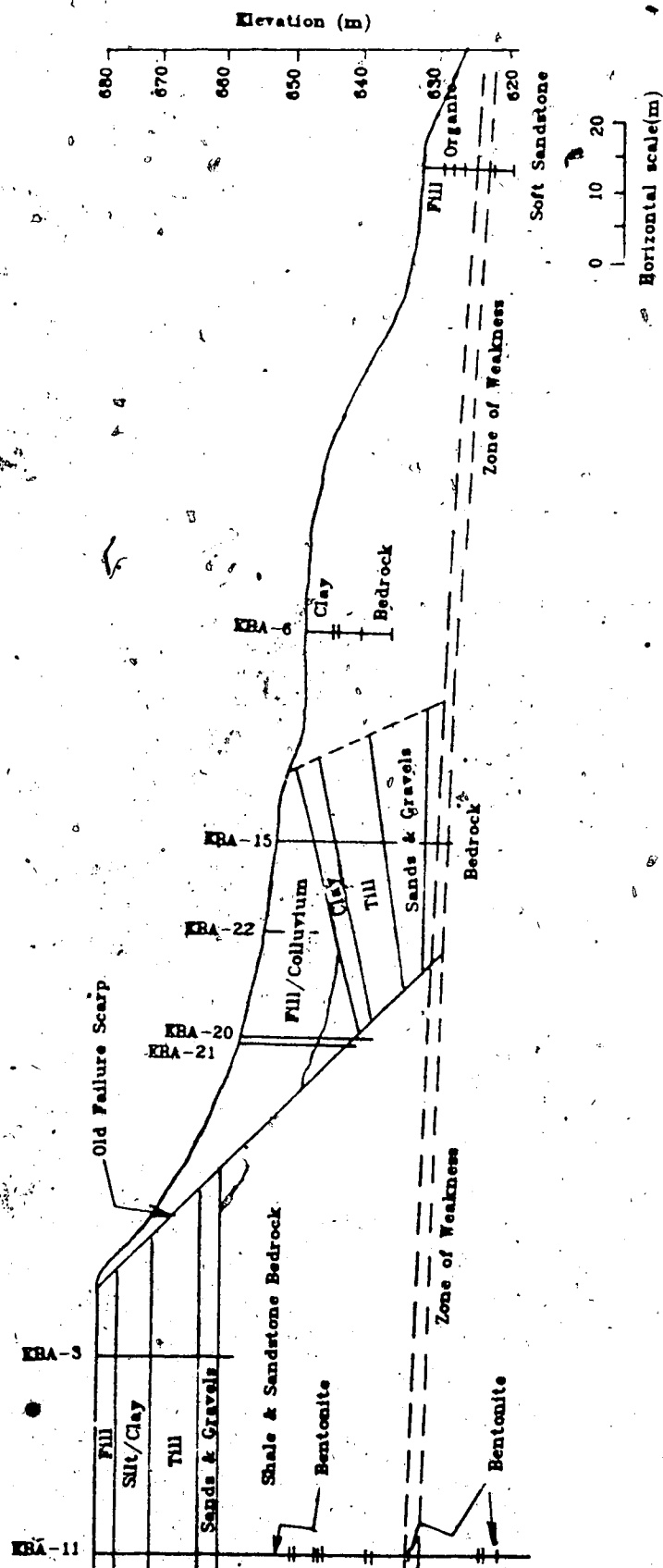
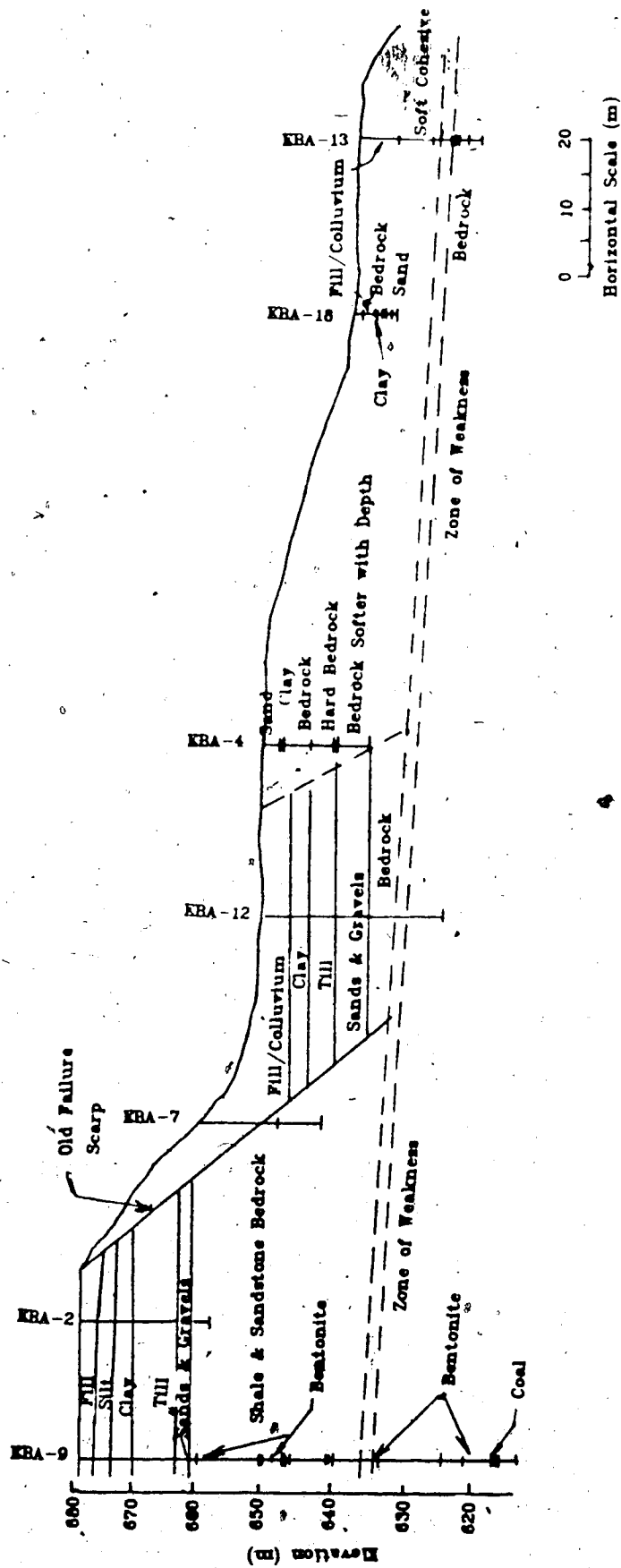


Figure 8.3: Soil Stratigraphy of Section A-A - EBA and NRM Consultants Ltd.



Stratigraphy Between Borehole
Locations is Inferred

Figure 6.4: Soil Stratigraphy of Section B-B - EBA and NRM Consultants Ltd.

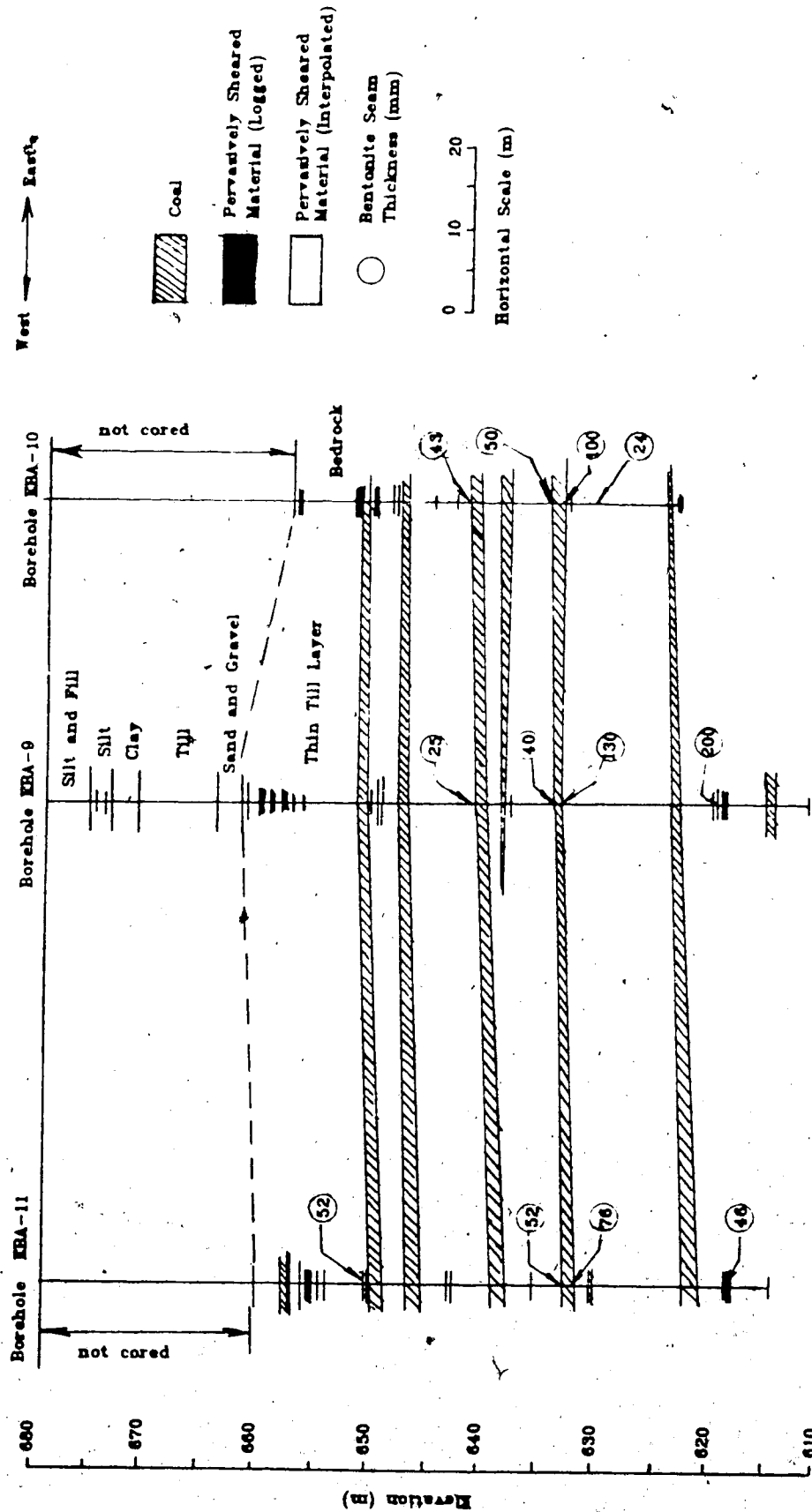


Figure 6.5: Soil Stratigraphy of Section C-C - EBA and NRM Consultants Ltd.

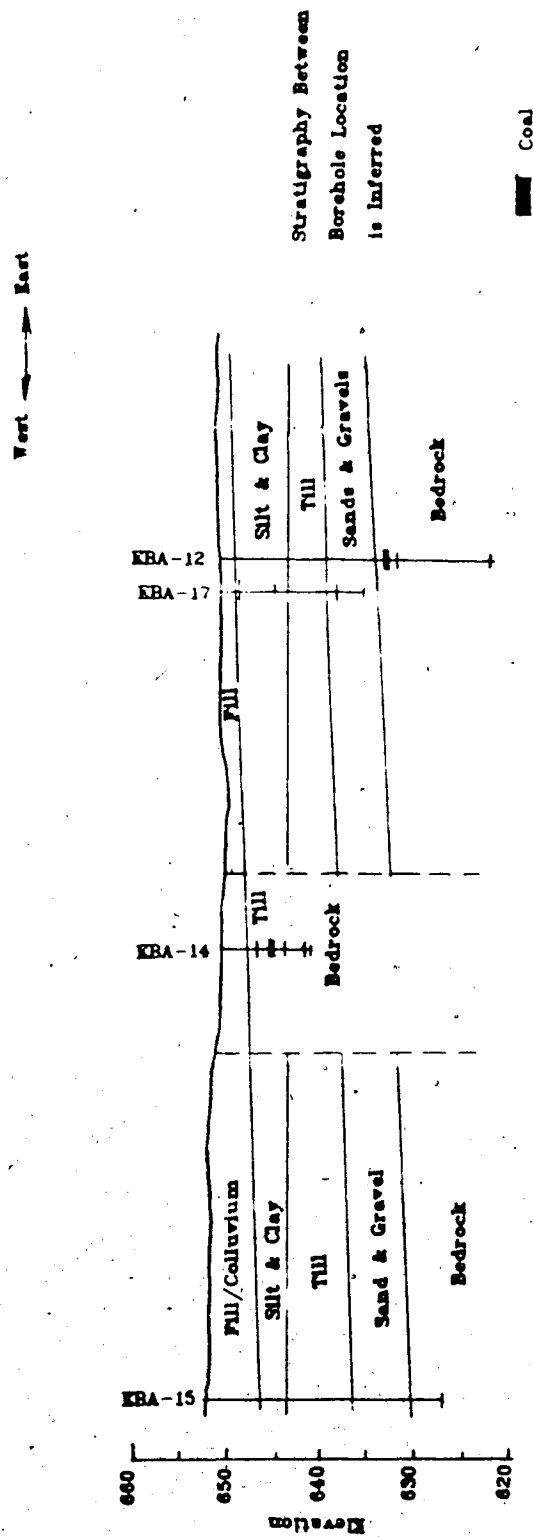


Figure 8.6: Soil Stratigraphy of Section D-D - EBA and NRM Consultants Ltd.

stability of the structure.

The coal beds are believed to be continuous at depths of 28,32,39,46,56 and 65 meters. The coal is a black, brittle, highly fractured and free draining material with a thickness varying from 0.3 to 0.5 m. The bentonite layers are found to be in co-existence and in contact with the coal and often separated by 10 to 50 mm of carbonaceous shale at a depth of 39.0 m to 45.1 m. The coal acts as a drain for the bentonite which tends to be softened by water.

The lower portion of the site is more complicated. Instead of finding clay-shale bedrock in the river valley, a clay-till-sand sequence was found in some boreholes. A careful interpretation of the borehole information was made and it was concluded that the lower portion of the site has been subjected to a major landslide failure. The failure was a translation sliding followed by a subsidence at the top of the slide as illustrated in Figure 6.7. The approximate zone of failure is identified and shown in Figures 6.3 and 6.4. A more detailed discussion of the interpretation of the borehole information and soil stratigraphy is given in a report by EBA (1978).

6.4.2 Ground Water

Ground water level is influenced by regional and local infiltration and seasonal effects. The drainage gallery installed in the late 1950's has lowered the water table of the slope and hence increased the stability. Thirteen

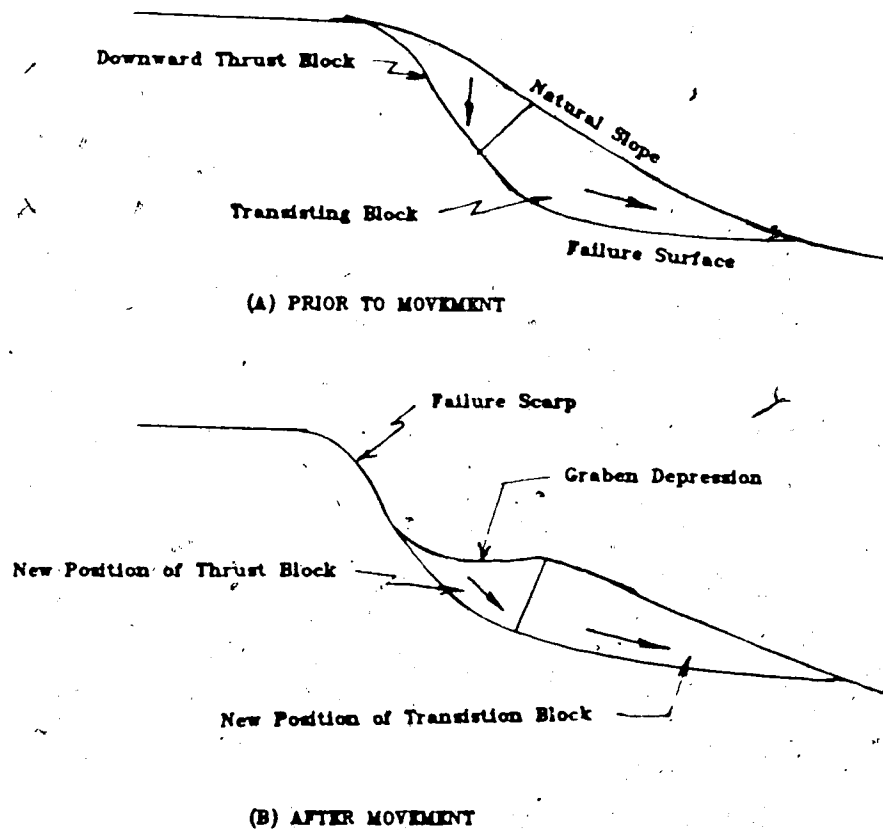


Figure 6.7: Schematic of Translational Failure -
EBA and NRM Consultants Ltd.

pneumatic piezometers have been installed in this site for the project. Perched water tables are observed at numerous locations due to the complex stratigraphy of interbedded shale, sandstone, gravel and coal layers. The ground water table in this area is probably close to river level which is well below the bottom of the excavation for the convention center.

6.4.3 Material Properties

Much of the information on the engineering properties of the soils and bedrocks in the Edmonton area have been collected. Table 6.1 summarizes the elastic and strength properties of the materials at the Edmonton Convention Center site. The elastic parameters are based on the research work on local soils performed at the University of Alberta over the past 10 years. Pressuremeter tests were used to determine the elastic modulus (Eisenstein, 1973) and have been applied to a number of structures with reasonable agreement between the computed and observed deformation behaviour. The elastic modulus of the shale is estimated to be 137900 kPa and increase at a rate of 28959 kPa/m below Elevation 655 m.

6.4.4 Material Properties of the Shear Zone and Bedrock

The strength and deformation properties of the bentonitic shale and bentonite in the Edmonton area have been measured by Sinclair and Brooker (Sinclair 1967).

Table 6.1: Geotechnical Parameters of the Edmonton Convention Site

	Atterberg Limits			Elastic Parameters			Strength Parameters		
	Natural Moist. %	Liquid Limit %	Plastic Limit %	Unit Wt. kN/m ³	Elast. Modul.	Poisson Ratio	Peak Frict. degree	Resid. Frict. degree	Peak Coh. kPa
Clay/Silt/Coluvium	35-45	55-70	20-30	19.0	48265	0.45	24		
Till	15-20	30-35	15-20	21.0	137900	0.42	40		
Sask. Sand & Gravel				18.5	241325	0.35	40		
Clay Shale	10-20	50-100	20-25	21.5	*	0.40	14-24	12-17	53-57
Bentonitic Shale	25-45	125-220	30-45	21.5	*	0.40	14	8-10	38-43
Bentonit. Sandstone	10-20	80-100	25-30	21.5	*	0.40			
Siltstone	35-45	70-25		21.5	*	0.40	20-35	20-35	168
Bentonite	50-70	80-400	50-60	21.5	*	0.40	14	5-10	38
Bentonitic Shale	67	47		21.5	*	0.40	27-36	14-19	-

* Elastic Modulus = 137900 between elevation 662 - 655 m and increases at a rate of 28959 kPa/m depth to elevation 580 m.

Data taken from EBA (1979)

Triaxial and direct shear tests had been performed under consolidation pressures ranging from 15 to 2000 psi, or 103 to 13790 kPa. Also Atterberg limits were obtained with LL = 125, PL = 44 and LI = 0.1 - 0.2 for the bentonitic shale and LL = 264, PL = 60 and LI = 0.02 - 0.03 for the bentonite.

The effective peak friction angle for the bentonitic shale is about 20° for pressures below 150 psi (1034 kPa) with negligible cohesion. For pressures above 150 psi, the failure envelope becomes concave downward with an effective friction angle of only 8.2° and an apparent cohesion of about 30 psi (345 kPa). The elastic modulus for this material can also be estimated from the tests. Depending on the confining pressure the elastic modulus ranged from 200,000 kPa at a high confining pressure of 3000 kPa to 50,000 kPa at low confining pressures. The results shown earlier obtained by Eisentein using the pressuremeter test reflect a similar order of magnitude of elastic modulus. These values will be used in the initial finite element analysis.

For the bentonite the effective peak friction angle is about 14° with a small cohesion from 0 - 30 kPa for a confining pressure less than 150 psi (1034 kPa). For a confining pressure above 150 psi the effective friction angle is reduced to 9.5° - 10° with an apparent cohesion of 10 psi (70 kPa). The residual frictional angle of the bentonite ranges from 7° - 8.5° . The elastic modulus is estimated from the stress strain curve as follows:

Using Hooke's Law and let $\sigma_2 = \sigma_3$, under triaxial test conditions, one obtains:

$$\epsilon_1 = \frac{\sigma_1 - 2\nu\sigma_3}{E}$$

or

$$E = \frac{(\sigma_1 - \sigma_3) + (1 - 2\nu)\sigma_3}{\epsilon_1} \quad (6.1)$$

The elastic modulus E can be determined from the $(\sigma_1 - \sigma_3)$ vs ϵ_1 plot knowing the confining pressure σ_3 and an assumed value of Poisson's ratio. It is noted that $(\sigma_1 - \sigma_3)$ is the same in terms of effective stress or total stresses. Therefore, if total stress σ_3 is used in equation (6.1), then E and ν are total stress parameters. If effective stress σ'_3 is used, then E and ν are effective stress parameters. Under fully undrained conditions, $\nu = 0.5$, the total stress parameter E is independent of the confining pressure σ_3 .

The elastic modulus for the bentonite is estimated to be 49,000 kPa for $\nu = 0.4$ at a high confining pressure of 120 psi (830 kPa). This value will be used for the deepest bentonite shear zone. At lower confining pressures, the elastic modulus E is in the order of 35,000 kPa for $\nu = 0.4$.

6.4.5 Excavation for the Convention Center

The construction of the Convention Center required a 20 meter deep excavation as shown in Figure 6.8. Excavation began in mid April 1980 and was essentially completed in December 1980. The excavation is supported by a tangent pile wall system on the North, East and West sides. High tensile anchors with steel bars and multiple strands were used to control the deformation of the adjacent soil. The actual sequence of excavation is given in the report by EBA (EBA 1981). Basically, the excavation for the upper exhibition floor, Figure 6.8, was performed in six levels starting from the east wall and progressing to the west. Anchors were installed at each excavation level and excavation for the next level was not allowed until the anchors had been stressed to the designed load. Approximately 235000 cubic meters of soil and soft rock were excavated.

6.4.6 Tangent Piles Wall and Anchor Support

The 20 meter deep excavation is supported by 312 tangent piles on the north, east and west sides. There are 73 piles on the east wall, 154 piles on the north wall and 85 piles on the west wall. Most of the piles were installed between March 6th and May 30th, 1980. The tangent piles are straight-shaft concrete piles of 1 meter diameter and 30 meters long. The length of the piles vary on the east and west wall depending on the surface topography.

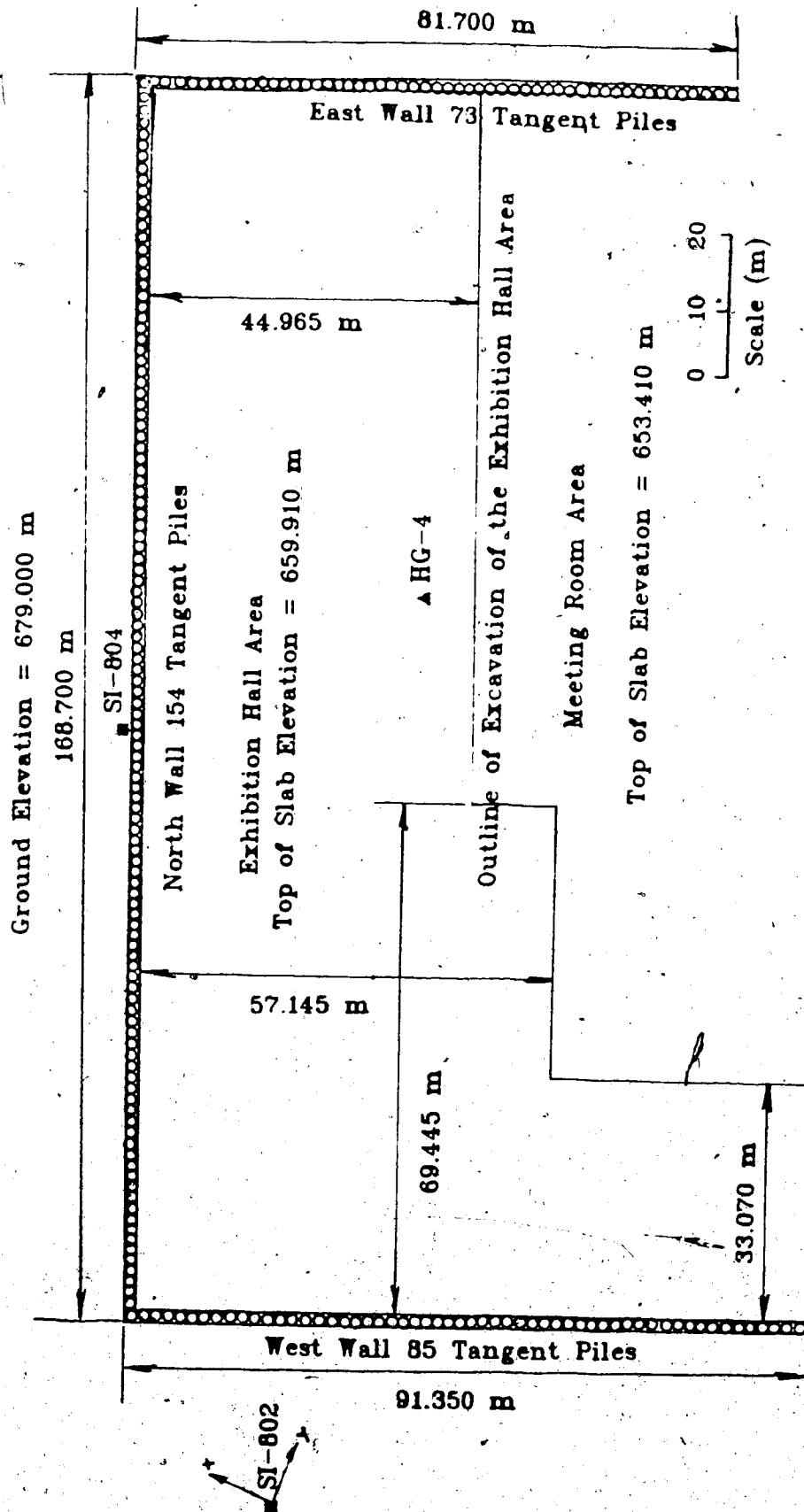


Figure 6.8: Floor Plan of the Excavation of the Edmonton Convention Center -
EBA and NRM Consultants Ltd.

The piles were installed using conventional drill rigs with a 1066 millimeter diameter auger. Casing was used on some piles to prevent seepage and sloughing from the Saskatchewan sands and gravels. In general, the walls of the pile holes were hard, intact, dry and clean with no significant seepage.

The top of the pile was about 2.5 meters below the original ground surface. H-piles and wood lagging were used to support the soil above the top of the tangent piles. The depth of the tangent piles were determined based on an elaborate study using the finite element method to provide adequate support to control deformation as well as long term stability (EBA 1980). The tangent piles terminate on the sandstone and shale bedrock just below the second zone of weakness at an elevation of 649 m (the City's elevation is 679 m). It was concluded in the analytical study that the piles are most effective if they terminate just below the second zone of weakness. To intercept the third (lowest) zone of weakness would require extremely long piles which was not economically feasible.

Six levels of pressure grouted anchors were used to support the tangent pile wall. A total of 1054 anchors were installed in which 490 anchors are 1 3/8 inch diameter threaded bars at the first and second levels. Depending on the working load of the anchors, the remaining levels consist of multi strands of 16 millimeter diameter cable with concrete waling. The anchors were installed at an angle

of 30 degrees with respect to the horizontal to a maximum length of approximately 41 m. The first two rows of anchors are embedded in till with a capacity of 120 kips/anchor. The rest of the anchors are embedded in the shale bedrock with a capacity of 320 kips/anchor. A grouting pressure in the range of 2 to 6 MPa was used. All anchors were stressed to the required load level before excavation below that anchor level could begin. Due to the consolidation and creep effects of the anchors, some anchors, especially the top 2 levels, had to be restressed. Permanent load cells are installed at all 6 levels to monitor the long term behaviour of the structure.

6.5 Excavation Performance

The excavation and the tie back wall system are heavily instrumented. There are 12 slope indicators, 5 heave gauges, 7 piezometers, 15 settlement plugs for the ground surface, 12 settlement plugs for the tangent pile walls and 54 load cells at various anchor levels. The location of some of the instruments are given in Figure 6.2. A brief discussion of the results of the instrumentation will be given below. Details of all the instrumentation can be found in reference (EBA 1984).

6.5.1 Slope Indicators

The depths of the slope indicators range from 25 meters to 50 meters below ground surface. Slope indicators

SI-80-11. SI-80-4, SI-80-12 and SI-80-2 are 50 meters deep and are used to monitor the movement at great depths on the east, north and west walls. The rest of the slope indicators are 25 to 30 meters deep. Most slope indicators show movement of the tangent pile walls into the excavation of the order of 10 to 20 millimeters at the top of the piles. Movements gradually decrease with depth except for slope indicators SI-80-4 and SI-80-2. The measurements of slope indicator SI-80-4 is given in Figure 6.9. These figures clearly illustrate that intensive shearing occurs at a depth of around 46.3 meters. The direction of movement of slope indicator SI-80-4 on the north wall is about 30 degrees to the normal of the wall while movement of slope indicator SI-80-2 is almost parallel to the west wall. The zone of intensive movement coincides with the lowest zone of weakness. Movement of the order of 30 mm was observed when the excavation was completed. Moreover there seems to be a direct correlation between the movement at this depth and the amount of material being excavated. Figures 6.10 and 6.11 show the deflection-volume of excavated material relationship for slope indicators SI-80-4 and SI-80-2. The relationship shown in Figure 6.10 is practically linear. In addition, there seems to be a threshold value of excavated material before accelerated movements began. This threshold value is somewhere between 50 to 100 thousand m³ of excavated material which corresponds approximately to excavation level 1 (5 m deep) and level 2 (11 m deep)

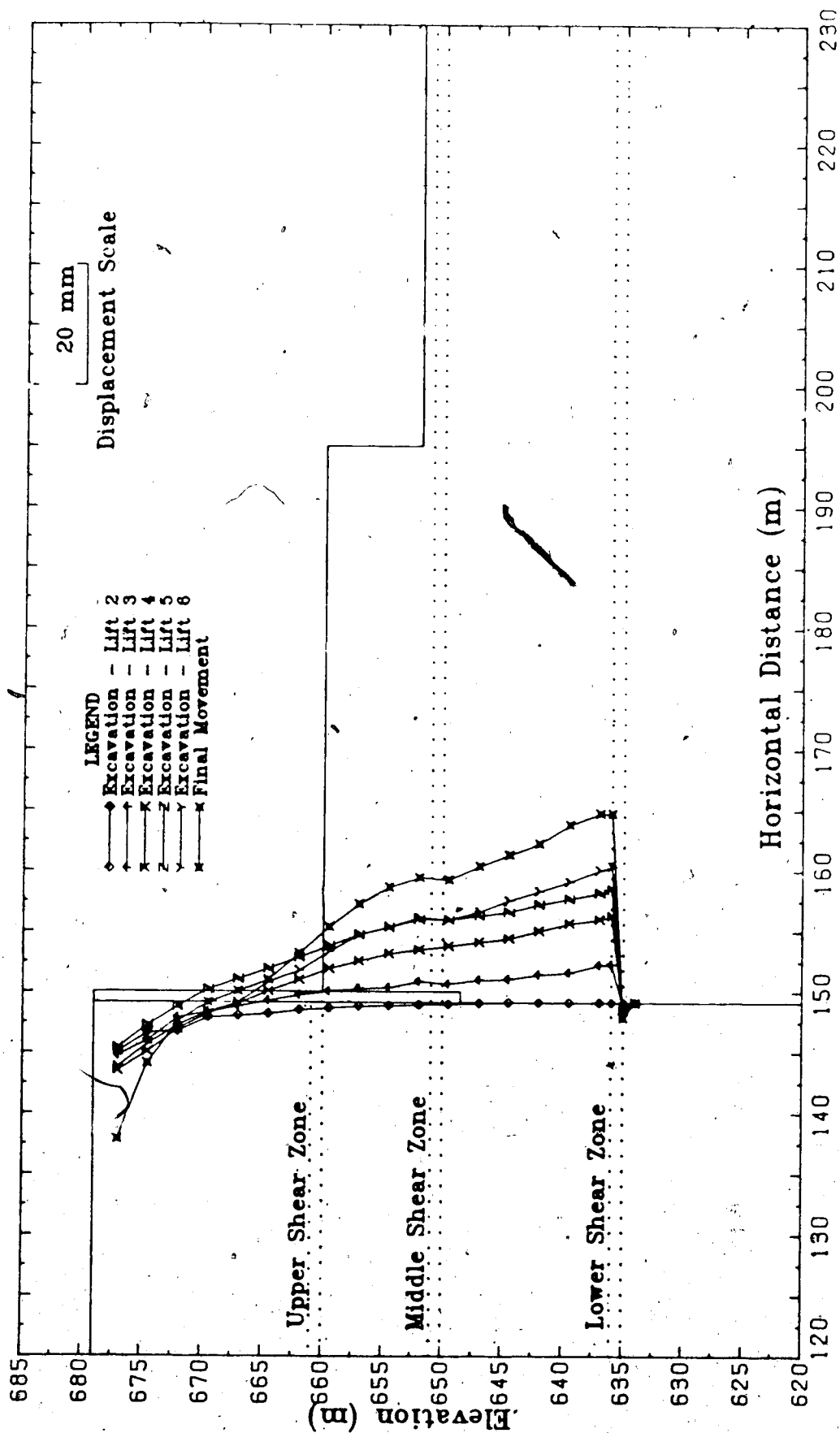


Figure 6.9: Observed Movement of Slope Indicator (SI-804) —
EBA and NRM Consultants Ltd.

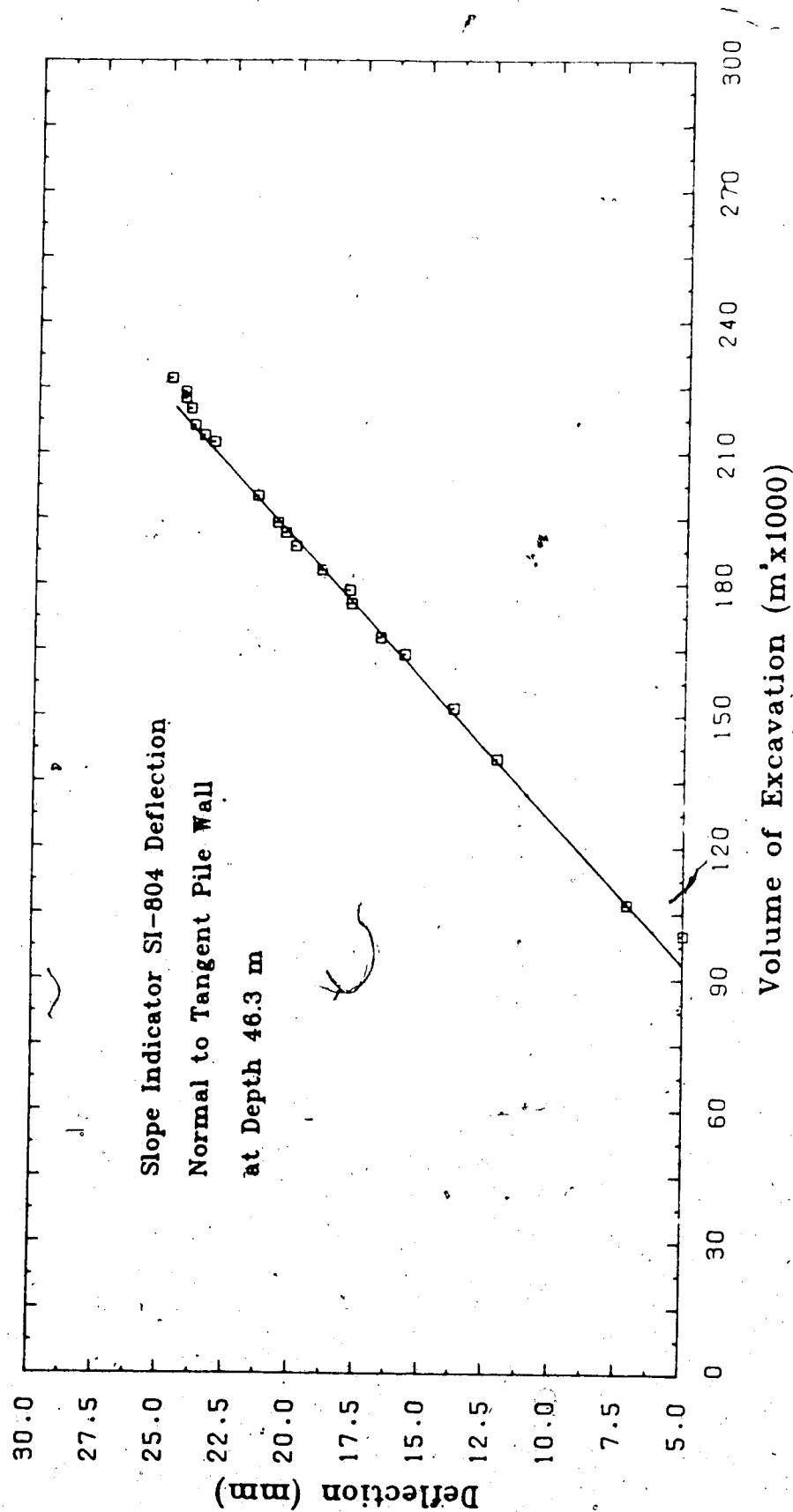


Figure 6.10: Slope Indicator (SI-804) Movement vs Volume of Excavation –
EBA and NRM Consultants Ltd.

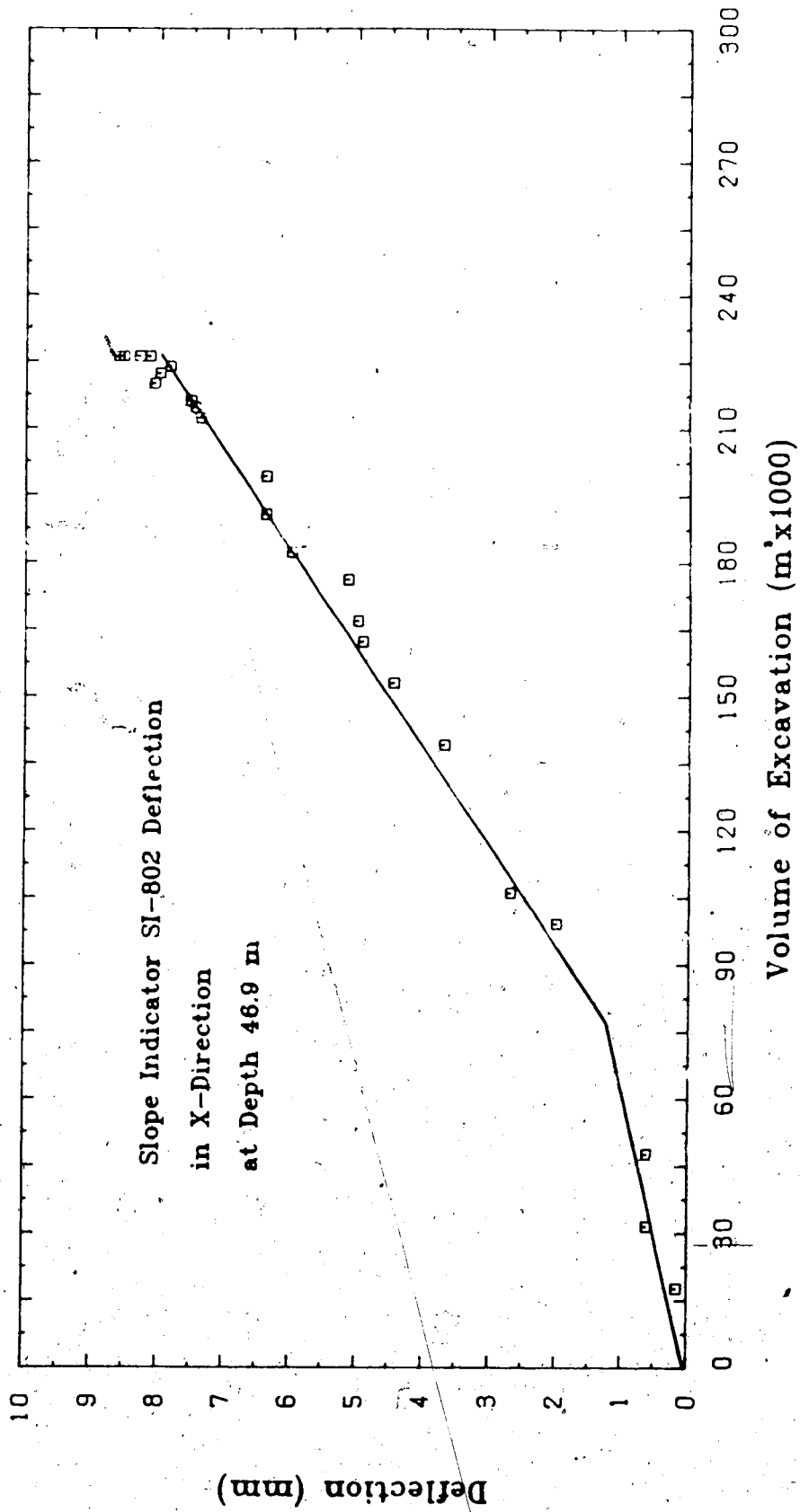


Figure 6.11: Slope Indicator (SI-802) Movement vs Volume of Excavation –
EBA and NRM Consultants Ltd.

respectively. Figure 6.9 also shows movement into the soil between a depth from 3 meters to about 18 meters. This is due to the heavy tie back forces applied to the tangent pile wall. The large displacement near the ground surface is the result of the use of H-piles and wood lagging support which is not integrated with the tangent pile wall system.

Slope indicator SI-80-12 which is located 80 meters north of SI-80-4 showed considerably less movement. However, about 10 months after the excavation was completed, SI-80-12 showed 4 mm of movement at a depth of 48 meters which corresponds to the lowest zone weakness. Slope indicator SI-80-4 showed continuous movement after excavation was completed before it eventually stopped at a total displacement of 30 mm.

6.5.2 Heave Gauges and Settlement Plugs

Three of the five heave gauges were damaged during construction. Only heave gauges HG-4 and HG-5, which are located at the center and near the east wall of the excavation as shown in Figure 6.8, gave complete records of the upward movement of the excavation floor. The amount of heave was measured to be about 100 mm at elevation 646.45 meters (19 meters below original ground level) to 50 mm at elevation 638.366 m (27.234 m below original ground level) as shown in Figure 6.12.

The movement of the adjacent ground and the tangent pile walls are basically upward of the order of 5 to 15 mm.

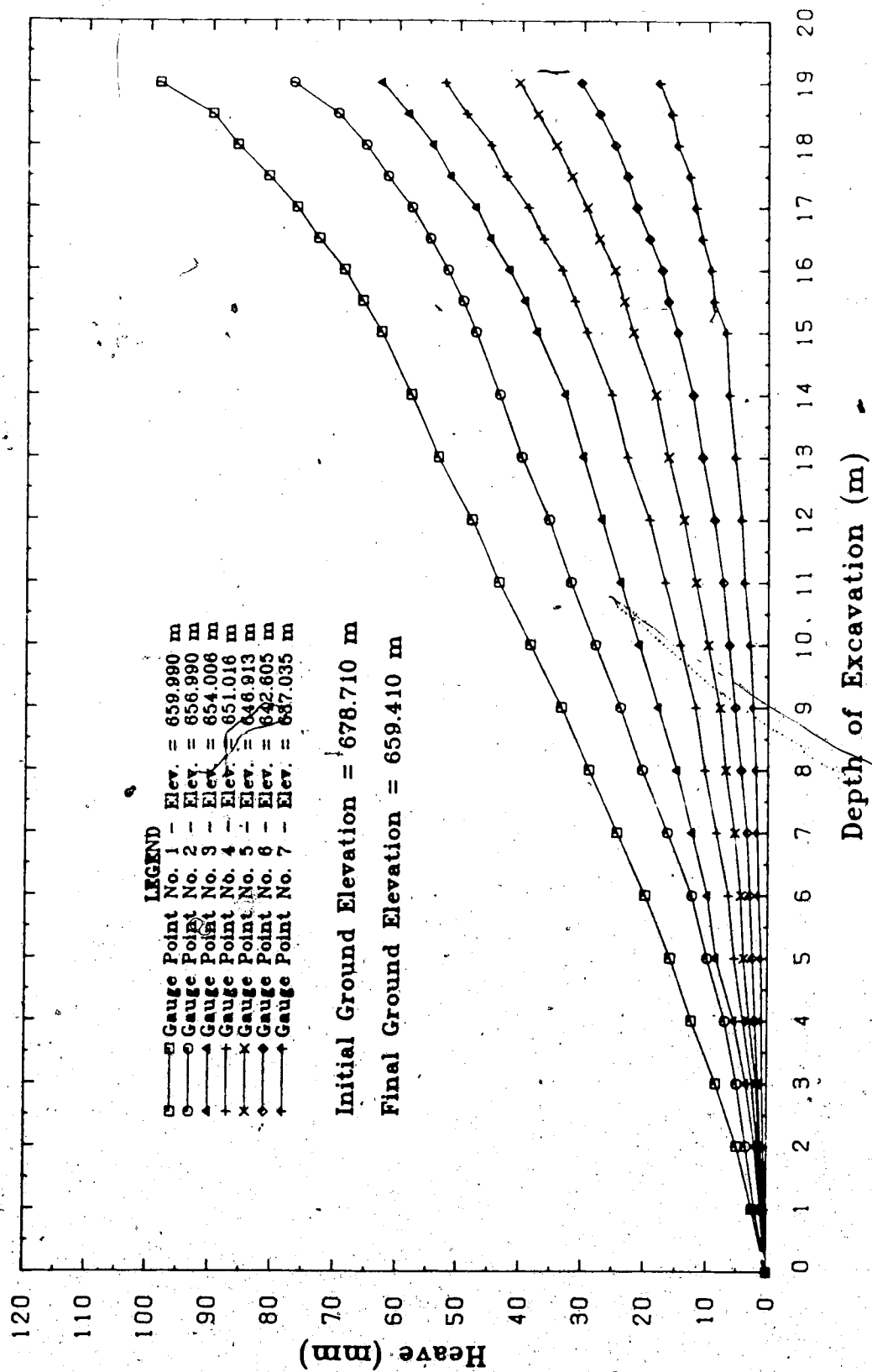


Figure 6.12: Heave of Excavation Floor (HG-4) - EBA and NRM Consultants Ltd.

The wall plugs show about 5 mm horizontal movement into the soil at the mid-point of the north wall and 20 and 10 mm movement at the east and west end of the north wall respectively. The west wall moved slightly into the excavation while the east wall moved slightly into the soil. The magnitude of movements were about 5 to 15 mm.

6.6 Linear Elastic Finite Element Analysis

A series of linear elastic finite element analyses was performed to obtain a basic understanding of the behaviour of the structure. EBA Engineering Company had performed similar elastic analyses but their main concern was to obtain information for designing the tangent pile wall and for the stability of the excavation. The objective here is to back analyze the deformation of the structure and study the effect of various factors in affecting the behaviour of the excavation. It is hoped that the result of the linear elastic analyses will provide some insight into various factors involved and also form a basis of comparison for the non-linear analysis.

One of the major difficulties in analyzing geotechnical structures is to obtain representative values for the properties of the material. In an elastic analysis the amount of deformation is directly related to the values of the elastic modulus and the Poisson's ratio. Although the range of the values of the Poisson's ratio is not very large, the elastic modulus of the soil can vary considerably.

especially in the case of the shale bedrock. The values given in Table 6.1 are believed to be the most representative values for this site, however it is not surprising that the actual values may be different.

In addition to the uncertainty in the material properties, the in-situ stress field is also a major unknown factor. Previous analysis performed by EBA Engineering Company employed a switch-on-gravity technique to incorporate the in-situ stress field. The material parameters used in the in-situ stress analysis are the same as the material parameters used in modelling the excavation. Therefore, the in-situ stress field cannot be varied unless the material parameters are changed. Local experience in the Edmonton area indicates that the k_0 value should be less than 1.0 in the till layer and may be close to 1.0 or slightly higher than 1.0 in the shale bedrock. However, the presence of the river valley will definitely create some stress relief in the adjacent soil. The phenomenon of valley rebound (Matheson, 1973) may introduce some flexural shear in the bedrock and consequently reduce the horizontal stress in the soil and bedrock. It is estimated that the k_0 value can range from 0.65 to 1.0 or slightly higher than 1.0 for this site.

To model different k_0 conditions, fictitious values for the Poisson's ratio for all materials are assigned during the switch-on-gravity analysis and then the material parameters will be changed to their most representative

values in subsequent analyses. This will enable the incorporation of different k_0 conditions without affecting the material properties in subsequent analyses. In fact k_0 is mainly affected by the Poisson's ratio. The elastic modulus only affects the amount of deformation for a homogeneous material. For a one dimensional problem with no lateral deformation, Poisson's ratio ν will result in a k_0 value of $\nu/(1 - \nu)$. The elastic parameters used in the switch-on-gravity analysis are fictitious in order to incorporate a self equilibrium initial stress field. Since the displacements and often the strains derived from the switch-on-gravity analysis are generally neglected, the elastic modulus can be assigned any value without affecting the stress field, assuming that the soil is perfectly homogeneous. An alternative method of creating in-situ stresses is to impose an initial stress field on the structure. However, the stress field must be itself in equilibrium otherwise numerical instability is to be expected in a non-linear analysis. Since it is very difficult to determine the stress at every point in the soil, the switch-on-gravity technique is usually preferred.

The value of k_0 has a considerable effect on the amount of shearing in the soil. A k_0 value of 1.0 indicates that both the horizontal and vertical stresses are equal and if one assumes that they are the principal stresses, then the soil is under a state of hydrostatic compression and the deviator stress and shear stress will be zero. A k_0 value

other than unity will induce shear stresses and the further away from unity, the higher the initial shear stress. However, in the case of an excavation, a lower k_0 value will result in less stress relief but the initial shear stress is higher. If the deformation of the soil can be assumed linear elastic, a lower k_0 normally results in less deformation. However, if the deformation is large enough to induce local failure during the excavation process, a lower k_0 may not always result in less deformation because the higher initial shear stress may lead to more extensive yielding than a higher value of k_0 . This is particularly true for a strain softening material.

A two dimensional idealization of the Convention Center site is shown in Figure 6.13 and the stratigraphic sequence used in the finite element analysis is shown in Figure 6.14. Eight node and six node rectangular and triangular elements are used with a total of 826 nodes and 269 elements. There are 3 horizontal shear zones at Elevations 635, 650 and 660 m. The concrete wall is assumed to be 20 m deep and is terminated at an elevation of 639 m. The H-piles and wood lagging support system near the ground surface are not incorporated in this model. The thickness of the wall is assumed to be 0.9 m while the actual diameter of the piles is 1064 mm. The thickness of the wall in this model is calculated by assuming the flexural stiffness in the 2-dimensional plane strain model is the same as the circular piles. The anchor loads are modelled as point loads applied

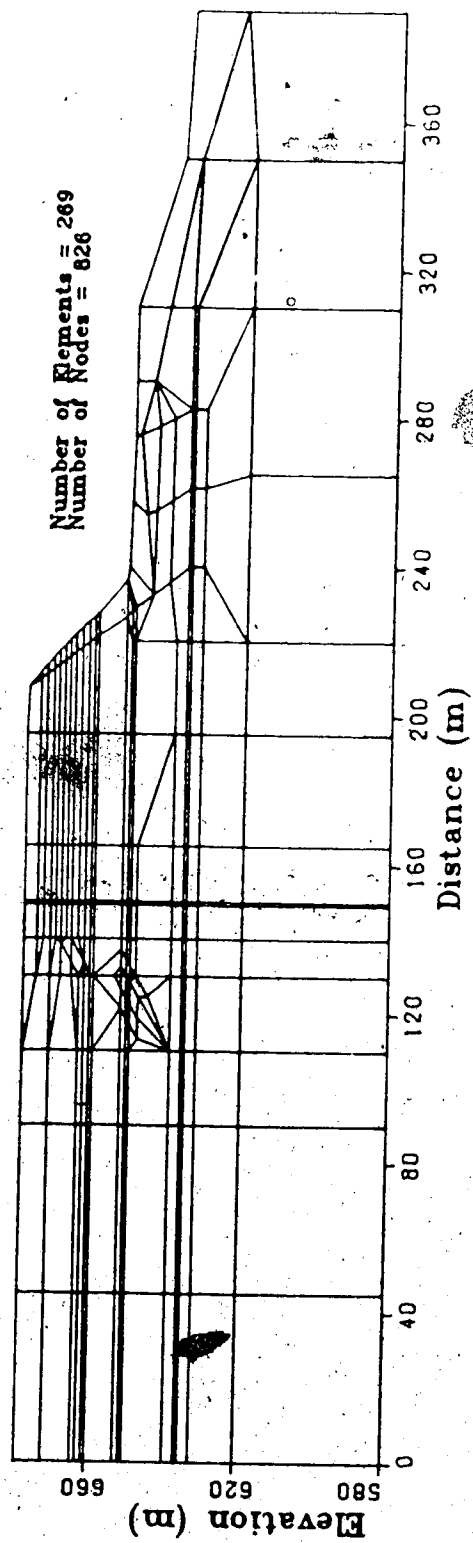


Figure 8.13: Finite Element Idealization of the Edmonton Convention Center Site

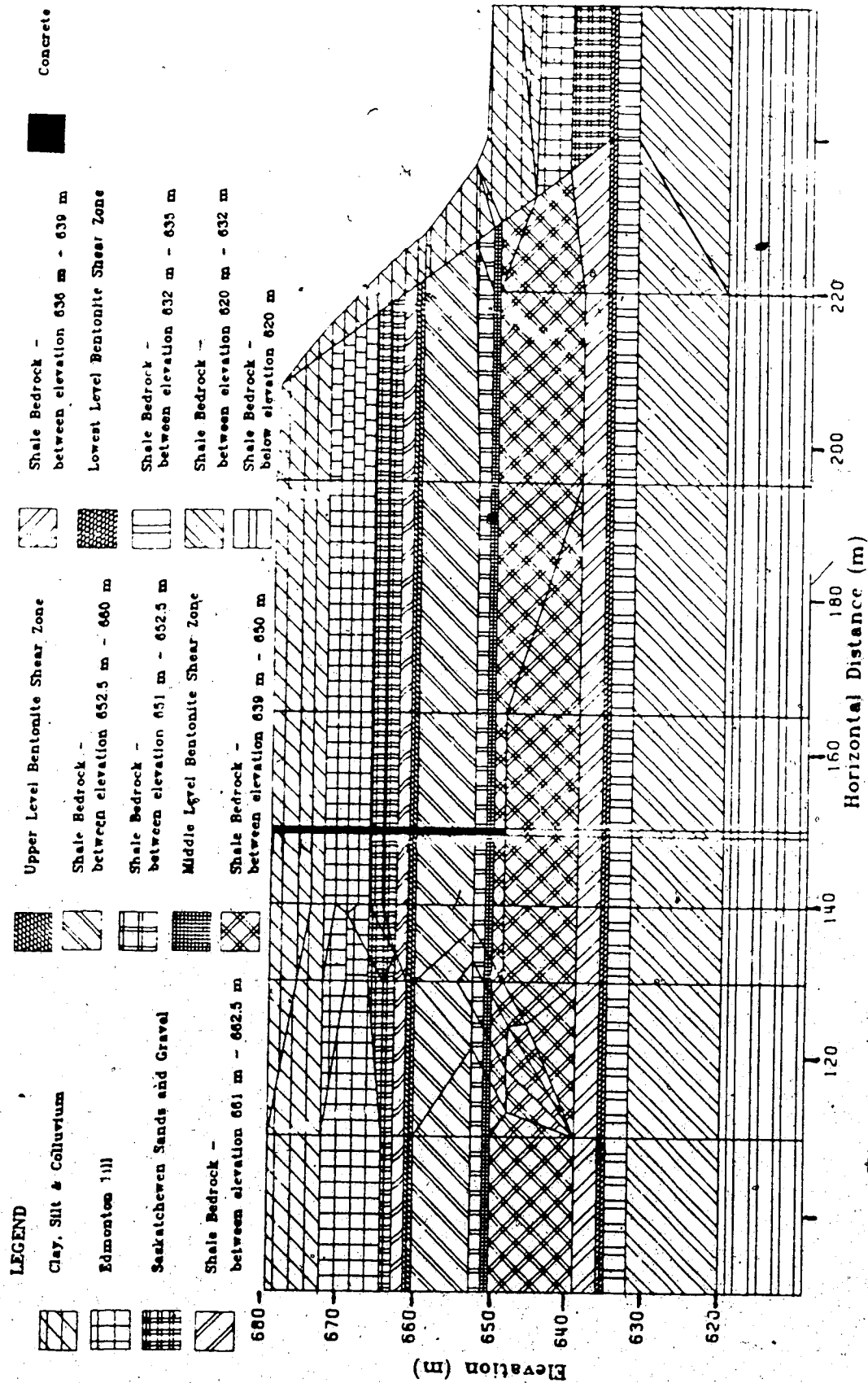


Figure 6.14: Material Sequence used in the Finite Element Analysis

on the tangent piles and the reaction from the anchors are modelled as uniform distributed traction over the length of the grouted section of the anchor. All anchors loads are applied at 30° with respect to the horizontal.

To minimize the effect of boundary conditions on the sizes and the bottom boundary of the finite element model, the boundaries are taken to be 150 m from both sides of the excavation and the foundation is taken to be 80 m below the bottom of the excavation. A no slip boundary condition is assumed on the bottom boundary.

To model the actual excavation sequence accurately, the excavation was performed in six stages. The elevations of the excavation floor were 675.5 m, 672 m, 669 m, 666 m, 662.5 m and 660 m for the first, second, third, fourth, fifth and sixth layers respectively. For the sixth level of excavation, an additional excavation was made close to the valley wall for the meeting room area to elevation 652.5 m (see Figure 6.8). In simulating the excavation process in the finite element model, the elements inside the excavation were removed and an equivalent load due to the stress relief of the excavation was applied on the surface of the excavation to obtain a boundary with zero nodal forces. This approach introduced an error in load of an amount equal to half the size of the element inside the excavation adjacent to the excavated surface. This error can be reduced by providing a thin element adjacent to the excavated surface.

The anchor loads on the tangent pile wall were applied simultaneously at the corresponding level of excavation because in the actual construction sequence, no excavation below a certain level was allowed unless the anchors for that level were installed and tested to the required specification. The anchor loads used in this analysis were the average anchor forces measured from the anchor load tests. Table 6.2 summarizes the average loads on each level of anchor per unit width of excavation. It was observed from the field measurements that the anchor forces on level 1 and 2 had decreased to unacceptably low values during the third and fourth level of excavation. These anchors were then restressed and these changes in anchor loads are also given in Table 6.2. No significant load reduction was observed at levels 3, 4, 5 and 6 and therefore no adjustment of loads were made in the finite element model. The reaction of the anchor loads were assumed to be uniformly distributed over the grouted section of the anchors.

6.7 The Effect of k_0 on the Behaviour of the Excavation

As discussed previously, the in-situ stress field and the value of k_0 are usually unknown. However, the approximate value of k_0 for this site is believed to be 0.8 with a possible range from 0.65 to 1.00. The value of k_0 of 0.65 is believed to be the lowest limit and this value may occur near the valley wall. In order to determine whether or not the behaviour of the excavation is sensitive to the

Table 6.2 Anchor Forces Applied in the Finite Element Analysis

Stage	I	II	III	IV	VI
1	599	571	-	571	-
2	629	-81	599	490	599
3	830	-88	-91	402	502
4	831	19	-7	599	495
5	835	0	134	599	629
6	809	0	0	599	629

I - Final Anchor Force* on Each Level

II - Change of Anchor Force on Level 1

III - Change of Anchor Force on Level 2

VI - Total Anchor Force on Level 1 at each Stage

V - Total Anchor Force on Level 2 at each Stage

* Forces are expressed in kN / m of wall.

value of k_0 , a series of linear elastic analyses were performed. This will provide insight into the effect of k_0 .

The switch-on-gravity technique was used to generate the in-situ stress field. The elastic modulus of the material given in Table 6.1 was used in the switch-on-gravity analysis. However, the Poisson's ratio varied from 0.394 to 0.499 to give k_0 values of approximately 0.65 to 0.99. The unit weight of each material given in Table 6.1 were used to generate the in-situ stresses by applying body forces due to gravity. The displacements and strains due to the switch-on-gravity analyses are neglected in subsequent analyses.

After the switch-on-gravity analysis, the material properties of all the elements are replaced by the values given in Table 6.1. The material properties of the elements located at the tangent pile wall location are replaced by that of concrete. The effect of drilling and installing the tangent pile wall on the behaviour of the entire excavation is believed to be minimal and such details are not incorporated in the finite element model. The excavation was then performed in six stages as described earlier. Since the amount of movement of the tangent pile wall and upward heave of the foundation floor of the excavation were measured in the field, interpretation of the results from the linear elastic analysis focussed on these areas. Also the mobilization of shear strength along the lower shear zone is of interest since it will affect the movement of the tangent

pile wall.

Figure 6.15 shows the mobilized internal friction angle at the location of the lower shear zone assuming zero cohesion due to the switch-on-gravity stress field. It is seen that the lower value of k_0 results in higher mobilized friction along the lower shear zone as expected. Also the mobilized friction increases towards the river valley wall with the ϕ value ranging from 11° for $k_0 = 0.99$ to 17° for $k_0 = 0.65$. The peak friction for the bentonite is around 14° which indicates instability is quite possible close to the valley wall. In fact, land slides have occurred in this region as discussed earlier.

Remote from the valley, the ϕ values range from 2° for $k_0 = 0.99$ to 13° for $k_0 = 0.65$. The ϕ values at the location of the tangent pile wall are very close to these values as well. This re-affirms the idea that the shear zone is not pre-sheared due to the in-situ stress field. The most probable value of k_0 for this site is believed to be 0.80. For a k_0 of 0.80, the mobilized ϕ value near the tangent pile wall is about 7° and increases to 13° towards the river valley.

The mobilized friction along the lower shear zone when the excavation was completed is shown in Figure 6.16.

Similar to the previous results, lower k_0 values show higher mobilization of shear strength. However the maximum ϕ values occurred beneath the excavation instead of near the river valley. The ϕ value ranged from 16° for $k_0 = 0.65$ to around

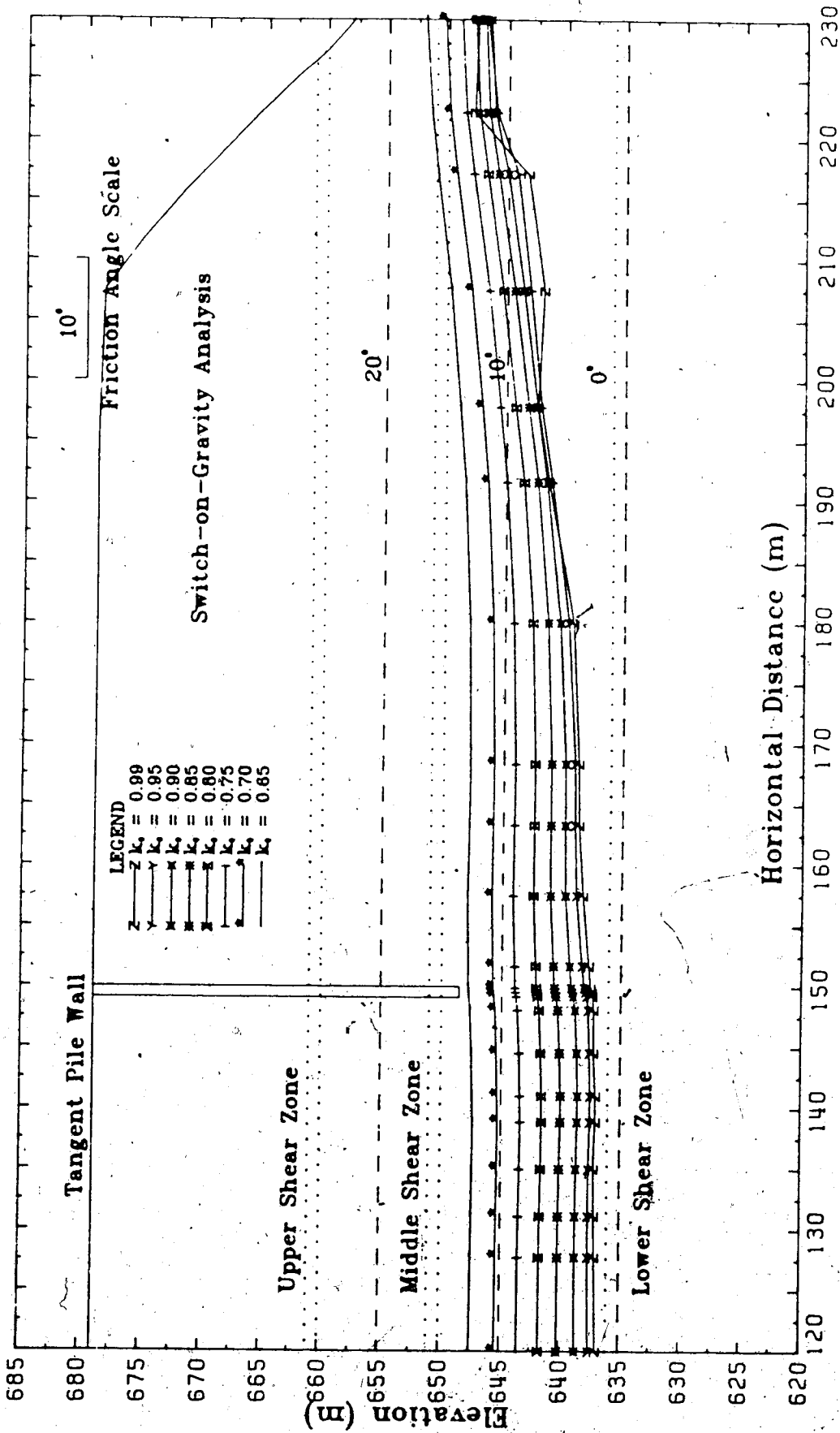


Figure 6.15: Mobilized Friction along Lower Shear Zone - (Switch-on-Gravity Analysis)

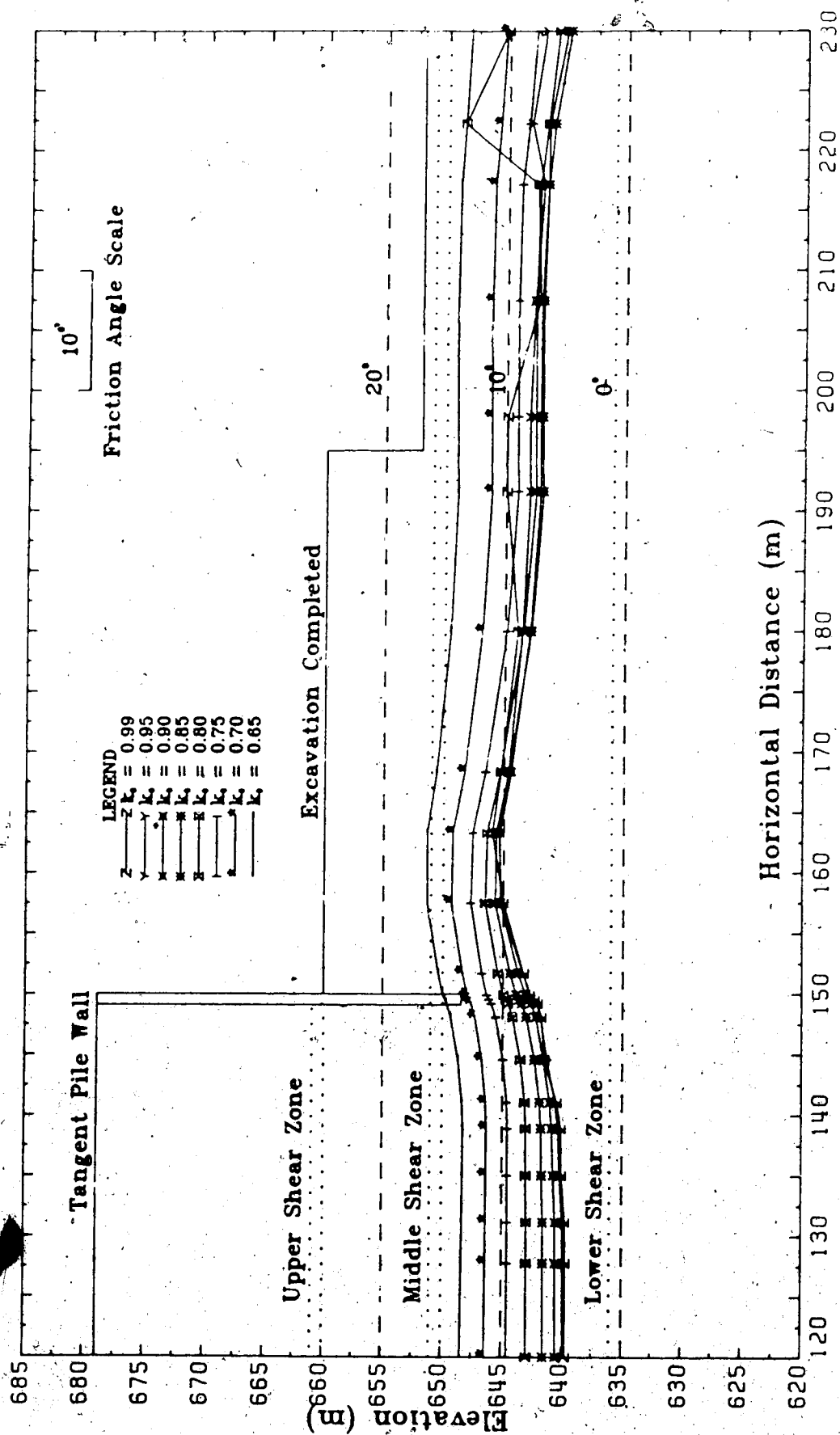


Figure 6.16: Mobilized Friction along Lower Shear Zone - Linear Elastic Analysis

10° for $k_0 = 0.99$. For $k_0 = 0.80$ the maximum ϕ value is about 11.5° . Since 7° is mobilized due to the initial stress field the effect of the excavation is only 4.5° . The peak ϕ friction of the bentonite is around 14° which is not very far from 11.5° . Field observation from slope indicators showed that movement had started at the second to third level of excavation. According to the elastic analysis there should have been no failure at this stage.

The movement of the soil behind the tangent pile wall is shown in Figure 6.17. It is seen clearly that the value of k_0 has very little effect on the horizontal movement at the lower shear zone. The movement at the lower shear zone is close to 8 mm as compared to 30 mm observed in the field. The only difference among different values of k_0 is the movement of the soil behind the tangent pile wall between elevation 679 m and 660 m. Higher values of k_0 result in less movement than lower values of k_0 due to the higher horizontal stresses being relieved by the excavation. The anchor forces applied on the tangent pile wall tend to push the wall into the soil. If the stress relief due to the excavation is higher, as in the case of high value of k_0 , then the movement into the soil will be smaller.

The heave of the foundation floor is insensitive to the value of k_0 as shown in Figure 6.18. The maximum heave calculated is about 33 mm compared to the 100 mm observed.

It is seen from the above discussion that the elastic analysis has under predicted the mobilized friction and

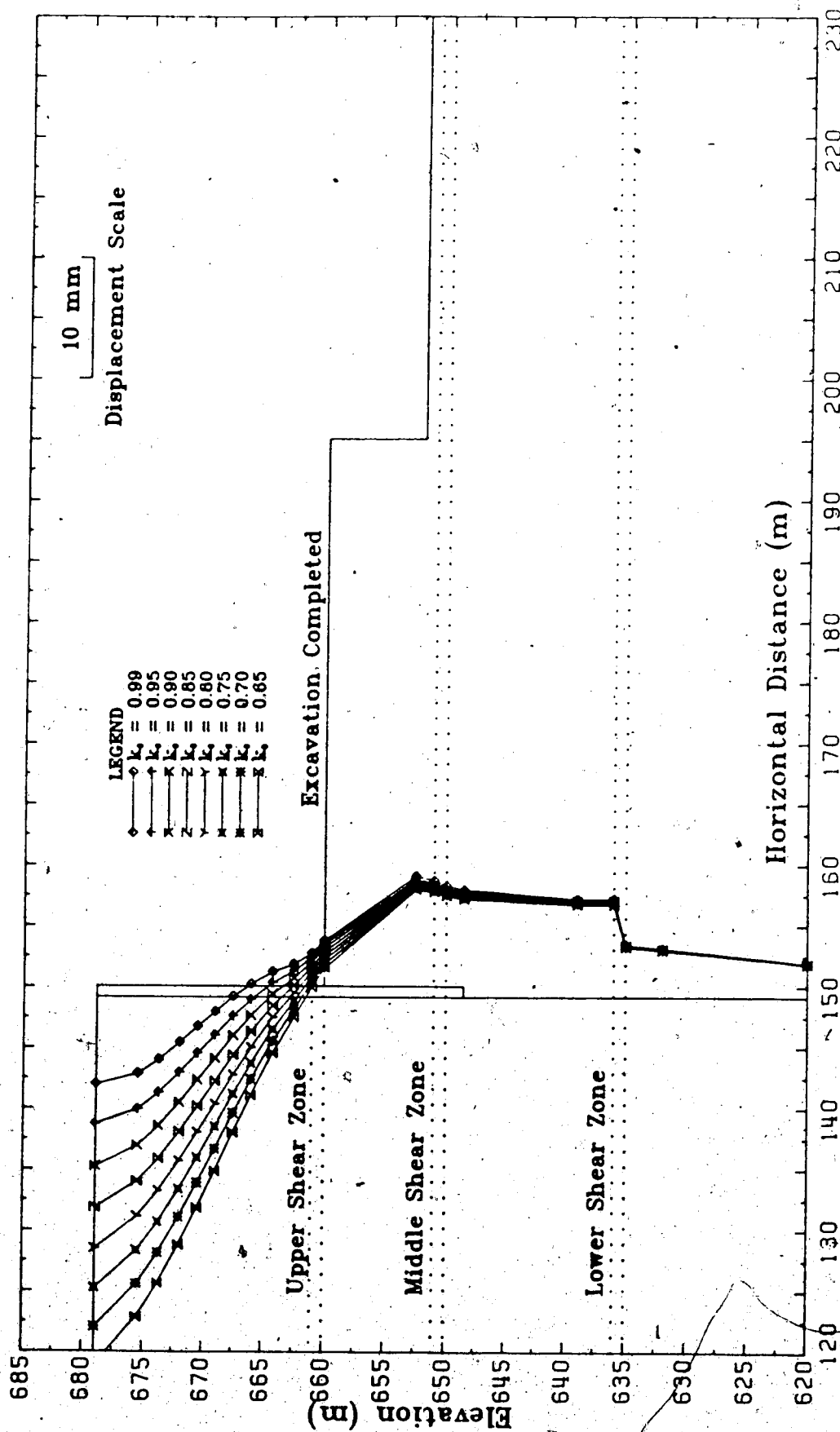


Figure 6.17: Movement of Soil behind Tangent Pile Wall - Linear Elastic Analysis

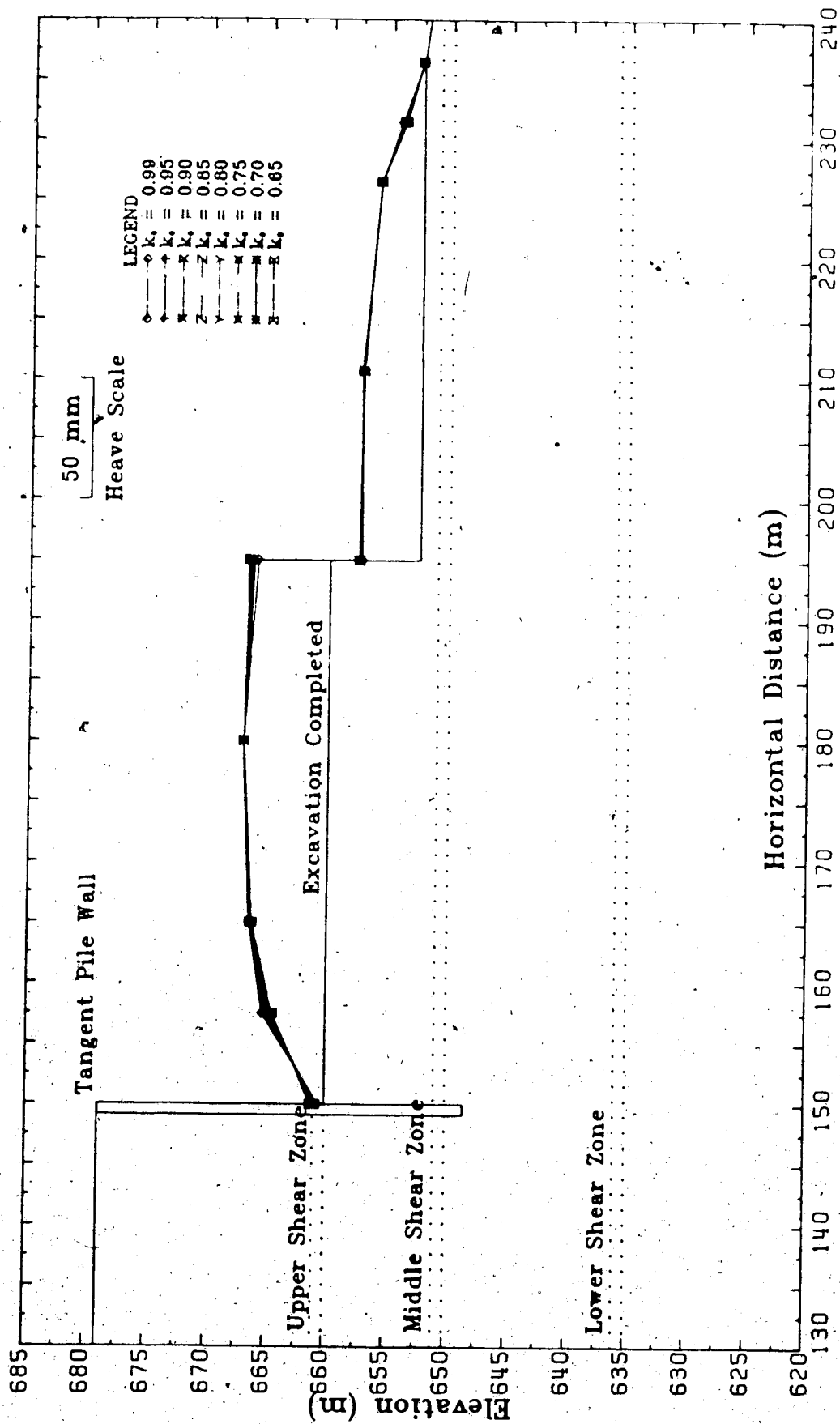


Figure 6.18: Heave of Excavation Floor - Linear Elastic Analysis

movement along the lower shear zone and the heave of the excavation floor. The effect of the value of k_0 on both the horizontal movement behind the tangent pile wall and the heave of the excavation floor is not very significant for the most probable range of k_0 values for this site. The k_0 value of 0.80 is believed to be the most representative value and will be used in subsequent analyses. Results in this section indicate that slight departures from the value of 0.80 will not affect the results significantly and definitely cannot account for the discrepancy between the predicted and observed movement of the excavation.

6.8 The Effect of Elastic Parameters on the Behaviour of the Excavation

One of the reasons for the under prediction of the amount of movement at the lowest shear zone and the heave of the foundation floor is due to the overstiffening of the material. Since the elastic modulus and Poisson's ratio are the only material parameters used in the elastic analysis, the results here suggest that the elastic parameters are probably too high. To observe the effect of the stiffness of the material on the behaviour of the excavation, the elastic modulus for each material were varied.

Six case will be considered as summarized in Table 6.3. In the first case the E value for the Edmonton Clay is reduced by 50%. The E value for the till is reduced by 33% in the second case. The E value for the Saskatchewan sands

Table 6.3 Summary of the values of the Elastic Modulus in the Linear Elastic Analyses

Case	Clay	Till	Shale	Shear Zone
1	24,133	137,900	>139,700	49,000
2	24,133	91,933	>139,700	49,000
3	24,133	91,933	90,000	49,000
4	24,133	91,933	90,000	3,000
5	24,133	91,933	90,000	1,000

Note - All values of Elastic Modulus are in kPa.

The Elastic Modulus of the shale for cases 1 and 2 increase with depth.

and gravel and the colluvium and fill are kept constant. In the third case the E value for the shale is reduced to 90,000 kPa and in the final 2 cases the E value for the lower shear zone are reduced to 3,000 kPa and 1,000 kPa respectively.

Figure 6.19 shows the effect of varying the elastic modulus on the mobilized friction along the lower shear zone. The reference case is taken from the result of $k_0 = 0.8$ with the E values used in previous analysis. The result of case 1 is obtained by reducing the E value of the clay from the reference case and the result of case 2 is obtained by reducing the E value of the till from case 1 and so on. It is seen that there is practically no change in ϕ value by varying the E values of the clay and till material. However the mobilized friction is increased by reducing the E value of the shale. The maximum mobilized friction is close to 14° as compared to 11.5° obtained earlier. By reducing the E value of the shear zone, the mobilized friction is reduced due to the fact that softer material tends to redistribute stresses to the adjacent stiffer material.

The effect of reducing the E value of the clay and till have an insignificant effect on the movement at the lower shear zone and only some effect on the movement of the soil behind the tangent pile wall as shown in Figure 6.20. By reducing the elastic modulus of the shale without reducing the elastic modulus of the lower shear zone (trying to simulate the condition of no shear failure at the lower

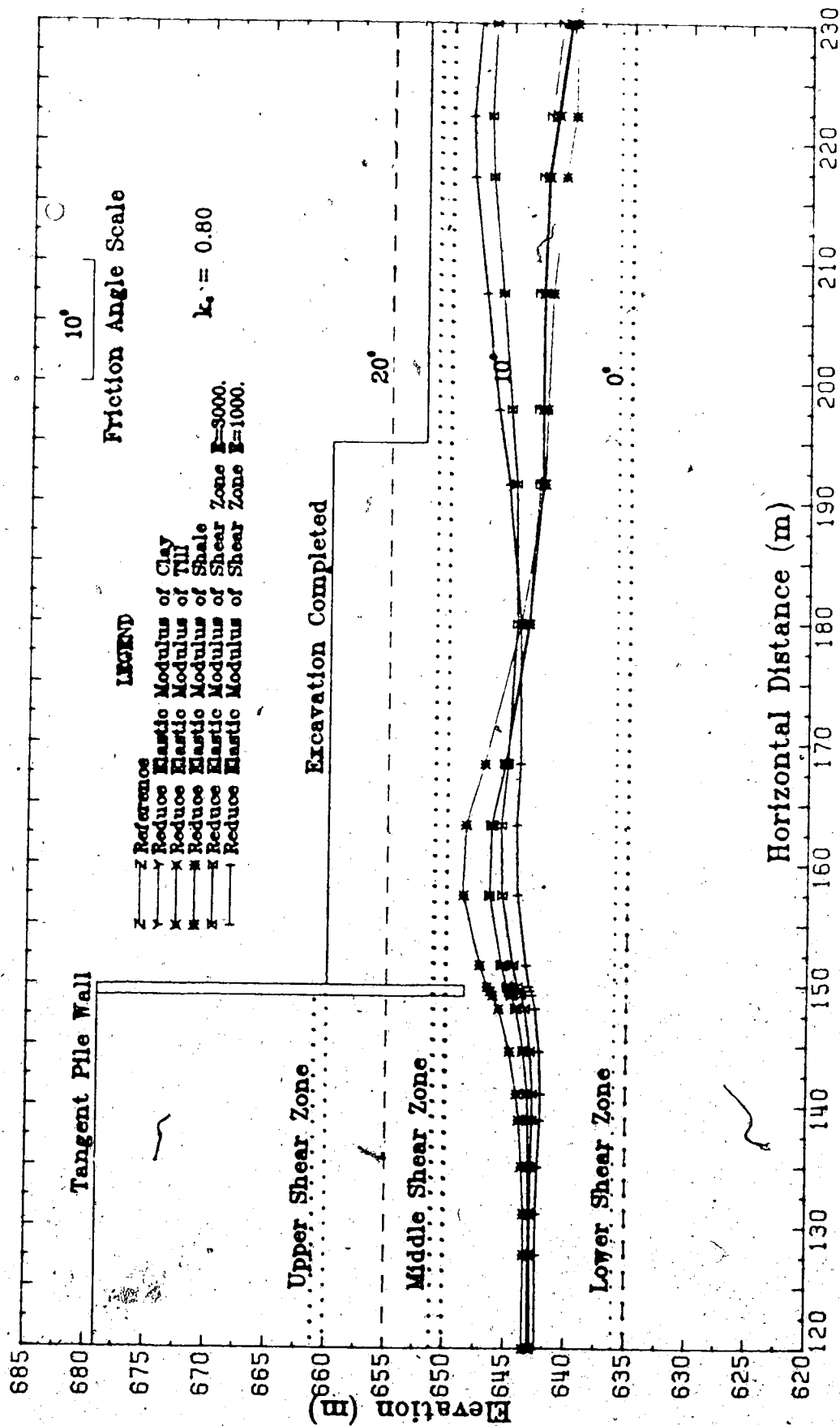


Figure 6.19: Mobilized Friction along Lower Shear Zone -Linear Elastic Analysis

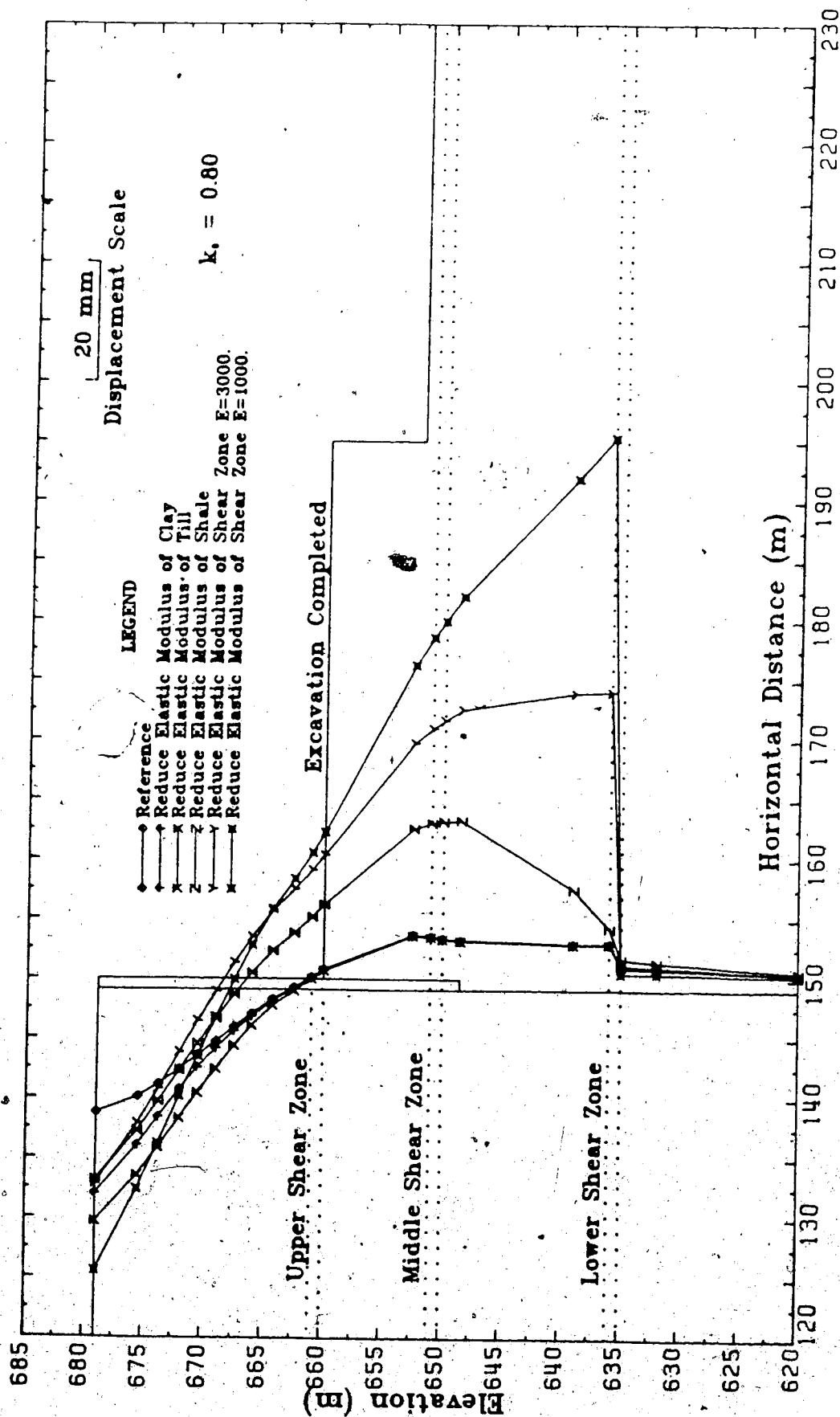


Figure 6.20: Movement of Soil behind Tangent Pile Wall - Linear Elastic Analysis

shear zone) increases the horizontal movement in the shale but not the movement at the shear zone. However substantial movement occurs at the lower shear zone when the E value of the lower shear zone is reduced. By comparing the results of case 4 and the observed movement of the slope indicator behind the tangent pile wall, close agreement can be obtained by varying the E values of the shale and the shear zone. This indicates that the E value for the shale in previous analyses was too high and shear failure at the lower shear zone has most likely occurred. Since the mobilized friction at the end of excavation is only 14° for case 4 as shown in Figure 6.19, the results here indicate that the actual peak friction in the shear zone may be lower than 14° and shear failure at the lower shear zone may have occurred prior to the completion of the excavation. There is no point in comparing the actual movement at the shear zone with calculated values from the elastic analysis because one can get close agreement by simply varying the E values of the material. However, with E values of 3,000 kPa, the movement at the lower shear zone is about 50 mm which is much higher than the observed value. Nevertheless the deflection of the soil behind the tangent pile wall from the elastic analysis closely resembles the actual observation.

The heave of the excavation floor is shown in Figure 6.21 and similar conclusions can be made. The effect of varying the E values for the clay and till have practically no effect on the heave but the E value of the shale is very

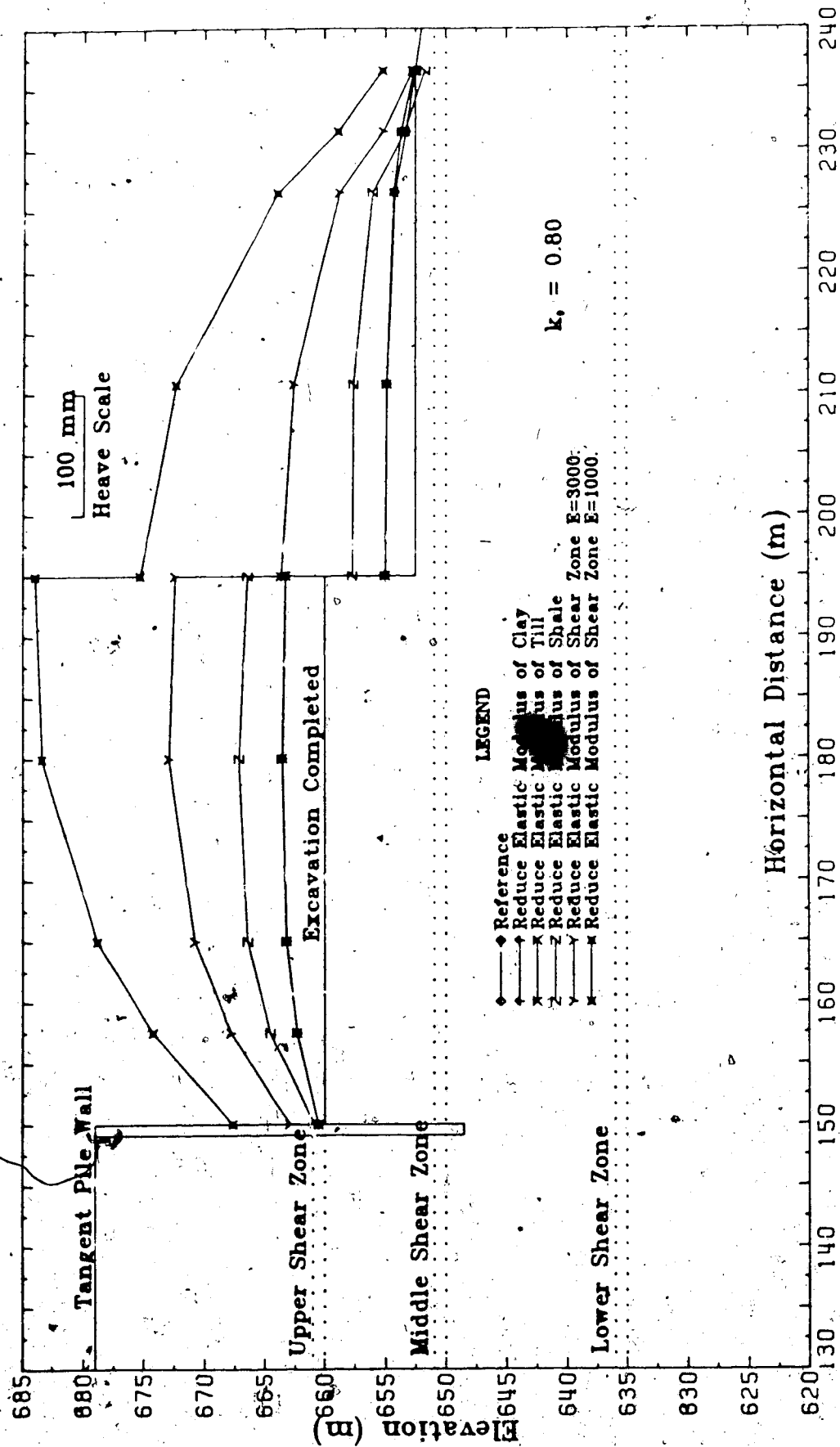


Figure 6.21: Heave of the Excavation Floor - Linear Elastic Analysis

important. Upward movement of 90 mm is obtained by reducing the E value of the shale to 90,000 kPa and more heave is obtained by reducing the E value of the shear zone. The increase in heave due to reducing the E value of the shear zone is unrealistic because if shear failure occurred at the lower shear zone, it is not likely that the volumetric deformation characteristics of the material will be decreased by the same amount as the shearing characteristics which are implicitly assumed in the elastic model.

The results from this analysis are very informative. It is seen from these results that the stiffness of the shale is very important with respect to the mobilized friction along the lower shear zone, on the deflection of the tangent pile wall and on the heave of the excavation floor. This is because movement of the soil above the middle shear zone is controlled by the tangent wall which then transfers the load to the underlying shale. The effect of the excavation causes stress relief and upward movement of the shale which in turn transmits such effects to the lower shear zone. If the shale is very stiff, the transmission of the effect of the excavation to the lower shear zone is reduced. This results in lower mobilized shear strength at this location. Also stiffer shale will give less movement of the tangent pile wall as well as less upward movement of the excavation floor. Moreover, the flow of the soil between the tip of the tangent pile wall and the lower shear zone is impeded because of the stiffness of the shale. Therefore, unless the

stiffness of the shale is reduced, it is unlikely that the finite element model will yield movement comparable to the actual field observations.

6.9 Non-Linear Finite Element Analysis

It is seen from the previous section that the elastic finite element model does not give accurate results in predicting the behaviour of the excavation. Moreover, it is not realistic to assume a very low value of elastic modulus for the entire lower shear zone simply in order to match the observed movement. In addition, the elastic model cannot predict the extent of the shear zone in the evaluation of the stability of the excavation.

Before presenting the results of the non-linear analysis, it will be useful to first summarize the results of the linear elastic analysis. The result from the linear elastic analysis indicate the following:

1. The effect of K_0 for $1.0 > k_0 > 0.65$.
 - a. Due the switch-on-gravity stresses, the maximum mobilized friction angle at the lower shear zone ranged from 11° to 17° for k_0 of 1.0 to 0.65 respectively at a location close to the face of the slope. Over the majority of the shear zone underneath the excavation the mobilized friction ranged from 2° to 13° .
 - b. At the completion of the excavation, the maximum mobilized friction occurred at a location about 15m

from the tangent pile wall with values ranging from 10° to 16° for k_0 of 1.0 to 0.65 respectively.

- c. There are some effects on the amount of movement of the tangent pile wall above the bottom of the excavation but very little or no effect below the bottom of the excavation and practically no effect on the heave of the excavation floor.

2. With a K_0 value of 0.8, the effect of the elastic modulus of various material are:

- a. The elastic moduli of the clay and till have very little effect on the shear zone movement and the amount of heave.
- b. The elastic modulus of the shale above the lower shear zone has a very important influence on the heave of the excavation floor. The elastic moduli for the shales presently used are too high and result in a very stiff layer and under prediction of the amount of heave.
- c. The finite element model has under predicted the movement at the location of the lower shear zone. Reducing the elastic modulus at this location increases the amount of movement. This implies that shearing has very likely occurred at this location. This leads to a reduction of shearing resistance.
- d. The mobilized friction at the final stage at the lower shear zone when excavation is completed for $k_0 = 0.8$ varies from 10° to 14° . Reducing the modulus

of shale increases the mobilized friction from 10° to 14° .

It seems clear that the properties of the shale are very important with regard to the heave of the foundation floor. The value of k_0 is important to the amount of mobilized strength along the shear zone which, in turn, affects the movement of the tangent pile wall at the location of the lower shear ~~zone~~.

Since the heave of the foundation floor is sensitive to the properties of the shale and from field observation that the amount of heave is not linear in relation to the volume of excavation, a non-linear model seems necessary in order to model the behaviour of the shale accurately. The hyperbolic model is a simple and effective model and was found to be applicable to a variety of soils, hence this model will be used here. The formulation of the model will not be discussed here. Those who are not familiar with the model should refer to the publications by Duncan and Cheng (1970), Konder (1963), Kulhawy (1972). However, there are some aspects of this model which deserve some attention.

There are several versions of the hyperbolic model and the one that is used here uses the elastic modulus and bulk modulus as the principal material parameters rather than the elastic modulus and the Poisson's ratio which are more commonly used (Duncan 1980). The hyperbolic model is developed based on triaxial stress conditions in which the tangent elastic modulus is derived from a deviator stress

versus axial strain plot. It is normally assumed that the strain at the beginning of the test is zero and the sample is subjected to isotropic stress condition. However, if the stress state is not isotropic, as is the case of $k_0 \neq 1$ in the field, then the soil is initially subjected to a nonzero deviator stress. If the definition of strain is still referenced to this state, then the hyperbola will not start from the origin. As discussed in chapter 4, the reference state of zero strain is quite arbitrary and therefore one can shift the origin of the strain measure and this problem will not exist.

The hyperbolic model was originally developed to simulate the non-linear behaviour of the soil during the construction of dams and other engineering structures. The application of the model to excavations has been made but one must realize that excavations are not the same problem as dam construction because excavation involves unloading and dam construction involves loading, although both types of loading could be monotonic. Loading here refers to an increase in deviator stress and unloading refers to a decrease in deviator stress. If $k_0 \neq 1$, then the stress path of a point in the soil will undergo unloading and should not follow the loading path of the hyperbola. Instead the unloading modulus should be used which is often assumed to be independent of the deviator stress and only dependent upon the confining stress. In applying the hyperbolic model to the unloading situation, the soil parameters must be

derived from the laboratory test with a similar stress path, that is, the laboratory test must be related to the field conditions as close as is possible.

In realizing these problems and the lack of time to perform laboratory tests, the parameters for the hyperbolic model have been estimated from actual field observations. The heave of the excavation floor provides a continuous record of the amount of upward movement which can be used to obtain the parameters for the hyperbolic model. Based on this information, EBA Engineering Company has suggested the following parameters for the shale:

c = Cohesion = 48 kPa

ϕ = Friction angle = 21°

K = Modulus number = 327.3

n = Modulus exponent = 1.59

K_B = Bulk modulus number = 273.

n = Bulk modulus exponent = 1.59

R_f = Failure Ratio = 0.0.

These parameters were obtained by assuming one dimensional deformation and triaxial stress condition of the shale below the excavation. This leads to an over estimation of the stiffness of the shale as will be seen later. Since the actual condition is closer to plane strain than plane stress or axisymmetric conditions, the apparent modulus under plane

strain conditions is larger than that under plane stress or axisymmetric conditions due to the lateral constraint imposed by the plane strain condition. The modulus number in the hyperbolic model reflects the pressure dependent behaviour of the material. An n value equal to 1 implies linear increases in elastic modulus with increase in σ_3 . Therefore an n value greater than 1 indicates more rapid increases in modulus than the increase in σ_3 . If σ_3 is linearly related to the depth of the soil, then the depth effect is amplified. The variation of elastic modulus shown earlier indicates that the depth effect is constant or diminishing and therefore the n value should be equal to or less than 1. The failure ratio R_f reflects the change in elastic modulus due to the shearing effect. Since excavation represents the unloading process and the unloading modulus is not dependent upon the R_f value, therefore the value of R_f is not used in the present model. The values of n , m , K , K_B for the shale will be varied in the non-linear analysis in order to obtain agreement with field observations.

In selecting the value of k_0 for the non-linear analysis, it is believed, from geological evidence that a preglacial channel is present to the north of the excavation and due to the proximity of the river valley south of the excavation that the k_0 value for the site should not be greater than 1. Also from local experience on various engineering structure, k_0 values of higher than 1 are very unlikely. From the result of linear elastic analysis, it is

seen that for k_0 values less than 0.65, the mobilized friction along the shear zone will be higher than 14° which indicates that the lower shear zone will be pre-sheared due to the formation of the river valley and the gravity stresses. Following careful examination of a soil sample obtained at the location of the lower shear zone, Dr. N. Morgenstern indicated that the bentonite layer was not pre-sheared before the excavation. Therefore k_0 values of 1.0 and 0.65 are considered to be the most probable limits. For a k_0 value of 0.8, the elastic analysis indicates that the maximum mobilized friction at the lower shear zone at the completion of the excavation process is about 14° . Therefore shearing occurs only at the final stage of the excavation which seems to be a little late because substantial movement had been observed after the second level of excavation. From the results of the elastic analysis, it is seen that a lower E value of the shale increased the mobilized strength. Therefore the use of the hyperbolic model for the shale may help to increase the amount of mobilized strength at the lower shear zone. Also a slightly lower friction angle of 13° is used to trigger an earlier failure with k_0 of 0.8.

A final point is that the shearing of the upper and lower shear zone is impeded by the tangent pile wall. The shearing of these two shear zones will not affect the overall movement of the excavation and linear elastic models are used for these two shear zones.

Based on these assumptions and arguments, the first non-linear analysis, Case 1, was performed. The result of the non-linear analysis is shown in Figures 6.23 and 6.24. The material parameters used in different cases are summarized in Table 6.4. The mobilized friction at the lower shear zone shown in Figure (6.23) is less than 13° and no failure has occurred. Because of no failure at the shear zone the movement at the lower shear zone is only 7 mm. The heave of the foundation is around 69 mm which is much less than the observed value of 100 mm. The movement of the tangent pile wall indicates that the n value used in the hyperbolic model is too high which results in a rapid increase of the elastic modulus with depth. The report by Duncan (1980) has quoted n values for a wide variety of material and reveals that the n value is between 0 and 1. Therefore, a n value of 1 is used for the next trial.

As shown in Figures 6.22 to 6.24 for Case 2, decreasing the value of n has led to larger horizontal and upward heave of the shale. However, the mobilized strength at the lower shear zone is still less than 13° and therefore very little slip has occurred. The final heave of the foundation floor is 94 mm which is close to the observed value. It seems that with k_0 of 0.8 and these values of the soil parameters, a failure at the lower shear zone is not likely to be triggered. To note the effect of shearing at the lower shear zone on the movement at point A (Figure 6.23) and the heave of the excavation floor, a residual friction of 7° was used.

Table 6.4: Summary of Material Parameters in Non-Linear Analysis

Case	Ko	Till E (kPa)	Clay E (kPa)	Shale				Lower Shear Zone			
				n	k	m	b	E (kPa)	$\sigma(p)$	$\sigma(r)$	
1	0.8	91933	24133	1.59	327.3	1.59	272.8	49000	13	7	
2	0.8	91933	24133	1.00	327.3	1.00	272.8	49000	13	7	
3	0.8	91933	24133	1.00	327.3	1.00	272.8	49000	7	7	
4	0.8	91933	24133	1.00	327.3	1.00	272.8	34500	7	7	
5	0.8	91933	24133	0.80	430.8	0.80	359.0	49000	7	7	
6	0.65	91933	24133	1.00	330.0	1.00	550.0	49000	14	7	

Note:

$$\nu(\text{till}) = 0.42$$

$$\nu(\text{clay}) = 0.45$$

$$E(\text{Sands and Gravel}) = 241325 \text{ kPa}$$

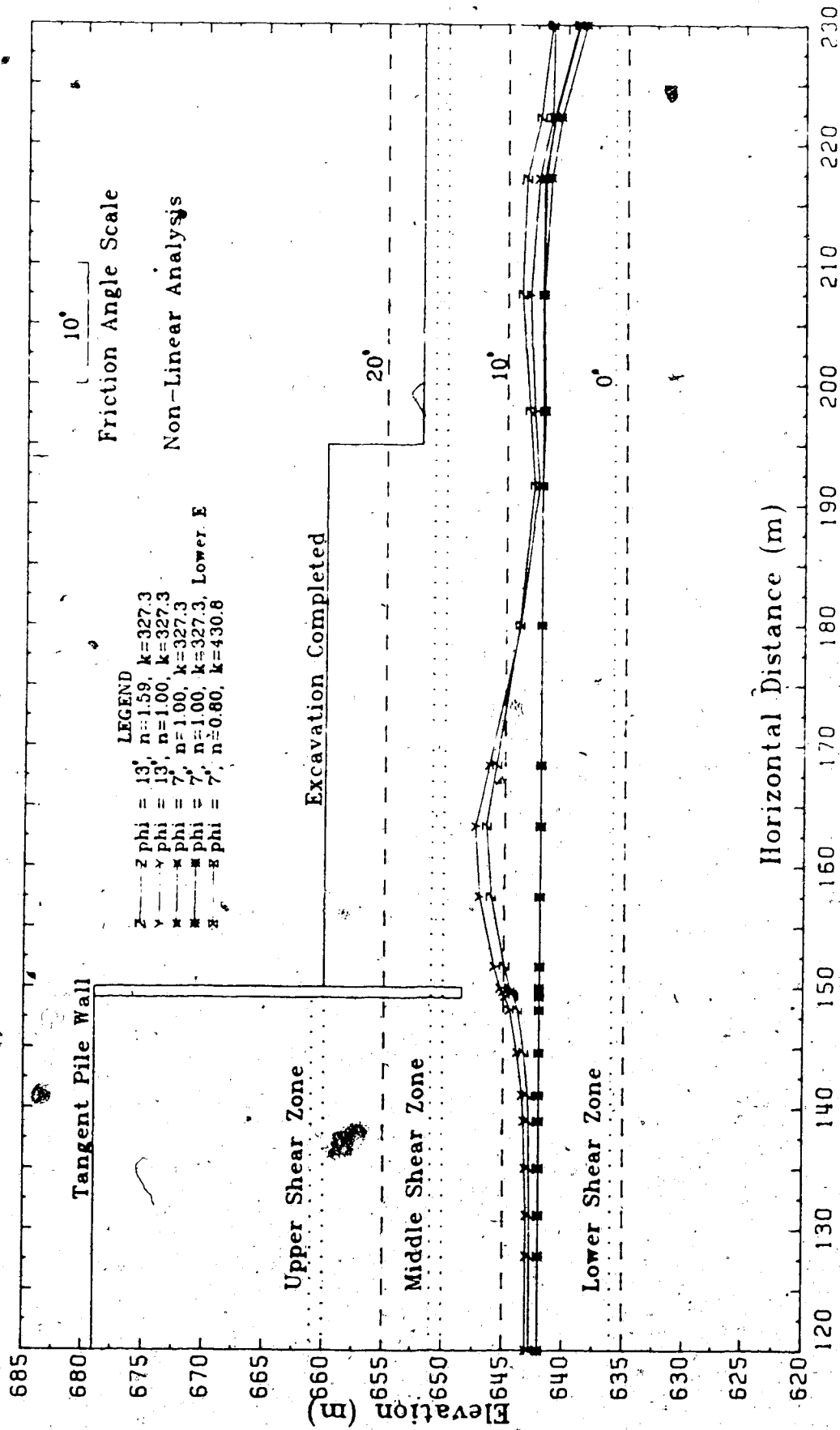


Figure 6.22: Mobilized Friction along Lower Shear Zone - Non-Linear Analysis

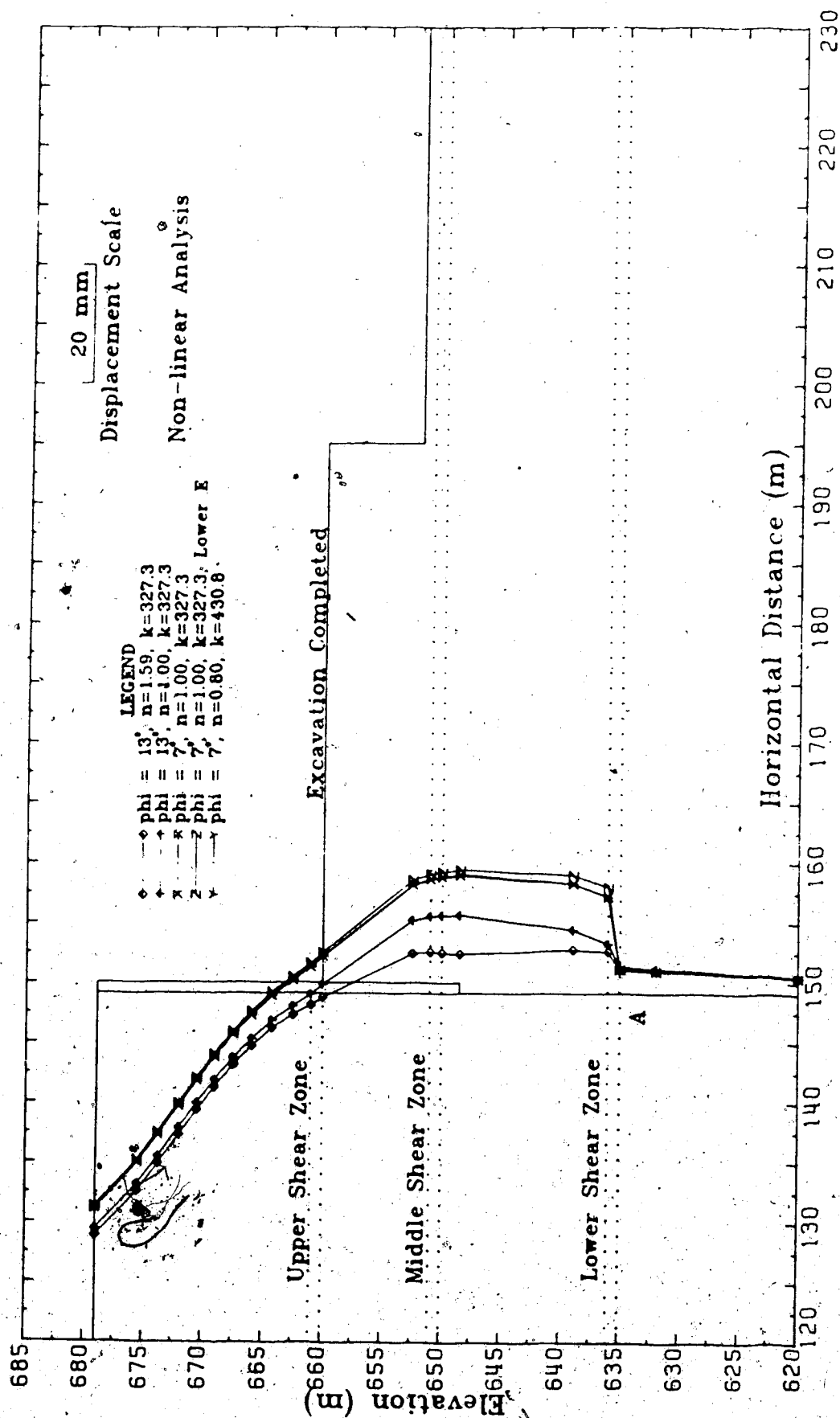


Figure 6.23: Movement of Soil behind Tangent Pile Wall - Non-Linear Analysis

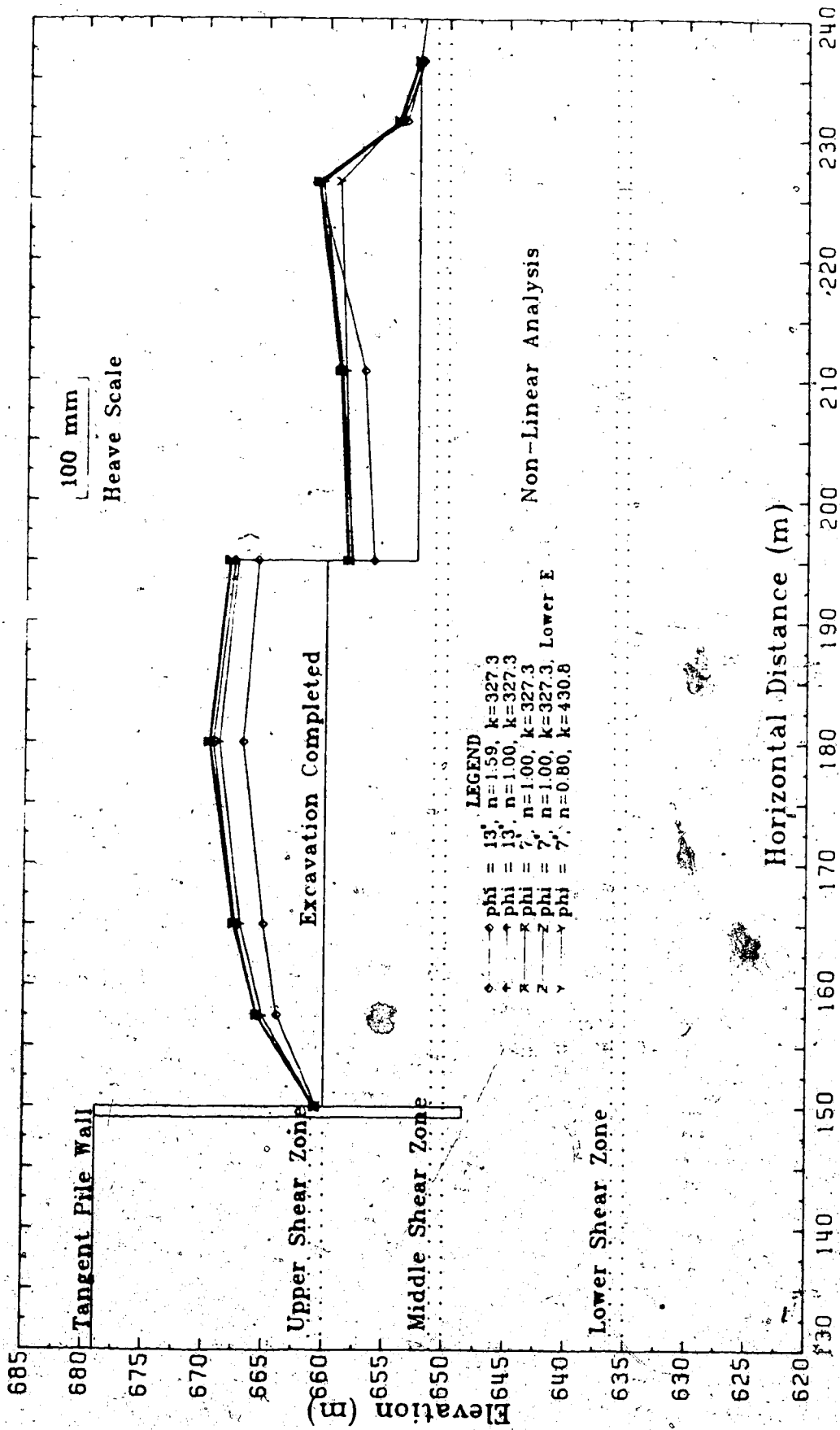


Figure 6.24: Heave of Excavation Floor - Non-Linear Analysis

for the lower shear zone. This does not imply that the shear zone has been pre-sheared but to investigate whether or not the amount of movement can be matched if the lower shear zone has yielded with the values of the material parameters used in the analysis.

The results of Case 3 shows about 16 mm of movement at the lower shear zone (point A, figure 6.23) as compared to 30 mm observed in the field at the completion of the excavation. There is a noticeable but small increase in the heave of the foundation floor. The mobilized strength at the lower shear zone is, of course, 7° .

At this stage, it seems that even if the lower shear zone has been sheared, the movement at the lower shear zone is still lower than the observed value. Before the entire situation is re-analyzed, two more analyses were performed to study the sensitivity of other variables which have not been mentioned so far. A lower elastic modulus was used in case 4 for the lower shear zone and the movement increased to 18 mm which is still too low. The n value of the shale was decreased to 0.8 in case 5 but the elastic modulus of the shale at 40 m depth was maintained by increasing the K value. This is to check the effect of a slower rate of increase of the elastic modulus with depth. No significant increase in movement was observed.

It is seen from the above discussion that better agreement of the heave of the foundation floor is obtained by using the hyperbolic model with a lower value of n but

the movement at the lower shear zone is underestimated by the finite element model even assuming the residual friction angle at the lower shear zone. At this stage it seems appropriate to reconsider the assumptions made earlier in this analysis.

The first assumption that should be reconsidered is the value of k_0 . It is seen that k_0 of 0.8 will not trigger movement at the lower shear zone for a friction angle of 13° even with the use of the hyperbolic model in modelling the shale. Also, results indicate that the mobilized friction at the completion of the excavation is around 13° . Even if the peak friction for the shear zone has been over estimated by about 2° , the failure of the lower shear zone will still occur too late. It is observed from the slope indicator measurements that substantial movement has occurred after the second lift of excavation. With this value of k_0 it is not likely to mobilize 12° to 14° of friction at the second lift of excavation. Moreover, even though the soil has been pre-sheared before which contradicts observation, the movement at the lower shear zone is still under-predicted by the finite element model. Based on this argument a different k_0 value should be used.

Since the k_0 value is believed to lie between 0.65 and 1.0, a value of k_0 of higher than 0.8 will only decrease the mobilized friction at the lower shear zone. Moreover it is observed that slip had occurred at the earlier stage of the excavation, therefore, the mobilized friction due to the

in-situ stresses should be close to the peak value. It is seen from Figure 6.25 that k_0 of 0.65 gives a mobilized friction less than but close to 14° on most parts of the lower shear zone. Therefore k_0 of 0.65 was used for the next trial.

Decreasing the value of k_0 will result in less energy release due to excavation (Bjerrum, 1967). Since the excavation is very close to the river valley, a slight decrease will not have a very significant effect on the amount of strain energy released. Since the lower shear zone is modelled using the elastic brittle plastic model discussed in Chapter 3 with a peak friction of 14° and a residual strength of 7° and due to the brittle behaviour of the material, there will be some energy released once the shearing process has been triggered.

Many trial and error analyses have been performed to study the effect of the n and K values on the amount of heave and movement at the lower shear zone. The results of these trials will not be presented here but basically it was found that decreasing the n and K values will lead to more movement at the lower shear zone and also will result in a larger heave of the foundation. To obtain a horizontal movement of about 30 mm at the lower shear zone requires an n value of about 0.5 with a K value of 327.3. But a final heave in excess of 150 mm will result. Therefore, there must be other parameter(s) which are essential but, to this point, have not received sufficient attention.

In the hyperbolic model, the parameters other than n and K parameters, are the m and K_B parameters which represent the variation of the bulk modulus with σ_3 . Presently the n and m values are taken to be the same, therefore the minor principal stress σ_3 will have the same effect on the elastic modulus and the bulk modulus. The value of K_B is chosen to give a Poisson's ratio of 0.3. It is seen from Table 6.1 that the Poisson's ratio for the shale should be about 0.4. A lower value of Poisson's ratio indicates that less deformation will occur in one direction when the material is strained in the other direction. Also a lower Poisson's ratio represents more volume change or a lower bulk modulus. Since the bottom of the excavation floor is 20 m above the lower shear zone, the effect of the excavation is transmitted to the lower shear zone by the deformation of the shale. By having a lower Poisson's ratio for the shale, the material is able to deform more easily due to its ability to change volume, and therefore the stress and energy release due to the excavation can be absorbed more easily by the shale and less energy is transmitted to the lower strata than in the case with a higher Poisson's ratio. In other words the effect of the excavation is reduced due to a lower Poisson's ratio. In realizing these facts, a Poisson's ratio of 0.4 was used. The material parameters used in the final case, case 6, are summarized in Table 6.4.

The results for case 6 are shown in Figures 6.25 to 6.29. Figure 6.25 compares the observed heave in the shale (Heave Gauge No. 4) and the heave predicted by the finite element model. Measurements were made at seven different depths in the shale and not all of these point may coincide with the nodal coordinates in the finite element model. Point 3 is not shown for comparison because the nearest nodal point is at least 3 m away. Average values from points 5 and 6 are used to obtain vertical movement between these points for comparison with the finite element model. Figure 6.25 shows that the finite element model not only predicts the final amount of heave at the end of excavation, but also yields reasonable agreement throughout the depth of the shale and at different stages of the excavation. Figure 6.26 shows the heave of the excavation floor at different stages of the analysis.

Figure 6.27 shows the movement of the tangent pile wall and the shale at different stages of the excavation. In comparing the results from the finite element analysis with field observation it is seen that the response of the actual excavation is not instantaneous as in the case of the finite element model. Movement is observed some time after the completion of the excavation. The horizontal movement at the lower shear zone was measured to be 18 mm at the completion of the excavation but eventually increased to 30 mm several months later. Therefore, movement recorded at the time of the completion of certain stage of the excavation does not

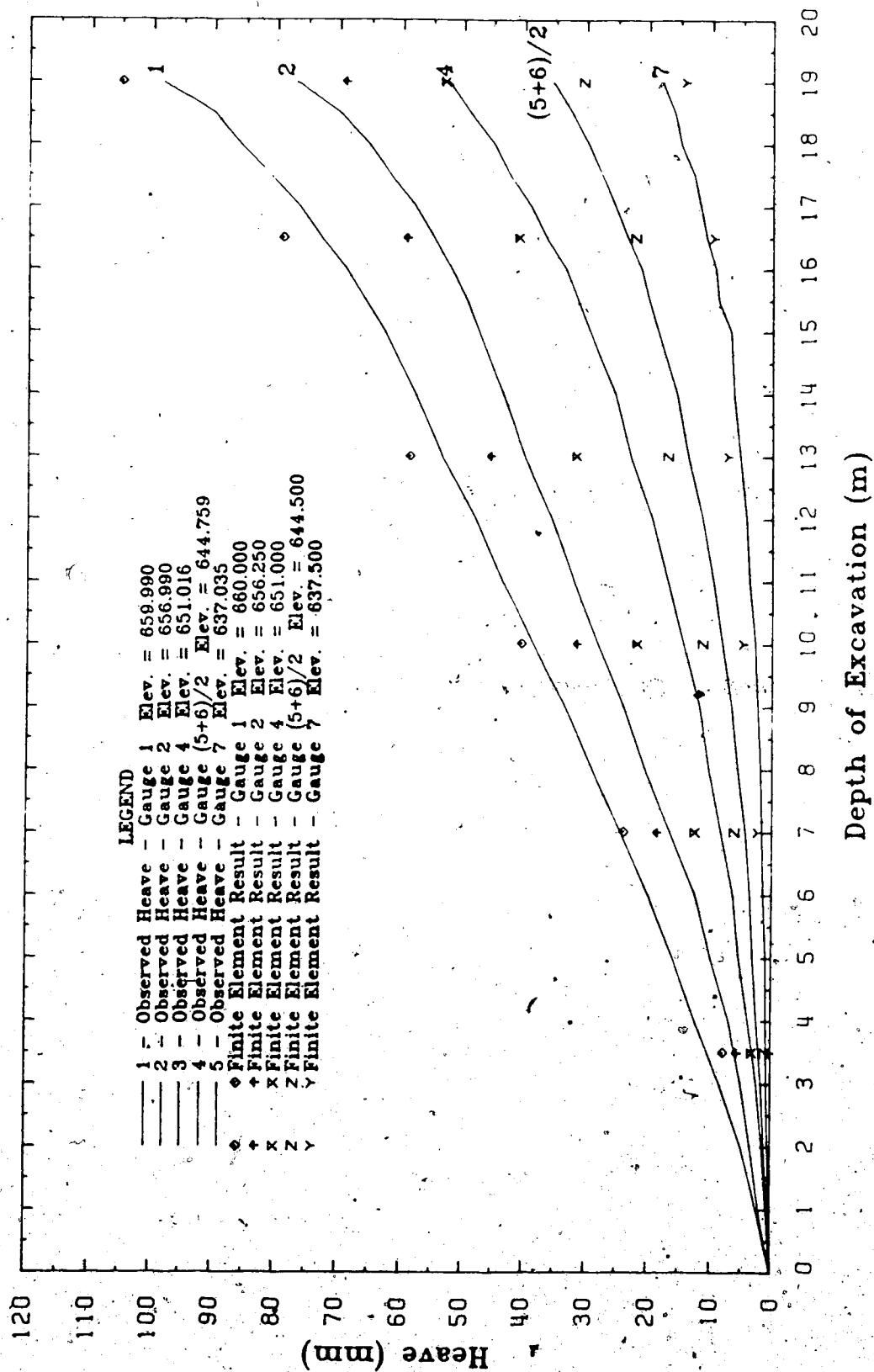


Figure 6.25: Comparison of Observed and Computed Heave -
Final Non-Linear Analysis

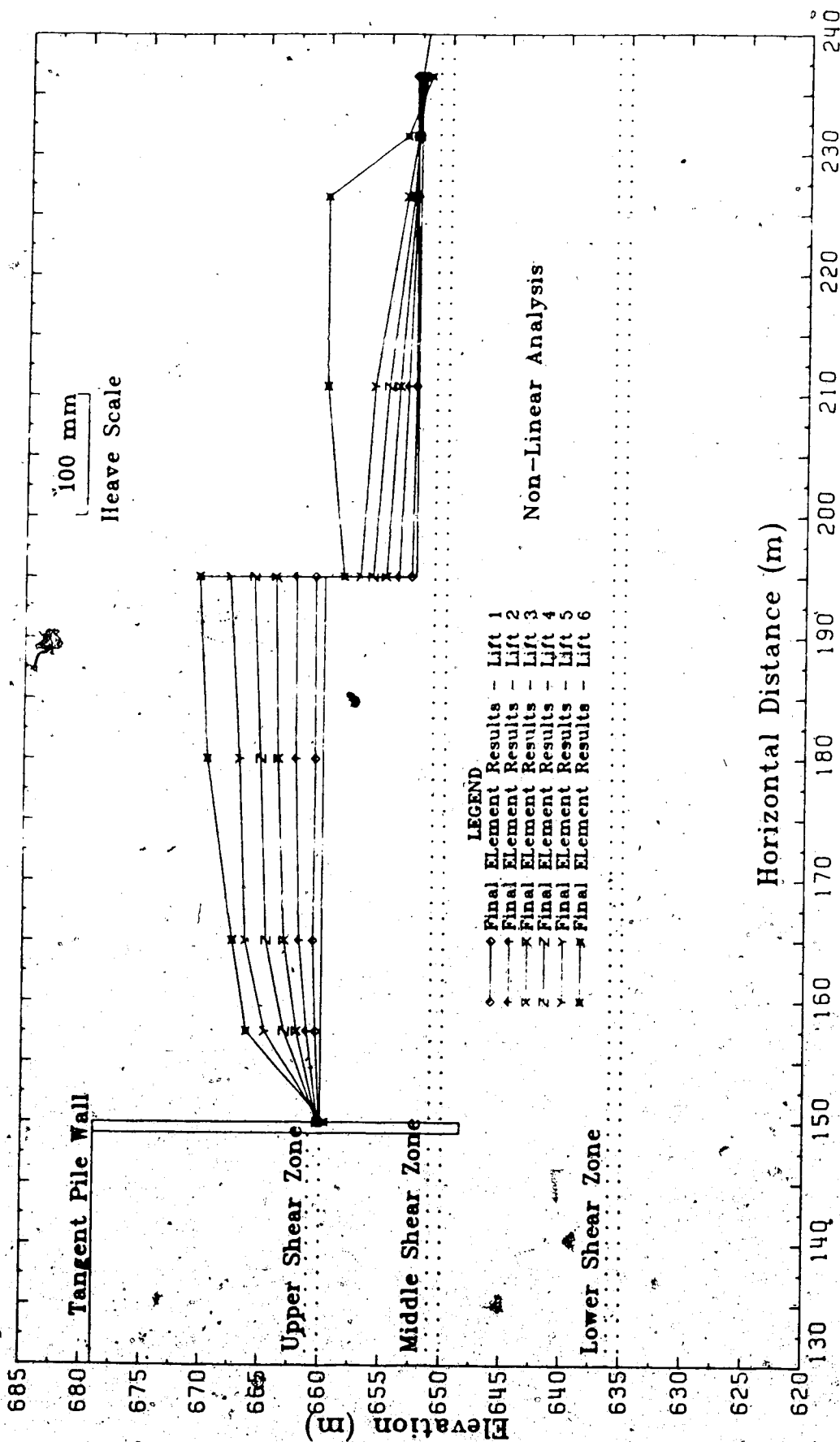


Figure 6.26: Heave of Excavation Floor - Final Non-Linear Analysis

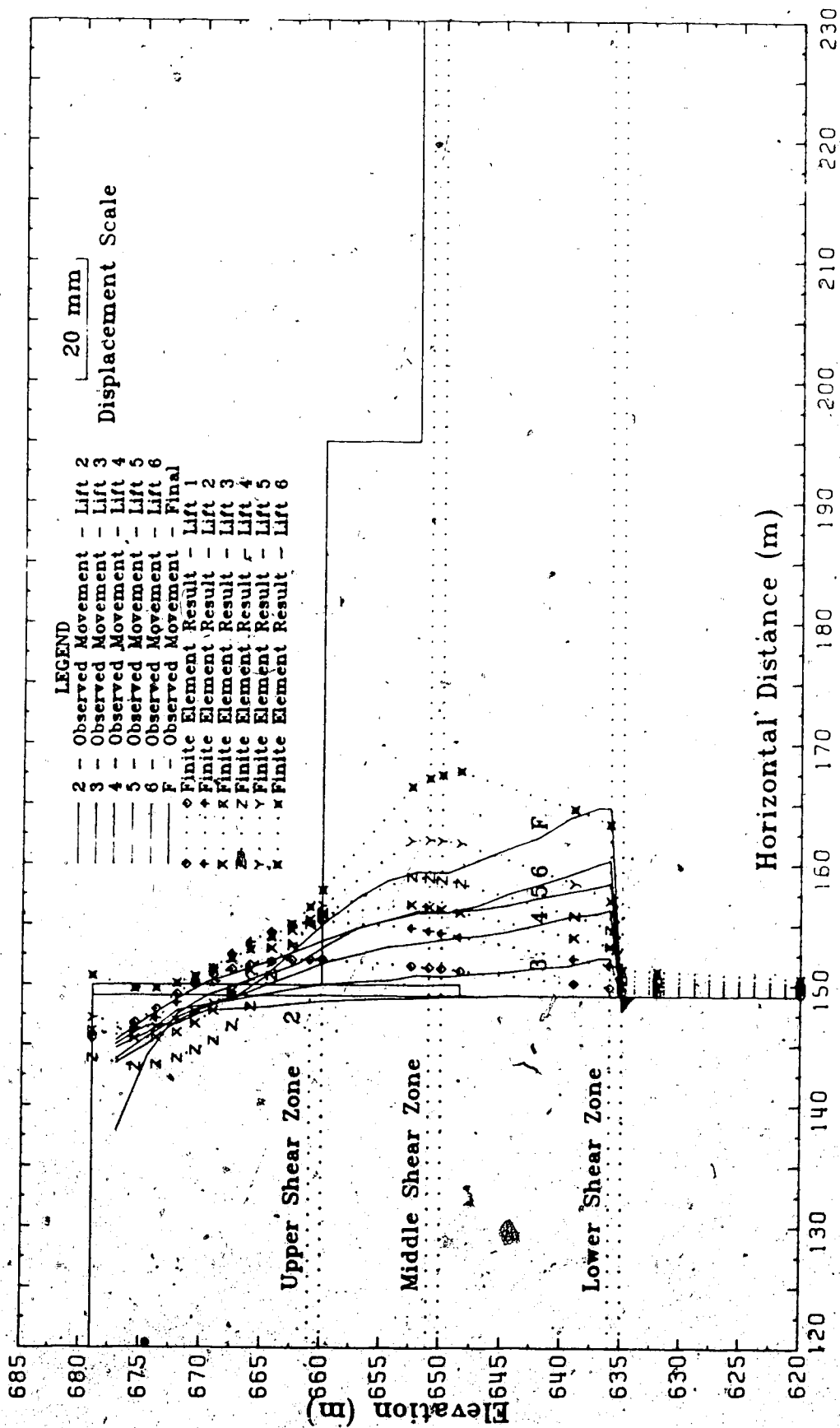


Figure 6.27: Movement of Soil behind Tangent Pile Wall -
Final Non-linear Analysis

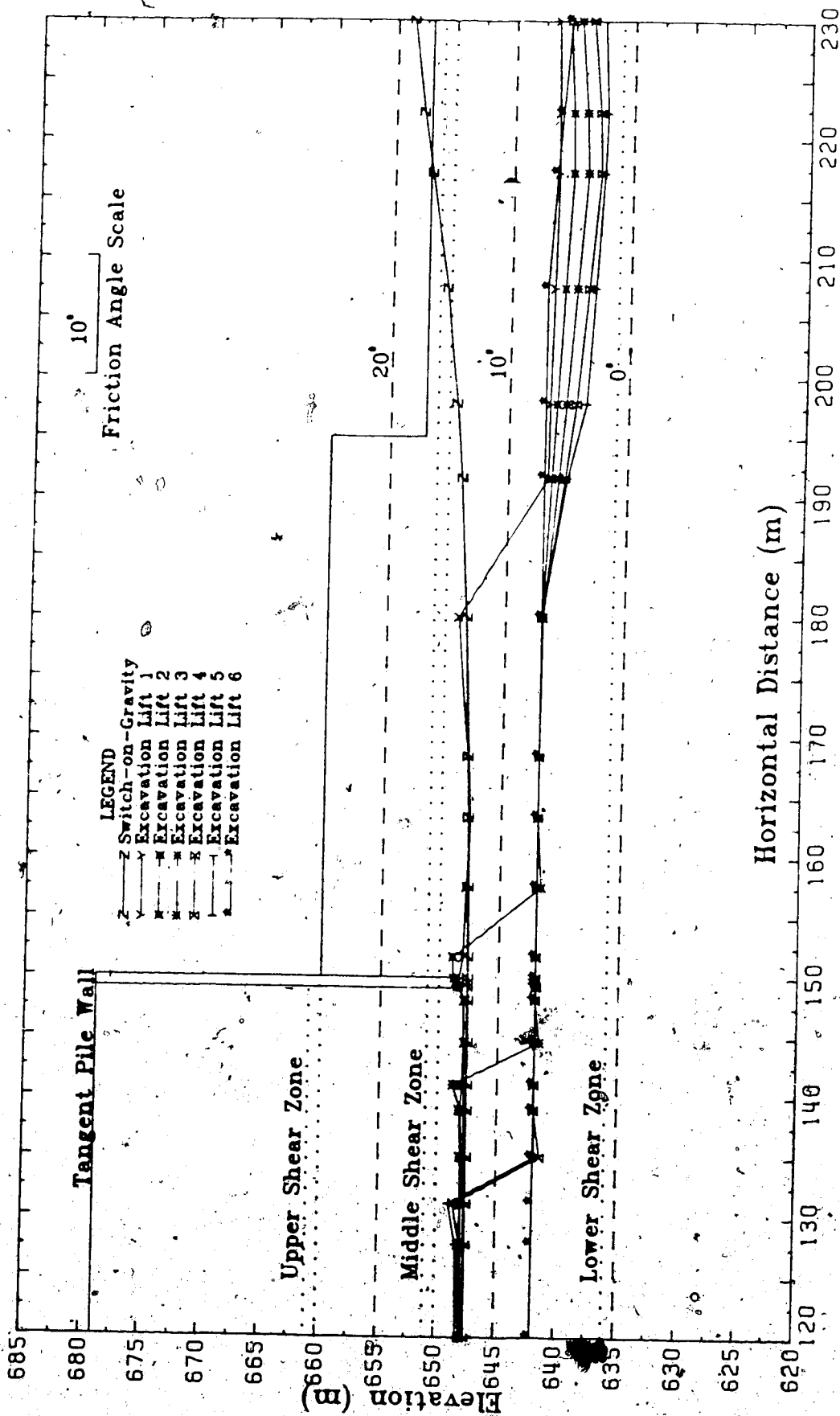


Figure 6.28: Mobilized Friction along Lower Shear Zone -
Final Non-linear Analysis (1)

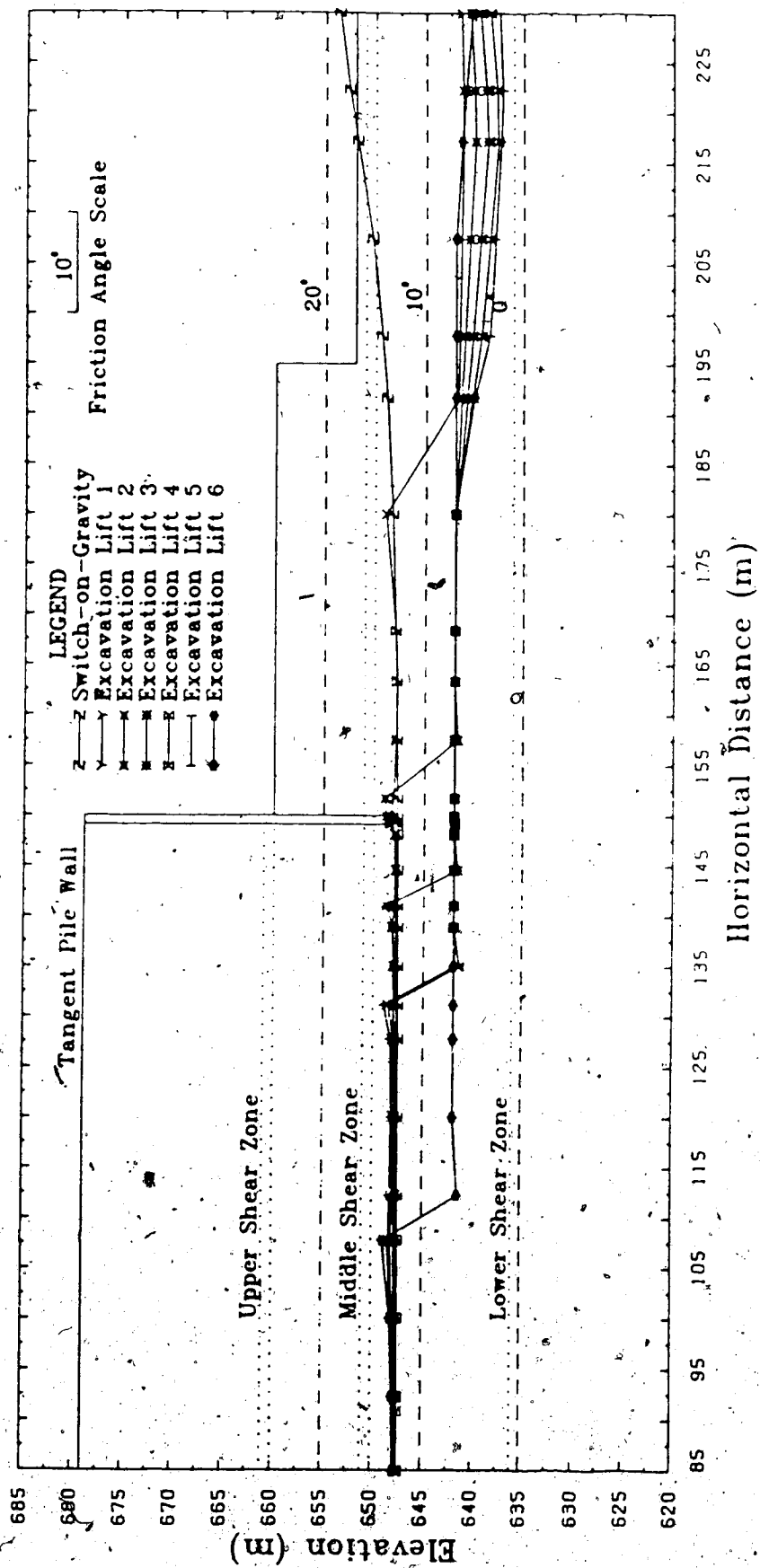


Figure 6.29: Mobilized Friction along Lower Shear Zone - Final Non-Linear Analysis (2)

correspond to the effect of that stage of the excavation. The actual movement due to that stage is larger and occurs at a later time. Since the excavation process is continuous and did not allow movement of the soil to stabilize before construction proceeded further, the exact amount of movement was difficult to estimate until the excavation was completed. Therefore, the finite element solution is the result of assuming equivalent stiffnesses over the duration of loading.

Figure 6.27 shows a final movement of 28 mm at the location of the lower shear zone predicted by the finite element model as compared to 30 mm observed. The final slope indicator reading was taken five months after the completion of the excavation when movement had more or less stabilized. The finite element results show a larger movement in the shale than that actually observed. The cause of this discrepancy is not thoroughly understood but it is suspected that anisotropy and the swelling behaviour of the shale may be part of the cause.

The mobilized friction at the lower shear zone at different stages of the analysis is shown in Figures 6.28 and 6.29. The mobilized strength due to the switch-on-gravity stress is below 14° for the most part of the shear zone except near the valley wall. Therefore, it is expected that the shear zone may be pre-sheared near the valley wall. The effect on the mobilized strength due to the first lift of excavation is quite large. The decrease in

mobilized friction near the valley wall is due to the switch-on-gravity stresses and is not due to the excavation process. Initiation of the shear zone occurs at the second stage of the excavation. The shear zone at this stage has propagated in excess of 25 m to a position near the tangent pile wall. At the same time unloading at the shear zone occurs near the valley wall, therefore the mobilized strength has decreased to a value below the residual friction angle of 7° . Excavation of the third lift extended the region of shearing by about 10 m to a position just past the tangent pile wall and the slope indicator SI-804. Observation from this slope indicator showed substantial movement and shearing during the second lift of the excavation. This agrees with the prediction from the finite element model. An additional 10 m of propagation of the shear zone is obtained in the fourth lift of excavation. However, essentially no propagation for the fifth lift is obtained. As shown in Figure 6.27 the tangent pile wall shows a slight forward tilt towards the excavation both predicted by the model and observed by the slope indicator. The excavation of this lift corresponds to the removal of the Saskatchewan sands and gravel which is a rather stiff layer in comparison with the rest of the material. The sands and gravels have been acting as a lateral support therefore removal of this rather stiff support lead to a slight forward movement. In reality the stiffness of the sands and gravel is highly stress dependent, and therefore a gradual

decrease in stiffness during the excavation process will be more realistic. Although very little propagation of the shear zone is predicted during the excavation of the fifth lift, movement in the order of 5 mm at the lower shear zone is obtained. The final lift of excavation has triggered a substantial shear zone propagation to about 40 m behind the tangent pile wall. Note that the mobilized friction at the shear zone near the valley wall increased during the excavation process. This is because the shear zone has propagated to a sufficient extent and the shearing resistance is so low that the whole excavation is moving towards the river valley and thus increases the mobilized strength near the valley wall. Slope indicator measurements also have indicated substantial movement in the order of 15 mm for the final stage of the excavation. This is in agreement with the prediction by the finite element model.

6.10 Conclusion

The finite element models presented in this thesis have been applied to the analysis of a realistic engineering problem. It is seen that although the model is capable of modelling the behaviour of the soil and structure in this case, the lack of knowledge of the actual site conditions, the uncertainty concerning the most representative model, and the values of the associated parameters, present much difficulty in obtaining the actual behaviour of the structure. The usefulness of the linear-elastic analysis is

demonstrated clearly in understanding the behaviour of the structure and the importance of various components to the overall response of the system. This information is subsequently used in guiding the non-linear analysis.

It is noted that the behaviour of the excavation is sensitive to various factors which include the value of k_0 and the stress strain behaviour of the shale as well as the brittleness of the shear zone. Therefore, it is seen that accurately modelling the behaviour of only part of the structure, for example the shear zone, is not sufficient to obtain the correct response. The interaction with the adjacent material in producing the overall response is equally important. Nonetheless the results here are very encouraging in applying the finite element model to real engineering analyses.

7. CONCLUSIONS

7.1 Conclusions

The ability to model strain softening material is a necessary condition to obtain a solution to the problem of progressive failure as outlined in Chapter 1. It has been demonstrated clearly that the the plasticity formulation presented in Chapter 2 can be applied in a strain softening material model. The strain softening model discussed in Chapter 2 was introduced by Prevost and the finite element formulation is derived in this research. This model is limited to two independent material parameters when four independent material parameters are usually most desirable. In analyzing strain softening materials using the finite element method, there are some departures from the usual approach since the stiffness matrix for elements of strain softening material will not be positive definite. This requires a non-positive matrix solution scheme which is discussed in Appendix E.

The problem of positive definiteness is elaborated in some detail in Chapter 3 during the discussion of shear band bifurcation. The necessary conditions for shear band bifurcation are shown to be satisfied using the finite element formulation presented in Chapter 2 for some plasticity models. The ability to capture shear band bifurcation is demonstrated in the exercise of modelling the process of the formation of shear bands in a plane strain

test and also under a dam foundation. An elastic brittle plastic model is introduced in this chapter to model the behaviour of very sensitive soil. Interesting results are obtained using this model in simulating the plane strain test experiment. It is seen that although the material is a brittle plastic material with distinct peak and residual strengths, the load-displacement response from this test actually reveals the material is elastic perfectly plastic without any decrease in strength after peak. This is due to the progressive failure of the sample and the brittle behaviour of the material. This aspect is studied further in Chapter 4 during the discussion of the hyperbolic strain softening model.

In Chapter 4 a new strain softening model termed the 'hyperbolic strain softening model' is introduced. This model has four independent parameters which are capable of modelling materials with different rates of post peak softening. The assumption, approximating the post peak behaviour of a real soil using a hyperbola, is demonstrated using the triaxial test results of a stiff clay. Reasonable agreement between the finite element model and the actual soil behaviour is obtained for this soil. The exercise of analyzing the bearing capacity of a strip footing reveals some very interesting results. It is demonstrated that different rates of post peak softening lead to different limit loads. This illustrates the effect of progressive failure on the capacity and the deformation response of the

soil mass comprising strain softening material. The conclusion from this exercise is that the observed deformation response of a soil mass, which can be a triaxial sample, is a system response which is dependent upon the rate of softening of the material and the extent of progressive failure occurring within the mass. Therefore, strictly speaking, one cannot deduce the material response from this system response for a strain softening material.

The formulation presented in Chapter 5 is a very general one in applying the principle of effective stress in fully drained or fully undrained analyses. This formulation can be used in any one of the models presented in this thesis which are all available in the computer program SAFE. The intent of this chapter is to introduce the use of effective stress parameters in finite element analyses. The formulation incorporates both the A and B pore pressure parameters. The pore pressure generated by the shearing of the material results in a non-symmetrical constitutive matrix. The deformation and pore pressure response of a thickwalled cylinder and a strip footing were obtained with an interesting pore pressure distribution for both cases.

In order to gain some confidence in the formulation being presented in real engineering problems, the deformation behaviour of an excavation for the Edmonton Convention Center is analyzed using the finite element model. A series of elastic analyses were performed to understand the mechanism of deformation which indicate that

○

the shear zone deformation in this case is highly affected by the deformation of the adjacent soil. Non-linear analysis indicates that shear band propagation can be captured by using the appropriate values of the material models. Initiation of the shear band in this case is affected by the in-situ stress field.

This research has not only provided a deeper understanding of the effect of progressive failure and the behaviour of strain softening material on the deformation response of soil masses, but also powerful analytical tools have been developed to perform quantitative analyses and calculations on the extent and amount of failure in real engineering structures. This enables engineers to adopt a more rational approach in the design and back analysis of soil structures when progressive failure may or may not be a threat to the safety of these structures. By no means has this research completely solved the problem of progressive failure. In fact, this is only a step forward towards the ultimate goal of analyzing progressive failures with great confidence and ease. This study may be considered to be the beginning of the analytical era in the problem of progressive failure. However, the sophistication of the analyses must not overshadow the calibre of the data used in the analysis. These analyses do not replace the judgement required in any engineering design but enhance it. Some recommendations for further research are given below in light of this research as the next step in approaching this

ultimate goal.

7.2 Recommendation for Further Research

Although the formulation and analysis presented in this thesis shows promising results in applying the theory of plasticity and the finite element method in analyzing progressive failure problems, there is much to be learnt in understanding the behaviour of strain softening material and the progressive failure problem. More case histories should be studied to have more comprehensive evaluations of the methods used in different real engineering problems. Obviously, such records are not easy to obtain especially in estimating the material parameters for the soil in order to make objective predictions of the observed measurement. It is felt in this research and from other experience, that the uncertainty in the in-situ stress conditions and the strength and deformation parameters of the soil often leads to unexpected variations in results.

In the analysis of the Edmonton Convention Center, it is seen that the value of k_0 can vary from 1.0 to as low as 0.65 which has definite effects on the mobilization of the shear strength at the shear zone. Also the elastic parameters of the clay, till and shale bedrock are not known to the desired accuracy in order to predict movement in the order of millimeters. Needless to say the variation of the values of the elastic and strength parameters have a direct effect on the confidence in the prediction of the soil

movement using the analytical models.

From the preceeding, in order to advance our ability to make accurate engineering predictions, the development of sophisticated computer models must be accompanied by comparable gain in confidence in obtaining material parameters for these computer models. This will require better laboratory testing equipments and procedures simulating the appropriate stress path in order to obtain the proper material parameters. This is especially important for strain softening material.

In the course of this research, considerable difficulties were encountered in obtaining stable convergence for some non-linear problems. Not only is the computational cost of the non-linear analysis an order of magnitude higher than for the elastic analysis, but sometimes it is difficult to obtain a converged solution for problems with strain softening material behaviour and for problems with stress concentration effects. To obtain the limit load and the extent of the yield zone of the bearing capacity problem presented in Chapters 4 and 5 required many load increments and iterations and careful monitoring of the applied load. There are few guidelines in determining the size of the load step which must be applied to avoid divergence and oscillation. The value of the tolerance is quite arbitrary and the value used in this research is based on present experience to minimize the accumulation of error which could eventually lead to divergence.

In order to solve the problem of convergence, one must gain further understanding of the convergent characteristics of non-linear problems with or without strain softening material behaviour initially for more specific problems and then search for more universal criteria in detecting divergence and a better definition for convergence. Unless these difficulties are overcome and thoroughly understood, the problem of convergence will always be an obstacle in making non-linear analysis more attractive to industry.

The effective stress finite element formulation presented in Chapter 5 serves as a starting point in introducing the effective stress approach in the analysis of soil structures. Due to the limitations of the time available, this approach has not been applied to real engineering problems. However, the results shown in Chapter 5 reveal a promising future for this approach. To obtain confidence in this approach, some case histories are required to compare the finite element prediction of pore pressure and soil movement with observed measurements. This approach can further be improved by incorporating the variation of the pore pressure λ parameter with straining. As discussed in Chapter 5, the result of the undrained analysis can be applied as the initial stress condition for consolidation problems.

For the three strain softening models presented in this thesis, only the elastic brittle plastic model can be used for frictional material. The other two models are restricted

to frictionless material which can only be used to analyze short term undrained soil behaviour. Extension of these two models to frictional material can be made. This is very useful in analyzing long term stability of brittle material under fully drained conditions.

BIBLIOGRAPHY

- Bathe, K.J. 1982. Finite Element Procedure in Engineering Analysis, New Jersey: Prentice Hall Inc..
- Bathe, K.J. and Wilson, E.L. 1976. Numerical Methods in Finite Element Analysis, New Jersey: Prentice Hall.
- Bjerrum, L. 1967. "Progressive Failure in Slopes of Over-Consolidated Plastic Clay and Clay Shales". Journal of the Soil Mechanics and Foundation Division, A.S.C.E., Vol. 93, SM 5, pp 3-49.
- Bland, D.R. 1957. "The Associated Flow Rule of Plasticity". Journal of the Mechanics and Physics of Solids, Vol. 6, pp 71-78.
- Burland, J.B., Londworth, T.I. and Moore, J.F.A. 1977. "A Study of Ground Movement and Progressive Failure caused by a Deep Excavation in Oxford Clay". Geotechnique, Vol. 27, No. 4, pp 557-591.
- Christian, J.T. and Whitman, R.V. 1969. "A One Dimensional Model for Progressive Failure". Proceedings of the Seventh International Conference on Soil Mechanics and Foundation Engineering, Mexico City, Vol. 2, pp 541-545.
- Christoffersen, J. and Hutchinson, J.W. 1979. "A Class of Phenomenological Corner Theories of Plasticity". Journal of the Mechanics and Physics of Solids, Vol. 27, pp 465-487.
- Cleary, M.P. and Rudnicki, J.W. 1976. "The Initiation and Propagation of Dilatant Rupture Zones in Geological Materials". The Effect of Voids on Material Deformation, Vol. 16, Editor: S.C. Cowen, New York: A.S.M.E., pp 13-30.
- Desai, C.S. and Christian, J.T. 1977. Numerical Method in Geotechnical Engineering, New York: McGraw Hill.
- Drucker, D.C. and Prager, W. 1951. "Extended Limit Design Theories for Continuous Media". Quarterly of Applied Mathematics, Vol. 9, pp 381-389.
- Drucker, D.C. and Prager, W. 1952. "Soil Mechanics and Plastic Analysis of Limit Design". Quarterly of Applied Mathematics, Vol. 10, pp 157-165.
- Drucker, D.C. 1956. "On Uniqueness in the Theory of Plasticity". Quarterly of Applied Mathematics, Vol. 14,

pp 35-42.

- Duncan, J.M., Byrne, P., Wong, K.S. and Mabry, P., 1980. "Strength, Stress-Strain and Bulk Modulus Parameters for Finite Element Analysis of Stresses and Movements in Soil Masses". Report No. UCB/GT/80-01, University of California.
- Duncan, J.M. and Chang, C.Y. 1970. "Nonlinear Analysis of Stress and Strain in Soils". Journal of the Soil Mechanics and Foundation Division, A.S.C.E., Vol. 96, SM 5, pp 1629-1653.
- Eisenstein, Z. and Morrison, 1973. "Prediction of Foundation Deformation in Edmonton using In-situ Pressure Probe". Canadian Geotechnical Journal, Vol. 10, pp 193-210.
- EBA Engineering Consultant Ltd. and Norbert R. Morgenstern Engineering Consultant Ltd. 1979. "Edmonton Convention Center - Geotechnical Evaluation". A report submitted to the City of Edmonton.
- EBA Engineering Consultant Ltd. and Norbert R. Morgenstern Engineering Consultant Ltd. 1979. "Edmonton Convention Center - Analytical Studies". A report submitted to James Wensley and Associates Architects Ltd.
- EBA Engineering Consultant Ltd. and Norbert R. Morgenstern Engineering Consultant Ltd. 1981. "Edmonton Convention Center - Final Construction Inspection Report". A report submitted to the City of Edmonton, Department of Real Estate and Housing.
- EBA Engineering Consultant Ltd. and Norbert R. Morgenstern Engineering Consultant Ltd. 1984. "Edmonton Convention Center - Geotechnical Instrumentation Report". A report submitted to the City of Edmonton, Department of Real Estate and Housing.
- Gates, R.H. 1972. "Progressive Failure Model for Clay Shale". Proceedings of the Symposium on Application of the Finite Element Method in Geotechnical Engineering, Vicksburg, Mississippi, U.S. Army Corps of Engineers, Waterways Experimental Station, pp 327-347.
- Ghaboussi, J., Wilson, E. and Isenberg, J. 1973. "Finite Element for Rock Joints and Interfaces". Journal of the Soil Mechanics and Foundation Division, A.S.C.E., Vol. 99, SM 10, pp 833-848.
- Goodman, R.E., Taylor, R.L. and Brekke, T.L. 1970. "A Model for the Mechanics of Jointed Rock". Journal of the Soil Mechanics and Foundation Division, A.S.C.E., Vol. 94, SM 3, pp 637-659.

- Henkel, D.J., 1960. "The Shear Strength of Saturated Remoulded Clays". Proceedings of the A.S.C.E. Research Conference on Shear Strength of Cohesive Soil, Boulder, Colorado, pp 533-544.
- Hill, R. 1953. The Mathematical Theory of Plasticity, London: Oxford at the Clarendon Press.
- Hill, R. 1956. "New Horizons in the Mechanics of Solids". Journal of the Mechanics and Physics of Solids, Vol. 5, pp 66-74.
- Hill, R. 1961. "Discontinuity Relations in Mechanics of Solids". Progress in Solid Mechanics (Chapter 6) Vol. 2.
- Hill, R. 1961. "Bifurcation and Uniqueness in Non-linear Mechanics of Continua". Problem of Continuum Mechanics, Editor: Laurente M.A., Society of Individual and Applied Mathematics.
- Hill, R. 1962. "Acceleration Waves in Solids". Journal of the Mechanics and Physics of Solids, Vol. 10, pp 1-16.
- Hodge, P.G. and White, G.N. 1950. "A Quantitative Comparison of Flow and Deformation Theories of Plasticity". Journal of Applied Mechanics, Vol. 17, pp 180-184.
- Hoeg, K. 1972. "Finite Element Analysis of Strain-Softening Clay". Journal of the Soil Mechanics and Foundation Division, A.S.C.E., Vol. 98, SM 1, pp 43-58.
- Hoeg, K., Christian, J.T. and Whitman, R.V. 1968. "Settlement of Strip load on Elastic-Plastic Soil". Journal of the Soil Mechanics and Foundation Division, A.S.C.E., Vol. 94, SM 2, pp 431-445.
- Houlsby, G.T. and Wroth, P. 1980. "Strain and Displacement Discontinuities in Soil". Journal of the Engineering Mechanics Division, A.S.C.E., Vol. 106, EM 4, pp 753-771.
- Hwang, C.T., Morgenstern, N.R. and Murray, D.W. 1971. "On Solutions of Plane Strain Consolidation Problems by Finite Element Methods". Canadian Geotechnical Journal, Vol. 8, pp 109-118.
- Kathol, C.P. and McPherson, R.A. 1975. "Urban Geology of Edmonton", Research Council of Alberta, Bulletin 32.
- Law, K.T. and Lumb, P. 1978. "A Limit Equilibrium Analysis of Progressive Failure in the Stability of Slopes". Canadian Geotechnical Journal, Vol. 15, pp 113-122.

- Lo, K.Y. 1972. "An Approach to the Problem of Progressive Failure". Canadian Geotechnical Journal, Vol. 9, pp 407-429.
- Lo, K.Y. and Lee, C.F. 1970. "Analysis of Progressive Failure in Clay Slopes". Proceedings of the Eighth International Conference on Soil Mechanics and Foundation Engineering, pp 251-258.
- Lo, K.Y. and Lee, C.F., 1973. "Stress Analysis and Slope Stability in Strain Softening Material". Geotechnique, Vol. 23, pp 1-11.
- Matheson, D.S. and Thomson, S. 1973. "Geological Implication of Valley Rebound". Canadian Journal of Earth Science, Vol. 10, pp 961-978.
- May, R.W. and Thomson, S. 1978. "The Geology and Geotechnical Properties of Till and Related Deposits in the Edmonton, Alberta, Area". Canadian Geotechnical Journal, Vol. 15, pp 362-370.
- Morgenstern, N.R. and Tchalenko, J.S. 1967. "Microscopic Structure in Kaolin Subjected to Direct Shear". Geotechnique, Vol. 17, pp 309-328.
- Nayak, G.C. and Zienkiewicz, O.C. 1972. "Elasto-Plastic Stress Analysis, A Generalization for Various Constitutive Relations including Strain Softening". International Journal for Numerical Methods in Engineering, Vol. 5, pp 113-135.
- Palmer, A.C. and Rice, J.R. 1973. "The Growth of Slip Surfaces in the Progressive Failure of Over-Consolidated Clay". Proceedings of the Royal Society of London, A 322, pp 527-548.
- Pende, G.N. and Sharma, K.G. 1979. "On Joint/Interface Elements and Associated Problems on Numerical Ill-Conditioning". International Journal for Numerical and Analytical Methods in Geomechanics, Vol. 3, pp 293-300.
- Pietruszczak, St. and Morz, Z. 1981. "Finite Element Analysis of Deformation of Strain Softening Materials". International Journal for Numerical Methods in Engineering, Vol. 17, pp 327-334.
- Poulos, H.G. and Davis, E.H., 1974. Elastic Solution for Soil and Rock Mechanics, New York: John Wiley Inc..
- Prevost, J.H. and Hoeg, K. 1975. "Soil Mechanics and Plasticity Analysis of Strain Softening". Geotechnique,

Vol. 25, pp 279-297.

Rice, J.R. 1976. "The Localization of Plastic Deformation", Theoretical and Applied Mechanics, Edited by Koiter W.T., North-Holland Publishing Company, pp 207-220.

Rice, J.R. and Rudnicki, J.W. 1980. "A Note on some Features of the Theory of Localization of Deformation". International Journal of Solids and Structures, Vol. 16, pp 597-605.

Rudnicki, J.W. 1977. "The Inception of Faulting in a Rock Mass with a Weakened Zone". Journal of Geophysical Research, Vol. 82, No. 5, pp 844-854.

Rudnicki, J.W. 1979. "The Stabilization of Slip on a Narrow Weakening Fault Zone by Coupled Deformation-Pore Fluid Diffusion". Bulletin of the Seismological Society of America, Vol. 69, No. 4, pp 1011-1026.

Rudnicki, J.W. 1981. "Theoretical Studies of Rupture Processes in Geological Materials". U.S. Geological Survey Contract No. 14-08-0001-19146, open file no. 81-956.

Rudnicki, J.W. and Rice, J.R. 1975. "Condition for the Localization of Deformation in Pressure-Sensitive Dilatant Material". Journal of the Mechanics and Physics of Solids, Vol. 23, pp 371-394.

Simmons, J. 1981. "Shear Band Yielding and Strain Weakening". Ph.D. Thesis, University of Alberta, Edmonton, Alberta.

Sinclair, S.R. and Brooker, E.W., 1967. "The Shear Strength of Edmonton Shale". Proceedings of the Geotechnical Conference, Oslo, pp 295-299.

Skempton, A.W., 1964. "Long Term Stability of Clay Slope". Geotechnique, Vol. 14, No. 2, pp 77-102.

Terzaghi, K. 1943. Theoretical Soil Mechanics, New York: John Wiley and Sons Inc.

Terzi, A.I., Kalteziotis, N.A. and Menzies, B.K. 1982. "Finite Element Analysis of Strip Footing on Stain-Softening Isotropic Clay". International Symposium on Numerical Models in Geomechanics, Surich, pp 740-748.

Tribus, M. 1969. Rational Descriptions Decision and Designs. New York: Pergamon Press.

Zienkiewicz, O.C. Humpheson, C. and Lewis, R.W. 1975. "Associated and Non-Associated Visco-Plasticity and

Plasticity in Soil Mechanics". Geotechnique, Vol. 25,
No. 4, pp 671-689.

Zienkiewicz, O.C. 1977. The Finite Element Method, London:
McGraw Hill.

APPENDIX A

Methods of Stress Calculation for Non-linear Problems

A.1 Introduction

Several methods used in the calculation of stresses will be discussed in this appendix. It is sometimes argued that stresses and strains are secondary variables in the finite element analysis. Since displacements are the prime variables, stresses are not as sensitive as the displacements. However, the entire non-linear finite element formulation presented in this thesis is dependent upon the current state of stress and strain, therefore accurate stress calculation during the analysis is not only important in obtaining an accurate solution, but also vital in obtaining any solution at all.

The stresses in a finite element analysis in general can be calculated from the strains and the constitutive relationship of the material which is given by:

$$\sigma_i = \int C_{ijmn} d\epsilon_{mn} \quad (A.1)$$

where

C_{ijmn} is the elasto-plastic constitutive matrix which can be in terms of total stress or effective stress parameters.

It is understood that the constitutive matrix is stress and strain dependent, that is:

$$C_{ijklmn} = C_{ijklmn}(\sigma_{ij}, \epsilon_{ij}). \quad (A.2)$$

To simplify notation, the second order stress and strain tensors will be reduced to vector quantities and the fourth order constitutive tensor will be reduced to a second order tensor. Therefore Equation (A.1) can be rewritten as:

$$\sigma_i = \int C_{ij} d\epsilon_j \quad (A.3)$$

where

$$\sigma_i = \sigma_{xx}, \sigma_{yy}, \sigma_{xy}, \sigma_{zz}, \sigma_{yz}, \sigma_{xz}, \text{ for } i = 1, 2, \dots, 6;$$

$$\epsilon_i = \epsilon_{xx}, \epsilon_{yy}, \epsilon_{xy}, \epsilon_{zz}, \epsilon_{yz}, \epsilon_{xz}, \text{ for } i = 1, 2, \dots, 6.$$

Note that the summation is taken from 1 to 6 and not from 1 to 3 here. The symmetrical properties of the stress and strain tensors are used to reduce Equation (A.1) to Equation (A.3) but the constitutive tensor can still be unsymmetric. The integration limit in Equation (A.3) is taken from the strains of the previous step (loading step) to the strains of the latest equilibrium iteration of the current step.

That is:

$$\Delta\sigma_i = \int_{\epsilon_j^m}^{\epsilon_j^{m+1}} C_{ij} d\epsilon_j \quad (A.4)$$

where

the back subscripts m and $m+1$ represent the loading step m and $m+1$ respectively;

the back superscripts i denote the i -th equilibrium iteration of the current loading step;

and Δ denotes the change in stresses or strains from loading step m to $m+1$.

It is important to realize that the integration is always performed from the strains of the previous step to the latest iteration of the current step and not from the previous iteration of the current step to the latest iteration. The reason is that before the solution has converged, the current displacement, and hence strains, are only approximated, and therefore there will be error in calculating the stresses during the iterative scheme. By performing the integration from the converged strains of the previous loading step, the error during the iterative process will not be accumulated. This will lead to a more (stable solution process.

To evaluate the integral in Equation (A.4), a numerical procedure must be used due to the complicated form of the constitutive tensor and the fact that it is stress and strain dependent. One can approximate the integral of Equation (A.4) by a summation in which the limits of integration are divided into n equal sub-intervals. That is:

$$\Delta \sigma_j = \sum_{k=1}^n C_{ij}^k (\Delta \epsilon_j / n) \quad (A.5)$$

where

$$\Delta \epsilon_j = \epsilon_{j, m+1} - \epsilon_{j, m},$$

and the front superscript k denotes subinterval k .

Equation (A.4) can be recovered from (A.5) by taking the limit as n approaches infinity.

Since the constitutive tensor depends on the current stress state which is unknown prior to the calculation, it

presents a problem when one wants to determine the stresses exactly. The methods presented below will give an approximate solution to Equation (A.5). Discussion of these methods for a single variable can be found in Keryszig(1972) and Milne(1970). The objective of all these methods is to calculate the stresses and strains at subinterval $k+1$ given that the stresses and strains at subinterval k are known. Since it is assumed that they are known at the lower limit of the integration Equation (A.4), one can then proceed the integration from the lower limit to the upper limit.

A.2 Euler Forward Method

In the Euler Forward Method, the constitutive tensor C_{ij}^k is evaluated based on the latest calculated stresses and strains state at subinterval $k-1$. Therefore, Equation (A.5) should be rewritten as:

$$\Delta \sigma_i = \sum_{k=1}^n \Delta \sigma_i^k = - \frac{1}{n} \sum_{k=1}^n C_{ij}^{k-1} \Delta \epsilon_j, \quad (A.6)$$

where

$$C_{ij}^{k-1} = C_{ij}(\sigma^{k-1}, \epsilon^{k-1}).$$

Hence, the constitutive tensor is always one subinterval behind in the calculation. This method is also called the first order method because the error introduced in the calculation is of the second order of $(1/n)^2$, i.e. $O(1/n)^2$.

This can be shown as follows:

Approximate the exact stresses at subinterval $k+1$ by a Taylor series in the neighbourhood of ϵ^k :

$$\sigma\{^{k+1}\} = \sigma\{^k\} + \frac{\partial \sigma\{^k\}}{\partial \epsilon_j} (\epsilon_j^{k+1} - \epsilon_j^k) +$$

$$\frac{1}{2!} \frac{\partial^2 \sigma\{^k\}}{\partial \epsilon_j \partial \epsilon_m} (\epsilon_j^{k+1} - \epsilon_j^k) (\epsilon_m^{k+1} - \epsilon_m^k) +$$

$$\frac{1}{3!} \frac{\partial^3 \sigma\{^k\}}{\partial \epsilon_j \partial \epsilon_m \partial \epsilon_n} (\epsilon_j^{k+1} - \epsilon_j^k) (\epsilon_m^{k+1} - \epsilon_m^k) (\epsilon_n^{k+1} - \epsilon_n^k) +$$

. higher order terms (A.7a)

$$= \sigma\{^k\} + \frac{1}{n} \frac{\partial \sigma\{^k\}}{\partial \epsilon_j} \Delta \epsilon_j + \frac{1}{2! n^2} \frac{\partial^2 \sigma\{^k\}}{\partial \epsilon_j \partial \epsilon_m} \Delta \epsilon_j \Delta \epsilon_m +$$

$$\frac{1}{3! n^3} \frac{\partial^3 \sigma\{^k\}}{\partial \epsilon_j \partial \epsilon_m \partial \epsilon_n} \Delta \epsilon_j \Delta \epsilon_m \Delta \epsilon_n +$$

. higher order terms (A.7b)

where

$\sigma\{^{k+1}\}$ are the exact stresses at strains ϵ_j^{k+1} , that is
 $\sigma\{^{k+1}\} = \sigma_i(\epsilon_j^{k+1})$.

It is important to distinguish the quantities that have brackets around the superscripts and those without brackets. Those with brackets in the front superscripts are true or exact values and those without brackets are approximated values evaluated on the basis of Equation (A.6) or other methods discussed later. Since the strains are the independent variables, it is not necessary to distinguish

between exact and approximate quantities.

Differentiating Equation (A-3) with respect to ϵ_j and evaluating at subinterval k gives:

$$\frac{\partial \sigma_j^k}{\partial \epsilon_j} = C_{1j}^k. \quad (\text{A.8})$$

From Equation (A.6) and (A.8):

$$\begin{aligned} \sigma_j^{k+1} &= \sigma_j^k + \frac{1}{n} C_{1j}^k \Delta \epsilon_j \\ &= \sigma_j^k + \frac{1}{n} \frac{\partial \sigma_j^k}{\partial \epsilon_j} \Delta \epsilon_j, \end{aligned} \quad (\text{A.9a})$$

$$\approx \sigma_j^k + \frac{1}{n} \frac{\partial \sigma_j^k}{\partial \epsilon_j} \Delta \epsilon_j. \quad (\text{A.9b})$$

Comparing Equation (A.9) and (A.7), it is seen that the second order term, $(1/n)^2$, and the higher order terms are neglected. The error resulting from truncating the higher order terms of the Taylor series is called the truncation error. This error can be reduced by increasing the number of subintervals n and hence reducing the size of the subintervals. However, increasing the number of subintervals will increase the round off error due to the finite number of digits used in the calculation. More detailed discussion of calculation errors will be given later. Graphical interpretation of the Euler method is illustrated in Figure A.1.

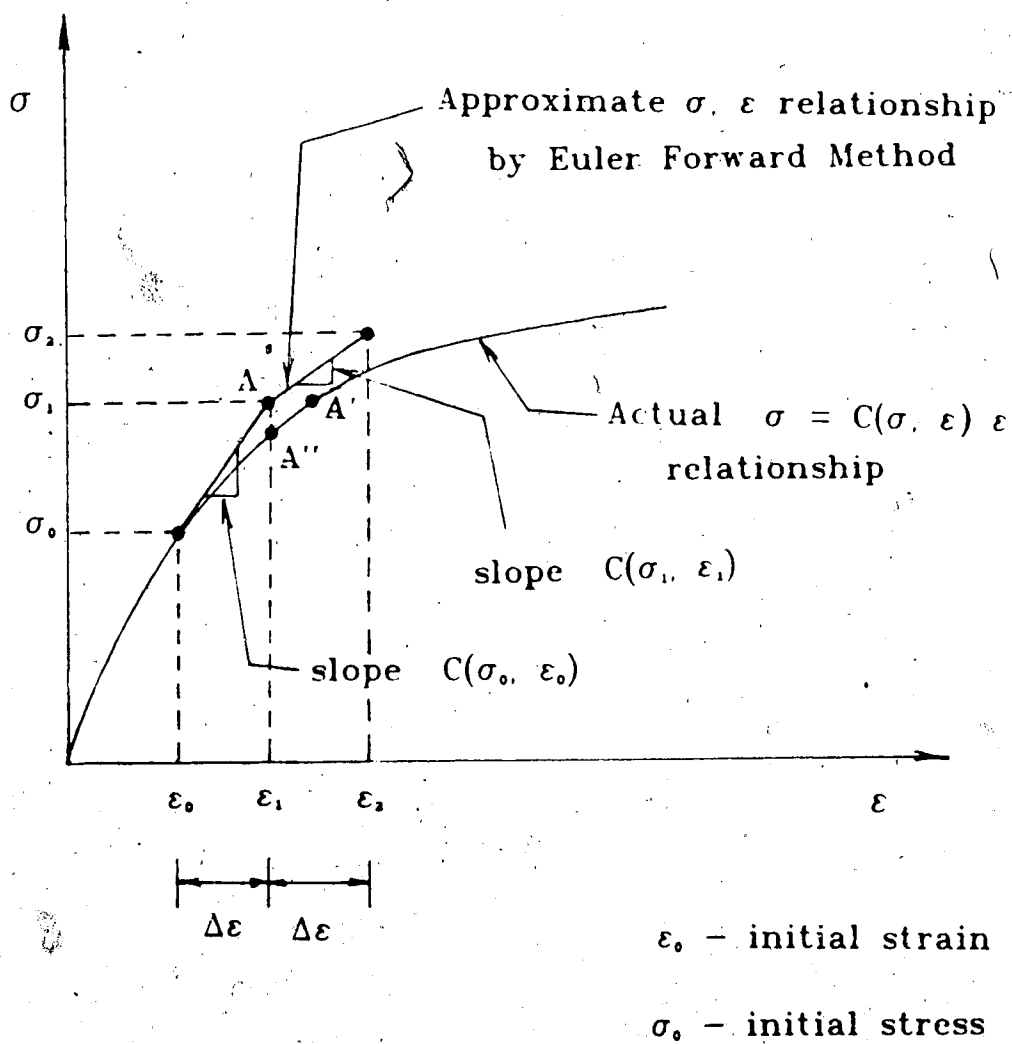


Figure A.1: Illustration of the Euler Forward Method

In Figure A.1 let us assume that the integration begins at σ_0 and ϵ_0 which is located on the exact stress strain curve as shown. Then, using the current state of stress and strain, the incremental constitutive matrix is determined and approximate stress σ_1 is calculated. In the next subinterval, the evaluation of the constitutive matrix is based on the stress state σ_1 at point A and strain state ϵ_1 . But it is seen that the stress state σ_1 will have an actual strain state corresponding to point A', or the strain ϵ_1 will have an actual stress state of A". If the constitutive relationship depends on the stress state only, the slope of the stress strain curve at point A' will be used in the next subinterval. However, if the constitutive relationship is dependent upon both the current state of stress and strain, using the slope at point A' will introduce inconsistency since point A is not on the actual stress strain curve. This will result in an error in the evaluation of the constitutive matrix. Moreover the error introduced is accumulated during the integration process and will not be reduced by the equilibrium iteration process. This creates a problem in obtaining rapid and stable convergency for sensitive material.

A.3 Improved Euler Method

Since the Euler Method does not account for the stress state at the $k+1$ interval when evaluating the constitutive tensor C_{ij} , the Improved Euler Method will first estimate

the stress state at the $k+1$ interval before calculating the final stresses. The estimation of the stresses are given by:

$$\sigma_{ij}^{*k+1} = \sigma_{ij}^k + \frac{1}{n} C_{ij}^k \Delta \epsilon_{ij}, \quad (A.10)$$

and the final stresses are given by:

$$\sigma_{ij}^{*k+1} = \sigma_{ij}^k + \frac{1}{2n} (C_{ij}^k + C_{ij}^{*k+1}) \Delta \epsilon_{ij}, \quad (A.11)$$

where

$C_{ij}^{*k+1} = C_{ij}(\sigma_{ij}^{*k+1}, \epsilon_{ij}^{*k+1})$ is evaluated based on the approximated stresses from Equation (A.10).

This procedure essentially calculated half the stress changes using C_{ij} based on the previous stress state and the other half on the approximated current stress state. The graphical interpretation of the method is shown in Figure A.2. The Improved Euler Method is a second order method because the truncation error is of the order of $(1/n)^2$. This can be shown by approximating the term C_{ij}^{*k+1} using the Taylor series as:

$$C_{ij}^{*k+1} = C_{ij}^k + \frac{1}{n} \frac{\partial C_{ij}^k}{\partial \epsilon_m} \Delta \epsilon_m + \frac{1}{2!n^2} \frac{\partial^2 C_{ij}^k}{\partial \epsilon_m \partial \epsilon_n} \Delta \epsilon_m \Delta \epsilon_n + \dots$$

. . . higher order terms ,

(A.12a)

$$\text{and } \frac{\partial C_{ij}^k}{\partial \epsilon_m} = \frac{\partial^2 \sigma_{ij}^k}{\partial \epsilon_j \partial \epsilon_m}, \quad \frac{\partial^2 C_{ij}^k}{\partial \epsilon_m \partial \epsilon_n} = \frac{\partial^3 \sigma_{ij}^k}{\partial \epsilon_j \partial \epsilon_m \partial \epsilon_n} \quad (A.12b)$$

Substitute Equations (A.12) and making the approximation

that $C_{ij}^{*k+1} \approx C_{ij}^{*k+1}$, then:

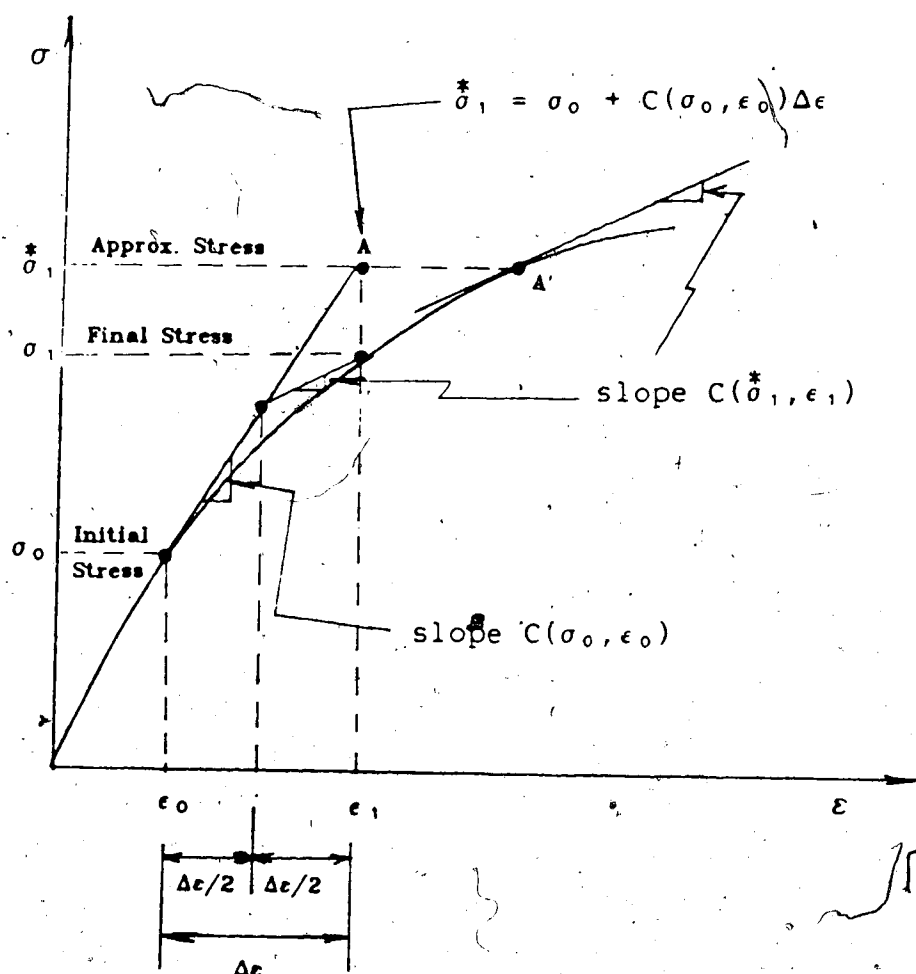


Figure A.2: Illustration of the Improved Euler Method

$$\sigma_i^{k+1} = \sigma_i^k + \frac{1}{2n} [C_{i,j}^k + C_{i,j}^{k+1}] + \frac{1}{n} \frac{\partial^2 \sigma_i^k}{\partial \epsilon_j \partial \epsilon_m} \Delta \epsilon_m$$

$$+ \frac{1}{2!n^2} \frac{\partial^3 \sigma_i^k}{\partial \epsilon_j \partial \epsilon_m \partial \epsilon_n} \Delta \epsilon_m \Delta \epsilon_n + \dots$$

... higher order terms $]\Delta \epsilon_j$

$$= \sigma_i^k + \frac{1}{n} C_{i,j}^k + \frac{1}{4n^2} \frac{\partial^2 \sigma_i^k}{\partial \epsilon_j \partial \epsilon_m} \Delta \epsilon_j \Delta \epsilon_m$$

$$+ \frac{1}{4n^3} \frac{\partial^3 \sigma_i^k}{\partial \epsilon_j \partial \epsilon_m \partial \epsilon_n} \Delta \epsilon_j \Delta \epsilon_m \Delta \epsilon_n + \dots$$

... higher order terms (A.13)

Making the approximation $\sigma_i^k \cong \sigma_i^{(k)}$, and $C_{i,j}^k \cong C_{i,j}^{(k)}$, the truncation error of Equation (A.11) can be calculated by subtracting Equation (A.7) from (A.13):

$$\text{error} = \frac{1}{12n^3} \frac{\partial^3 \sigma_i^k}{\partial \epsilon_j \partial \epsilon_m \partial \epsilon_n} \Delta \epsilon_j \Delta \epsilon_m \Delta \epsilon_n + \dots$$

... higher order terms (A.14)

which is of the order $(1/n)^3$.

A.4 Runge-Kutta Method

The Runge-Kutta Method is a more accurate method than the Improved Euler Method since the truncation error is of the order of $(1/n)^4$. In this method, the following

quantities are first calculated:

$$\sigma_1 = -\frac{1}{n} C_{11}(\sigma_1^k, \epsilon_1^k) \Delta \epsilon_1 ; \quad (\text{A.15a})$$

$$\sigma_2^1 = -\frac{1}{n} C_{11}(\sigma_1^k + \frac{1}{2} \sigma_1, \epsilon_1^k + \frac{1}{2n} \Delta \epsilon_1) \Delta \epsilon_1 ; \quad (\text{A.15b})$$

$$\sigma_2^2 = -\frac{1}{n} C_{11}(\sigma_1^k + \frac{1}{2} \sigma_2^1, \epsilon_1^k + \frac{1}{2n} \Delta \epsilon_1) \Delta \epsilon_1 ; \quad (\text{A.15c})$$

$$\sigma_2^3 = -\frac{1}{n} C_{11}(\sigma_2^2, \epsilon_1^{k+1}) \Delta \epsilon_1 ; \quad (\text{A.15d})$$

and the final stress is given by:

$$\sigma_1^{k+1} = \sigma_1^k + \frac{1}{6} (\sigma_1 + 2\sigma_2^1 + 2\sigma_2^2 + \sigma_2^3). \quad (\text{A.16})$$

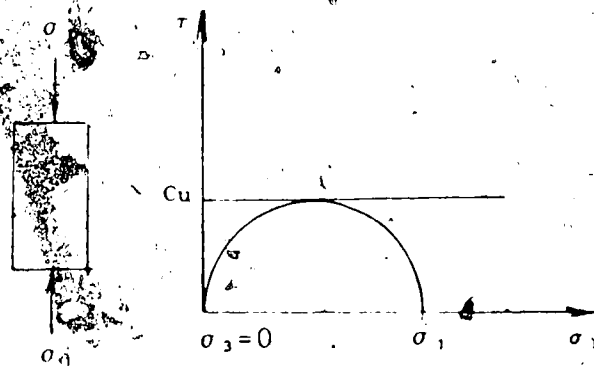
The advantage of all these methods is that only the constitutive tensor need be calculated and no derivatives are required which sometimes can be quite difficult to determine. Therefore, it is not necessary for the derivatives to be finite, and in fact, it is only required that the constitutive tensor be piece-wise continuous within the strain subintervals. However, for the case of elastic brittle perfectly plastic material model discussed in Chapter 3, the constitutive tensor is piece-wise continuous but the transition from the peak strength to the residual strength cannot be determined from these methods or any other integration scheme because the constitutive relationship is not defined at the transition. The method for stress calculation for this case is discussed in Appendix D. All of these methods are used in calculating stresses in the computer program SAFE. In order to provide some guidance in selecting these methods, the choice of the

number of subintervals, and the error involved, a detailed discussion on the errors in these methods are given below.

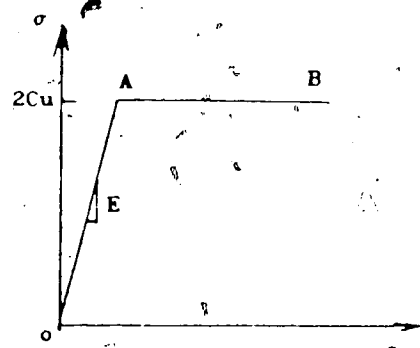
A.5 Comparison of various Stress Calculation Methods

The three methods discussed above are used in calculating stresses for non-linear problems. In all of these methods, if the changes in stresses in any subinterval do not result in changes in the constitutive matrix, then all of these methods will lead to the same result. This is not only true for linear elastic material but for non-linear material along certain stress paths in which the constitutive matrix remains unchanged during the integration process. For example, the stress path of an unconfined compression test is shown in Figure A.3. The material is assumed to be linear elastic perfectly plastic with Tresca yield criterion. The stress path indicates that once yielding has occurred, the direction of the plastic strain, i.e. the normal to the yield surface, remains unchanged and hence the elasto-plastic matrix remains unchanged during plastic deformation.

A second example is shown in Figure A.4 of an expansion of a thickwalled cylinder. The stress path also indicates that the direction of the plastic strain remains unchanged once yielding has occurred. The above is true whether the material obeys Tresca or von-Mises yield criteria. Therefore, in calculating stresses, it is not necessary to subdivide the integral into subintervals regardless of the



Mohr's Circle of Frictionless Material



Elastic Perfectly Plastic Material

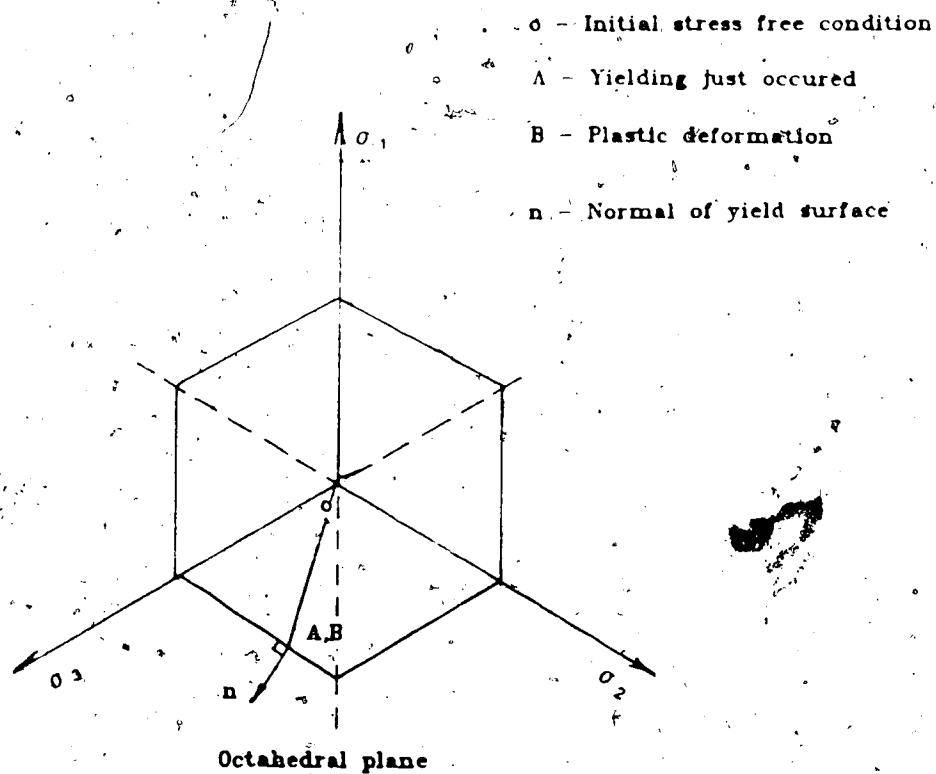
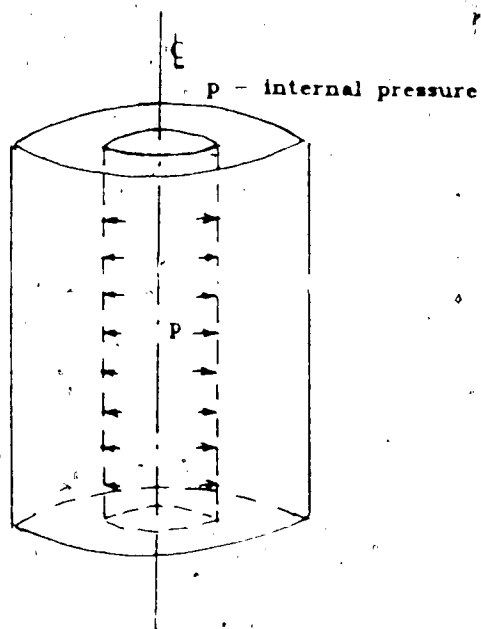
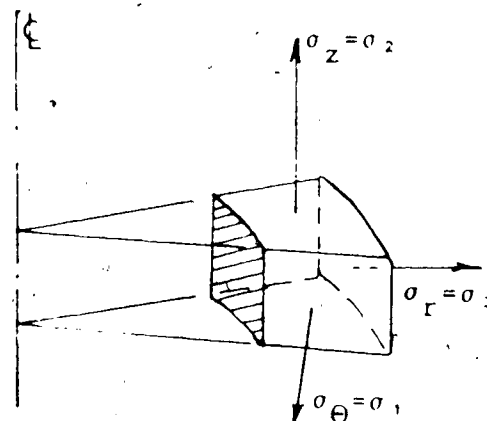


Figure A.3: Stress Path of Uniaxial Plane Strain Test



Thickwalled Cylinder Subjected to
Internal Pressure



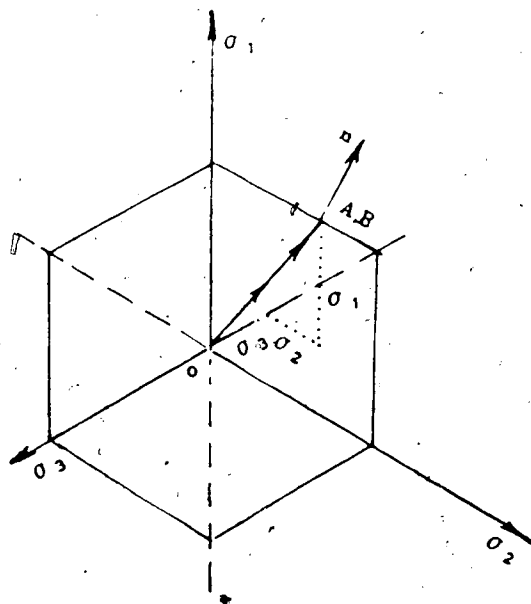
Principal Stress Direction of an Element

o - Initial stress free condition

A - Yielding just occurred

B - Plastic deformation

n - Normal of yield surface



Octahedral plane

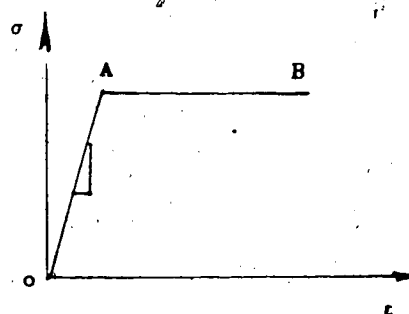


Figure A.4: Stress Path of Expansion of
Thickwalled Cylinder

methods of numerical integration used? It is seen that one can make use of the above observation in stress calculation and updating the stiffness matrix in non-linear problems if the stress path of the material can be identified. The elasto-plastic matrix needs to be updated once. This will have the same effect as updating it in every iteration.

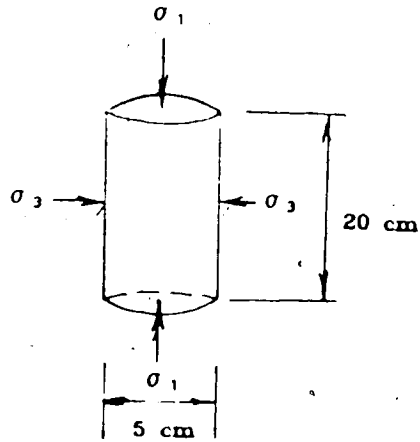
To evaluate the effectiveness of the different methods of stress calculation, three cases will be considered. The hyperbolic non-linear elastic model (Duncan and Chang 1972) will be used in the first case. Since this is an elastic model and the tangent elastic modulus is dependent on the stress level, the problem discussed in the previous paragraph will not occur here. An axisymmetric uniaxial compression test is simulated here as shown in Figure A.5. The finite element model and material parameters are given in this figure. An axial strain of 0.4% is imposed on the specimen. The stresses are calculated using all three methods discussed and compared with the exact solution of 76.74131032 which is summarized in Table A.1.

The material models for the second and third cases are linear elastic perfectly plastic models with Tresca and von-Mises yield criteria. An uniaxial plane strain test is simulated using the finite element method. As discussed earlier, the stress path in this test will lead to a constant constitutive matrix and the result is independent of the method of stress calculation or the number of subintervals. Therefore, the stress path in these two cases

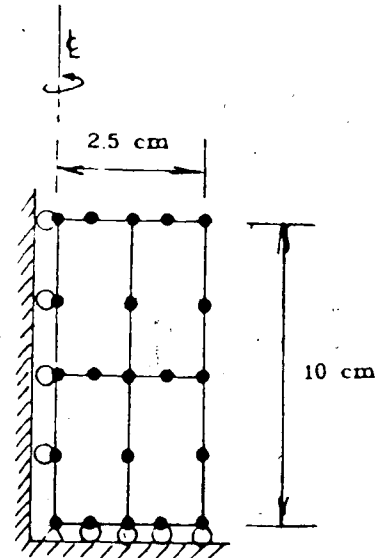
Table A.1 Summary of Result of Stress Analysis

			Hyperbolic	Tresca	von-Mises
Exact Solution			76.74131032	9.16515139	10.51581088
Euler Forward Scheme	n u m b e r	4 err	82.67610799 7.73 %	9.39199419 2.48 % (10)	10.77216770 2.44 % (8)
		20 err	77.82494686 1.14 %	9.21484835 0.54 % (7)	10.62473948 1.13 % (6)
Improved Euler Scheme	o f i t e r a t i o n s	2 err	75.40459019 1.74 %	9.17491675 0.11 % (6)	10.60234440 0.82 % (6)
		10 err	76.69396018 0.06 %	9.16908650 0.04 % (6)	10.59945449 0.80 % (6)
Runge- Kutta Scheme		1 err	76.74711398 0.0076%	9.16977211 0.050% (6)	10.59964206 0.0797% (6)
		5 err	76.74119752 0.00015%	9.16904539 0.043% (6)	10.59943858 0.0795% (6)

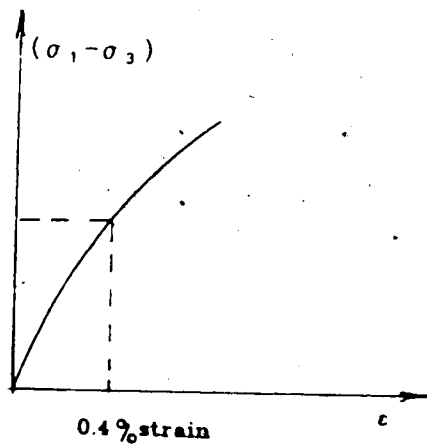
() indicates the number of equilibrium required to obtain convergence.



Uniaxial Compression Test



Finite Element Model



Hyperbolic Relationship

$$(\sigma_1 - \sigma_3) = \epsilon / (1/E_t + \epsilon R_f / (\sigma_1 - \sigma_3)_f)$$

$$(\sigma_1 - \sigma_3)_f = (2 C \cos \phi + 2 \sigma_3 \sin \phi) / (1 - \sin \phi)$$

Material Parameters.

P_a = Atmospheric Pressure = 101.28 kPa

$k=295$ $n=0.65$ $R_f=0.90$

c =cohesion=0

ϕ =friction angle=30.4

σ_c =98 kPa

$$E_t = k P_a (\sigma_3 / P_a)^n$$

Figure A.5: Uniaxial Compression of Hyperbolic Elastic Soil

will be slightly more complicated. Initially the specimen will be loaded uniaxially until yielding occurs as shown in Figure A.6. Then uniform shear stresses are applied around the specimen which leads to a rotation of principal stresses. The vertical displacement, or strain, will be maintained constant during the application of shear stresses. The rotation of principal stresses while maintaining the vertical strain constant must be accompanied by a decrease in vertical stress if the yield criterion is to be satisfied. The exact final stress condition is given in Figure A.7. This will be used in the comparison with the finite element solution. The horizontal stress will remain constant throughout this process. The stress path on the octahedral plane is also shown in Figure (A.7) for both the Tresca and von-Mises yield criteria. The application of shear stress result in a path along the yield surface which leads to a rotation of the principal plastic strain directions. It is noted that plane strain condition is assumed in the analysis and the stress path in the elastic range will be affected by the Poisson's ratio. A Poisson's ratio of 0.3 is used in these two cases. The parameters used in these two examples are given in the figure.

Table A.1 summarizes the results of the analyses. Since the use of the Improved Euler Scheme requires the evaluation of the constitutive matrix twice for every subinterval and four times for the Runge-Kutta Method, therefore, the number of sub-intervals used for these two methods will be half and

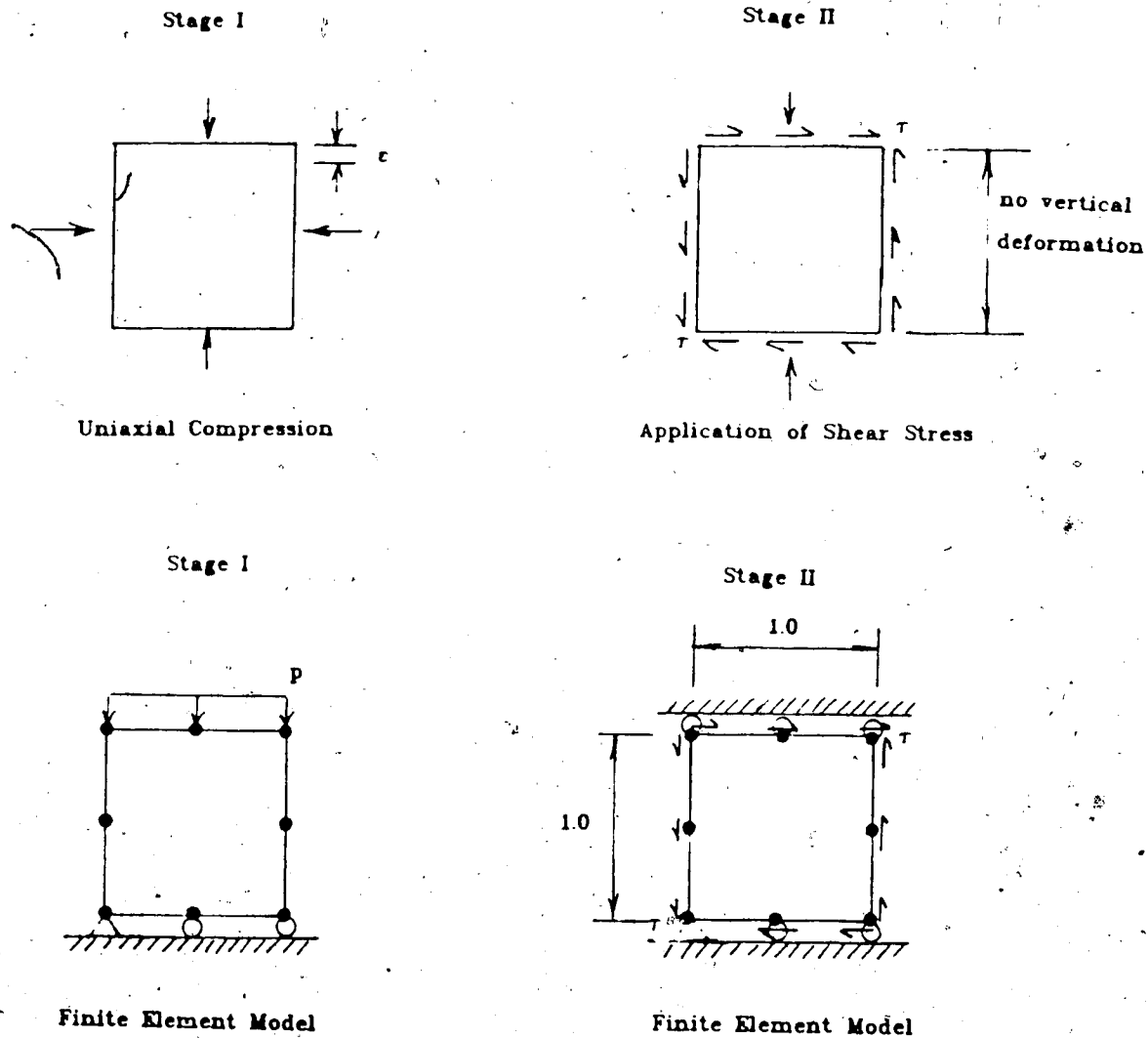
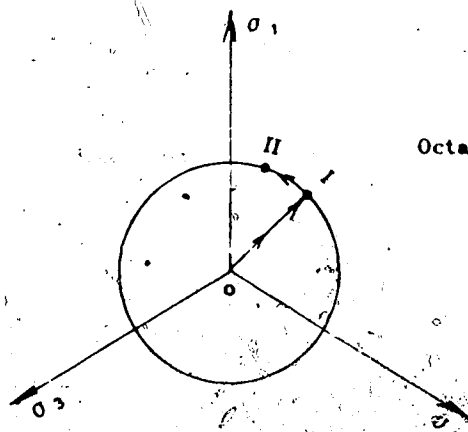
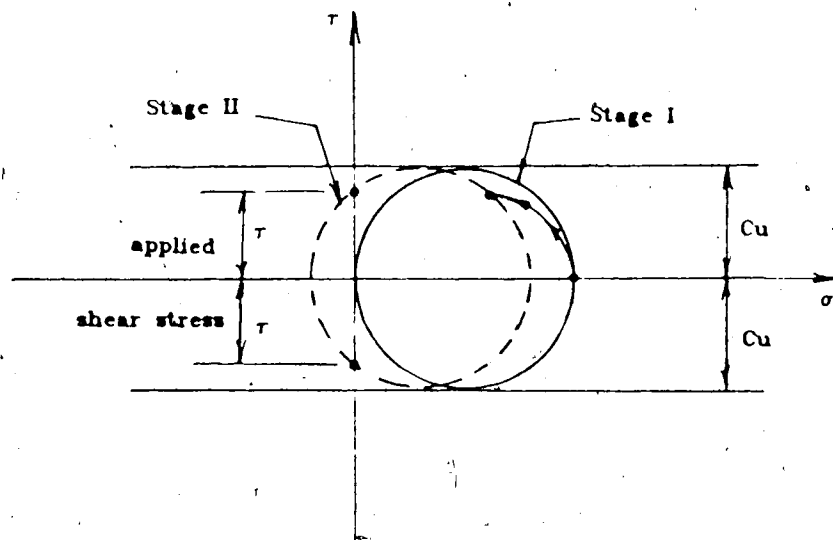
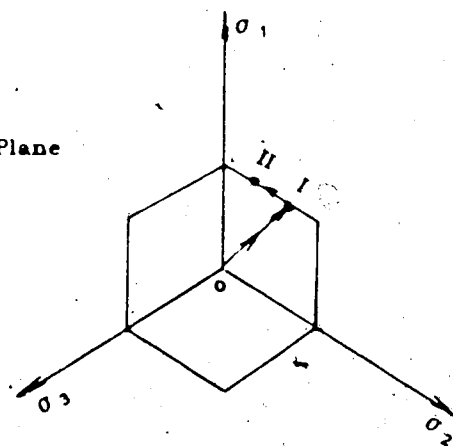


Figure A.6: Plane Strain Compression Test of Elastic Perfectly Plastic Material



von Mises Yield Criterion

Octahedral Plane



Tresca Yield Criterion

Figure A.7: Stress Path of Plane Strain Test

one quarter of that in the Euler Forward Scheme respectively. Four and twenty sub-intervals are used in the Euler Forward Scheme while 2 and 10, and 1 and 5 sub-intervals are used in the Improved Euler Scheme and the Runge-Kutta Scheme respectively. The results in Table A.1 show consistently that the Runge-Kutta Scheme gives more accurate results than the Improved Euler Scheme which in turn is more accurate than the Euler Forward Scheme for the same amount of computational effort. This supports the proof of the errors involved in all these methods. For the case of elastic perfectly plastic materials, an iterative procedure is required to obtain convergence since constant shear stresses are applied on the specimen boundary. The number of equilibrium iterations required for each case are shown and the same displacement tolerance of 0.00001 is used for all three cases (refer to Chapter 2 for definition of displacement convergence tolerance).

It is clear that the Improved Euler and the Runge-Kutta scheme discussed here result in more accurate stresses than the Euler Forward Scheme. Accurate stress calculation is important in obtaining stable and effective solution procedures for incremental analyses. All three schemes are available in the computer program SAFE.

APPENDIX B

Solution of Non-Linear Equation using the Interval Halving Technique

The interval halving technique is a simple and effective way of obtaining a solution for an equation of the form:

$$f(x) = 0 . \quad (B.1)$$

Usually only one independent variable is considered. The purpose is obviously to find a value of x , for example $x = x_0$, which will satisfy Equation (B.1). If there is more than one value of x satisfying Equation (B.1), then all the values of x can be obtained by specifying the appropriate interval. In order to obtain a solution, the following conditions must be satisfied:

1. F must be continuous in x .
2. The upper and lower values of $x=x_0$ are known, that is:

$$f(x_1) > 0 , \quad (B.2a)$$

$$f(x_2) < 0 , \quad (B.2b)$$

where x_1 and x_2 define the range of x_0 .

For the case where f is the yield function and x is the ratio R defined in Chapter 2, condition (1) is always satisfied. Otherwise, the yield surfaces will have a hole in it which does not exist for all the yield surfaces under consideration. Since the range of R must lie between 0 and 1, the second condition can be satisfied easily.

A solution of Equation (B.1) can be obtained by following these steps:

1. Determine the mid point of the interval,

$$x_m = \frac{x_1 + x_2}{2}$$

2. Check if $f(x_m) = 0$ or is within tolerable limit?

If yes, then $x_0 = x_m$ and a solution is obtained.

If no, proceed to the next step.

3. Check if $f(x_m) < 0$?

If yes, assign x_m to x_2 and repeat steps 1 and 2.

If no, then $f(x_m)$ must be less than zero; assign x_m to x_1 and repeat steps 1 and 2.

The procedure is graphically shown in Figure B.1. The convergence rate of this technique is usually slower than other techniques, however, this technique will guarantee convergence which is an important feature in obtaining solutions for non-linear equations as long as $f(x)$ is continuous. It can be shown that the number of iterations required for this method is approximately given (to the nearest digit for $0 \leq x \leq 1$) (Tribert 1969) by:

$$n = \log_2(m+1) \quad (B.2)$$

where

n is the number of iterations required and m is the number of significant digits of x .

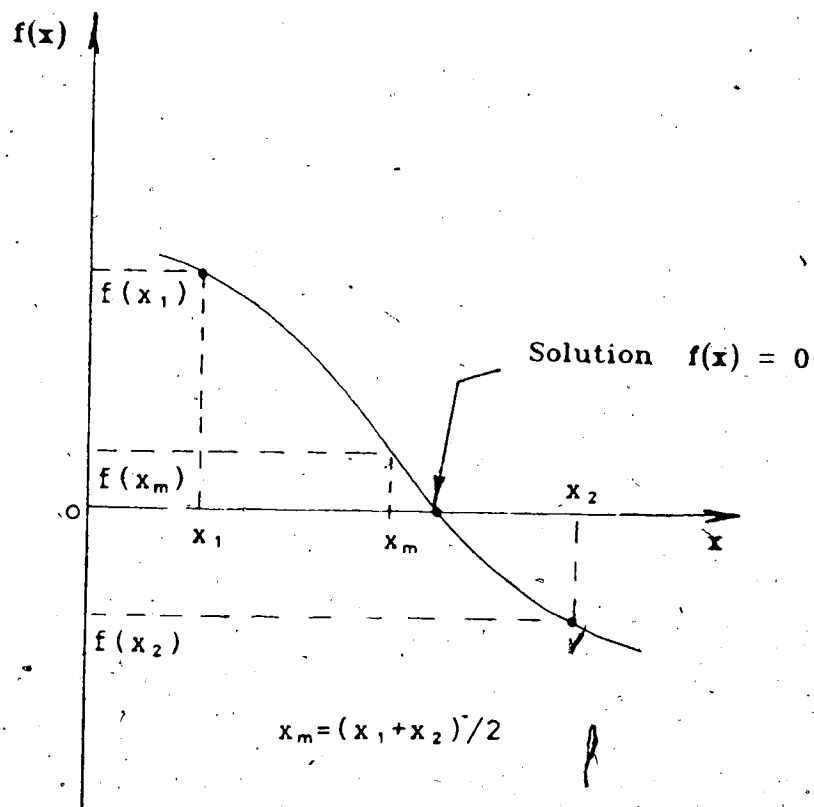


Figure B.1: Solution Procedure of Interval Halving Technique

For example, if single precision is used with six significant digits, then the number of iterations required to determine x without any loss of accuracy is $\log_2 7 = 23.25$, or 23 iterations. Normally it is not necessary to perform that many iterations because there is some loss in accuracy in evaluating the function $f(x)$. Another advantage of this method is that it is not necessary to have the derivatives of f being continuous. Therefore yield surfaces with corners can be solved without any difficulty.

APPENDIX C

Method of Stress Calculation for Elastic Brittle Plastic Material

The methods of stress calculation discussed in Appendix A are for material models with well defined and smooth stress strain relationships. One of the material models used in this research is an elastic brittle plastic model as illustrated in Figure 3.3. Such a model is an idealization of the real behaviour of very sensitive material such as quick clay. The procedure to calculate stresses for this model differs from that of the methods presented in Appendix A since there is a discontinuity in the stress strain relationship of the material.

It is assumed that the material behaves elastically prior to the peak strength, the stresses can simply be calculated from Equation (2.37) using the elastic constitutive relationship which is stress independent. For post peak deformations, any of the methods discussed in Appendix A can be used because the material behaves in a perfectly plastic manner with well defined yield criteria and stress strain relationships. The problem here is at the transition of the stress state from peak strength to residual strength. Since the transition is not well defined in the model and in fact, no consistent mathematical law is available yet, an empirical approach is necessary.

In plasticity analyses, if the stress state is outside the yield surface, which is physically inadmissible, it is often assumed that the real stress state can be found by projecting the current stress state onto the yield surface. The sudden contraction of the yield surface after the peak strength has been mobilized for a brittle plastic material, will leave the state of stress outside the yield surface when the strength of the material has been decreased to residual. Therefore, it is assumed that the stress state after the peak strength will be the projection of the peak stress on to the yield surface. This method can be expressed mathematically as follows. Let $\langle \sigma \rangle^P$ and F^P be the stress state and yield criterion at peak strength and $\langle \sigma \rangle^R$ and F^R be the stress state and the yield criterion at residual strength, then:

$$F^P(\sigma^P) = 0 \quad (C.1a)$$

just before softening occurs and:

$$F^R(\sigma^R) = 0 \quad (C.1b)$$

just after softening has occurred.

The difference in stresses $\langle d\sigma \rangle$ is assumed to be perpendicular to the yield surface at the residual stress state. That is:

$$\langle d\sigma \rangle = \lambda \left\{ \frac{\partial F^R}{\partial \sigma}(\sigma) \right\} \quad (C.2)$$

where

λ is an undetermined constant, and σ is the current state of stress which initially is the state of stress at peak strength.

$$\text{Since } dF = \left\langle \frac{\partial F}{\partial \sigma} \right\rangle \{d\sigma\} \quad (C.3a)$$

$$\text{and } dF = F^R(\sigma) - F^P(\sigma)$$

$$= F^R(\sigma) \quad (C.3b)$$

where $F^R(\sigma)$ is evaluated at the current stress state,

From Equation (C.3b) and (C.2), the value of λ can be evaluated.

$$F^R(\sigma) = \left\langle \frac{\partial F}{\partial \sigma} \right\rangle \lambda \left\{ \frac{\partial F}{\partial \sigma} \right\}$$

$$\text{and } \lambda = \frac{F^R(\sigma)}{\left\langle \frac{\partial F}{\partial \sigma} \right\rangle \left\{ \frac{\partial F}{\partial \sigma} \right\}} \quad (C.4)$$

The change in stresses is therefore given by:

$$\{d\sigma\} = \frac{F^R(\sigma)}{\left\langle \frac{\partial F}{\partial \sigma} \right\rangle \left\{ \frac{\partial F}{\partial \sigma} \right\}} \left\{ \frac{\partial F}{\partial \sigma} \right\} \quad (C.5)$$

$$\text{and } \{\sigma\} = \{\sigma\}^P + \{d\sigma\} \quad (C.6)$$

If $\{\sigma\} = \{\sigma\}^R$, then dF will be zero and $\langle d\sigma \rangle$ will also be zero.

Since $\langle d\sigma \rangle$ in Equation (C.6) is dependent upon the current state of stress $\langle \sigma \rangle$, Equation (C.6) must be solved by an iterative process. Therefore at any iteration i , the current stress is calculated from:

$$\{\sigma_i\} = \{\sigma_{i-1}\} + \{d\sigma_{i-1}\} \quad (C.7)$$

This method of stress calculation is illustrated graphically in Figure C.1

This method of stress calculation is not only restricted to use in elastic brittle plastic material, it can also be used in finite element plasticity analysis in making corrections to the stress state whenever it is outside the yield surface (Zienkiewicz 1972). Although the methods discussed in Appendix A provide fairly accurate stress calculation procedures, it is not uncommon that the state of stress lies outside the yield surface. It is important that the yield criteria should be satisfied as accurately as possible because this error will be accumulated during the analysis and may eventually lead to numerical instability or incorrect results. This procedure can be combined with the methods in Appendix A to ensure that the yield criteria are satisfied at all times in the analysis. It is noted that the stress increments calculated using this procedure may violate the flow rule locally but actually, the flow rule is undefined at this discontinuity on the stress strain relationship.

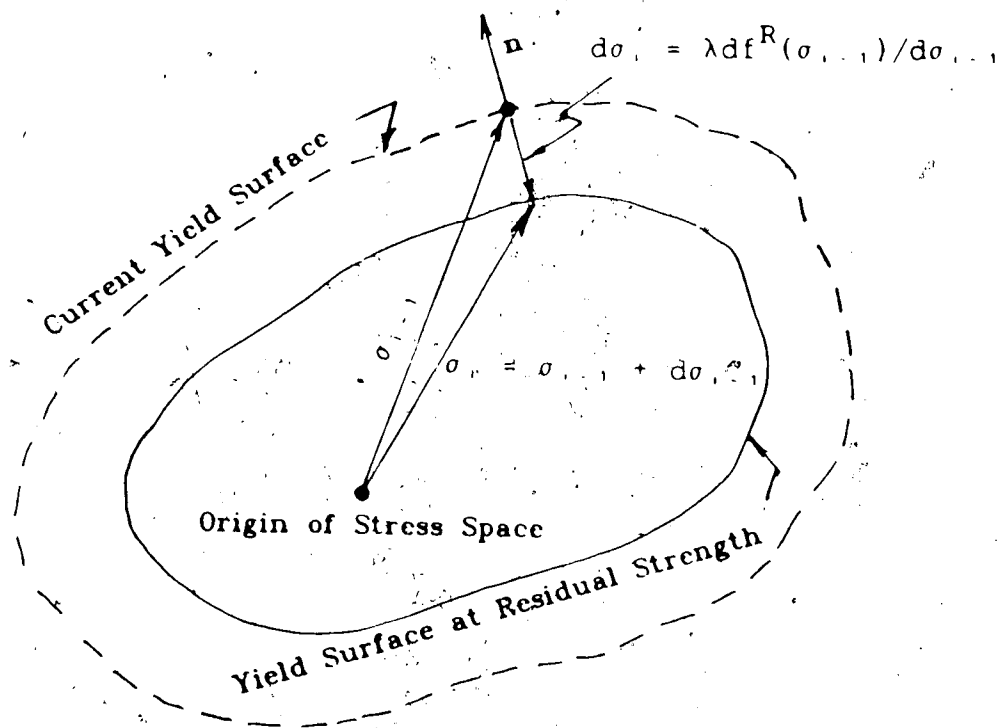


Figure C.1: Stress Calculation Method for
Elastic Brittle Plastic Material

All these methods of stress calculation are available in the computer program SAFE.

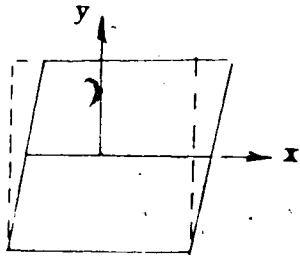
APPENDIX D

Mechanics of Localized Deformation

The theory of localized deformation is based on the hypothesis that localization can be considered as a result of the instability in the constitutive relationship of the material (Rice 1976, 1980, Rudnicki, 1975, 1977, 1979). It is assumed that the constitutive relationship allows bifurcation to occur from an initial uniform deformation field to a non-uniform deformation field in a narrow band under conditions of continuing equilibrium and continuing homogeneous deformation outside the zone of localization. A state of deformation in which all the strain components are constant in a body is called homogeneous deformation. The conditions for shear band bifurcation will be derived from first principles below. The basic conditions that must be satisfied are compatibility and equilibrium which allow stress and strain discontinuities to occur across any arbitrary surface or surfaces.

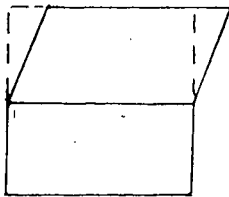
The study of discontinuous surfaces in continuum mechanics was pioneered by Hill (1961) and subsequently extended to study the propagation of waves in solids (1962). It has been shown that shear band type of localized deformation corresponds to a stationary wave with components of velocity being discontinuous across the front. Houlsby and Wroth (1980) have classified the mode of deformation into five main categories, see Figure D.1. The first type of

Continuity of



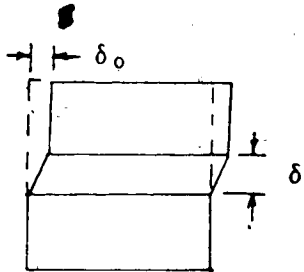
(i) All Quantities Continuous

$u, v, du/dx, dv/dx, du/dy, dv/dy$



(ii) Strain Discontinuous

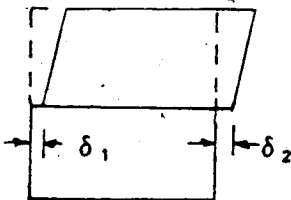
$u, v, du/dx, dv/dx$



(iii) Velocity Discontinuous

$u, v, du/dx, dv/dx$

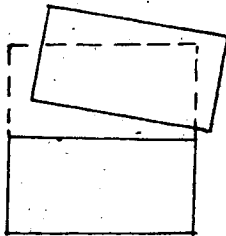
$\delta \rightarrow 0, \delta_0 \neq 0$



(iv) Rupture

$u, v, du/dx, dv/dx$

$\delta_1 \neq \delta_2$



(v) Fracture

none

Figure D.1: Compatibility Relationships of Discontinuity

deformation represents uniform deformation with all displacements and displacement gradients being continuous. Types 2 and 3 are cases with some components of displacements and displacement gradients being discontinuous. These two types are of interest in the present study because they represent the shear band type of bifurcation. The last two types involve rupture and fracture of material which will not be considered here. The compatibility equations for certain quantities (strain in this case) that are discontinuous across an arbitrary surface will be derived below.

Consider a function $f(x_j)$ in Cartesian coordinates x_j ($j=1,2,3$) which is required to satisfy the following conditions in region N and surface Σ in Figure D.2:

1. f is constant in Σ ;
2. f is continuous in N and on Σ ;
3. the first partial derivative (one side derivative) of f exists in N and is finite when approaching Σ .

The function f must have the following form:

$$\frac{\partial f}{\partial x_j} = \lambda \nu_j, \quad (D.1)$$

where

ν_j is the components of the unit normal of Σ and λ is an arbitrary scalar function.

Equation (D.1) can be proved as follows. Since f satisfied

conditions (2) and (3), therefore:

$$df = \frac{\partial f}{\partial x_j} dx_j, \quad (D.2)$$

exists in region N and on Σ .

From condition (1), f is constant on Σ , therefore,

$$df = 0,$$

$$\text{or } \frac{\partial f}{\partial x_j} dx_j = 0 \quad \text{on } \Sigma, \quad (D.3a)$$

for arbitrary dx_j satisfying:

$$\nu_j dx_j = 0. \quad (D.3b)$$

From Equation (D.3a) and (D.3b), $\frac{\partial f}{\partial x_j}$ must be in the direction of the unit normal ν_j , but its magnitude is undefined. Thus Equation (D.1) is obtained.

The result of Equation (D.1) can be generalized to a vector \bar{u} with components u_j ($j=1,2,3$). The above argument can be applied to the individual components of \bar{u} , therefore,

$$u_{i,j} = \lambda_i \nu_j. \quad (D.4)$$

The quantities \bar{u} can be interpreted as the infinitesimal displacements or velocities with x_j being the Lagrangian coordinates.

The discussion so far is restricted to a function f being defined in region N and on surface Σ . Let us now consider a surface of discontinuity Σ separating a body into

two regions N_1 and N_2 as shown in Figure D.2. The function f is assumed to satisfy conditions (2) and (3) but not necessarily (1). That is, f is continuous across Σ but the one-side derivative can be discontinuous across Σ and f can vary along Σ . Consider the function f_1 in region N_1 to be denoted as f_1 on one side of Σ and being continuous across Σ with the first derivative also continuous across Σ . The value of f_1 in region N_1 will not be the same as the actual value of f in region N_1 , which is denoted as f_2 , and the difference is given by $(f_2 - f_1)$ as shown in Figure D.2b. The difference $(f_2 - f_1)$ vanishes on Σ (since f is continuous), thus satisfying condition (1), and it also satisfies conditions (2) and (3) in region N_1 because both f_1 and f_2 are continuous functions in N_1 and on Σ , and the first derivative of $(f_2 - f_1)$ is finite on Σ . Therefore from Equation (D.1), it follows that:

$$\frac{\partial(f_2 - f_1)}{\partial x_j} = \lambda \nu_j, \quad (D.5a)$$

$$\text{or} \quad \frac{\partial f_2}{\partial x_j} - \frac{\partial f_1}{\partial x_j} = \lambda \nu_j, \quad (D.5b)$$

must be satisfied on Σ at the N_1 side. Since $\frac{\partial f}{\partial x_j}$ is continuous across Σ , Equation (D.5b) represents the change in $\frac{\partial f}{\partial x_j}$ from the region N_1 to N_2 . The jump in $\frac{\partial f}{\partial x_j}$ across the surface of discontinuity is denoted by Δ and rewriting

Equation (D.5b) as:

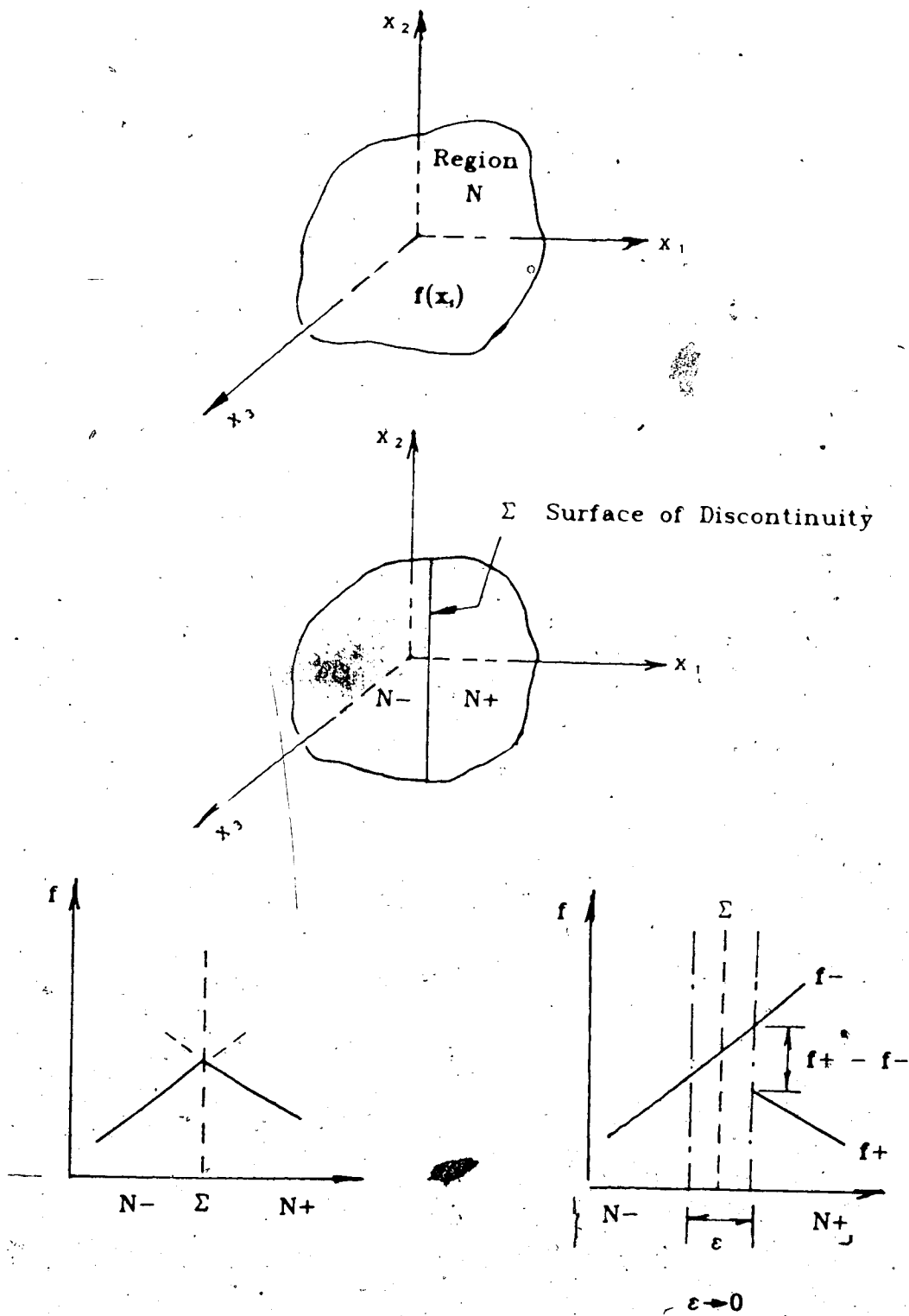


Figure D.2: Body with one Surface of Discontinuity

$$\Delta \left[\frac{\partial f}{\partial x_j} \right] = \lambda \nu_j, \quad (D.6)$$

Equation (D.6) indicates that the change in the gradient of f between the discontinuous surface and the adjacent region must be proportional to the direction of the normal of the discontinuity. Generalizing the above result to a vector \bar{u} with \bar{u} being not necessarily constant on Σ , gives:

$$\Delta[u_{i,j}] = \lambda_i \nu_j. \quad (D.7)$$

Equation (D.7) is the compatibility relationship that must be satisfied at the surface of the discontinuity. It must be emphasized that the functions u_i in Equation (D.7) must be continuous across the discontinuity Σ , therefore, it is only applicable to discontinuity types (ii) and (iii) in Figure D.1.

The equilibrium requirement at the discontinuity is given by:

$$\nu_i \Delta \sigma_{ij} = 0, \quad (D.8)$$

where

$\dot{\sigma}_{ij}$ is the material time derivative of the Cauchy stress tensor;

ν_i are the components of the unit normal;

and Δ denotes the difference of the stresses within the discontinuity and the outside field.

Equation (D.8) can be shown as follows.

Rewriting (D.8) as:

$$\nu_i (\dot{\sigma}_{ij} - \dot{\sigma}_{ij}^o) = 0$$

where the superscript "o" denotes the stress field at the discontinuity and "°" denotes the outside field. Then,

$$\nu_i \dot{\sigma}_{ij} = \nu_i \dot{\sigma}_{ij}^o.$$

Since $\nu_i \dot{\sigma}_{ij}$ is the traction rate on the surface of the discontinuity, when equilibrium is satisfied, it must be equal to the traction $\nu_i \dot{\sigma}_{ij}^o$ of the outside fields. Hence Equation (D.8) is obtained.

Equation (D.8) is valid because the variation of stress field within the discontinuity is restricted by the compatibility relation of Equation (D.7) which allows variation of the velocity gradient across the discontinuity only.

D.2 Restriction on the Constitutive Relationship for the Discontinuity

The two basic conditions that must be satisfied at incipient localization were discussed in the previous section. Let us study the consequences of the above conditions on the constitutive relationships of the discontinuity. Rewriting Equation (D.7) in terms of the velocity gradient:

$$\Delta u_{i,j} = \lambda_{ij} \nu_j, \quad (D.9)$$

and from Equation (D.8):

$$\nu \dot{\Delta \sigma}_{ij} = 0. \quad (D.10)$$

Since the rate of the Cauchy stress tensor is not invariant under rigid body rotation, it is convenient to introduce the Jaumann stress rate defined as:

$$\overset{\nabla}{\sigma}_{ij} = \dot{\sigma}_{ij} - \sigma_{ik} \Omega_{kj} - \sigma_{jk} \Omega_{ki}, \quad (D.11)$$

where

$\Omega_{ij} = 1/2(\dot{u}_{i,j} - \dot{u}_{j,i})$ is the spin tensor.

Assume that the constitutive relationship is of the form:

$$\overset{\nabla}{\sigma}_{ij} = C_{ijmn} D_{mn}, \quad (D.12)$$

where

$D_{ij} = 1/2(\dot{u}_{i,j} + \dot{u}_{j,i})$ is the velocity strain tensor; and C_{ijmn} is the incremental modulus tensor.

It can be shown that $\overset{\nabla}{\sigma}_{ij}$ and D_{ij} are energy conjugates.

From Equation (D.12), the constitutive relationship at the discontinuity is given by:

$$\overset{\nabla}{\sigma}_{ij} = C_{ijmn} D_{mn}^i, \quad (D.13)$$

and the outside field is given by:

$$\overset{\nabla}{\sigma}_{ij} = C_{ijmn} D_{mn}^o. \quad (D.14)$$

From Equation (D.11), rewriting the Cauchy stress rate in terms of the Jaumann stress rate and substituting it into the equilibrium equation, Equation (D.10), one obtains:

$$\nabla \nu_i [(\sigma_{ij} + \sigma_{ik} \Omega_{kj} + \sigma_{jk} \Omega_{ki}) - \nabla (\sigma_{ij} + \sigma_{ik} \Omega_{kj} + \sigma_{jk} \Omega_{ki})] = 0, \quad (D.15)$$

Substituting Equations (D.13) and (D.14) into (D.15):

$$\nu_i [(C_{ijmn} D_{mn}^1 - C_{ijmn}^0 D_{mn}^0) + (\sigma_{ik} \Omega_{kj} - \sigma_{ik}^0 \Omega_{kj}^0) + (\sigma_{jk} \Omega_{ki} - \sigma_{jk}^0 \Omega_{ki}^0)] = 0. \quad (D.16)$$

Since

$$D_{ij}^1 - D_{ij}^0 = 1/2(\dot{u}_{ij} - \dot{u}_{ji}^0) + 1/2(\dot{u}_{ji} - \dot{u}_{ij}^0),$$

and from Equation (D.7):

$$\dot{u}_{ij} - \dot{u}_{ji}^0 = \lambda_i \nu_j,$$

then,

$$D_{ij}^1 - D_{ij}^0 = 1/2(\nu_j \lambda_i + \nu_i \lambda_j),$$

or

$$D_{ij}^1 = 1/2(\nu_j \lambda_i + \nu_i \lambda_j) + D_{ij}^0. \quad (D.17)$$

Similarly,

$$\Omega_{ij}^1 = 1/2(\nu_i \lambda_j - \nu_j \lambda_i) + \Omega_{ij}^0. \quad (D.18)$$

Substitute Equation (D.17) and (D.18) into (D.16):

$$\nu_i [(C_{ijmn} (1/2(\nu_n \lambda_m + \nu_m \lambda_n) + D_{mn}^0) - C_{ijmn}^0 D_{mn}^0) + \{\sigma_{im} (1/2(\nu_m \lambda_j - \nu_j \lambda_m) + \Omega_{mj}^0) - \sigma_{im}^0 \Omega_{mj}^0\} + \{\sigma_{jm} (1/2(\nu_m \lambda_i - \nu_i \lambda_m) + \Omega_{mi}^0) - \sigma_{jm}^0 \Omega_{mi}^0\}] = 0. \quad (D.19)$$

Since

$$\nu_i (\sigma_{ik} \Omega_{kj}^0 - \sigma_{ik}^0 \Omega_{kj}^0) = \nu_i (\sigma_{ik} - \sigma_{ik}^0) \Omega_{kj}^0 = 0,$$

from Equation (D.10), and

$$\nu_i (\sigma_{jk} \Omega_{ki}^0 - \sigma_{jk}^0 \Omega_{ki}^0) = 0 ,$$

also

$$C_{ijmn} (1/2(\nu_n \lambda_m + \nu_m \lambda_n)) = C_{ijmn} \nu_n \lambda_m ,$$

because it is assumed that $C_{ijmn} = C_{ijnm}$, then Equation

(D.19) becomes:

$$\begin{aligned} & \nu_i (C_{ijmn} \nu_n \lambda_m) + \nu_i (C_{ijmn} - C_{ijnm}^0) D_{mn}^0 + \\ & 1/2 \nu_i \sigma_{jk} \nu_k \lambda_j - 1/2 \nu_i \sigma_{jk}^0 \nu_j \lambda_k + 1/2 \nu_i \sigma_{jk}^0 \nu_k \lambda_j - \\ & 1/2 \nu_i \sigma_{jk}^0 \nu_j \lambda_k = 0 . \end{aligned} \quad (D.20)$$

Also,

$$1/2 \nu_i \sigma_{jk}^0 \nu_k \lambda_j = (1/2 \nu_i \sigma_{jm}^0 \nu_m \delta_{kj}) \lambda_k$$

$$1/2 \nu_i \sigma_{jk}^0 \nu_k \lambda_j = (1/2 \nu_k \sigma_{jm}^0 \nu_m) \lambda_k$$

and $1/2 \nu_i \sigma_{jk}^0 \nu_j \lambda_k = 1/2 \sigma_{jk}^0 \lambda_k$ because $\nu_i \nu_i = 1$,

Equation (D.20) thus further reduced to:

$$\begin{aligned} & (\nu_i C_{ijmn} \nu_n) \lambda_m + 1/2 [(\nu_i \sigma_{jm}^0 \nu_m \delta_{kj}) \lambda_k - (\nu_i \sigma_{jk}^0 \nu_j) \lambda_k + \\ & (\nu_k \sigma_{jm}^0 \nu_m) \lambda_k - (\sigma_{jk}^0) \lambda_k] = \nu_i (C_{ijnm}^0 - C_{ijmn}) D_{mn}^0 \end{aligned}$$

$$\text{Let } A_{kj} = 1/2 (\nu_i \sigma_{jm}^0 \nu_m \delta_{kj} - \nu_i \sigma_{jk}^0 \nu_j + \nu_k \sigma_{jm}^0 \nu_m - \sigma_{jk}^0) ,$$

$$\therefore (\nu_i C_{ijmn} \nu_n + A_{mj}) \lambda_m = \nu_i (C_{ijnm}^0 - C_{ijmn}) D_{mn}^0 . \quad (D.21)$$

At incipient localization, if one assumes that the incremental moduli, C_{ijmn} , within the discontinuity is the same as that in the adjacent field, that is :

$$C_{ijmn} = C_{ijnm}^0 , \quad (D.22)$$

then Equation (D.21) simplifies to:

$$[\nu_i C]_{jmn} \nu_n + A_{mj}] \lambda_m = 0 . \quad (D.23)$$

For non-trivial solution of λ_k , that is for localization to occur, the following must be true:

$$\det[\nu_i C]_{jmn} \nu_n + A_{mj}] = 0 , \quad (D.24)$$

where

$\det| \quad |$ denotes the determinant of the matrix in bracket.

Equation (D.24) gives the constraints on the possible form of the constitutive relationship for the discontinuity at the incipient of localization. The term A_{mj} in Equation (D.24) is non zero when rotation of the material element is large. If small spin is assumed, that is:

$$\overset{\nabla}{\sigma}_{ij} \approx \sigma_{ij} ,$$

then $A_{mj} = 0$ and Equation (D.24) becomes:

$$\det[\nu_i C]_{jmn} \nu_n] = 0 . \quad (D.25)$$

The discussion here is restricted to only one surface of discontinuity, that is case (ii) in Figure D.1. Before discussing further implications of Equations (D.24) and (D.25), let us derive a similar set of equations for two surfaces of discontinuity which is type (iii) in Figure D.1.

D.3 Conditions for Localization with Two Surfaces of Discontinuity

Consider a body with two surfaces of discontinuity separating the body into three regions as shown in Figure D.3. The constitutive relationships for each region are given by:

$$\nabla \sigma^1_{ij} = C^1_{ijmn} D^1_{mn} \quad \text{for region 1;} \quad (D.26)$$

$$\nabla \sigma^2_{ij} = C^2_{ijmn} D^2_{mn} \quad \text{for region 2;} \quad (D.27)$$

$$\nabla \sigma^3_{ij} = C^3_{ijmn} D^3_{mn} \quad \text{for region 3.} \quad (D.28)$$

The compatibility relations at the discontinuities (1) and (2) are:

$$\Delta u^1_{ij} = \lambda^1_{ij} \nu^1_j \quad \text{at discontinuity (1);} \quad (D.29)$$

$$\text{and } \Delta u^2_{ij} = \lambda^2_{ij} \nu^2_j \quad \text{at discontinuity (2).} \quad (D.30)$$

Equilibrium conditions at discontinuities (1) and (2) are:

$$\nu^1_i \Delta \sigma^1_{ij} = 0 \quad \text{at discontinuity (1);} \quad (D.31)$$

$$\text{and } \nu^2_i \Delta \sigma^2_{ij} = 0 \quad \text{at discontinuity (2);} \quad (D.32)$$

The superscripts 1, 2 and 3 in Equations (D.26) to (D.28) denote the quantities in regions 1, 2 and 3 respectively while the superscripts 1 and 2 in Equations (D.29) to (D.32) denote the quantities at discontinuities 1 and 2 respectively.

For discontinuity 1, using Equations (D.26), (D.27), (D.29) and (D.31) and performing the same algebraic manipulations as that for the single discontinuity, one

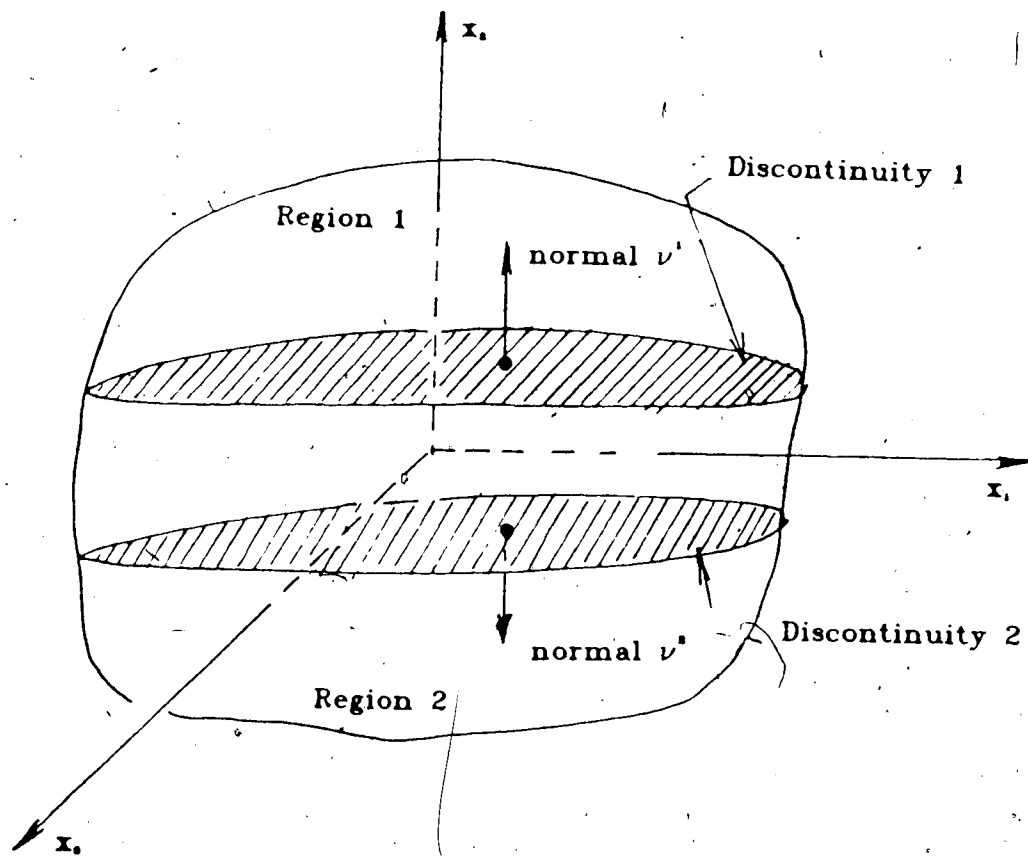


Figure D.3: Body with Two Surfaces of Discontinuity

obtains a similar expression for localization as Equation (D.21), namely;

$$(\nu | C_{jmn}^1 | \nu_n^1 + A_m^2) \lambda_m^1 = \nu | (C_{jmn}^1 - C_{jmn}^2) D_{mn}^1, \quad (D.33)$$

where

$$[A_m^2] = 1/2(\nu | \sigma_{jk}^1 | \nu_k^1 \delta_{mj} - \nu | \sigma_{jm}^2 | \nu_j^2 + \nu_m^1 \sigma_{jk}^2 | \nu_k^1 - \sigma_{jm}^1)$$

The double superscripts are explained below.

For discontinuity 2, since the stress field and strain field can vary in region 2 between the two discontinuities, the stress tensor in region 2 at discontinuity 1 may not be the same as that at discontinuity 2. The variation of stresses within region 2 is denoted as $d\sigma_{ij}^2$. Therefore:

$$\dot{\sigma}_{ij}^2 = \dot{\sigma}_{ij}^1 + d\sigma_{ij}^2, \quad (D.34)$$

where

$\dot{\sigma}_{ij}^1$ denotes the Cauchy stress rate tensor in region 2 at discontinuity 2;
and $\dot{\sigma}_{ij}^2$ denotes the quantity in region 2 at discontinuity 1.

Similar expressions are obtained for strain and incremental moduli. They are given by:

$$\dot{u}_{ij}^2 = \dot{u}_{ij}^1 + du_{ij}^2, \quad (D.35)$$

$$C_{jmn}^2 = C_{jmn}^1 + dC_{jmn}^2. \quad (D.36)$$

Using Equations (D.34), (D.35) and (D.36) in addition to the equilibrium and compatibility equations, Equations (D.32) and (D.30), and the constitutive relationships (D.27) and

(D.28), one obtains the following equations:

$$[\nu^i(C^i)_{mn} + dC^i_{jmn})\nu_n^2 + A^i_{jm} + dA_{jm}]\lambda_m^2 = \nu^i[C^i_{jmn} - (C^i)_{mn} + dC^i_{jmn}D_{mn}^i], \quad (D.37)$$

where

A^i_{jm} is the same as in Equation (D.33);

$$\text{and } dA_{jm} = 1/2(\nu^i d\sigma^i_k \nu_k^2 \delta_{jm} - \nu^i d\sigma^2_m \nu_j^i + \nu_m^2 d\sigma^i_k \nu_k^i - d\sigma^i_m).$$

Equations (D.33) and (D.37) thus become the governing equations for shear band initiation. Let us consider the following special cases:

D.3.1 Uniform Stress Field across the Shear Band

If the stress field and strain field are uniform across the shear band, then:

$$dC^i_{jmn} = 0 \quad \text{and} \quad d\sigma^i_j = 0^*,$$

$$\therefore dA_{jm} = 0.$$

Equation (D.37) reduces to:

$$[\nu^i C^i)_{mn} \nu_n^2 + A^i_{jm}]\lambda_m^2 = \nu^i(C^i_{jmn} - C^i)_{mn})D_{mn}^i. \quad (D.38)$$

D.3.2 Two Surfaces of Discontinuity are Parallel

If the two surfaces of discontinuity are parallel, then:

$$\nu^i = -\nu^i,$$

and Equation (D.38) is further reduced to:

$$[\nu(C^1_{ij})_{mn}\nu^1_n + A^2_m]\lambda^2_m = -\nu[(C^1_{ij})_{mn} - (C^2_{ij})_{mn}]D^1_{mn} \quad (D.39)$$

D.3.3 Uniform Stress Field outside the Shear Band

If we further assume the stress field outside the band is uniform, that is:

$$D^1_{mn} = D^2_{mn}, \quad \text{and} \quad C^1_{ijmn} = C^2_{ijmn},$$

then Equations (D.33) and (D.39) can be rewritten as:

$$[\nu(C^1_{ij})_{mn}\nu^1_n + A^2_m]\lambda^1_m = \nu[(C^1_{ij})_{mn} - (C^2_{ij})_{mn}]D^1_{mn}, \quad (D.40)$$

and

$$[\nu(C^1_{ij})_{mn}\nu^1_n + A^2_m]\lambda^2_m = -\nu[(C^1_{ij})_{mn} - (C^2_{ij})_{mn}]D^1_{mn}. \quad (D.41)$$

Equation (D.40) and (D.41) are identical equations if $\lambda^1_m = -\lambda^2_m$. Therefore, under the above assumptions, the governing equation for shear band bifurcation reduces to either Equation (D.40) or (D.41).

The above conditions are precisely the same as if the thickness of the region is reduced to zero. We see in this case that Equations (D.40) or (D.41) are identical to Equation (D.21) for a single discontinuity under the condition that the outside field is uniform. Therefore Equations (D.33) and (D.37) represent the general governing equations while Equation (D.21) is only a special case of (D.33) and (D.37).

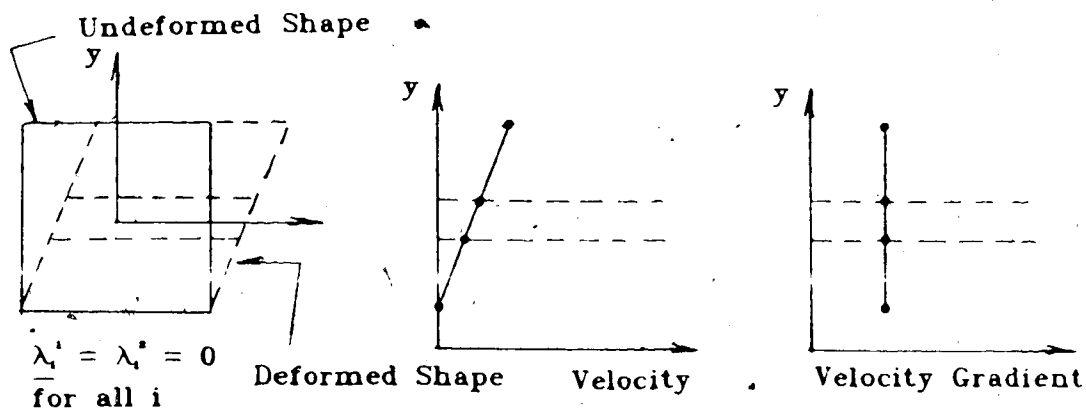
There are three possible solutions for λ^1_m and λ^2_m in Equations (D.33) and (D.37):

1. $\lambda^1_m = -\lambda^2_m = 0$ for all λ^1_m and λ^2_m ;

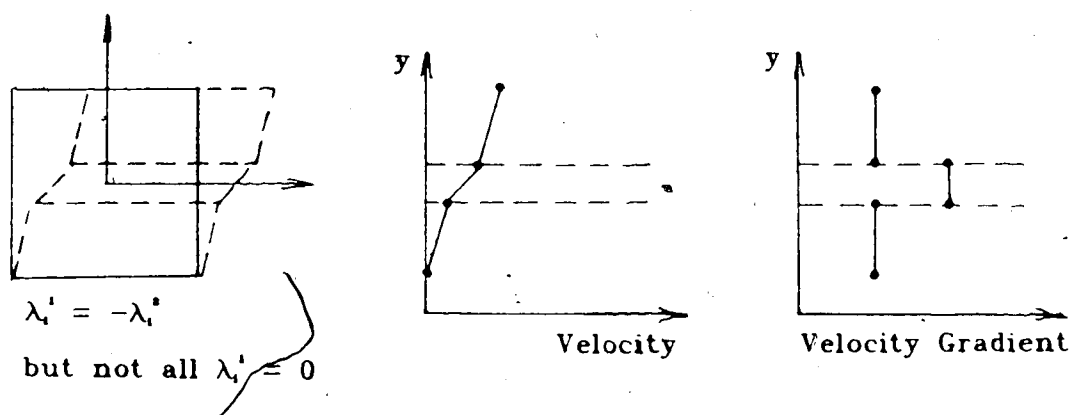
2. $\lambda_k^1 = -\lambda_k^2$ but not all $\lambda_k^1 = 0$ or $\lambda_k^2 = 0$;
3. $\lambda_k^1 \neq -\lambda_k^2$ for at least one λ_k^1 , and at least one λ_k^1 or one λ_k^2 not equal to zero.

The first solution is a trivial solution which indicates no shear band bifurcation as shown in Figure D.4a. The structure may undergo elastic or plastic deformation but the variation of velocity gradient throughout the domain is continuous (not necessarily constant as shown in Figure D.4a for simplicity). The second solution represents shear band bifurcation from a uniform field in which Equations (D.33) and (D.37) degenerate into one equation, Equation (D.21). The velocity gradient is discontinuous as shown in Figure D.4b. Even if the thickness of the shear band is reduced to zero, the velocity gradient is not necessarily continuous. The third solution can only be obtained by solving equations (D.33) and (D.37) simultaneously. This represents shear band bifurcation from a non-uniform stress field as shown in Figure D.4c.

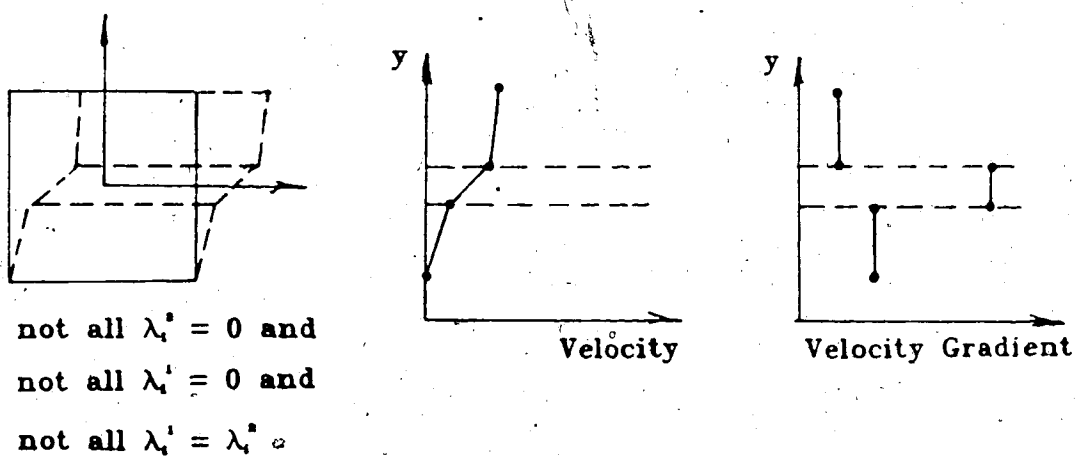
The first case is not particularly informative since it gives no real solution to the problem. The third case is difficult to solve because of the non-uniform variation of stresses both inside and outside the shear band. Most research effort is focused on the second case to explore the characteristic of shear bands.



(a) No Shear Band Bifurcation



(b) Shear Band Bifurcation from a Uniform Field



(c) Shear Band Bifurcation from a Non-Uniform Field

Figure D.4: Different Modes of Shear Band Bifurcation

APPENDIX E

Solution of a Non-symmetric Matrix using the Extended Skyline Method

E.1 Introduction

The use of the finite element method requires the solution of simultaneous algebraic equations. The basic equations can be written in matrix form as:

$$[K] \{U\} = \{R\} , \quad (E.1)$$

where $[K]$ is the stiffness matrix;

$\{U\}$ is the displacement vector;

$\{R\}$ is the load vector.

The stiffness matrix $[K]$ normally has the following properties:

1. $[K]$ is positive definite;
2. $[K]$ is banded;
3. $[K]$ is symmetric.

Many schemes have been proposed to obtain the solution for Equation (E.1) which makes use of the above properties of $[K]$. The analysis of strain softening material results in a stiffness matrix which does not necessarily have all of the above properties. That is:

1. $[K]$ is not necessarily positive definite;
2. $[K]$ is usually banded;

3. $[K]$ is not necessarily symmetric.

If the material model possesses strain softening behaviour, then the stiffness matrix $[K]$ can be non-positive definite as a result of the post peak deformation. When the non-associated flow rule is used in a plasticity formulation or in a fully undrained analysis, the matrix $[K]$ is no longer symmetric. However $[K]$ is usually banded and the number of non-zero elements above or below the diagonal of the matrix must be the same. Although $[K]$ is banded, there are still many zero elements within the bandwidth. The skyline method proposed by Bathe and Wilson (1976) makes use of this property of the stiffness matrix in which only calculation of the non-zero elements and some of the zero elements are performed. This results in a more efficient scheme in terms of the amount of in-core storage required and the computational time. However, the skyline method can only be used to solve symmetrical matrices. The extension of this method to non-symmetric matrices will be given below together with a brief review of the skyline method.

E.2 Direct Solution Scheme using Gauss-Elimination Method

A solution to Equation (E.1) can be obtained by using the Gauss-Elimination method. The solution is obtained by reducing the stiffness matrix $[K]$ into an upper triangular matrix and the vector $\{u\}$ can be determined by back substitution. Operations performed on matrix $[K]$ must also be done on $\{u\}$. Gauss elimination can be performed using

elementary matrices denoted by $[L_i^{-1}]$, where

$$[L_i^{-1}] = \begin{bmatrix} 1 & & & & \\ & \ddots & & & \\ & & 1 & & \\ & & -1 & \dots & 1 \\ & & -1 & \dots & 2 \\ & & & \ddots & \\ & & & & 1 \\ & & & & & 1 \end{bmatrix} \quad \begin{array}{l} \text{elements} \\ \text{not shown} \\ \text{are zeros} \end{array} \quad ; \quad (E.2)$$

$$-1_{i, j} = \frac{k_{i, j}^{(1)}}{k_{i, i}^{(1)}} ;$$

and $k_{m, n}^{(1)}$ is the element of the m -th row and n -th column of matrix $[K^{(1)}]$ and

$$[K^{(1)}] = [L_{i+1, i}^{-1}] \cdots [L_{1, 1}^{-1}] [K] , \quad (E.3)$$

where matrix $[L]$ is a lower diagonal matrix:

$$\begin{aligned} l_{ij} &= 1_{ij} & \text{if } i > j \\ &= 1 & \text{if } i = j \\ &= 0 & \text{if } i < j . \end{aligned}$$

Lower case letters and subscripts in this appendix represent the elements of the matrix and are not tensor quantities.

Therefore the summation convention for tensors does not apply here. If $[K^{(1)}]$ is pre-multiplied by $[L_i^{-1}]$, the elements in the i -th column of $[K^{(1)}]$ below the diagonal will be reduced to zero. Let

$$[L^{-1}] = [L_{n-1}^{-1}] \dots [L_1^{-1}] , \quad (E.4)$$

where n is the size of matrix $[K]$,
such that

$$[L^{-1}] [K] = [S] , \quad (E.5)$$

and $[S]$ is an upper diagonal matrix:

$$\begin{aligned} s_{ij} &= s_{ij} & \text{if } i \leq j \\ &= 0 & \text{if } i > j . \end{aligned}$$

Therefore pre-multiply Equation (E.1) by $[L^{-1}]$, then

$$[L^{-1}] [K] \{u\} = [L^{-1}] \{R\} , \quad (E.6)$$

and from Equation (E.5),

$$[S] \{u\} = [L^{-1}] \{R\} . \quad (E.7)$$

Since $[S]$ is an upper triangular matrix, $\{u\}$ can be solved from (E.7) by back substitution. It is assumed in Equation (E.2) that the matrix $[K^{(1)}]$ must not contain zero diagonal elements. Note that it is not necessary to have positive diagonal elements in matrix $[K^{(1)}]$, therefore non-positive definite matrices can be solved using this scheme. If $[K]$ is symmetric, then $[S]$ can be written as:

$$[S] = [D] [\tilde{S}] \quad (E.8)$$

where $[D]$ contains only the diagonal elements of $[S]$.

It can be shown easily that:

$$[\dot{S}] = [L] [\dot{L}]^T \quad (E.9)$$

However, for non-symmetric matrices, such convenient relationships cannot be found and both the matrices $[S]$ and $[L]$ must be determined.

E.3 Computer Implementation of the Extended Skyline Method

The solution scheme using the skyline method has been discussed in detail by Bathe and Wilson (1976). The elements of the stiffness matrix are stored in a one-dimensional array as shown in Figure E.1. The skyline of any column j is defined as the difference between j and the row number of the first non-zero element. Elements above the skyline are zero and they are not stored or being operated during the solution procedure. However, the zero elements below the skyline are stored and they usually become non-zero during the matrix reduction process. Since the matrix shown in Figure E.1 is symmetric, only half of the matrix $[K]$ is stored. To identify the corresponding elements of matrix $[K]$ in array A , the addressing of the diagonal elements of A must be determined. The array MAXA stores all the addressing of the diagonal elements of A . The relationship between the addressing for any element in array A and the matrix $[K]$ is given in Figure E.1.

For non-symmetrical matrices, it is clear that all of the non-zero elements above or below the diagonal of the matrix $[K]$ must be stored. The storage scheme is very similar to the case for a symmetric matrix and is shown in

Half Bandwidth

| <-----> |

$$[K] = \begin{bmatrix} k_{11} & k_{12} & k_{13} & 0 & 0 & 0 & 0 & 0 & 0 \\ & k_{22} & k_{23} & 0 & k_{25} & k_{26} & 0 & 0 & 0 \\ & & k_{33} & k_{34} & 0 & k_{36} & 0 & 0 & 0 \\ & & & k_{44} & k_{45} & k_{46} & k_{47} & 0 & 0 \\ & & & & k_{55} & k_{56} & 0 & 0 & k_{59} \\ & & & & & k_{66} & 0 & k_{68} & k_{69} \\ & & & & & & k_{77} & k_{78} & k_{79} \\ & & & & & & & k_{88} & k_{89} \\ & & & & & & & & k_{99} \end{bmatrix} ; k_{ij} = k_{ji} ;$$

symmetric

$$\{A\} = \begin{bmatrix} a(1) & a(3) & a(6) & & & & & & \\ & a(2) & a(5) & & a(12) & a(17) & & & \\ & & a(4) & a(8) & a(11) & a(16) & & & \\ & & & a(7) & a(10) & a(15) & a(21) & & \\ & & & & a(9) & a(14) & a(20) & & a(29) \\ & & & & & a(13) & a(19) & a(24) & a(28) \\ & & & & & & a(18) & a(23) & a(27) \\ & & & & & & & a(22) & a(26) \\ & & & & & & & & a(25) \end{bmatrix}$$

symmetric

$$MAXA = \langle 1, 2, 4, 7, 9, 13, 18, 22, 25, 30 \rangle$$

$$k_{ij} = a(L) \quad \text{where } L = MAXA(j) + j - i \quad \text{if } i \leq j$$

$$\text{and } L = MAXA(i) + i - j \quad \text{if } i > j$$

Figure E.1: Reduced Storage Scheme of the Skyline Method

Figure E.2. It is assumed that the number of non-zero elements below and above the skyline are the same. That is the form of the matrix is symmetric but the values of the elements are not necessarily the same.

To obtain a solution of $\{u\}$ using Equation (E.7), both the $[S]$ and $[L]$ matrices must be determined. The stiffness matrix $[K]$ can be written as:

$$[K] = [L] [S] \quad (E.10)$$

After the reduction process, both the $[S]$ and $[L]$ matrices are conveniently stored in the same storage location for matrix $[K]$. That is the elements above and including the diagonal elements will be replaced by the elements of matrix $[S]$, and the elements below the diagonal elements by matrix $[L]$.

Let us consider reducing a typical column and row of matrix $[K]$ into the corresponding column and row of matrices $[S]$ and $[L]$ as shown in Figure E.3. It is assumed that the elements above and to the left of this typical row i and column i respectively, contain the elements of matrices $[S]$ and $[L]$ described earlier. The objective is then to reduce this row i and column i . Once the solution scheme for this typical row and column has been established, then the procedure can be repeated for the entire matrix.

The Gauss-elimination process using the elementary matrices described by Equations (E.2) to (E.5) is used to perform the following operations. In order to eliminate the

Half Bandwidth

|<----->|

$$[K] = \begin{bmatrix} k_{11} & k_{12} & k_{13} & 0 & 0 & 0 & 0 & 0 & 0 \\ k_{21} & k_{22} & k_{23} & 0 & k_{25} & k_{26} & 0 & 0 & 0 \\ k_{31} & k_{32} & k_{33} & k_{34} & 0 & k_{36} & 0 & 0 & 0 \\ 0 & 0 & k_{43} & k_{44} & k_{45} & k_{46} & k_{47} & 0 & 0 \\ 0 & k_{52} & 0 & k_{54} & k_{55} & k_{56} & 0 & 0 & k_{59} \\ 0 & k_{62} & k_{63} & k_{64} & k_{65} & k_{66} & 0 & k_{68} & k_{69} \\ 0 & 0 & 0 & k_{74} & 0 & 0 & k_{77} & k_{78} & k_{79} \\ 0 & 0 & 0 & 0 & 0 & k_{86} & k_{87} & k_{88} & k_{89} \\ 0 & 0 & 0 & 0 & k_{95} & k_{96} & k_{97} & k_{98} & k_{99} \end{bmatrix} ; k_{ij} \neq k_{ji} ;$$

$$\{A\} = \begin{bmatrix} a(1) & a(3) & a(6) & & & & & & \\ a(49) & a(2) & a(5) & & a(12) & a(17) & & & \\ a(48) & a(47) & a(4) & a(8) & a(11) & a(16) & & & \\ & & a(46) & a(7) & a(10) & a(15) & a(21) & & \\ a(45) & a(44) & a(43) & a(9) & a(14) & a(20) & & a(29) & \\ a(42) & a(41) & a(40) & a(39) & a(13) & a(19) & a(24) & a(28) & \\ & & a(38) & a(37) & a(36) & a(18) & a(23) & a(27) & \\ & & & a(35) & a(34) & a(22) & a(26) & & \\ & & & a(33) & a(32) & a(31) & a(30) & a(25) & \end{bmatrix}$$

$$MAXA = \langle 1, 2, 4, 7, 9, 13, 18, 22, 25, 30 \rangle$$

$$k_{ij} = a(L) \quad \text{where } L = MAXA(j) + j - i \quad \text{if } i \leq j$$

$$\text{and } L = 2 MAXA(n+1) - MAXA(i+1) + 2i - j - n - 1 \quad \text{if } i > j$$

n = size of the $[K]$ matrix.

Figure E,2 Reduced Storage Scheme of the Extended Skyline Method

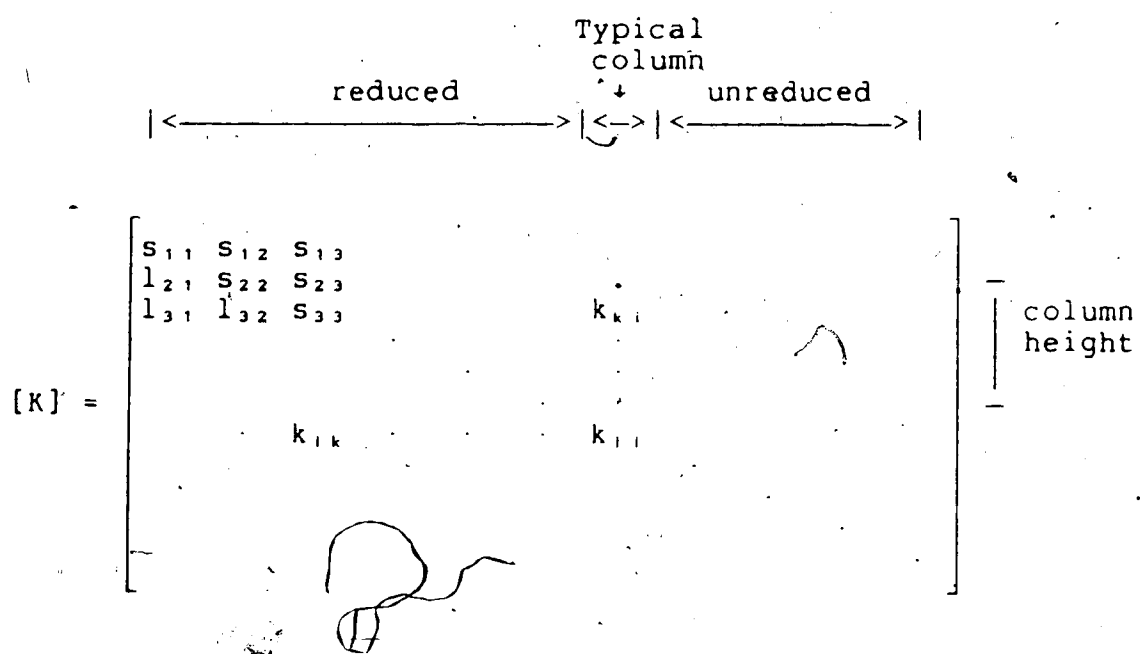


Figure E.3 Matrix Reduction using Gauss Elimination Method

non-zero elements of matrix [K] below the diagonal in row i and column j , where $i > j$ and $k_{ij} \neq 0$, k_{ij} is subtracted from row j multiplied by the pivot k_{ij}/s_{jj} , where k_{ij} is the element of [K] to be reduced to zero and s_{jj} is the diagonal element of the j -th row of the upper triangular matrix [S]. The subtraction is performed for every element in row i . Therefore for a typical element above the diagonal in column i which is to be reduced to matrix [S], the operation required is:

$$s_{ij} = k_{ij} - \sum_{t=m_j}^{i-1} l_{it} s_{tj} \quad \text{for } i < j \quad (\text{E.11})$$

where m_j is the first non-zero element of column j .

All the quantities in Equation (E.9) are defined since it is assumed that all the elements of the [L] and [S] matrices to the left and above the column j and row i are known.

To obtain the matrix [L], a similar procedure is followed. By defining:

$$g_{ij} = k_{ij} - \sum_{t=m_j}^{j-1} l_{it} s_{tj} \quad (\text{E.12})$$

where m_j is the column number of the first non-zero element of row i , and:

$$l_{ij} = g_{ij} / s_{jj}, \quad \text{for } i > j \quad (\text{E.13})$$

and for the diagonal elements:

$$s_{ij} = g_{ij} = k_{ij} - \sum_{t=m_j}^{i-1} l_{it} s_{it} \quad (E.14)$$

The quantities s_{ij} , l_{ij} , s_{ij} will replace the corresponding elements of the original stiffness matrix. It is noted that the [S] matrix is calculated by column and the [L] matrix is calculated by row. This procedure is in harmony with the storage scheme used in storing the elements of the stiffness matrix.

Once the [S] and [L] matrices are determined, the load vector on the right side of Equation (7) can be calculated.

Let

$$\{V\} = [L] \{R\} \quad (E.15)$$

then

$$v_i = r_i - \sum_{t=m_i}^{i-1} l_{it} v_t \quad (E.16)$$

where $v_i = r_i$

and $i = 2, 3, \dots, n$;

m_i = first non-zero element of row i ;

n = size of vector $\{R\}$.

The calculation progresses from the first element of $\{R\}$ to the last element of $\{R\}$ and all the quantities in Equation (E.16) are known. Once the vector $\{R\}$ has been reduced using Equation (E.15) and (E.16), the unknown displacements can be obtained by back substitution,

$$u_i = y_i - \sum_{j=i+1}^n a_{ij} u_j \quad (E.17)$$

Since the process of matrix reduction and back substitution can be performed independently in the computer program, this scheme can be very effective when the modified Newton-Raphson iterative procedure is used. The matrix reduction process need only be performed once and solution can be obtained by reduction of the load vector and back substitution. Since the operations for load vector reduction and back substitution processes require the same amount of effort for non-symmetrical matrices as for symmetrical matrices, this can lead to substantial saving in computer time. A listing for the source code of the Subroutine SOLVER in Fortran IV is given in Figure E.4.

```

1 SUBROUTINE SOLVER(A,V,MAXA,NEO,KKK,IOUT)
2 P R O G R A M
3 TO SOLVE NON-SYMMETRIC FINITE ELEMENT STATIC EQUILIBRIUM
4 EQUATION IN CORE, USING COMPACTED STORAGE AND COLUMN
5 REDUCTION SCHEME
6 INPUT VARIABLES -
7 A(NMK) - STIFFNESS MATRIX STORED IN COMPACTED FORM
8 V(NEO) - RIGHT-HAND-SIDE LOAD VECTOR
9 MAXA(NMK) - VECTOR CONTAINING ADDRESSES OF DIAGONAL
10 ELEMENT OF STIFFNESS MATRIX OF A
11 NEO - NUMBER OF EQUATIONS
12 NMN - NUMBER OF ELEMENTS BELOW SKYLINE & DIAG. OF MATRIX
13 KKK - INPUT FLAG
14 NMN - INPUT FLAG
15 EQUAL 1 TRIANGULARIZATION OF STIFFNESS MATRIX
16 EQUAL 2 REDUCTION AND BACK-SUBSTITUTION OF LOAD VECTOR
17 EQUAL OTHER INTEGER DO BOTH
18 IOUT1 - OUTPUT DEVICE NUMBER
19
20 C
21 C
22 C
23 C
24 C
25 C
26 C
27 C
28 C
29 C
30 MAXA2=2*MAXA(NEO+1)
31 IF(KKK.EQ.2) GO TO 30
32 DO 15 JCOL=1,NEO
33 KU=MAXA(JCOL+1)-1
34 KL=MAXA(JCOL)+1
35 KH=KU-KL
36 IF(KH) 14,8,1
37 1 K=JCOL-KH
38 KLT=KH
39 DO 4 J=1,KH
40 KLT=KLT-1
41 K1=MAXA2-MAXA(K+1)+K-NEO-1
42 NO-MAXA(K+1)-MAXA(K)-1
43 IF(NEO) 4,4,2
44 2 NO-MINO(J,NO)
45 AA=O.DO
46 DO 3 L=1,NO
47 3 AA=AA+(K1+L)*A(KLT+L)
48 A(KLT)=A(KLT)-AA
49 K=K+1
50 5 KN=MAXA2-MAXA(JCOL+1)+JCOL-NEO-1
51 KLT=KN+KH
52 K=JCOL-KH+1
53 A(KLT+1)=A(KLT+1)/A(MAXA(K))
54 IF(KH) 14,13,8
55 6 DO 11 J=1,KH

```

```

56 K=K+1
57 NO-MAXA(K+1)-MAXA(K)-1
58 IF(NEO) 11,11,7
59 7 NO-MINO(J,NO)
60 AA=O.DO
61 K1=MAXA(K)
62 DO 9 L=1,NO
63 9 AA=AA+(K1+L)*A(K1+L)
64 A(K1)=A(K1)-AA/A(MAXA(K))
65 11 KLT=KLT-1
66 AA=O.DO
67 K1=MAXA(JCOL)
68 NO-KH+1
69 DO 12 L=1,NO
70 12 AA=AA+(K1+L)*A(K1+L)
71 A(K1)=A(K1)-AA
72 GO TO 14
73 13 A1MAXA(JCOL)=A1MAXA(JCOL)-A1KN+1)*A(MAXA(JCOL)+1)
74 14 IF(A1MAXA(JCOL)) EQ 0 DO GO TO 889
75 CONTINUE
76 IF(KKK EQ 1) RETURN
77 C
78 C
79 C
80 DO 18 JCOL=1,NEO
81 KH=MAXA(JCOL+1)-MAXA(JCOL)-1
82 IF(KH) 18,18,18
83 16 K1=MAXA2-MAXA(JCOL+1)+JCOL-NEO-1
84 AA=O.DO
85 DO 17 K=1,KH
86 17 AA=AA+(K1+K)*V(JCOL-K)
87 V(JCOL)=V(JCOL)-AA
88 CONTINUE
89 C
90 C
91 C
92 K1=NEO
93 DO 21 JCOL=1,NEO
94 KLT=NEO-JCOL+1
95 KL=MAXA(KLT)+1
96 KU=MAXA(KLT+1)-1
97 V(KLT)=V(KLT)/A(MAXA(KLT))
98 IF(KU KL) 21,19,19
99 K=K1
100 AA=V(KLT)
101 DO 20 L=KL,KU
102 K=K+1
103 20 V(K)=V(K)-A(L)*AA
104 21 K1=K1-1
105 RETURN
106
107 999 WRITE(OUT,1,20) JCOL,A1MAXA(JCOL)
108 STOP
109 201 FORMAT(//,2X, ' STOP - STIFFNESS MATRIX NOT POSITIVE. '
110 1 ' DEFINITE',//,2X, ' NON POSITIVE PIVOT FOR EQUATION ',18,
111 2 '//, ' PIVOT = ',E20.12)
112 END

```

Figure E.4: Listing of Subroutine SOLVER